

Human Retinal Oximetry using Hyperspectral Imaging

by

Ied Alabboud



Submitted for the Degree of
Doctor of Philosophy
at Heriot-Watt University
on Completion of Research in the
School of Engineering and Physical Sciences
Dec 2009

The copyright in this thesis is owned by the author. Any quotation from the thesis or use of any of the information contained in it must acknowledge this thesis as the source of the quotation or information.

Abstract

The aim of the work reported in this thesis was to investigate the possibility of measuring human retinal oxygen saturation using hyperspectral imaging. A direct non-invasive quantitative mapping of retinal oxygen saturation is enabled by hyperspectral imaging whereby the absorption spectra of oxygenated and de-oxygenated haemoglobin are recorded and analysed. Implementation of spectral retinal imaging thus requires ophthalmic instrumentation capable of efficiently recording the requisite spectral data cube. For this purpose, a spectral retinal imager was developed for the first time by integrating a liquid crystal tuneable filter into the illumination system of a conventional fundus camera to enable the recording of narrow-band spectral images in time sequence from 400nm to 700nm. Post-processing algorithms were developed to enable accurate exploitation of spectral retinal images and overcome the confounding problems associated with this technique due to the erratic eye motion and illumination variation.

Several algorithms were developed to provide semi-quantitative and quantitative oxygen saturation measurements. Accurate quantitative measurements necessitated an optical model of light propagation into the retina that takes into account the absorption and scattering of light by red blood cells. To validate the oxygen saturation measurements and algorithms, a model eye was constructed and measurements were compared with gold-standard measurements obtained by a Co-Oximeter. The accuracy of the oxygen saturation measurements was $(3.31\% \pm 2.19)$ for oxygenated blood samples. Clinical trials from healthy and diseased subjects were analysed and oxygen saturation measurements were compared to establish a merit of certain retinal

diseases. Oxygen saturation measurements were in agreement with clinician expectations in both veins ($48\% \pm 9$) and arteries ($96\% \pm 5$). We also present in this thesis the development of novel clinical instrument based on *IRIS* to perform retinal oximetry.

Acknowledgements

I would like to thank all the people who have contributed to this work. First I would like to thank my supervisor Professor **Andy Harvey** who introduced me to the vast field of spectral imaging and gave continuing support during my years of here at Heriot-Watt University. I would like to thank him for his excellent scientific guidance, for reviewing and correcting all my thesis drafts and for his encouragement.

I would like to thank the clinical scientists in the ophthalmology unit at Cheltenham general hospital, Professor Andy McNaught and Dr. David Mordant for their valuable clinical comments.

My warm thanks to Dr Gonzalo Muyo for his unlimited support and advice.

My thanks to Al-baath University in Syria for funding me during this study.

Declaration

This thesis has been composed by myself in the Department of Electrical, Electronic and computer Engineering, Heriot-Watt University and has not been accepted in any previous application for a degree. The work reported in this thesis was carried out entirely by myself, the contributions made to my research by collaborators have been acknowledged in the course of the thesis. The sources of information have been distinguished and acknowledged by means of references.

Important contributions were made in the following areas:

1. Chapter 3: Sonny Ramachanran initiated the modifications to the fundus camera (integrating the liquid crystal tuneable filter into the camera body) but because of his unfortunate death, the rest of modifications and development to the system were carried out by me.
2. Chapter 9: As part of the research to investigate and analyse retinal images recorded from diseased subjects, the camera system was moved to Cheltenham General Hospital. Clinical data and comments were provided by our collaborators: David Mordant and Prof Andy McNaught.
3. Chapter 10: The modification and development of the snapshot camera was achieved by Dr.Gonzalo Muyo. Clinical data and snapshot images were recorded in Cheltenham General Hospital.

Ied AlAbboud

Nov 2009

List of publications

1. I. Alabboud, D.Mordant, A. I. McNaught, A.R.Harvey, "Time sequential technique for retinal blood oximetry".
2. I. Alabboud, D.Mordant, G. Muyo, A. I. McNaught, A.R.Harvey, "Model eye for retinal blood oximetry: validation and accuracy".
3. G. Muyo, I.Alabboud,A. Gorman, D. Mordant, A. McNaught, A. R. Harvey, "Snapshot hyperspectral imaging for blood oximetry in retinal vasculature".
4. A.R.Harvey, I.Alabboud, A.Goreman, A.McNaught, S.Ramachandran, E.Theofanidou, Spectral imaging of the retina. *Proc. SPIE* 6047:604713/1-604713/9, 2005.
5. I.Alabboud, G. Muyo, A. Gorman, D. Mordant, A. McNaught, C.Petres, Y. R. Petillot, A. R. Harvey, "New spectral imaging techniques for blood oximetry in the retina. *Proc. SPIE*, 6631: 66310L, 2007.
6. I.Alabboud, A.McNaught, D.Mordant, and A. R. Harvey," Quantitative Spectral Imaging of the Retina", Invest. Ophthalmol. Vis. Sci,48: E-Abstract 2581, 2007.
7. D. J. Mordant, I. Alabboud, A. R. Harvey, and A. I. McNaught, "Hyperspectral Imaging of the Human Retina-Oximetric Studies". Invest. Ophthalmol. Vis. Sci, 48: E-Abstract 148, 2007.
8. G. Muyo, A. Gorman, I. Alabboud, D. J. Mordant, A. I. McNaught, and A. R.Harvey, "En Face Snapshot Spectral Imaging of the Retina". Invest. Ophthalmol. Vis. Sci, 48: E-Abstract 2582, 2007.

9. A. R. Harvey, E. Theofanidou, I. AlAbboud, M. Graham, and A. C. Hargreaves,” Spectral Imaging of the Rat Retina”. Invest. Ophthalmol. Vis. Sci, 48: E-Abstract 3844, 2007.
10. A. R. Harvey, G. D. Muyo, I. Alabboud, A. Gorman, D. Mordant, and A. I. McNaught, “ Development of a Clinical Snapshot Spectral Imaging Camera for Blood Oximetry”. Invest. Ophthalmol. Vis. Sci, 49: E-Abstract 4256, 2008.
11. D. J. Mordant, I. Alabboud, A. R. Harvey, and A. I. McNaught, “Retinal Vessel Oximetry Using Hyperspectral Imaging in Retinovascular Disease”. Invest. Ophthalmol. Vis. Sci, 49: E-Abstract 4263, 2008.
12. A. I. McNaught, D. J. Mordant, I. Alabboud, P. A. Ritchie, G. D. Muyo, and A. R. Harvey. “Development of a Model Eye to Validate Oximetric Measurements in the Human Retinal Vasculature Using Hyperspectral Imaging”. Invest. Ophthalmol. Vis. Sci, 49: E-Abstract 921, 2008.
13. D. J. Mordant, I. AlAbboud, G. D. Muyo, A. R. Harvey, and A. I. McNaught, “Retinal Vessel Oxygen Saturation Measurements in Asymmetrical Primary Open Angle Glaucoma Using Hyperspectral Imaging”. Invest. Ophthalmol. Vis. Sci, 50: E-Abstract 5803, 2009.
14. G. Muyo, I. Alabboud, A. Gorman, D. J. Mordant, A. I. McNaught, and A. R. Harvey,”Two-dimensional Snapshot Spectral Imaging for Blood Oximetry in Retinal Vasculature. Invest. Ophthalmol”. Vis. Sci, 50: E-Abstract 3303, 2009.

Contents

Chapter 1

Introduction.....	1
1.1 Introduction to Hyperspectral imaging	1
1.2 Spectral imaging techniques	3
1.3 Retinal oximetry	6
1.3.1 The principle of oximetry	7
1.3.2 Retinal oximetry: historical developments	9
1.4 Summary	24
1.5 Aims of the research	25
1.6 Conclusion	28

Chapter2

The eye	30
2.1 The Anatomy of Eye	30
2.2 The retina	30
2.3 Blood supply of the retina.....	32
2.4 Retinal oxygen	36
2.5 Retinal diseases.....	37
2.5.1 Diabetic retinopathy	37
2.5.2 Glaucoma	38
2.5.3 Retinal vein occlusion.....	38
2.6 Fundus reflectance	39
2.7 Conclusion	44

Chapter3

Instrument Construction

3.1 Fundus camera	45
3.2 Optical system description.....	45
3.3 Time sequential technique implementation	46
3.3.1 Liquid Crystal Tunable Filter (LCTF)	47
3.4 Instrument construction	49
3.4.1 LCTF integration	50
3.4.2 Glare and black dot relocation	51
3.4.3 Field of view	53
3.4.4 Data flow and system control	54
3.5 LCTF spectral bands	57
3.6 CCD detector chip	59
3.7 Conclusion	63

Chapter 4

Calibration and image registration.....	64
4.1 Image processing and data analysis	64
4.2 Calibration	65
4.2.1 Dark images	67
4.2.2 Camera function.....	69
4.3 Image Registration	70
4.3.1 Retinal image registration method	72
4.3.2 Steps in image registration.....	75
4.3.2.1 Pre-processing.....	75
4.3.2.2 Feature selection	75
4.3.2.3 Image Enhancement.....	76
4.3.2.4 Cross-correlation.....	80
4.3.3 Validation of co-registration algorithm	84
4.3.3.1 Vessel tracking and fitting to a centre line	84
4.3.3.2 Registration accuracy evaluation	85
4.3.3.3 Results.....	87
4.4 Conclusion	91

Chapter5

Light propagation and oximetric techniques	93
5.1 Light propagation in the eye	93
5.2 Absorption	95
5.2.1 Ocular media.....	95
5.2.2 Melanin	96
5.2.3 Blood.....	96
5.3 Scattering	98
5.4 Lambert-Beer's Law	98
5.5 Modified Lambert-Beer Law	99
5.6 Principle of oximetric measurement	101
5.6.1 Two wavelength oximetry	102
5.6.2 Three-wavelength oximetry	104
5.6.3 Optical model of the fundus layers and the primary optical paths	106
5.7 Wavelength selection and error minimizing.....	113
5.7.1 Photometric error	115
5.7.2 Optimum selection for two-wavelength oximetry	117
5.7.3 Optimum selection for three-wavelength oximetry	120
5.7.4 Optimum selection for multiple wavelength oximetry (76 & 16 bands) ..	122
5.8 Conclusion	124

Chapter 6

Semi-quantitative oximetry	127
6.1 Spectral processing techniques	127
6.1.1 Principle component analysis (PCA)	129
6.1.2 Linear Spectral Unmixing	130
6.2 Semi-quantitative oximetry	132
6.2.1 Optical density map	134
6.2.2 Endmember selection	140
6.3 Results	143
6.3.1 Retinal Vein Occlusion	147
6.3.2 Retinal Artery Occlusion	148
6.3.3 Asymmetrical Primary Open Angle Glaucoma	149
6.4 Conclusion	150

Chapter 7

Image processing and data analysis towards quantitative oximetry	152
7.1 Optical density measurement	153
7.2 Vessel tracking	154
7.2.1 Fast marching algorithm	155
7.2.2 Nonlinear mapping	156
7.2.3 Fast marching algorithm	157
7.3 Transmission profile extraction	158
7.4 Fitting transmission profiles to a model	161
7.5 Non-linear fit to a physical model	169
7.6 Error sources and error quantification	171
7.6.1 Reproducibility of optical density measurement	171
7.6.2 The effect of background non-uniformity on optical density measurements	175
7.6.3 The effect of finite bandwidth of LCTF transmission bands	182
7.7 Conclusion	184

Chapter 8

Model eye	186
8.1 Background	186
8.2 Construction of the artificial eye	187
8.3 Experimental set-up and acquisition of spectral images	191
8.4 Ray-tracing simulation of the artificial eye	194
8.5 Spectral analysis for blood oximetry: physical model of light propagation in the retina	195
8.6 Results	198
8.6.1 Experimental calculation of the optical path length η	198
8.6.2 Oxygen saturation measurements using empirical scattering function	200
8.6.3 Oxygen saturation measurements assuming constant scattering	204
8.7 Conclusion	205

Chapter 9

Quantitative retinal oximetry of healthy and diseased subjects.....	207
9.1 Retinal blood vessels	207
9.2 Recording the spectral cube	208
9.3 Measurement of retinal vessel oxygen saturation.....	209
9.3.1 Measuring oxygen saturation in normal (healthy) subjects	209
9.3.2 Reproducibility	215
9.3.3 Ischemia – related retinal diseases	217
9.4 Conclusion	230

Chapter 10

Chapter 10	231
IRIS:Image Replicating Imaging Spectrometer	231
10.1. Introduction.....	231
10.2. Instrumentation: Retinal oximeter	232
10.3. Post-processing and data analysis.....	238
10.4. Retinal oximetry	239
10.4.1 Semi-quantitative retinal oximetry	240
10.4.2 Quantitative oximetry using two-wavelength.....	241
10.5. Conclusion	243

Conclusion and future work	245
---	------------

Appendix A.....	254
-----------------	-----

Appendix B.....	258
-----------------	-----

Appendix C.....	260
-----------------	-----

Chapter 1

Introduction

Spectral imaging is a relatively modern technique with applications in many fields such as medicine, geology, chemistry, physics, meteorology and many potential machine vision applications. This section will provide an introduction to spectral imaging, and highlight reasons which justify why hyperspectral imaging (HSI) could be used as a diagnostic tool for detection of retinal diseases. The most common spectral techniques applied to the retina are then presented. Finally, the principles and historical development of retinal oximetry are reviewed.

1.1 Introduction to Hyperspectral imaging

Spectral imaging is an extended form of spectroscopy in which two-dimensional spatial mapping can be produced. This technique is able to record images with high spectral resolution information for each pixel in a scene (Magotra et al. 1999). It is a powerful tool in geographical information systems (GIS), which enables remote classification of: for example, crops and mineral deposits using subtle spectral variations in scenes. Figure 1.1 shows the general concept of spectral imaging.

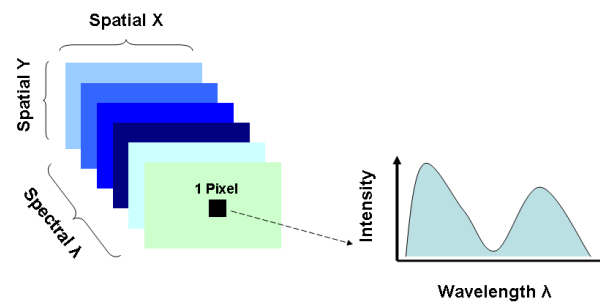


Figure 1.1: Spectral imaging.

This type of imaging provides advanced mapping solutions to solve complex environmental problems. The higher spectral resolution allows for improved determination of the composition of materials at a sub-pixel level. This simply means that even if an object is not spatially resolved in the scene, its spectral contribution can be detected and mapped. Spectral imaging is classified as a passive technique as it depends upon the sun or emission. Furthermore, in hyperspectral imaging, a large number of images is recorded from contiguous regions of the spectrum rather than disjointed with much finer resolution. As the resolution of spectrum sampling increases, great increase in information is provided.

Hyperspectral imaging holds great promise in the field of medicine and ophthalmology, where it can provide spectral information useful to scientists and clinicians alike. Potentially, HSI could be used to provide diagnostic information using a comfortable, rapid and noninvasive method. The importance of HSI arises from its ability to detect specific spectral signatures which can be attributed to changes in biochemical and metabolic processes. This technique may improve and accelerate the diagnosis of retinal diseases compared to other modalities such as optical coherence tomography and confocal-laser-scanning systems which provide information on the structure changes within the eye. For example, the detection of increased levels of the yellow pigments xanthophyll and lutein in the macula may lead to an earlier diagnosis of age related macular degeneration (ARMD) (Magotra et al. 1999). It has been shown that detection of the spectral signatures from oxygenated and de-oxygenated haemoglobin may provide an earlier indication of many other retinal diseases.

1.2 Spectral imaging techniques

Spectral imaging systems can be implemented by using electronically controlled devices such as acousto-optical tunable filters and liquid crystal tunable filters or passive devices such as diffractive optics and *IRIS* (Image Replicating Imaging Spectrometer). Regardless of the instrument used, the output data form is an image spectral cube (two spatial dimensions and wavelength as the third dimension) including the full spectral response at every pixel in a two-dimensional scene. Spectral imaging techniques can be divided conveniently into two rough classes: direct or indirect. In direct techniques, the spectrum is recorded directly in which each pixel detects only radiation of a particular wavelength for the duration of scene integration time. These techniques depend on wavelength selective elements such as a prism or bandpass filter. Indirect methods adopt an inversion of measured intensities to recover spectral information for which a pixel records multiple frequencies during scene integration. The Fourier transform imaging spectrometer (FTIS) is an example of the latter approach. Three-dimensional data cube construction involves recording two of the dimensions and scanning the third dimension in time sequence. For direct imaging, this entails, recording either the whole spectrum of a linear array of pixels in a single snapshot and then spatially scanning through the scene or, alternatively, acquiring the complete scene (two-dimensional image) in a single exposure, and then stepping through wavelengths sequentially. It is possible to filter the light incident on or emerging from the object for spectral content.

Similarly, Fourier transform spectral imaging can either produce a two-dimensional scene through a time-sequentially scanned interferometer (typically a Michelson interferometers, although birefringent interferometers may also be used (Harvey & Holmes, 2004), or obtain the spectrum of one of the spatial dimensions through a one

dimensional imaging static Fourier-transform spectrometer (Truitt et al. 2000) and construct the data cube in a time sequential spatial scan.

There are a small number of snapshot techniques that enable recording of two-dimensional spectral and spatial information in a single exposure. Examples of such techniques are: (a) the image replicating imaging spectrometer (*IRIS*) (Harvey et al. 2002; Alabboud et al. 2007). *IRIS* is a spectral demultiplexer that employs polarizing interferometry and Wollaston prism polarizing beam splitters to simultaneously replicate images of the object in multiple spectral bands onto a single detector array; (b) Computer tomographic imaging spectrometer (CTIS) (Descour et al. 1997; Johnson et al. 2007) which employs a holographic element to spectrally smear images followed by computer algorithms for reconstruction of a spectral data cube and (c) dichroic filters to spectrally demultiplex an image into a small number spectral bands on a single detector array (Beach et al. 1999; Hardarson et al. 2006; Aloni et al. 2002).

The selection of spectral imaging techniques for the retina varies with the objective needed to be achieved (Harvey et al. 2005). One-dimensional techniques enable spectral imaging of a single line in the retina to be recorded in a single snapshot (Hammer et al. 1997). This offers an advantage by eradicating the spectral distortion associated when narrowband images are recorded in time sequence. However, a one-dimensional field of view is a major disadvantage of such techniques when applied on the retina in which an extended two-dimensional field of view suits the clinician's desire for routine retinal disease screening. Time sequential imaging techniques enable recording of the two-dimensional images of the retina that need to be registered in software to produce a spectral cube. Recording spectral images in time

sequence allows the number of recorded retinal images to be reduced to the minimum necessary, in which only images which contain the most useful spectral information can be acquired. Furthermore, in contrast to Fourier-transform spectral imaging where the light is filtered between the eye and the detector, the light is filtered before illuminating the retina, so the light intensity at the retina, and the associated discomfort and safety for the patient, is minimised. Spectral and spatial snapshot techniques present the possibility of acquiring two-dimensional spectral images of the retina in single snapshot with increased patient comfort and simplified calibration procedures.

Whichever spectral imaging method is employed, spectral retinal images show different contrast variations across the wavelength due to the spectral properties and spatial distribution of retinal chromophores.

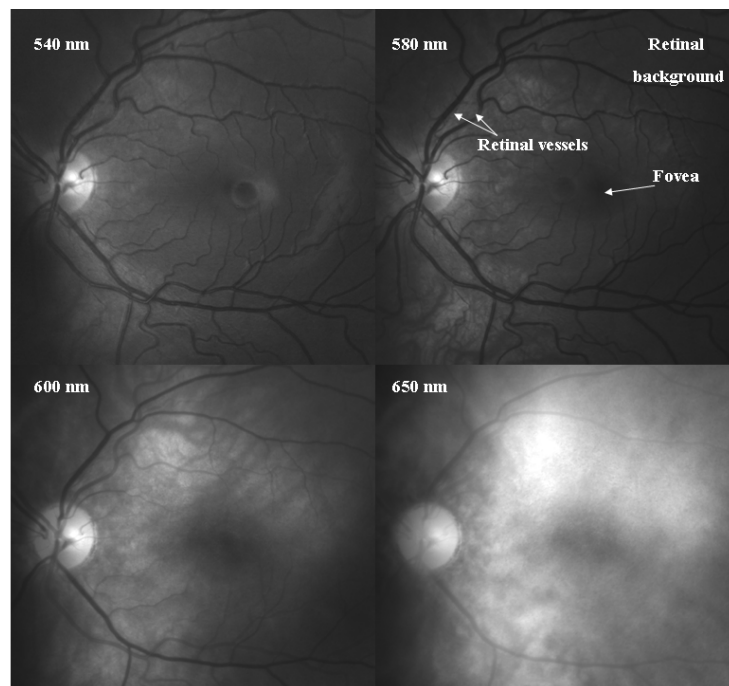


Figure1.2: Retinal images at four different wavelengths.

As can be seen in Figure 1.2(which shows spectral retinal images recorded by our system), retinal vessels show the greatest contrast from the surrounding retinal tissue in the region 540-580 nm. As wavelengths are increased (more than 600 nm), lower

contrast is noticed. The wavelength dependence of image appearance arises due to the absorption properties of the retinal chromophores, most significantly the blood.

1.3 Retinal oximetry

As the proper functioning of the retina depends on the availability of an adequate amount of oxygen, measuring the amount of oxygen present in the retinal vessels can be extremely valuable to detect and monitor some diseases such as glaucoma and diabetic retinopathy. The principal chromophore of blood is haemoglobin which is a special protein contained in red blood cells, *RBCs*, and responsible for delivering oxygen to the organs via the cardiopulmonary system. For our purposes, the most crucial information is how blood interacts with light. As light propagates through a blood sample, absorption and scattering take place. The absorption is due to the haemoglobin contained in the red blood cells and scattering is due to the discontinuities of refractive indices between *RBCs* and the plasma in which they are suspended. The absorption characteristics of blood can be expressed by the extinction coefficients of haemoglobin (Assendelft, 1970) which can be found into two states: oxygenated (HbO_2) and deoxygenated (Hb). Figure 1.3 shows the specific extinction coefficients of HbO_2 and Hb . All oxygen saturation measurements in this project are based on these values. Various approaches have been undertaken to non-invasively measure the oxygen saturation of blood in the retina and retinal vessels. Blood oxygen saturation is estimated based on the variation of blood spectra with oxygen saturation.

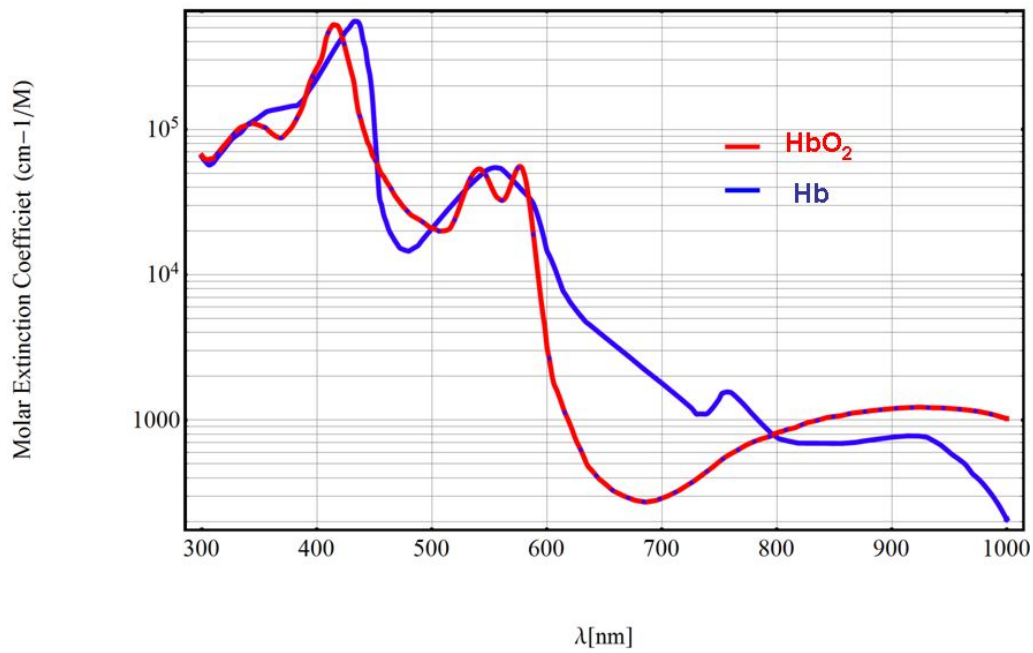


Figure 1.3: Extinction coefficient of oxygenated and deoxygenated haemoglobin.

An understanding of the layout of the retina is important to perform quantitative assessment of retinal chromophores. There are two primary vascular networks that provide retina with nutrition: the choroid and the retinal vessels. The choroid lies beyond the outer retina, with a capillary bed in contact with the retinal pigment epithelium. Retinal vessels occupy the inner half of the neural retina, extending outward from the optic disc in all directions. As the wavelength of illuminating light changes, light penetrates to different depths throughout the retina in which wavelengths between 530-580 nm illuminate the retinal background and retinal vessels. However, as wavelength increases ($\lambda > 600$ nm), light penetrates the retinal vessels and background to reach the choroid at $\lambda > 640$ nm.

1.3.1 The principle of oximetry

Oximetry is a specific application of spectroscopy that uses spectral information to deduce the oxygen saturation in blood. Assuming blood can be spectrally

characterized as comprising fully oxygenated haemoglobin (HbO₂) and de-oxygenated haemoglobin (Hb), the oxygen saturation OS is defined as:

$$OS = \frac{C_{HbO_2}}{C_{HbO_2} + C_{Hb}}, \quad (1-1)$$

where C_{HbO_2} , C_{Hb} are the molar concentrations of oxygenated and deoxygenated haemoglobin respectively.

A spectral sample of blood can be decomposed into a linear combination of the two components oxygenated and deoxygenated haemoglobin. Probably the most common application of oximetry is the pulse oximeter, which can continuously monitor arterial blood oxygenation by measuring the optical transmission at the fingertip. In the absence of scattering, the attenuation of light by a blood sample can be characterised as a linear sum of the attenuation by each component. This is the familiar Lambert-Beer relation, describing the measured attenuation A :

$$A(\lambda) = \sum_{i=1}^n \varepsilon_{ai}(\lambda) \cdot c_i \cdot d_i, \quad (1-2)$$

where ε_a is the extinction coefficient due to absorption at wavelength λ , c is the concentration of the chromophors, d is the straight path-length travelled by the photon through the sample, and i denotes the individual chemical species in which the light travels. Measuring the attenuation at several wavelengths equal to the number of chromophores is sufficient to calculate the concentration of each particular chromophor. Within scattering tissues, such as the retina, the path length is not well defined, rather, there is a distribution revealing a wide range of paths travelled. Therefore, to characterize the absolute chromophor concentration changes in a highly turbid media, it has been suggested that a modified Beer-Lambert law, which uses a multiple optical-path parameter η , can be applied. When the extinction in the media is

both scattering and absorptive, the modified Beer-Lambert law, as expressed in (1-3), includes the parameter S due to scattering losses, implying that the attenuation is a non-linear function of $\varepsilon_a C$. As a result, measuring the attenuation at multiple wavelengths is necessary to estimate the concentration of chromophores. In blood oximetry three wavelengths are sufficient when the scattering is assumed to be independent of wavelength.

$$A(\lambda) = \sum_{i=1}^n S_i(\lambda) + \varepsilon_{ai}(\lambda) \cdot c_i \cdot \eta_i \cdot d_i(\lambda) \quad (1-3)$$

1.3.2 Retinal oximetry: historical developments

Several study groups have employed the existing spectroscopic techniques to measure retinal blood oxygen saturation, which involves detecting the difference in light absorption between oxygenated and deoxygenated haemoglobin using multiple wavelength reflectance oximetry. As a result, numerous dual- and multiple-wavelength combinations sensitive to oxygen saturation have been utilized in various imaging systems. Consequently, a variety of analysis techniques have been described to calculate the oxygen saturation in retinal vessels. In the following section, we present a overview historical development of the existing spectral techniques to measure oxygen saturation in the retina.

1.3.2.1 Gloster: fundus reflectance oximetry:

Gloster presented one of the early reports on how the reflectance of different colours of light from the choroid changes with oxygen saturation (Gloster et al. 1967; Broadfoot et al. 1961). Three filters were used to filter the incident light and a

photomultiplier was used to amplify the light reflected from the eye. Experiments were performed to measure the amount of light reflected back from a model eye when the concentration and oxygenation of blood are altered. Results showed a change in reflectance for red and cyan colours as oxygenation and concentration changed. Experiments were performed on animals and humans. These experiments were one of the first descriptions of effects of oximetric changes on monochromatic fundus reflectance. However, it was not possible to establish quantitative measurements of oxygen saturation using these techniques.

1.3.2.2 Laing: the choroidal eye oximeter and photographic eye oximeter

A choroidal eye oximeter was developed by Laing et al. (1975) to measure choroidal blood oxygen saturation. Two wavelengths, one centred at 650 nm and isosbestic wavelength at 805 nm, were used to image the retina. The ratio of reflected light at each wavelength was used to calculate the oxygen saturation of choroidal blood. Results on humans showed an increase in choroidal saturation as the oxygen content in the room increased. A photographic oximeter was later developed by Laing et al. (1975) to measure the oxygen saturation in retinal circulation at different oxygen saturations in rabbits. Two interference filters at 470 and 515 nm were used to filter the reflected light from the fundus. Images at two wavelengths were recorded simultaneously on photographic films. Experiments were performed whereby the systemic oxygen saturation was systematically reduced and femoral artery samples were measured using a clinical oximeter to determine the actual oxygen saturation. Subsequent to this, Laing and Cohen (Cohen et al. 1976) compared the experimental calibration curve from the rabbit experiments to a calibration curve derived theoretically with the use of an improved retinal oximetry model based on Lambert-

Beer's law. The scattering by red blood cells was considered in a modified model using Twersky's theory (Twersky, 1970a; 1970b), although the reflecting layers of the fundus were assumed to be specular.

1.3.2.3 Hickam Technique

Hickam (1963) established a photographic method to estimate the oxygen saturation of retinal veins in humans. Two-wavelength imagers were assembled for this purpose, to illuminate the fundus with two wavelengths combinations: centred at 640 and 800 nm and 640 and 505 nm. In these systems, images of an extended area of the retina were sequentially acquired and recorded on photographic films. The developed films were used to produce absorption profiles with a microdensitometer as it was scanned perpendicularly across blood vessels. Based on experiments conducted on a model vessel, light was assumed to pass the vessels twice as having been reflected off underlying layer of the fundus. The optic disc in Hickam setup acted as the reflective background. Optical density measurements were performed for all the wavelengths and used to calculate the optical density ratios of the retinal vessels. The use of isobestic wavelengths simplified data reduction by obtaining a linear relationship between optical density ratios and oxygen saturation. The estimation of the oxygen saturation in retinal veins was determined from *in vivo* human experiments. This involved measuring the optical density ratios of retinal arteries in human subjects whose arterial oxygen saturation was altered by changing the inspired oxygen content through the use of various gas mixtures of oxygen and nitrogen. It was assumed that a non-scattering sample causes a calibration procedure to compensate for the finite effects of scattering on the measurement. The oxygen saturation of arterial blood was determined by analysis of brachial artery blood samples at the time of imaging and

was monitored during the imaging using an ear oximeter. Imaging of each subject during the calibration involved using both wavelength combinations. The average retinal venous oxygen saturation was calculated at 58 ± 10 % and 60 ± 16 % for the (640, 505 nm) pair. *In vitro* experiments were performed to validate the oximetric technique which involved obtaining images of heparinised venous blood samples at 640 and 800 nm from 4 normal subjects. The venous oxygenation was altered by exposing the venous blood to air and mixing it with venous blood not exposed to air. Oxygen saturation of Samples was determined using a photometric method (Hickam et al. 1949). Glass capillaries with internal diameters of 250 and 500 μm were used to hold the blood samples in front of a white background. A linear relationship between red-infrared optical density ratios and the measured oxygen saturation of blood samples was confirmed. The standard deviations of the optical density ratios from the measured oxygen saturation were relatively small: 6% and 9% oxygen saturation in 500 and 250 μm capillaries respectively. The two-wavelength photographic oximetry technique was limited by the influence of vessel diameter on oxygen saturation estimation. This was highlighted in the *in vitro* experiments where it was noted that changes in the internal diameter of the glass capillaries (path length) influenced the regression slop.

1.3.2.4 Pittman and Duling technique

Pittman and Duling (Pittman et al. 1975) studied the effect of scattering on oxygen saturation measurements by separating the concentration and pathlength in the saturation equation. Their technique was not developed directly for application to retinal oximetry. Three wavelengths were used, in which two of them were isobestic

wavelengths. The advantage of using two isobestic wavelengths was to estimate and eliminate the scattering contribution from the optical model. These three wavelengths must be closely placed across the considered range in which the scattering term can be assumed approximately constant. According to the modified Lambert-Beer law and considering two isobestic wavelengths, two equations at the isobestic wavelengths were used to derive the value of scattering. Accordingly, the scattering was a combination of known and measurable quantities, allowing for simple determination of the scattering. The previous linear relationship between oxygen saturation and optical density ratio was then used after compensating for the scattering effect. The linearity was also investigated over a range of hematocrit (3-34 %) and optical path lengths (0.1-2 mm) for the same wavelength range and found to be insensitive to the variations. The applicability of this method is restricted to a limited range of green band wavelengths which have been found less than optimal to perform retinal oximetry in terms of accuracy (Smith 1999). This technique was applied to oxygen saturation measurements on small blood vessels in hamster retractor muscles with a reported accuracy of 4.8% oxygen saturation.

1.3.2.5 Delori technique

Delori presented a three-wavelength photoelectric oximeter to determine oxygen saturation in retinal vessels (Delori 1988). A fundus camera incorporating three interference filters was used with a photomultiplier and a photocathode. A motorized filter wheel was used to enable filtering of the light reflected from the fundus to be filtered into wavelengths centered at 558nm, 569 nm, and 586 nm (7-8 nm FWHM). A small area of the fundus was illuminated, enabling a selected part of the retinal vessel to be scanned using a slit. Thirty-two vessel profiles at each wavelength were

acquired from the line scans and a vessel tracking and registration algorithm was used to ensure that the examined profiles were aligned. The transmittance of each vessel profile was determined and optical density was calculated for each wavelength. Oxygen saturation calculations were based upon the method of transmission oximetry described by Pittman and Duling (Pittman et al. 1975). The algorithm used the vessel transmission measurements at three wavelengths and the extinction coefficient of oxygenated and deoxygenated haemoglobin. The effects of haemoglobin concentration, vessel diameter, light scattering and fundus pigmentation were integrated into the algorithm. Initially, *in vitro* measurements were performed on glass capillaries containing flowing whole human blood and were used to calibrate the instrument with respect to a co-oximeter. The accuracy of oxygen saturation calculations was reported to be most accurate in the range of 50-100 % oxygen saturation, but in the range between 0-50%, there was a tendency towards overestimating the saturation. In *In vivo* experiments, the average oxygen saturation in retinal arteries was 98 ± 8 % and 45 ± 7 % in retinal veins. The variability of oxygen saturation measurements was found to be caused by a number of factors: eye movements, fundus pigmentation, characteristics of the central retinal reflex, and vicinity of neighboring structures such as the optic disc.

1.3.2.6 Schweitzer technique: the imaging ophthalmo-spectrometer

An imaging ophthalmo-spectrometer was developed by Schweitzer et al. (1992) to analyze the spectral reflectance of pigments such as melanin, xanthophyll, and rhodopsin in the fundus. The reflectance spectrum in the range 450nm to 700 nm with spectral resolution 2 nm was acquired from a small area using a spectrograph (see Figure 1.4).

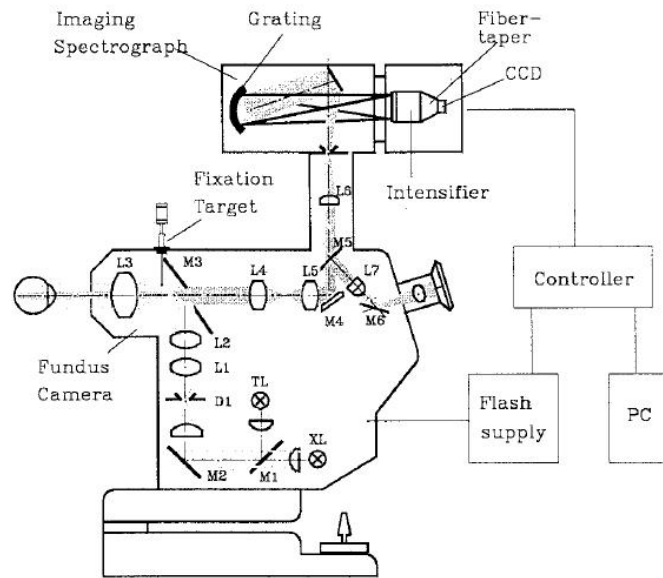


Figure 1.4 Schematic of imaging spectrometer (Schweitzer et al. 1999).

The system was also used to perform quantitative analysis of the retinal blood oxygen saturation (Schweitzer et al. 1999). The measurement of the oxygen saturation in retinal vessels involved extensive analysis of the properties of fundus reflectance and the multiple light pathways in the retina (Hammer et al. 2001). In calculating oxygen saturation, several parameters were taken into account, including the vessel size, hematocrit, reflectance of the fundus background, and specular reflection. The accuracy of the oxygen saturation was further improved by inclusion of complex algorithms to determine acceptance criteria for a given measured spectra, based on the image quality and signal-to-noise ratio (Thamm et al. 1998). The oximetry algorithm was applied on human subjects and the mean oxygen saturation of arterial blood found to be 92.2 ± 4.1 % and 57.9 ± 9.9 % for venous blood. Oximetry using the imaging ophthalmo-spectrometer was later applied on patients with dry and wet age-related macular degeneration (Schweitzer et al. 2000; 2001). Central retinal venous oxygen saturation was reported to be higher in the patients with age-related macular degeneration.

1.3.2.7 Smith: the Scanning laser eye oximeter

Smith et al. focused on the development of a prototype eye oximeter to study the effect of blood loss on retinal venous oxygen saturation, with a view to applying their technique to monitoring trauma patients (Smith et al. 1998). Two low power diode lasers emitting at 670 nm and 803 nm were initially used in the eye oximeter (EOX) to produce a line scan, 400 μ m in length, on a retinal vessel. A photodiode was used to measure the reflected light from the retina and blood vessel (see Figure 1.5).

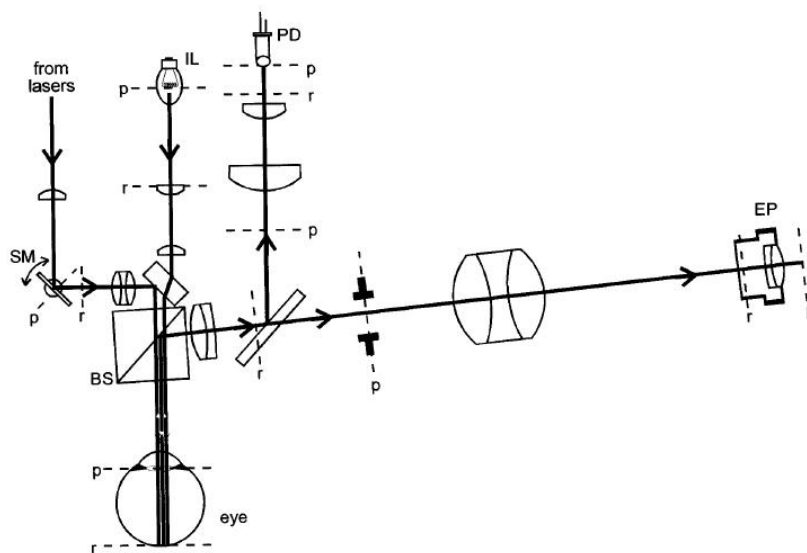


Figure 1.5: Schematic of the eye oximeter (Smith et al. 1998)

Optical densities were then calculated and the Lambert-Beer law was employed to calculate the oxygen saturation. The major limitation of this system was the ability to only measure the oxygen saturation of large ($> 50\mu$ m) retinal arteries and veins near the optic disc. This limitation was attributed to the use of the red and infrared wavelengths of light, of which less than 3% was reportedly absorbed by vessels smaller than 50μ m, thus occurring for difficulties and inaccuracies in vessel identification and oximetric calculations. Later, two modified versions of the eye

oximeter were produced. The modifications involved the inclusion of four diode lasers emitting at 629, 678, 821, 899 nm respectively for the first version (Drewes et al. 1999) and 488, 635, 670, and 830 nm for the second version (Smith et al. 2000). The selection of wavelengths is influenced by theoretical calculation and analysis of optimal wavelength combinations for accurate retinal oximetry (Smith, 1999). The modified eye oximeter illuminated the vessels with vertically polarized light and horizontally polarized light was recorded by the detector to reduce the specular reflection in the vessel wall (Denninhoff et al. 2000). A multiple scan at each wavelength across a single line on the retina was acquired and stored rapidly, but data reduction and calculation of oxygen saturation were done off-line. The device was compact, portable, and employed in a number of clinical studies (Smith et al. 1998; Denninghoff et al. 1997; Lompado et al. 2000). Although four wavelengths were available, oxygen saturation was typically determined depending on individual pairs of the lasers. Two-wavelength and three-wavelength oximetry were also considered by Smith to calculate the oxygen saturation in swine in a number of clinical studies. It was clearly demonstrated in clinical trials that the EOX was sensitive to changes in retinal vessel oxygen saturation, but reliable calibration of the system for normal physiological oxygenation levels was never achieved.

1.3.2.8 Beach: digital multispectral and hyperspectral imaging of the retina

A two-wavelength spectral imaging system was developed by Beach to measure the oxygen saturation in the retinal vasculature of diabetic subjects without clinical evidence of diabetic retinopathy, during a normoglycaemia and hyperglycaemia

(Tiedeman, 1998). An optical beam splitter was integrated into the system to enable the generation of two retinal images simultaneously, which were subsequently filtered using narrow bandpass interference filters centered at 569 nm and 600 nm with 4.5nm FWHM as shown in Figure 1.6.

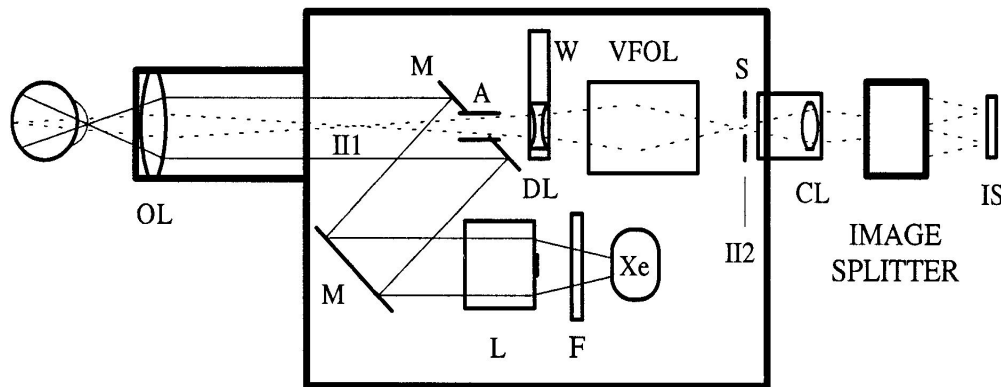


Figure 1.6: two wavelength imaging system (Beach et al 1999).

The optical density ratios were then used to calculate the oxygen saturation in linear relationship (Pittman et al. 1975a; 1975b). The influence of fundus pigmentation on retinal oximetry calculation was also investigated and three methods of calculating the optical densities were suggested to compensate for the absorption by fundal pigments (Beach et al. 1999). The three methods of calculating the optical densities and optical density ratio of the retinal arteries were compared. The first method was a “direct reflectance method. The second method used a corrected optical density calculation at 569nm to reduce the effects of light absorption by the fundal pigments. This correction involved substituting the measured reflected light intensity of the fundus at 569nm with that measured at 600nm (less absorption by the fundal pigments) and the introduction of a correction factor which estimated the amount of fundal pigmentation. The corrected optical density ratio was calculated using the corrected optical density calculation at 569nm. The third method attempted to reduce the light

absorbing influence of fundal pigmentation behind the blood vessels. The optical densities (and optical density ratio) in this method were calculated using estimates of intravascular reflectance at each wavelength, in place of perivascular fundus reflectance. Compensation for the fundus pigmentation reduced the variation of the retinal artery optical density ratios and was shown to improve the correlation between the retinal artery optical density ratios and the measured oxygen saturation. Retinal venous oxygen saturation in 5 subjects was calculated during normoxia and hyperoxia. During normoxia the mean retinal venous oxygen saturation was 55 ± 3.38 % and during hyperoxia (100% inspired oxygen) the mean retinal venous oxygen saturation increased by 19.2 ± 2.9 %.

More recently, a hyperspectral imaging system described by Khoobehi et al. (2004) was used to evaluate the relative oxygen saturation in the retinal vessels and optic nerve head tissues. This system consisted of a fundus camera with an attached prism-grating-prism spectrograph coupled to a CCD digital camera. The hyperspectral system functioned by collecting a sequence of line scans of a small area across the optic disc. Each line scan provided the spectral reflectance in the wavelength range 410-950 nm from a one dimensional area of the optic disc. A three-dimensional data cube was constructed by moving the imaging system to obtain the second spatial dimension. The hyperspectral imaging system was applied to measuring the spectral signatures of the optic nerve head in two anaesthetized monkeys. One monkey was exposed to hyperoxic conditions (100% oxygen saturation) and the hyperspectral signatures were compared to normoxia. A second monkey was exposed to high intraocular pressure through an infusion of saline in the anterior chamber and the hyperspectral signatures were compared to normal intraocular pressures. The reflectance spectral profiles between 450nm and 600nm of the retinal vessels and

temporal and nasal sections of the optic nerve head were analyzed to enable the comparison of the oxygenation under the various experimental conditions. Changes in the spectral profile of the retinal arteries, retinal veins and optic nerve head tissue under hyperoxic conditions were demonstrated, indicating an increase in blood oxygen. This was most apparent in the retinal veins suggesting the highest relative increase in oxygen saturation. Under high intraocular pressures, the documented changes in the spectral profile of the retinal vessels and optic nerve head tissues indicated a reduction in oxygenated blood. Semi-quantitative oxygen saturation maps, derived from a complex analysis of the spectral profiles of haemoglobin at high and low oxygenation between 530nm and 584nm, were used to demonstrate the oxygen saturation changes in the retinal vessels and optic nerve head tissues. The maps confirmed the detection of significant increases in the oxygen saturation of the retinal vessels and optic nerve head tissues during hyperoxia. During increased intraocular pressure the oxygen saturation maps showed a significant reduction in the oxygenation of the retinal vessels and optic nerve head tissues. Further improvements in the analysis of the hyperspectral data acquired by the hyperspectral imaging system have involved a correction for the blood volume and the illumination variation in the vessels overlying the optic nerve head and tissues (Beach, 2006). Spectral data were acquired from 5 anaesthetized monkeys at normal intraocular pressures and high intraocular pressures. The results indicated an improvement in the spatial quantification of relative oxygen saturation in the optic nerve head. An improved relative oxygen saturation map, under normal intraocular pressures, was demonstrated whereby capillary blood in the optic nerve head was shown to have an oxygen saturation intermediate to that of the retinal arteries and retinal veins. At high intraocular pressures it was again shown that there was a reduction in the oxygen

saturation of the retinal vessels and optic nerve head tissues. The oximetry results demonstrated by the hyperspectral imaging system have provided a useful insight into the potential of applying optic nerve oximetry in studying the mechanisms of glaucoma. However, this imaging technique is susceptible to motion artifacts which limit its use to anaesthetized animal experiments.

Stefansson adopted the two-wavelength oximetry technique described by Beach et al. (1999) and developed the technique that produced simultaneous retinal images at four wavelengths (Hardarson et al. 2006). This was performed using a beam splitter integrated into a fundus camera. The beam splitter enabled the replication of the original retinal image into four respective retinal images filtered at wavelengths of 542, 558, 586, and 605 nm. The images were aligned using a customized registration algorithm, and additional customized automated software enabled the calculation of the optical density ratios of the blood vessels using a vessel detection algorithm. Optical density ratios were calculated using the methods described by Beach et al. (1999) using only the 586 nm and 605 nm retinal images. Optical density ratios from first degree retinal arterioles and venules from 18 normal eyes were measured and used to generate a quantitative oxygen saturation model. This model was based on the assumption of a linear relationship between the oxygen saturation and the optical density ratios. The calculations of the retinal vessel oxygen saturations of sixteen normal eyes were compared at room air and during hyperoxia (100% oxygen saturation). Significant differences in the retinal vessel oxygen saturations were demonstrated. In the transition from normoxia to hyperoxia, the mean retinal arteriolar oxygen saturation increased from $96 \pm 9 \%$ to $101 \pm 8 \%$ and the oxygen saturation of retinal venules increased from $55 \pm 14 \%$ to $78 \pm 15 \%$. This experiment demonstrated that the retinal oximeter was capable of detecting oximetric changes in

the retinal vessels during hyperoxia. However, the validity of this technique is questionable since there is no attempt to directly address the influence of confounding factors such as light scattering, vessel diameter and fundus pigmentation.

1.3.2.9 Yoneya: Retinal oximetry using a Fourier Transform spectral retinal imager

Yoneya (2002) developed a Fourier-transform spectral imager to quantify oxygen saturation in human subjects with retinal vein occlusions. The imaging system consisted of a Sagnac interferometer, coupled to a fundus camera and a CCD camera which collected spectral data from two-dimensional retinal images. The oxygen saturation in each pixel was calculated depending on the spectral reflectance data between 480 and 600 nm. Lambert-Beer's law was used as an oximetry model where additional parameters were included to account for the wavelength dependent scattering of light in the eye. Quantitative oximetric maps were produced in which oxygen saturation in normal retinal arteries and veins was calculated between 90-98% and 60-70% respectively.

1.3.2.10 Johnson: the computed tomographic imaging spectrometer

Johnson et al. (2007) reported the development of a snapshot hyperspectral retinal imager employing a computed tomographic imaging spectrometer (CTIS) with a fundus camera and a digital colour CCD for improved calculation of spectral images (see Figure 1.7).

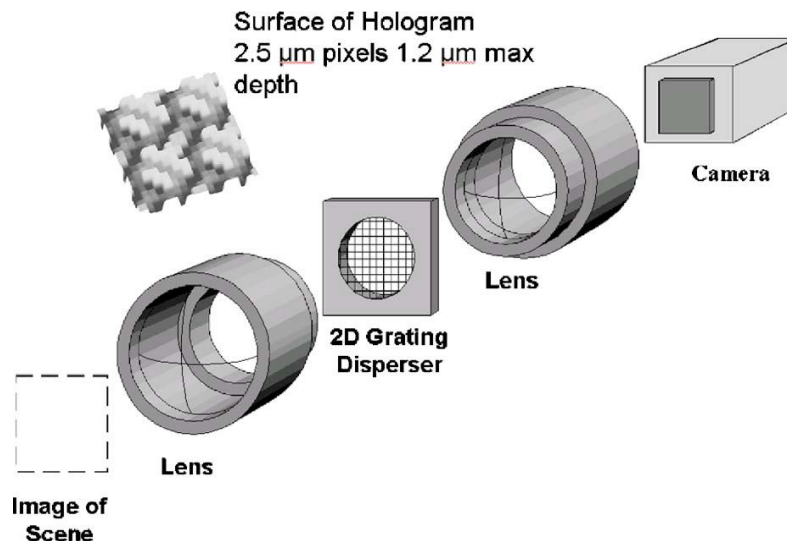


Figure 1.7: the construction of CITS system (Johnson et al 2007)

The CTIS system consisted of a computer generated hologram (CGH) disperser which was used to project the original image into an array of diffracted images onto the CCD detector. Each image array consisted of superimposed images which were recombined using a complex algorithm to recover the spectral data cube. Forty-eight contiguous spectral retinal images were produced from this system each representing discrete wavelength bands between 454 and 646 nm with a 4 nm bandwidth. Three randomly selected wavelength retinal images were selected and modified to represent an image taken with a spectral resolution of 1 nm. Modified Lambert-Beer's law was used as a model to measure the oxygen saturation, with an inclusion of parameters to account for light scattering in the ocular media and retinal layers, and further corrected for background scattering depending on Monte-Carlo simulation

1.3.2.11 Other retinal oximetry systems

Several researchers have reported a snapshot oximetric system that uses an array of either 6-lenslets or 18 lenslets coupled to a monochromatic digital CCD camera. The lenslets incorporated passband filtering of retinal images at specific wavelengths (Ramella-Roman et al. 2007). Arimoto et al. (2007) have reported a technique of

mapping the oxygen saturation in retinal vasculature using a modified fundus camera comprising a tunable filter and an electron-multiplying CCD camera. Sequential spectral images were recorded in the range 500-600 nm in 5 nm steps. A post processing algorithm was then applied to align the narrowband images and produce semi-quantitative oximetry maps.

1.4 Summary

In the previous section, we have shown that the variation in methodologies adopted to perform retinal oximetry reflects the uncertainties and challenges of establishing a gold standard retinal oximetric technique. The majority of previous retinal oximetry studies involved the use of either two or multiple wavelengths, in which different wavelength combinations have been suggested. Importantly, the oxygen saturations in the veins and arteries varied considerably (particularly the veins) amongst these research groups as presented in Table 1.1.

Authors	Technique	Wavelength	In Vitro	Oxygen saturation[%]	
		[nm]	measurements	Artery	Vein
Hickam et al.	Beam splitter +filters	640,800	6% and 9%	-	58%±10%
Beach et al.	Beam splitter +filters	600,569	-	-	55%±3.39%
Delori et al.	Filter wheel incorporating to fundus camera	586,569,558	3.5%-5.9%	98±8%	45%±7%
Schweitzer et al.	Line scan(spectrograph)	510 to 586	—	92%±4.1%	57.9%±9.9%
Hardarson et al.	Beam splitter+ filter	586,605	—	96% ± 9%	55% ±14%
Hammer et al.	Pass band filters	548,610	—	98%±10.1%	65%±11.7%

Table 1.1: Oxygen saturations veins and arteries of normal subjects at different wavelength combinations.

A possible reason for these variations was probably due to the error from the confounding influences in the retina affecting the optical measurements. These include the poorly characterised and controlled optical environment and structures within the retina to be imaged; the erratic motion of the eye ball; and the compounding effects of the optical sensitivity of the retina and the low numerical aperture of the eye. However, accurate measurements of retinal blood oximetry remain a significant challenge (Schweitzer 1999; Smith 2000). Retinal oximetry using dual- or three-wavelength techniques to detect early hypoxic changes in disease processes may result in inferior sensitivities. By using hyperspectral imaging much more information is available to account for the confounding influences in the retina which result in obtaining a noisy signal due to the absorption and scattering by different chromophores in the retina, in addition to the imaging system noise, and hence enables the detection of early hypoxic changes in the retina more accurately.

1.5 Aims of the research

The main purpose of this study is to investigate the feasibility of measuring blood oxygen saturation in the human eye using spectral imaging. There are two primary objectives of this thesis:

1. To build a hyperspectral camera suitable for recording high quality images.
2. To develop and appraise image processing algorithms and a physical model for accurately measuring the oxygen saturation in a retinal blood vessel tree.

My view in selecting a spectral imaging technique of the retina focused on the important features that enable efficient use of spectral retinal images. These features are: the feasibility of registering the retinal images in presence of eye movement, the

signal to noise ratio (SNR) obtained, the format of spectral images, the ability to calibrate the spectral images, and patient comfort and safety. To perform this, two-dimensional retinal images were recorded in a time sequential technique by modifying a commercial fundus camera to accommodate a liquid crystal tunable filter (LCTF) into the optical path, as shown in Figure 1.8. This system is able of recording spectral retinal images of the fundus in the range 400-700 nm in less than 20 minutes. In comparison to other techniques, such as one dimensional spectral imaging, the extended 2D field of view is an attractive property desired by clinicians for retinal disease screening. In the time sequential technique the number of recorded narrow spectral bands can be reduced to only a set of wavebands for which the most useful spectral information exists. As a result, the number of images that need to be recorded to construct informative spectral cube of the retina can therefore be the minimum necessary.

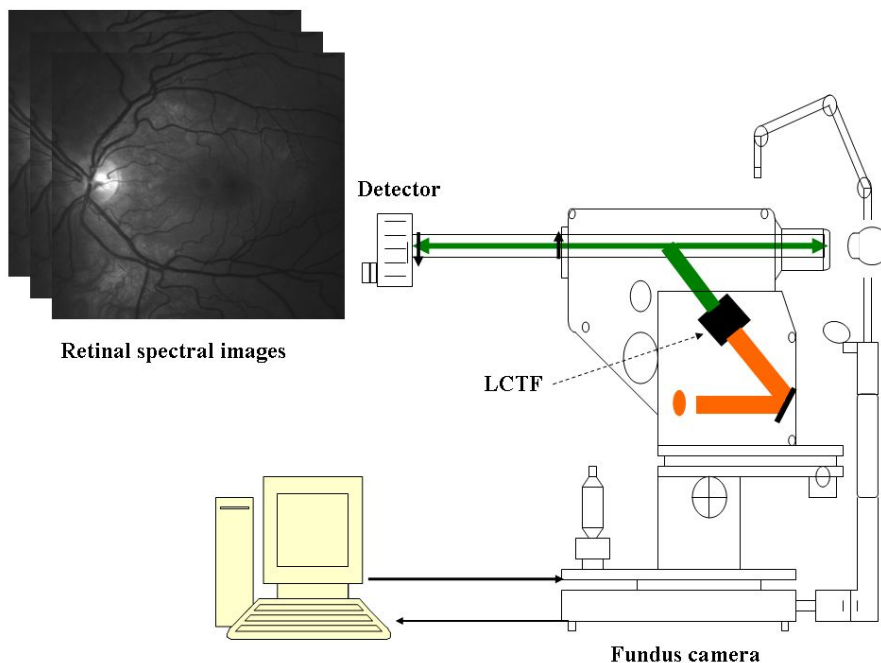


Figure 1.8: Retinal spectral imager

A minimum number of retinal spectral images offers higher *SNR* and rapid construction of spectral cube and hence reduces misregistration errors, compared with

Fourier transform techniques. Also, in contrast to FT techniques, the intensity of light is filtered before illuminating the retina in the time sequential technique. Filtering the light before reaching the retina has the advantage of minimizing the patient discomfort associated with light intensity.

Due to the nature of this technique and the time required to acquire the spectral retinal images, additional problems need to be addressed and solved for accurate restoration of spectral signatures from the spectral cube. These problems are the calibration (since no two images have identical illumination) and residual registration errors (due to the random movement of the eyeball). The time limitation of our system is constrained by the response of the LCTF, the flash charging time, and the integration time of the detector.

Following the introductory chapter, the thesis will begin with background information about the eye. Chapter 2 presents the anatomical, physiological and optical characteristics of the eye, with an emphasis on the retinal structure and its blood supply and continues with the properties of fundus reflectivity.

Chapter 3 provides information on modifying a fundus camera to insert a liquid crystal tuneable filter into the optical-path. Controlling the instrument and the data flow are also explained. Chapter 4, explains how recorded spectral retinal images were post-processed to correct for associated artefacts by developing calibration and registration algorithms. The main principles of retinal oximetry are explained in Chapter 5. The existing retinal oximetry techniques are also reviewed, in addition to the best combination of wavelengths to calculate the oxygen saturation accurately. So far in the thesis, oxygen saturation has been evaluated using two techniques: semi-quantitative and quantitative. Chapter 6 will look at the application of spectral

processing techniques such as linear spectral unmixing to produce semi quantitative oximetric maps. Clinical trials are also evaluated. In order to perform quantitative measurements, we developed algorithms, described in Chapter 7, to assess the oxygen saturation locally along the blood vessel tree. The errors encountered at each step were appraised and their contribution to the saturation error was evaluated.

Chapter 8 deals with the validation and accuracy of our oximetric technique, in which a model eye was built to mimic the human eye. The model eye enables application of the developed algorithm to measure the oxygen saturation in a well-controlled environment.

Retinal images recorded from healthy and diseased retinas were processed and results are shown in Chapter 9. The Oxygen saturation measurements of two common retinal diseases are analysed (glaucoma and vein retinal vein occlusion) and compared with those obtained from healthy subjects. The reproducibility of oxygen saturation measurements is also discussed. Chapter 10 will investigate the application of a novel snapshot technique which enables recording of both spectral and spatial information from the retina at the same time. A brief description of the instrument in addition to preliminary results will be presented. The conclusion and the future work, as the output of this project for extending this research into an application that will have clinical value, will be reviewed.

1.6 Conclusion

In this chapter a general introduction to spectral imaging and the existing spectral imaging techniques has been presented. The application of spectral imaging to calculate the oxygen saturation from the spectra of blood in the retina is also reported with an overview of the instruments and techniques described in the literature. The

following chapters in the thesis will deal with the most important properties of the human retina and instrument construction in addition to the implementation work to obtain oxygen saturation measurements from the retinal vessel.

Chapter 2

The eye

The structure of the eye is designed to supply us with information on depth, distance, dimension, and movement. The retina is the visual sense organ of the eye. It allows us to see under a wide range of illumination conditions, discriminate between different wavelengths thus allowing us to see colour, and provides us with sufficient precision of surrounding objects. The eye is an organ uniquely suited for diagnosis using spectral imaging. The nature of the tissue is primarily to allow light to travel along straight paths from the cornea to the retina, where light is detected by the rods and cones, stimulating electrical pulses that travel along the optic nerve and are used by the brain to develop images. With such a clear window into the retinal layer, the blood vessels are easy to image. In this chapter, a brief introduction to the anatomy of the eye is presented highlighting particularly the structure of the retina. Retinal blood supply and the importance of measuring retinal oxygen saturation are also discussed. Retinal diseases associated with alteration in oxygen saturation state are also reviewed. The main reflectors in the retina as light passes through the retina are presented.

2.1 The Anatomy of Eye

The human eye is spherical approximately 25 mm in diameter. Figure 2.1 shows the structure of the eye.

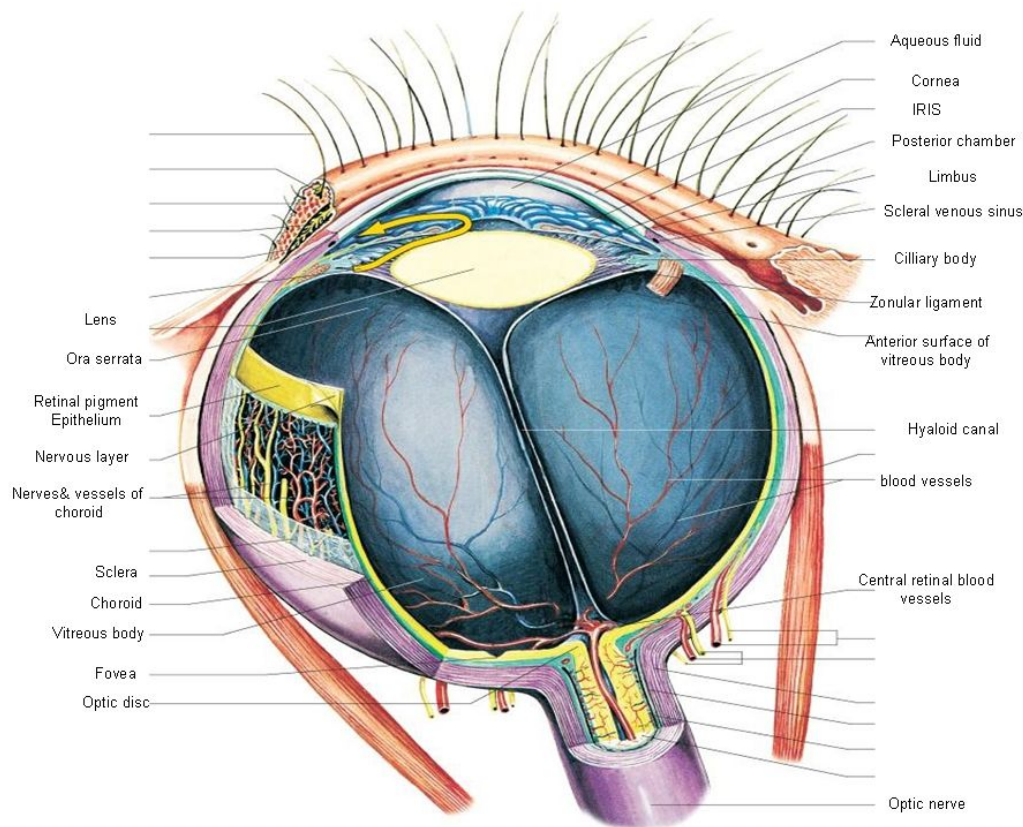


Figure 2.1: The structure of the eye (scanned from Gray's Anatomy: (Standring, 2008)).

Light is focussed onto the retina by the cornea and lens. The cornea, which is a part of the sclera, is the transparent window on the front of the eye and has a small radius of curvature. It is the principle refractive medium of the eye accounting for seventy percent of the total refractive power. The sclera extends all the way round the eye, and is lined with microscopically thin layers of tissue within which is a layer of fibrous tissue or stroma. These layers, known as the choroid, have a network of blood vessels that supply nutrients to the eye. At the front of the eye, the choroid becomes thicker and more complicated and is called the ciliary body.

The coloured part of the eye is known as the iris and is a muscular disc with a centred aperture. The aperture is the apparently black pupil whose diameter is controlled by the action of the iris. Behind the iris is the lens, set within the ciliary body of the choroid and held in place by a network of fibres known as the suspensory ligaments. The lens is bi-convex and consists of transparent epithelial cells in concentric layers

(like an onion). It is held in tension by a circular ligament, called zonula, which connects it to a circular ring of muscles, called the ciliary muscle. The function of the lens is to vary the power of the eye. Two chambers exist in the eye, the anterior (outer) chamber between the cornea and iris and the posterior chamber which is located between the iris, zonule fibres, and lens. Both of these chambers are filled with the aqueous humor. Fresh aqueous humor is constantly being produced. The vitreous chamber, between the lens and retina, is filled with the vitreous humor. This is a clear jelly-like substance through which the light which has been refracted by the cornea and the lens passes before reaching the retina.

2.2 *The retina*

The function of the retina is to transduce light into electrical impulses which are transmitted to the brain along the optic nerve. The retina is a circular concave disk which measures approximately 42 mm in diameter (Polyak 1941; Van Buren 1963). Figure 2.2 shows an image of the human retina which can be viewed through the pupil, using a fundus camera.

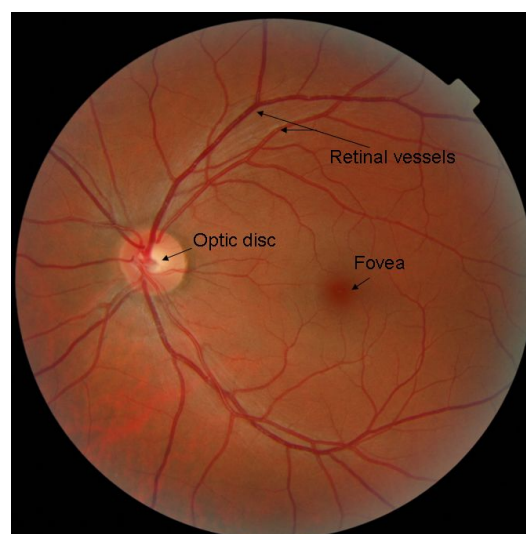


Figure 2.2: Human retina.

The most notable feature is the optic disk (a pinkish-yellow disc on nasal side of the fundus). This is where the optic nerve fibres exit on the way to the brain. Retinal arteries fan out the optic disk to supply the retina. Two and a half disc diameters to the left of the optic disk, the blood vessel free reddish spot known as the fovea can be seen. This is in the centre of the area known as the macula. The central retina is the circular field 6mm around the fovea and beyond this is the peripheral retina stretching to the ora serrata, 21 mm from the centre of the optic disc. The retina is held in place by a jelly-like mass of vitreous humor; any change in this vitreous humor leads to detachment of the retina. The retina has a very complex structure organized into layers as depicted in Figure 2.3.

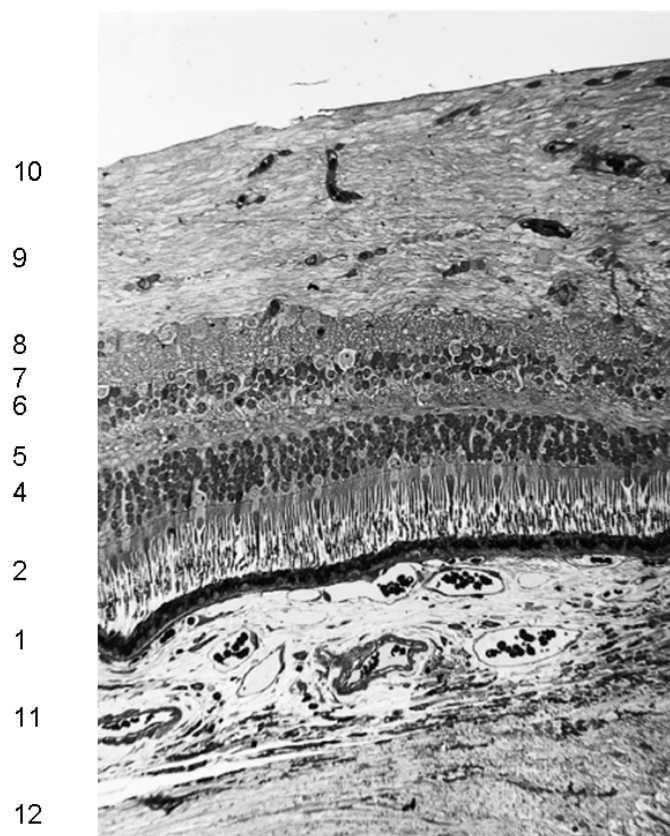


Figure 2.3: Retinal layers (scanned from Gray's Anatomy: (Standring, 2008)).

1. Retinal pigment epithelium layer, 2. Rod and Cone layer, 3. External limiting membrane,
4. Outer nuclear layer, 5. Outer plexiform layer, 6. Inner nuclear layer, 7. Inner plexiform layer.
8. Ganglion cell layer, 9. Nerve fibre layer, 10. Internal limiting membrane, 11. Choroid, 12. Sclera

These layers extend uniformly throughout the photoreceptive retina except at the exit point of the optic nerve fibres, at the optic disk, although certain layers are much reduced at the foveola, where the photoreceptive elements predominate. Each layer has a name which reflects the component embedded into this layer in addition to its position. Layers furthest from the vitreous are considered outer or external and those toward the vitreous are inner or internal. Beginning at the choroidal edge and passing towards the vitreous 10 layers are classified. These layers are:

Retinal pigment epithelium: this layer forms the back of the retina, and, works as the boundary with the choroid, from which it is separated by a thick composite basal lamina. This layer contains hexagonal cells with pigmented granules (melanin). The amount of melanin varies among humans and decreases with age. The highest intensity is in the macula.

Layers of photoreceptors: rods and cones

External limiting membrane: this layer consists of a zone of intercellular junctions of zonula adherens type between the processes of radial glial cells and photoreceptor processes.

Outer nuclear layer: this consists of several tiers of rod and cone cell bodies and their nuclei, the cone nuclei lying outermost. Mingled with these are the outer and inner fibres from the same cell bodies, directed outward to the bases of inner segments, and inwards towards the outer plexiform layer.

Outer plexiform layer (OPL): This is a region of complex synaptic arrangements between the processes of the cells whose cell bodies lie in the adjacent layers. The

outer plexiform layer contains the synaptic processes of rod and cone cells, bipolar cells, horizontal cells, and some interplexiform cells.

Inner nuclear layer (INL): This is composed of three nuclear strata. Horizontal cell nuclei form the outermost zone, then in sequence inwards, the nuclei and cell bodies of bipolar cells, radial glial cells, and the outer set of amacrine cells, including the interplexiform cells whose dendrites cross this layer.

Inner plexiform layer (IPL): This is divisible into three layers depending on the types of contact occurring. The outer or 'OFF' layer contains synapses between 'OFF' bipolar cells, ganglion cells and some amacrine cells; a middle or 'ON' layer contains synapses between the axons of 'ON' bipolars and the dendrites of ganglion cells and displaced amacrine cells; and an inner 'rod' layer contains synapses between rod bipolars and displaced amacrine cells. The on-bipolar cells hyperpolarise (increase the polarity of their transmembrane potential) in response to the receptor membrane potential generated. The off-bipolar cells depolarise (decrease transmembrane potential) in response to the same signal.

Ganglion cell layer: This layer contains the nuclei of the displaced amacrine cells. Its inner regions consist of the cell bodies, nuclei and initial segments of retinal ganglion cells of various classes.

Nerve fibre layer: This contains the unmyelinated axons of retinal ganglion cells. It forms a zone of variable thickness over the inner retinal surface, and is the only component of the retina at the point where the fibres pass into the nerve at the optic disc. The inner aspect of this layer contains the nuclei and processes of astrocytes which, together with radial glial cells, ensheath the nerve fibres. Between the nerve fibre layer and the ganglion cells there is another narrow, innermost plexiform layer,

where neuronal processes make synaptic contact with the axon hillocks and initial segments of ganglion cells.

Internal limiting membrane: This is a glial boundary between the retina and the vitreous body. It is formed by the end feet of radial glial cells and astrocytes, and is separated from the vitreous body by a basal lamina.

2.3 Blood supply of the retina

Two sets of vessels are present around the retina: the ciliary vessels of the choroid, and the branches of central retinal vessels. The retina depends on both circulations since neither is sufficient independently to save the function of the retina, due to the high demand of oxygen supply.

The central retinal artery enters the optic nerve as a branch of the ophthalmic artery and travels in the optic nerve towards its head. Then the central artery divides into two equal branches: superior and inferior. The superior and inferior branches then split into superior and inferior nasal, and superior and inferior temporal branches. Each branch supplies a corresponding quadrant of the retina. Corresponding retinal veins unite to form the central retinal vein. However, the courses of the venous and arterial vessels do not correspond exactly, and arteries often cross veins, usually lying superficially to them. The branches of the arteries are usually dichotomous and equal rami diverge at angles of 45-60°. Retinal vessels (veins and arteries) ramify in the nerve fibre layer near the internal limiting membrane, and that explains the possibility of seeing them through an ophthalmoscope. Arterioles travel deeply into the retina and penetrate to the internal nuclear lamina where the venules return the blood to larger superficial veins. Retinal blood vessels have the same structure as elsewhere in the body, except that the internal elastic lamina is absent from arteries, and muscle

cells may appear in their adventitia. The choroid has a capillary bed, called the choriocapillaries, in contact with the retinal pigment epithelium. The choroidal circulation has a fast flow and a small arteriovenous oxygen difference. The choriocapillaries occupy 35% of the volume of inner choroid.

2.4 Retinal oxygen

Oxygen is the main substrate in energy-producing biological reactions. The retina is one of the most metabolically active tissues, and, as a result, the demand for oxygen is high. The supply of oxygen to the retina is paramount because oxygen cannot be stored (Vanderkooi et al. 1991) and therefore the function of the blood and blood vessels in the transportation of oxygen is crucial in maintaining the viability of the retina. The integrity of the blood vessel structure and function, in addition to the oxygen content of blood, therefore plays a significant role in the pathophysiology of vascular diseases in the retina. The impairment of oxygen delivery to the retina results in retinal hypoxia which has been attributed to a number of disease processes. These events are potentially sight-threatening and have influenced the development of techniques to study and detect oxygen changes in the retina.

2.5 Retinal diseases

There are many diseases that impair vision; too many to cover in a brief explanation. Our consideration will focus on diseases associated with a change in blood oxygen saturation in retinal vessels. Direct monitoring of the oxygen saturation of the arteries and veins has already seen clinical use. Previous studies using various oximetric measurement and analysis techniques have reported measurable oxygen saturation changes in retinal vein occlusions (Yoneya et al. 2002; Hardarson 2006), glaucoma

(Michelson et al. 2006; Khoobehi et al. 2004; Siesky et al. 2008; Ito et al. 2008; Gottfredsdottir et al. 2008), age-related macular degeneration (Schweitzer et al. 2000), and diabetic retinopathy (Hardarson et al. 2008). In the following sections, a brief explanation of three common diseases: diabetic retinopathy, retinal vein occlusion, and glaucoma will be introduced.

2.5.1 Diabetic retinopathy

Diabetic retinopathy is characterized by irregularity and leakiness of the blood vessels in the eye which can lead to blindness in the case of a large vitreous haemorrhage (Ege et al. 2000). Visual abnormalities include microaneurysms (small aneurysms of the blood vessel), haemorrhages (due to structural deformations), exudates (blood vessel leaks of lipid; a bright matter), cotton-wool spots (retinal infarcts caused by thrombosis of the blood vessel – leading to ischemic damage in the surrounding area), venous irregularities, new vessels, and macular edema. Vessel narrowing also occurs, decreasing the blood flow and resulting in tissue hypoxia. The origin and development of diabetic retinopathy is still under investigation. Some studies have suggested that increases in haemoglobin oxygen level changes, and microvascular and haematological changes may contribute to the development of retinopathy.

2.5.2 Glaucoma

Glaucoma causes progressive damage to the optic nerve (optic neuropathy). High pressure in the eye is considered to be an important contributing factor to the development of glaucoma. Glaucoma can be recognized by the appearance of characteristic cupping of the optic disc associated with corresponding visual deficit. This condition causes gradual loss of retinal ganglion cells and their axons. Glaucoma

can be classified as primary, if the cause of elevated intraocular pressure (*IOP*) is unknown, and secondary, when the cause is known. Conventionally, the term primary open angle glaucoma (POAG) is applied to eyes with primary chronic glaucoma with open anterior chamber drainage angles and elevated IOP.

2.5.3 Retinal vein occlusion

This condition is a common retinal vascular disorder in which a blockage of the retinal vein occurs. As a result, blood in the blocked vein builds up and leaks from the blood vessels causing damage to the retina. Retinal vein occlusion can be classified according to whether the central retinal vein or one of its branches is obstructed. This leads a difference in respect to the pathophysiology, underlying systemic associations, average age of onset, clinical course, and therapy. Furthermore, central retinal vein occlusion can be divided into ischemic and nonischemic varieties. Both types of CRVO, ischemic and nonischemic, share similar findings, dilated tortuous retinal veins and retinal haemorrhages in all four quadrants. Discrimination between these two types helps clinicians in assessing the condition and monitoring the treatment.

2.6 Fundus reflectance

A fundamental requirement of retinal imaging is to illuminate the fundus through the pupil and collect the reflected light. Light entering the eye passes through the eye media and series of retinal layers, to finally reach the sclera. Incoming light will experience Fresnel reflection at the interfaces between layers, due to discontinuities in index of refraction between layers. As wavelength changes, the absorption properties of each layer also vary, depending on the chromophores embedded in each layer. Generally, in the visible range, the absorbance is highest for the violet and blue light

(300-500 nm). As shown in Figure 2.4, the reflectance increases up to 520 nm where a plateau is reached, extending to about 580 nm with distinct reflection minima at 540 and 575 nm corresponding to the absorption maxima of oxyhaemoglobin at those wavelengths. As wavelength increases, a further increase in reflectance is observed.

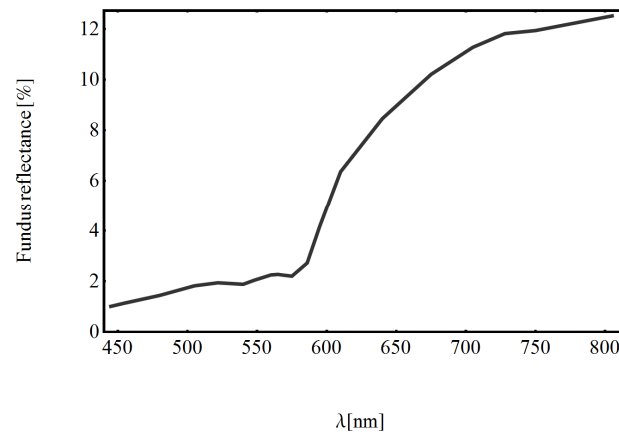


Figure 2.4: Reflectance spectrum from the nasal fundus (Delori 1989).

The reflectance spectrum of different locations across the retina is dominated by oxygenated and de-oxygenated haemoglobin in both choroidal and retinal vessels, and also by melanin components which vary depending on subjects and ethnicity (Delori 1989). As can be observed from the images in Figure 2.5 (which shows spectral retinal images acquired by our system), due to the spectral absorption characteristics of haemoglobin in its HbO₂ and Hb states, in addition to the depth at which scattering occurs, veins and arteries differ in appearance depending on the illumination wavelength. Both veins and arteries appear dark in wavelength range 560-580nm, while in the range 580-600nm arteries increase in transparency but veins remain opaque. At the isosbestic wavelengths (522, 542, 569, 586 nm) reflected light intensities from veins and arteries are similar for the same thickness, whereas at wavelengths longer than 650 nm, veins and arteries appear translucent and illumination light penetrates toward the choroidal layer. Figure 2.6 shows the

transmission spectra of 100 μ m thickness of oxygenated and deoxygenated blood columns. As can be seen from this Figure, the highest transmission occurs at longer wavelengths and higher oxygenation.

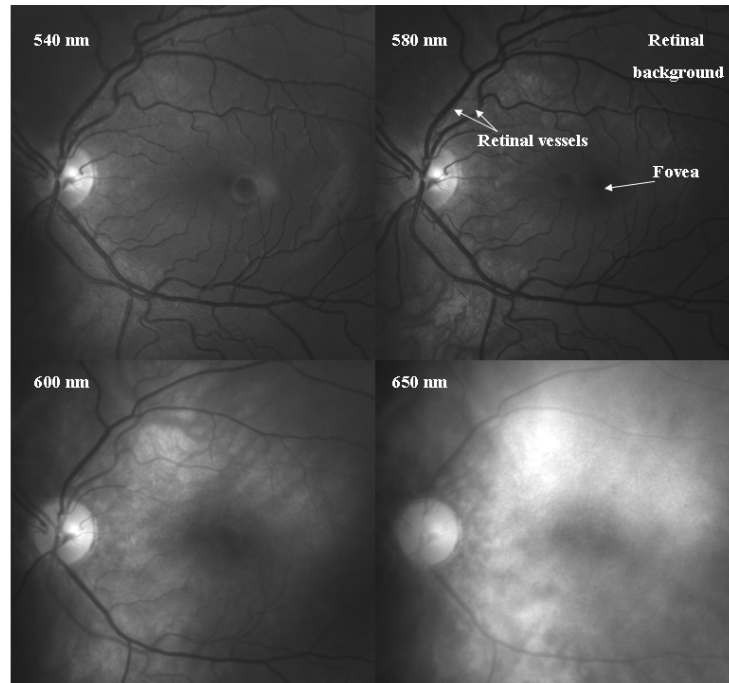


Figure 2.5: Retinal spectral images.

Changes in index of refraction at the air-cornea, cornea-aqueous humor, lens-aqueous humor and vitreous body interfaces cause the reflectance at the cornea and lens to greatly exceed the reflectance of the fundus (Liou and Brennan 1997). To understand the reflectance spectrum of the ocular fundus, it is important to understand the reflectance characteristic of each layer. The internal limiting membrane (ILM), the nerve fibre layer (NFL), the retinal pigment epithelium (RPE), and the sclera are the layers with the strongest reflectivities.

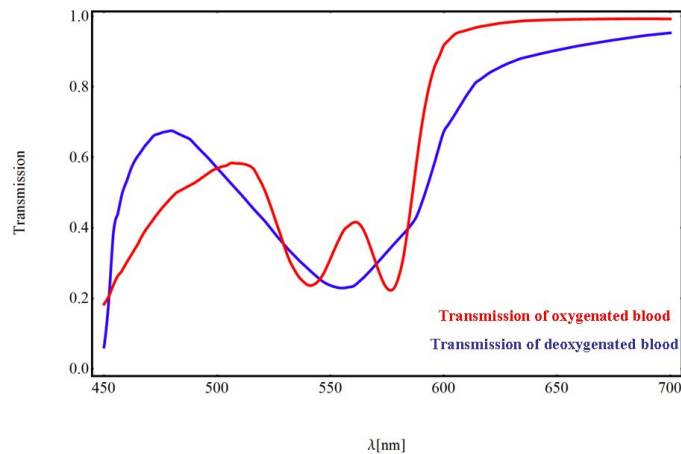


Figure 2.6: The transmission spectra of 100µm blood vessels for oxygenated and deoxygenated blood

2.6.1 Internal limiting membrane

A diffuse and specular reflection is apparent from the inner limiting membrane (ILM) (van de Kraats et al. 1996; Gorrand et al, 1984). The intensity of the specular reflection decreases with age (Gorrand and Delori 1999), and depends critically on curvature and orientation of the retinal surface, on the direction of the incoming light, and on the position of the exit pupil (Gorrand et al. 1984). Minor backscatter in the vitreous can generally not be distinguished from the ILM reflectance.

2.6.2 Nerve fibre layer

The reflectance spectrum of the nerve fibre layer can be characterized as having the same shape along arcuate region of the NFL. As the thickness of the nerve fibre layer decreases, the absolute reflectance decreases (Knighton et al. 1989). There is little change in reflectance between 680 and 560 nm and it rises by λ^{-n} from 560 to 460 nm. It further shows a strong directional dependence caused by scattering by cylindrical structures (Knighton et al. 1992; Knighton and Huang 1999). Therefore, the apparent intensity of the NFL will depend not just on its thickness but also on its orientation

relative to the imaging system (Knighton and Qian 2000). In the fovea, the NFL is very thin and its reflectance can be neglected.

2.6.3 Retinal pigment epithelium

A source of reflection at the level of the RPE was proposed by several authors. Its location was positioned alternatively between the photoreceptors and Bruch's membrane (the innermost layer of the choroid.) (Weale 1966), between the photoreceptors and the choriocapillaris (Gloster 1983), or close to the RPE (Charman and Jennings 1976; Delori et al. 1977; Zeimer et al. 1989 a, b). This has been confirmed by optical coherence tomography measurements in which an apparent reflection is visible at the level of the RPE (Hee et al. 1995; Puliafito et al. 1995; Fercher 1996). Many studies have modelled the RPE depending on absorption properties, neglecting the scattering effect (Norren and Tiemeijer 1986). Hammer et al. (1995) measured the optical properties of the RPE layer and found a scattering component. The dependency of the light reflected from the RPE is assumed to be wavelength independent.

2.6.4 The sclera

The sclera is a dense layer composed of randomly oriented collagen fibres; the sclera reflects 50% of the light (Alpern et al. 1965; Smith and Stein 1968). Measurements performed *in vitro* and *in vivo* on human scleras showed a slight decrease with increasing wavelength (Delori and Pflibsen 1989). In spite of the fact that the sclera has high reflectivity its effect on the overall reflectivity of the fundus is small, due to the absorption and scattering by the superior layers in which the majority of light is reported to backscatter in the choroidal layer (Preece and Claridge 2002).

2.7 Conclusion

In this chapter, we have presented background information on the human eye and the anatomical, physiological and optical properties. The retina and the retinal blood supply and some retinal diseases have been reviewed. We have also shown that as light propagates toward the eye, reflectance takes place at the boundaries between retinal layers due to the alteration in refractive indices. The internal limiting membrane (ILM), the nerve fibre layer (NFL), the retinal pigment epithelium (RPE), and the sclera are the layers with the strongest reflectivities. In the following chapters, the instrument construction and the associated algorithms will be presented in addition to the principles of light-tissue and light-blood interaction.

Chapter 3

Instrument construction

Several techniques have been reported for direct spectral imaging of the retina. In this chapter, we report the development of a time sequential retinal imager. Full description of the modification of a traditional fundus camera to accommodate a high resolution digital camera and liquid crystal tunable filter is provided.

3.1 Fundus camera

The fundus camera used is a Canon CF-60Z of the non-contact type with a 60° field of view. The camera was originally developed for fluorescein fundus angiography with 35mm film. Several modifications were made to integrate the LCTF into the optical path of the camera. To gain an appreciation of how the optics in the camera works, the mechanisms of the optical system need to be understood. As depicted in Figure 3.1, the optical system is divided into the following main parts:

- Observation and focusing optical system.
- Illumination system for observation and photographing.

3.2 Optical system description

The observation and focusing system of the fundus camera transfers the retinal image to the detector plane. The optical system of the fundus camera projects a ring of illumination through the dilated pupil as shown in Figure 3.2; the light then reflects off the retina, exits the pupil through the centre of illumination ring and continues through the fundus camera optics to form an image at the image plane.

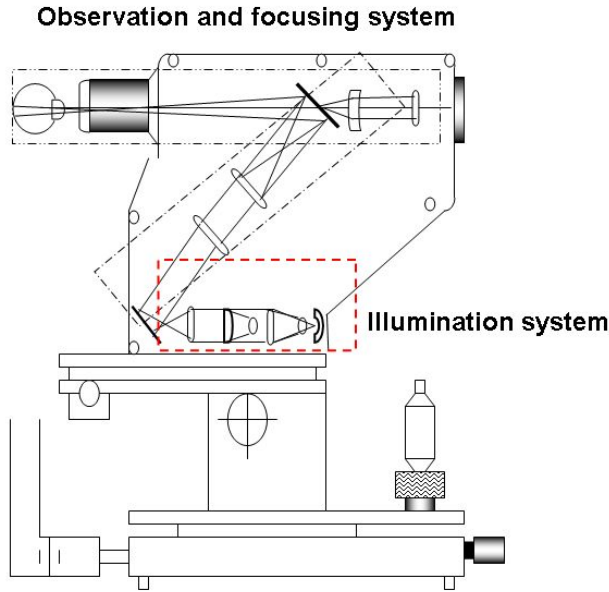


Figure 3.1: The main parts of the fundus camera.

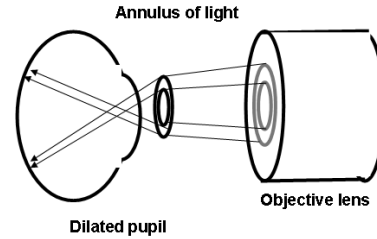


Figure 3.2: The ring of light.

The fundus camera is provided with two sources of illumination: a continuous light source (usually a tungsten bulb) for viewing the retina, which can be adjusted according to the patient's level of comfort and the photographer's ability to distinguish fine retinal details. The second source is a xenon flash tube, which provides a brief burst of intense light to expose the fundus photograph.

3.3 *Time sequential technique implementation*

As mentioned previously in chapter 1, the three dimensional spectral data cube can be easily acquired in time sequence. This traditionally involves one of the dimensions (usually the wavelength λ) to be scanned in time sequence, and that can be achieved by recording the 2D spatial scene in a single exposure, and then time sequentially stepping through wavelengths to build the data cube. The simplest implementation of a retinal spectral imager incorporates a bandpass filter wheel into the optical path of a

fundus camera. However the choice of filters in terms of number of filters, central wavelength and spectral bandwidth makes using more elaborate type of filters such as electronically tunable filters (ETF's) desirable.

A tunable filter is a device whose spectral transmission can be electronically controlled through the application of voltage or acoustic signal without moving parts and without discontinuity in the spectral transmission, thus providing finer spectral sampling, and rapid and random switching between wavelengths. There is a wide variety of different types of ETF's, which can be classified into three main categories: liquid crystal tunable filter (LCTF), acousto-optical tunable filter (AOTF), and Fabry-Perot (Poger et al. 2001). The decision to use one type over the others is application dependent. We have chosen to use LCTF in our setup as it offers a larger aperture and higher rejection ratio than AOTF (Stratis et al. 2001).

3.3.1 Liquid Crystal Tunable Filter (LCTF)

LCTF is based on a Lyot filter, (Lyot 1944; Ohman 1958), a filter built around a number of static optical stages each consisting of a birefringence retarder (quartz for LCTFs) sandwiched between two parallel polarisers (Hecht 2002,P 326). Figure 3.3 shows a schematic diagram of a single stage of a Lyot filter.

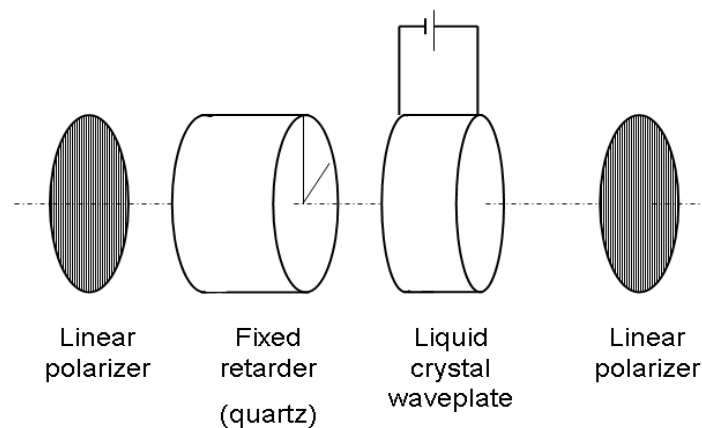


Figure 3.3: Schematic diagram of a single Lyot cell.

To pass a single narrow wavelength band, a stack of stages can be used together, where the thickness of the consecutive retarders varies by a factor of 2. When the incident linearly polarized light transverses the retarder, it is analysed into two rays, the ordinary and extraordinary, which experience different optical paths, the retardation between the two rays is given by

$$\Gamma(\lambda) = 2\pi \frac{\Delta d}{\lambda}, \quad (3-1)$$

where Δ is the birefringence and d is the thickness. As wavelengths pass through the retarder, the polarizer will pass only those in phase onto the next stage. The transmission of one stage is

$$T(\lambda) = \cos^2\left[\frac{\Gamma(\lambda)}{2}\right]. \quad (3-2)$$

The overlap of these continuously varying transmission curves determines which wavelengths are passed by filter stages as a whole. Figure 3.4 shows the transmission curves of a four stages Lyot filter and the final transmission band as a result of multiplying the transmission of each stage.

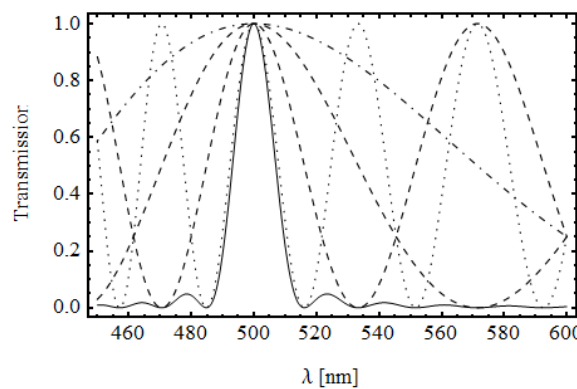


Figure 3.4: Transmission of a 4 stages Lyot filter, the bold line is the transmittance through all four stages.

By adding a liquid crystal layer to each stage, tunability can be introduced by creating minor changes in retardance which affects the position along the spectrum where the

curves constructively interact. Tunability is provided by the partial alignment of the liquid crystals (LC) along an applied electric field between the polarisers (i.e LC provides electronically tunable birefringence). As described previously, LCTF is polarization sensitive, which will reduce the transmission of light by (50%). When using a LCTF, one has to note that LCTF filtering is angle dependent and the maximum F-number that provides an off axis shift of less than 2 nm at the filter edge is ~ 2.5 . More details about the properties, types, and the construction of LCTF are discussed in Poger et al. (2001) and Gat (2000).

3.4 Instrument construction

It was important to select the best location to insert the LCTF into the optical path of the camera. We have chosen to use the *CRI VariSpecTM* tunable birefringent filter that is generally used for imaging and non-imaging spectral analysis. The unit is capable of transmitting wavelengths within the visible to the near infrared (400-700 nm) and is controlled electronically with bandwidth 10nm (varying with wavelength); Table 3-1 presents the general specifications of the LCTF.

<ul style="list-style-type: none"> • Tunes continuously and provides excellent imaging quality. • No moving parts and compact low power design. • Steps between wavelengths in $\Delta\lambda=2$ nm. • Fast random access wavelength selection. • Clear aperture 25 mm. • Field of view ± 7 degrees from normal. • Bandwidth (FWHM) 10 nm. • Wavelength range 400-700 nm.

Table 3.1: LCTF manufacture technical specifications (taken from the manual).

In the following section, we will present the steps involved to integrate a high resolution digital camera CCD (Hamamatsu-ORCA-AG) instead of the normal camera attached to the fundus camera body. This required an increase in the field of view, as the CCD chip is smaller than the film provided with original camera system. The process of setting the wavelength and capturing an image in parallel with firing the flash bulb is also described.

3.4.1 LCTF integration

There are two options to perform spectral imaging using LCTF: either by filtering the light illuminating the retina or by filtering the light reflected from the retina. To achieve the maximum of patient safety and comfort, light has to be filtered before illuminating the retina. As can be seen from Figure 3.5, the filter needed to be installed inside the fundus camera in such a place that it intercepts the light beam which is destined to illuminate the object in front of the camera body. The optics were fairly complicated and optimised, so it is important that any location chosen must prove to be one that does not significantly impair the performance of the camera. Figure 3.6 shows the best location to accommodate the LCTF unit inside the camera body, in which LCTF aperture (1 inch) is centred with the lenses which collimate the illumination. As The LCTF unit dimensions differ from those inside the camera system in size and in the positioning, a special mount was manufactured to hold the LCTF in position. The aim was that after mounting plates and rods, the LCTF unit will be free to move within the assembly, with its aperture perfectly centred over the lenses and can be locked into position with aid of a grub screw.

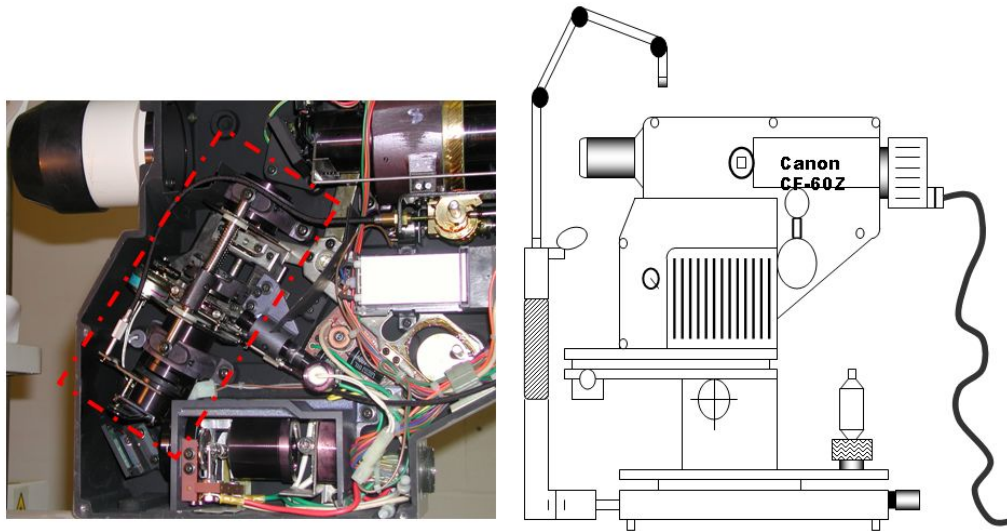


Figure 3.5: Inside the fundus camera.

3.4.2 Glare and black dot relocation

As LCTF inserted into the optical path of the fundus ophthalmoscope, a clear plate of glass with small dots printed on either side has to be moved. Figure 3.6 below shows where the plate was located and how it sat in the space now occupied by the LCTF unit.

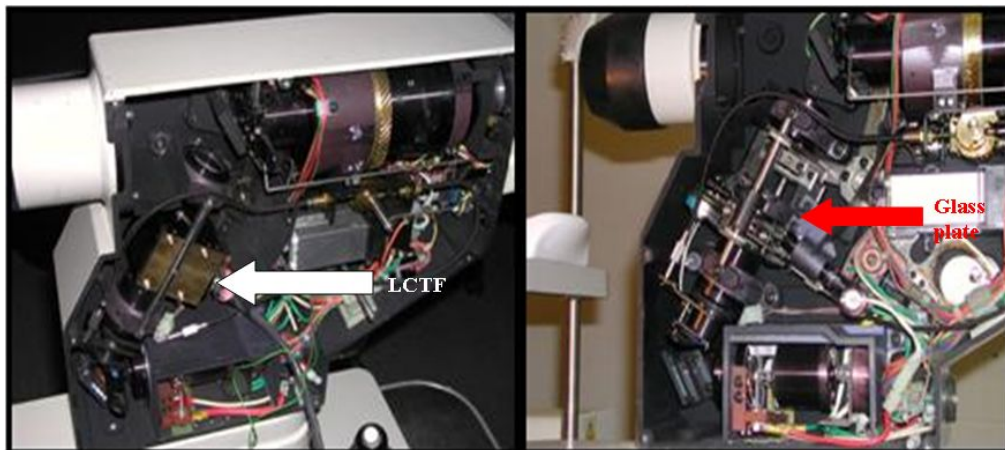


Figure 3.6: The position of the glass plate and LCTF.

After positioning the LCTF, a glare image was captured due to the absence of the glass plate component. Figure 3.7 below shows a close-up sketch of the key components in the glass plate and the glare image.

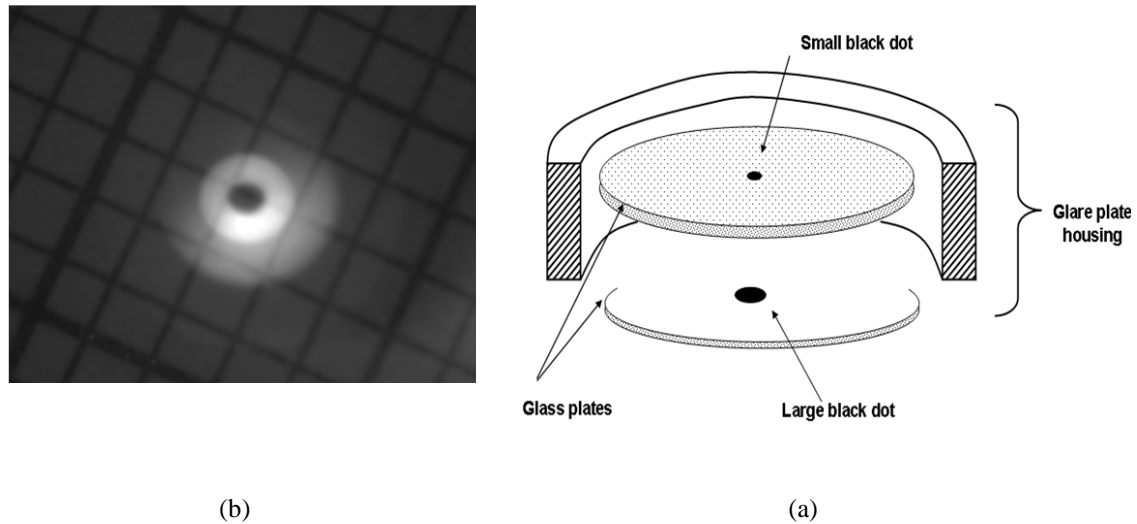


Figure 3.7: (a) A sketch of the glass plate (b) The glare image in absence of the black dots.

The glass plate, with its dots, has the effect of removing any glare produced from the reflection on the optical surfaces (of the objective lens) in the camera system. Black dots are imaged onto back and front surfaces of objective lens to reduce specular reflection. It can be seen in captured images (see figure 3.7 (b)) that there is a distinct glare in the absence of this component. It is clear from the image above that the effects of the glass plate are significant and it was therefore required to compensate its function. One possible solution was to use a linear polarizer in front of the detector to attenuate the glare, which is simply a specular reflection from the lens surface as the light illuminating the retina is linearly polarized after the LCTF. In Figure 3.8, two images of star target were captured before and after introducing a linear polarizer in front of the detector. The amount of glare was reduced significantly due to the effect of the polarizer.

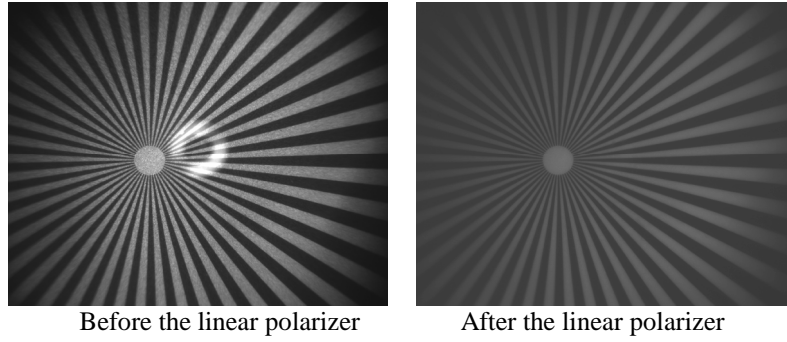


Figure 3.8: The effect of the linear polarizer in attenuating the glare

3.4.3 Field of view

As mentioned in the previous section, the original fundus camera system enables the recording of images of the retina in maximum 60° degree field of view on film size (35mm) $36 \times 24 \text{ mm}^2$. When the conventional camera was replaced with high resolution Hamamatsu CCD detector chip of dimensions $6.6 \times 8.9 \text{ mm}^2$, the field of view was decreased to less than 20° degrees as depicted in Figure 3.9 (a). To maintain the original field of view, the output image from the unmodified camera was re-imaged, which involved using a macro lens ($f=50 \text{ mm}$, $f/\# = 1.4$) to relay the image plane into the CCD chip after demagnifying the dimensions by a factor of around $M \approx 3.5$. Increased field of view was obtained (Figure 3.9 (b)), in which superior and inferior temporal areas as well as the macular area are captured. Figure 3.10 shows the new arrangement and the modified retinal camera.

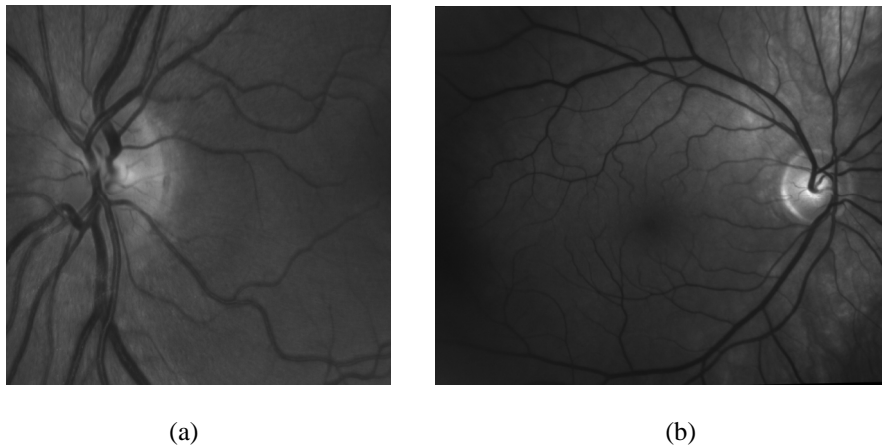


Figure 3.9: The field of view obtained (a) before, (b) after demagnifying the image plane.

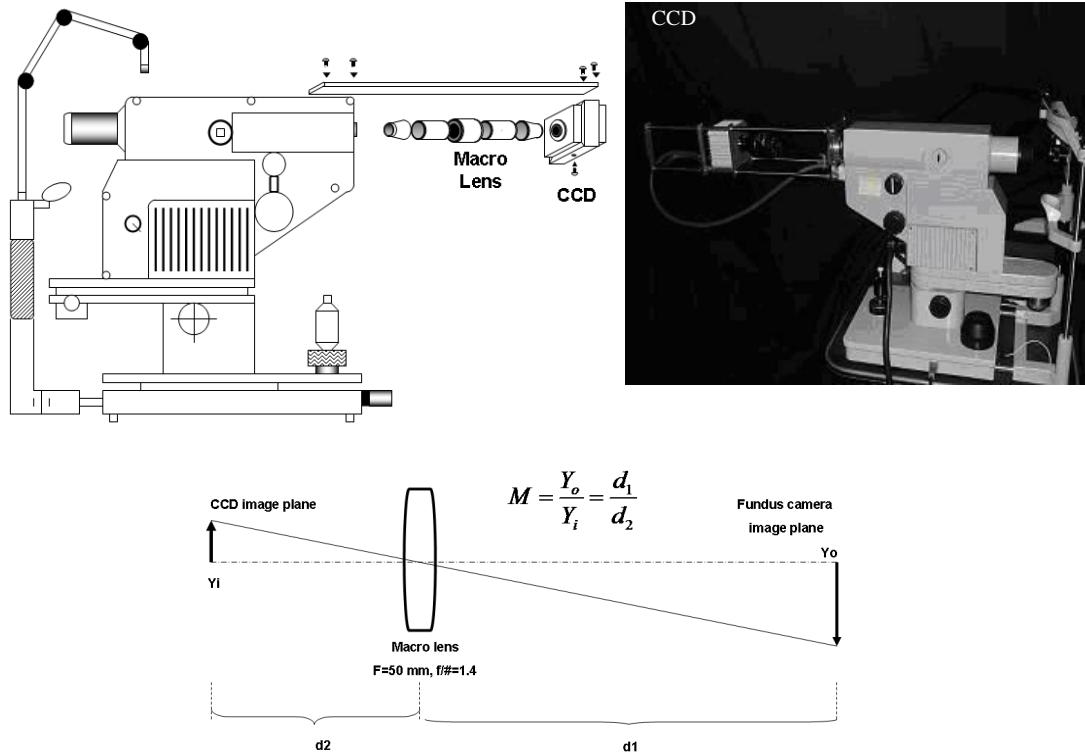


Figure 3.10: The modified fundus camera after increasing the field of view.

3.4.4 Data flow and system control

To perform spectral retinal imaging, it was a requirement to control the whole process of tuning the illumination wavelength and recording a retinal image in synchronization with triggering the flash gun. As described previously, the original fundus camera system employed two light sources: for observation (halogen lamp) and imaging (xenon flash system), and the intensity of light in both cases can be controlled and varied. A visual programming tool known as ‘*LabView*’ was used to:

1. Control the digital camera and capture an image.
2. Trigger the flash gun.
3. Control LCTF main unit.

There were two separate functioning *LabView VIs* (Visual Interfaces) that operate the LCTF and the digital camera/flash gun. The LCTF *VI* can be run to select a single wavelength, proceed through a sequence of bands or sweep incrementally through a defined range of wavelengths. The camera/flash gun *VI* offers functionality with the aid of a number of functions: control over the captured images, saturation display and a live feed. These *VIs* were integrated into a single Labview program which can be easily used by a clinician to capture high-quality images of the retina at single or multiple wavelengths and store them in an appropriate format so that they can be retrieved and analysed with ease. The following chart, Figure 3.11, presents the steps taken to control the process of recording spectral retinal images:

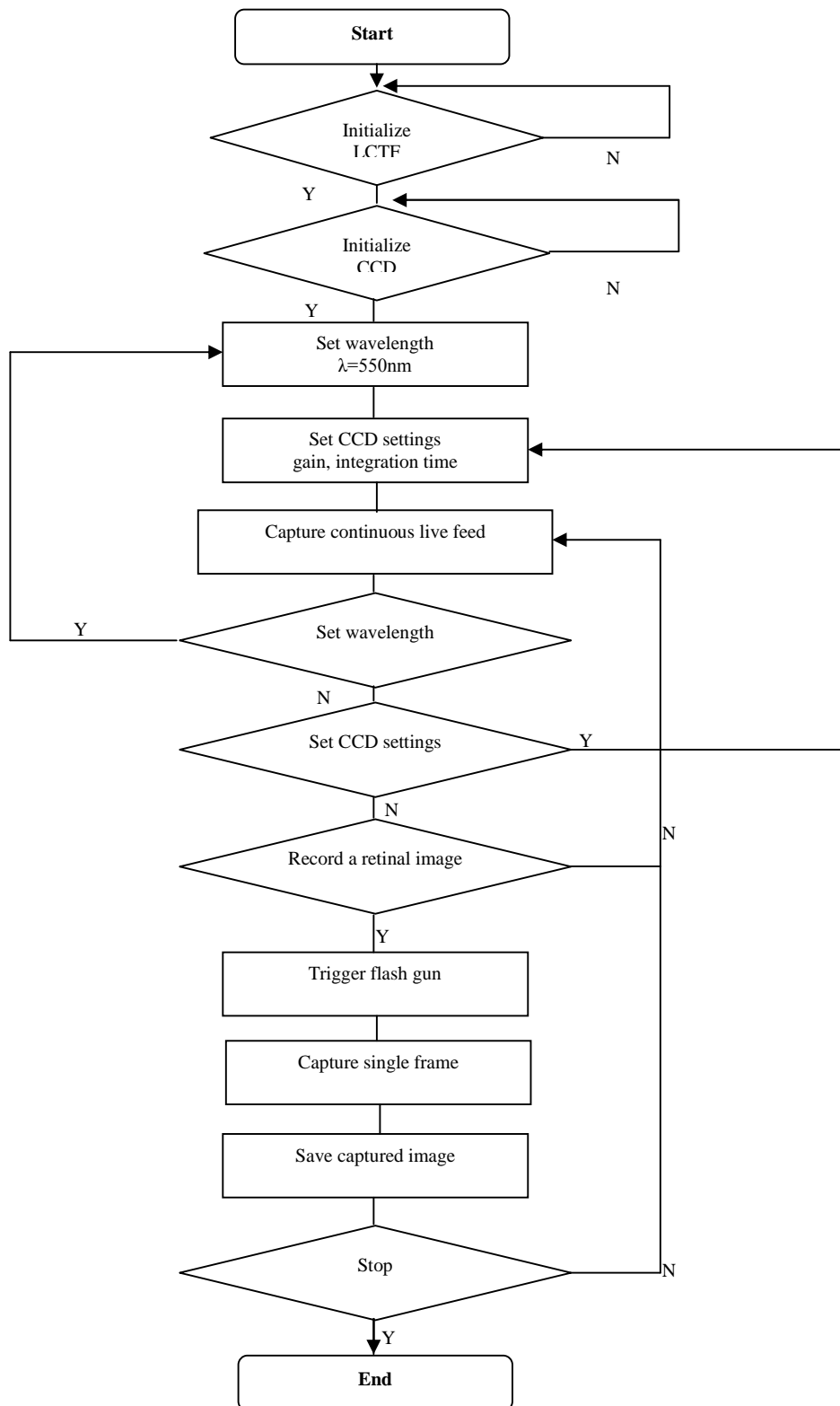


Figure 3.11: The process of controlling and recording spectral retinal images.

When images were viewed in the 'Live-feed' (for observation using the halogen lamp only) the camera gain was set to 100 to enable clear observation. At the moment an image needs to be captured (using the flash light), this value needs to be set to 0 and returned to 100 immediately after. Contrast parameters were adjusted to enable viewing and recording live-feed image clearly at different wavelengths. Different flash intensities equipped in the original camera system were used to compensate the variation in spectral transmission caused by the eye, LCTF, detector sensitivity, and flash lamp components. The system has the capability of recording 150 spectral retinal images in the range 400-700 nm at 2 nm. The time required to build the whole data cube is about 20 minutes. Several factors constrain fast construction of the data cube such as flash light charging time, the response of the LCTF, the integration time of the detector, and the time limitations of the software. One option to overcome these limitations is by using fast wavelength scanners such as fast scanning monochromators but the light power of such scanners to illuminate the retina is still questionable.

3.5 LCTF spectral bands

We have shown that the LCTF acts as a variable filter that can be adjusted to allow a particular wavelength to pass through. LCTF filter specifications are very important and critical to acquiring a high resolution spectral cube for accurate quantification of chromophore concentration. The spectral range of our LCTF was chosen in the range 400-700 nm which covers the spectral range of the most important absorbers that exist in the retina, such as haemoglobin and melanin. The width of the LCTF bands limits the accuracy of the spectral imager to perform fine discrimination between several chromophores. Spectral transmission rate is a very important characteristic that may

affect the overall performance of a spectral imaging system with narrow passband filters; LCTF has a transmission rate ranging between only 3% at 400 nm to 65 % at 700 nm in polarized light as can be seen from Figure 3.12. This poor performance at blue light can be improved through the system by means of increasing the exposure time of the detector (this is constrained to the duration of the flash illumination) or increasing the intensity of illumination light when short wavelengths (blue range) are selected.

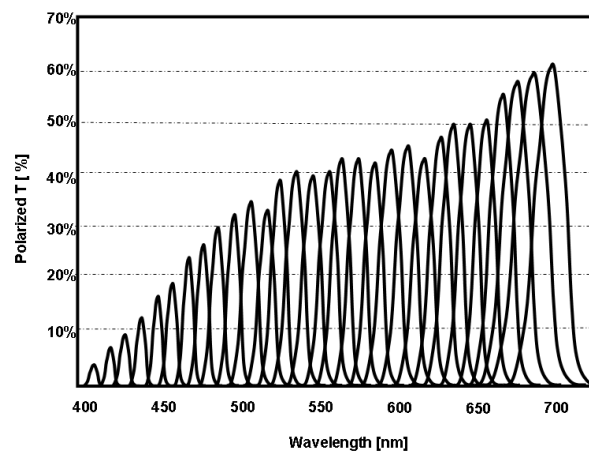


Figure 3.12: LCTF polarized transmission bands.

The experimental LCTF bands of our system were measured after integrating the LCTF into the optical path of the fundus camera in which a spectrometer (Ocean optic USB 4000) is mounted in front of the objective lens of the camera in the same plane of the patient's eye. Spectral bands were recorded at each wavelength in the wavelength range 500-650 nm by switching the LCTF to the desired wavelength λ and triggering the flash light in synchronization. A neutral density filter was used in front of the spectrometer sensor to avoid saturation, especially for longer wavelengths $\lambda > 600$ nm. During the measurement, a spectrum of the sensor bias signal was recorded in the absence of the flash light and then subtracted from each recorded spectral band. Modelling each transmission band as a Gaussian function enabled

calculation of the FWHM (full width half maximum) for each wavelength. This important measurement affects the signatures of oxygenated and deoxygenated haemoglobin, as will be described in Chapter 7. Figure 3.13 shows the experimental FWHM of the system, as a function of wavelength:

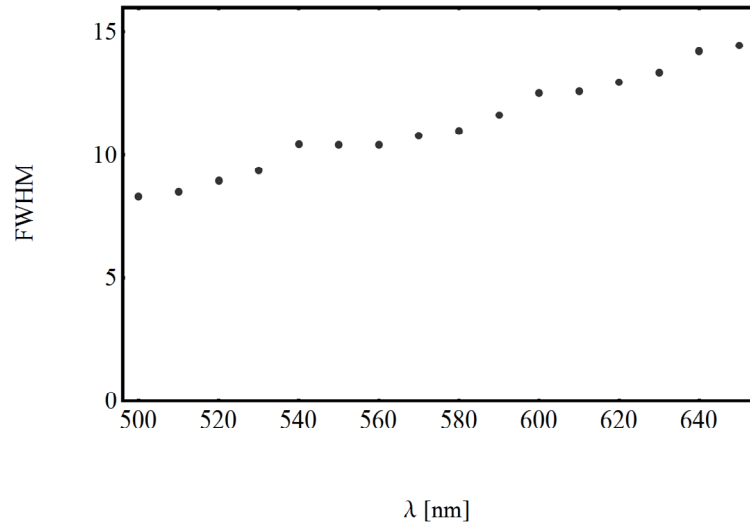


Figure 3.13: Experimental FWHM of LCTF transmission bands.

It can be seen that the measured FWHM of the spectral bands in our system increases approximately linearly with wavelength λ .

3.6 CCD detector

Detector signal to noise ratio is an important factor which needs to be considered, especially because CCD's quantum efficiency is typically poor in the blue range and peak in the red. The recorded image can be written as

$$I_R(\lambda) = F(\lambda)R(\lambda) + N_\sigma(x, y) + N, \quad (3-3)$$

where $I_R(\lambda)$ is the captured image at a wavelength λ , $F(\lambda)$ is the camera function, $R(\lambda)$ is the retinal albedo image, $N_\sigma(x, y)$ is additive fixed pattern noise, and N is random noise due to detector noise and photon shot noise. A multiplicative fixed pattern noise

$B(x,y)$ due to photo response non uniformity can be included in the camera function as: $F(\lambda) = F'(\lambda)B(x,y)$ where $F'(\lambda)$ is the camera function without noise. The general definition of signal to noise ratio (SNR) is given as:

$$SNR = \frac{S}{N} \quad (3-4)$$

The signal S is the mean voltage recorded by the detector due to the optical signal and N is the standard deviation of the noise. The signal S can be estimated from the recorded retinal images after reducing the effect of fixed pattern noise $B(x,y)$ and $N_o(x,y)$. The effect of $B(x,y)$ can be suppressed by calibrating the recorded images by flat field images (image of a white target) and $N_o(x,y)$ can be reduced by subtracting dark frames at each particular wavelength. Dark-frame subtraction reduces the amount of noise due to dark current in the detector, in addition to the associated artefacts (reflections on the surfaces of the objective lens of the fundus camera) (this is discussed in more detail in chapter 4). As a result the dominant noise in the recorded images is the random noise which consists mainly of the detector noise N_d and photon shot noise N_{Sh} . The signal to noise ratio can be expressed accordingly (Holst 1998)

$$SNR = \frac{S}{N} = \frac{S}{\sqrt{N_d^2 + N_{Sh}^2}} \quad (3-5)$$

As the signal S can be quantified in terms of the number of photons collected by the detector Q_s , (3-5) can be expressed as

$$SNR = \frac{S}{\sqrt{N_d^2 + N_{sh}^2}} = \frac{Q_s}{\sqrt{N_d^2 + Q_s}} \quad (3-6)$$

where the photon shot noise is $N_{sh} = \sqrt{Q_s}$.

Due to the low retinal reflectance and low transmission by LCTF at blue light, SNR was expected to be the lowest at this range. SNR measurements were performed on three areas: optic disc, fovea, and retinal background in the wavelength range 500 - 650 nm. In our setup we have used a high resolution cooled digital camera (12 bit, Hamamatsu-ORCA-AG, $N_d=6$ electrons) with high quantum efficiency in the visible and near infra red and well-depth 18000 photons which enables (4.4) detected photons per grey level. Figure 3.14 presents the signal to noise ratios calculated according to (3-6) and expressed in dB at three areas across the retina.

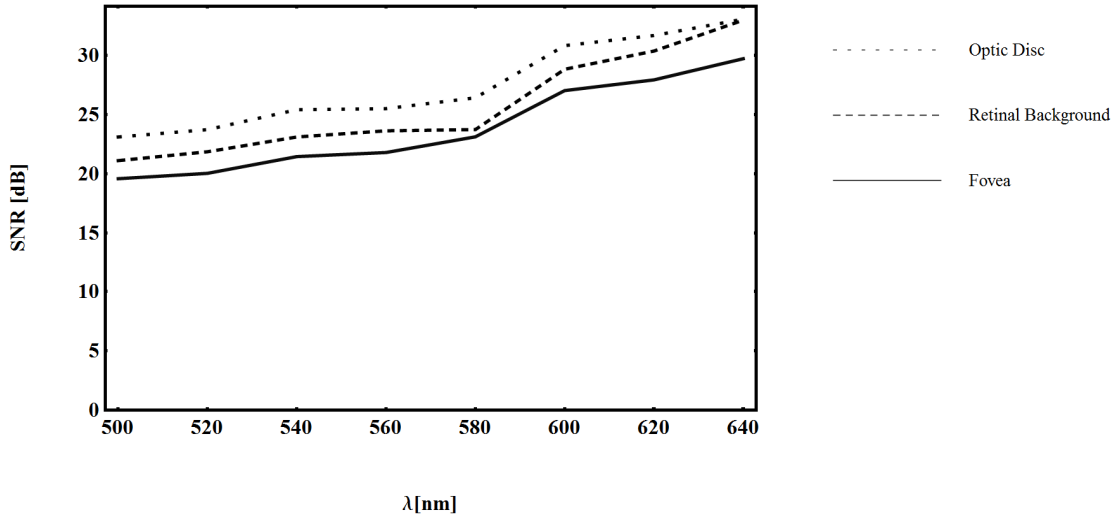


Figure 3.14: Signal to noise ratio at the optic disc, retinal background and fovea.

As noticed from the figure that signal to noise ratio increases with wavelength to reach 33 dB at 650 nm which is 9.5 dB lower than maximum SNR permitted by the

detector ($SNR_{Max}=42.5$ dB). However, Retinal images at shorter wavelengths, <500 nm, experienced very poor SNR ($SNR \ll 10$ dB).

To investigate the effect of the eye media and erratic eye motion on SNR measurements, spectral images of white spectralon were recorded through a model eye (see chapter 8 for more details on model eye) and SNR measurements were achieved in the wavelength range 450-700 nm. As can be noticed from Figure 3.15 higher SNR values are obtained in comparison to those that measured from retina. There are many factors preventing the achievement of higher SNR in the retina such as the absorption by eye media, erratic eye motion, the dependency of retinal albedo on wavelength and the imperfections in the optical system.

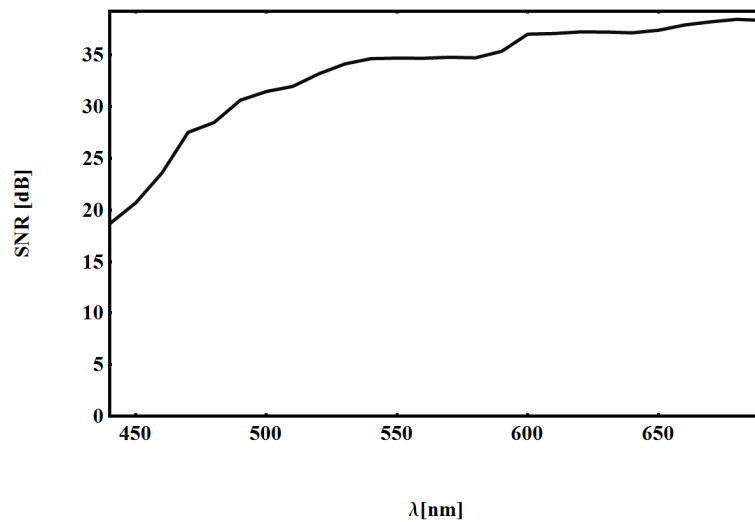


Figure 3.15: SNR obtained from white spectralon cube.

3.7 Conclusion

In this chapter, we have shown the work and modifications involved in constructing our spectral fundus imager. The lowest light intensities at the eye and the detector were measured for blue light due to the low LCTF transmission and low detector quantum efficiency at this range. The full width half maximum of the LCTF transmission bands was measured and found to increase linearly with wavelength. The signal to noise ratio of the detector across the wavelength range in both the retina and spectralon target was also investigated. The *SNR* ratio in retinal images was very low at wavelengths shorter than 500 nm in comparison to the *SNR* obtained from the spectralon cube. In the following chapter, algorithms to calibrate and register the retinal images will be presented.

Chapter 4

Calibration and image registration

In this chapter, we describe two main post-processing procedures to enable improved restoration of spectral signatures from recorded retinal images. These procedures are calibration and registration. Image registration is implemented to correct for translational and rotational misalignments between recorded retinal images due to the nature of the time sequential technique and eye movement. Image calibration is meant to reduce the effect of illumination variation between retinal images and system noise and artefacts such as reflections on the surfaces of optical components and detector noise. We also explain the implementation of a simple algorithm to measure the accuracy of registration.

4.1 Image processing and data analysis

Fundus photography involves using a fundus camera which illuminates the retina of the patient and simultaneously captures an image of the fundus. Both the optical system of the fundus camera and the optical components of the human eye are integrated to form an image of the fundus and that will make control over the entire system impossible. Illumination variations are therefore unavoidable as the spectral cube has to be constructed in time sequence. The optical system of the fundus camera, as discussed in Chapter 3, introduces some artefacts due to imperfection of optical components in the optical system, namely from reflection of the surfaces of the optical components, and displacements of the black dots, which have been employed to cancel specular reflection when LCTF is fitted into camera system body. System

calibration is vital to correct for these artefacts and minimize the errors encountered when retinal images are acquired. An Image registration algorithm has been used to realign the recorded images for accurate extraction of spectral signatures.

4.2 Calibration

To enable minimizing of errors and to enable calculation of retinal albedo, a mathematical model of image capture is required. In practice, when the fundus is uniformly illuminated and the optical system is perfect, the recorded retinal image $I_R(x, y)$ is the distribution of light falling onto the retina. In reality, neither the light flash nor the optical systems are perfect and that causes the intensity of the light reaching the retina to vary spatially and from flash to flash. Variation of flash light illumination and imperfections in the optical system can be incorporated into one camera function $F(x, y)$ as they can be considered multiplicative processes. Image recording is subject to two forms of noise: fixed pattern artefact and CCD detector chip noise.

The fixed pattern artefact is a result of reflection from the front and back surfaces of the optical system components (the objective lens) in the absence of the two black dots introduced into the original camera system (see chapter 3). Figure 4.1 presents a raw image of a healthy retina with a profile across the image to show the intensity of the artefact at the centre of the recorded image. As mentioned in the previous chapter, the intensity of the artefact was attenuated by introducing a linear polarizer in front of the detector.

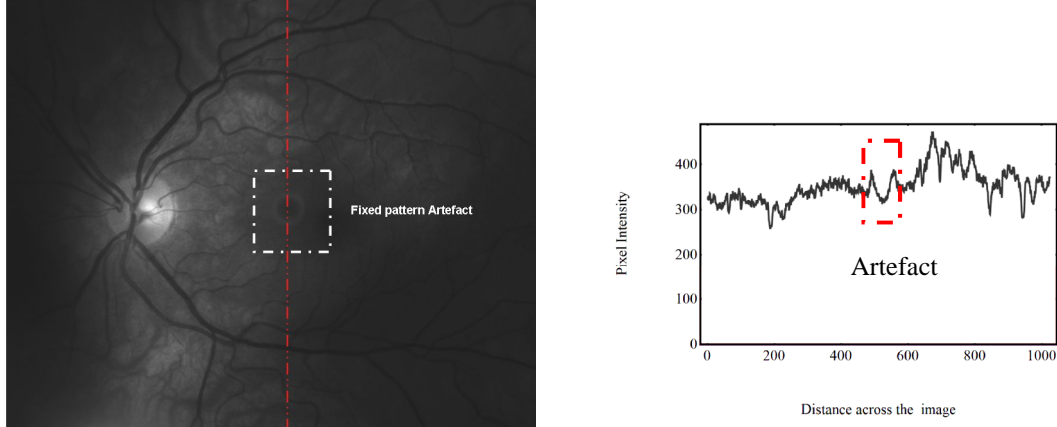


Figure 4.1: Raw retinal image with a profile across the image at the centre

Dark current, readout noise, and shot noise are the main contributors of CCD detector chip noise and their effect is additive to the whole noise produced in the system in addition to the fixed pattern artefact. The basic model of image capture can be expressed mathematically

$$I_R(x, y, \lambda) = F(x, y, \lambda)R(x, y, \lambda) + I_b(x, y, \lambda), \quad (4-1)$$

where $I_R(x, y, \lambda)$ is the recorded image, $F(x, y, \lambda)$ is the camera function, $R(x, y, \lambda)$ is the retinal albedo image, $I_b(x, y, \lambda)$ is the noise and λ is the wavelength.

The noise term in the previous equation can be expressed as a sum of fixed pattern artefact and CCD noise

$$I_b(x, y, \lambda) = I_{DC}(x, y) + I_N(x, y, \lambda) \quad (4-2)$$

where $I_{DC}(x, y)$ is the noise in the detector chip due to dark current and readout noise and shot noise. $I_N(x, y)$ is the fixed pattern artefact as a result of reflection by optical components in the system. The point (x, y) is taken to describe a location on the two-dimensional imaging plane (all dimensions are considered in pixels). Quantitative analysis of retinal chromophores demands restoring the best estimation of the albedo retinal image $R(x, y)$. The obvious way, according to (4-1), is to subtract the effect of noise and artefact during image capture from the recorded image at each wavelength and divide by the camera function $F(x, y, \lambda)$ as illustrated

$$R(x, y, \lambda) = \frac{I_R(x, y, \lambda) - I_b(x, y, \lambda)}{F(x, y, \lambda)} \quad (4-3)$$

The problem is to determine a useful approximation for both the system noise $I_b^*(x, y, \lambda)$ and camera function $F^*(x, y, \lambda)$.

4.2.1 Dark images

To estimate system noise and hence invert (4-1), two sets of dark images are recorded. The first set is acquired at the end of each session of recording retinal image cube by mounting a black target in front of the camera system at the same plane as the patient's eye and recording dark images in the whole wavelength range. These dark images $I_N(\lambda)$ represent an approximation of the artefact introduced in the optical system of the fundus camera.

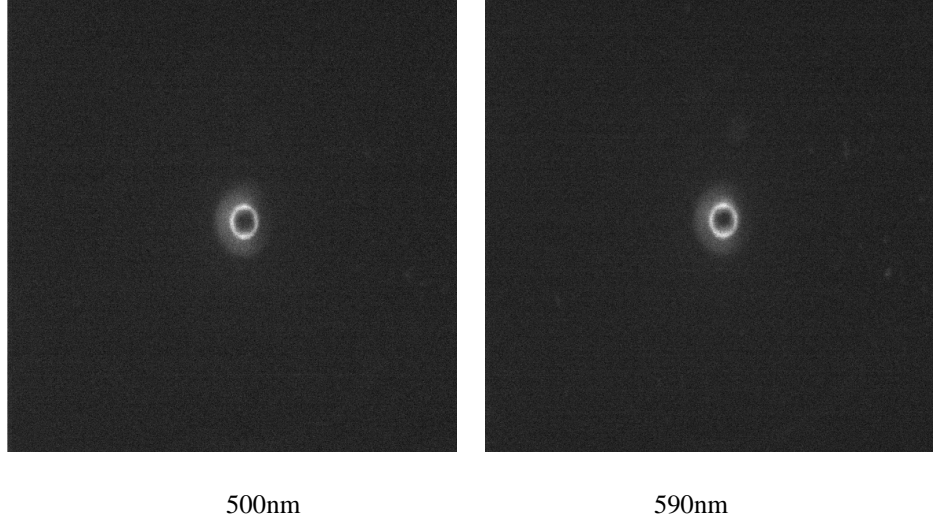


Figure 4.2: Dark images recorded at various wavelengths

Figure 4.2 shows dark images taken at various wavelengths, in which it can be seen that the fixed pattern artefact is centred. Recording the dark images can be used to reduce the effect of reflection from the optical system by an optimization process employing a subtraction of the artefact $I_N(x, y, \lambda)$ from each corresponding retinal image $I_R(x, y, \lambda)$ as expressed mathematically

$$\hat{I}_R(x, y, \lambda) = I_R(x, y, \lambda) - \alpha(\lambda)I_N(x, y, \lambda), \quad (4-4)$$

where $\alpha(\lambda)$ is a wavelength-dependent variable optimised to minimize the artefact, based on scene variance in the area where the artefact is. Due to the fixed pattern, artefact recorded images showed apparent variation in pixels intensity at the centre. One way to attenuate this effect was by searching for the proper value that decreases the artefact area variance for each particular wavelength.

The second set of dark images I_{DC} represents the noise generated in the CCD detector chip. These images can be obtained when the light sources in the camera system are switched off. Subtracting I_{DC} can effectively reduce most unwanted effects of dark current, readout noise, and shot noise. Figure 4.3 shows a calibrated retinal image at 580 nm after minimizing the effect of both fixed pattern artefact and detector chip

noise. It is clear from the spatial intensity profiles across the area of the artefact that the intensity of the artefact has reduced significantly.

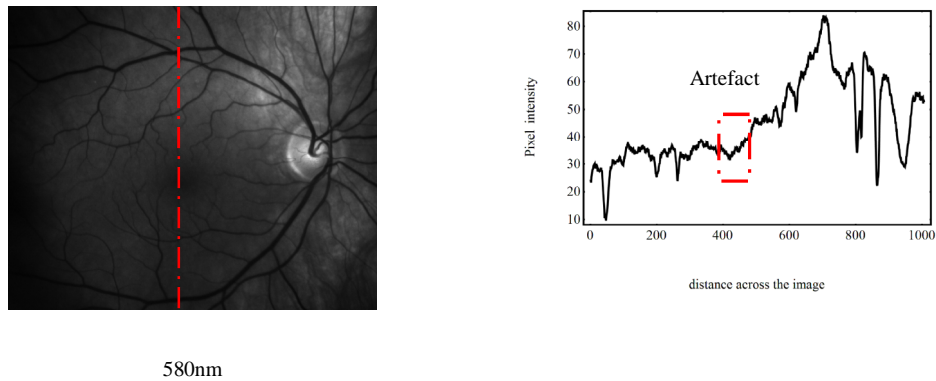


Figure 4.3: Calibrated retinal image (Left); A spatial across intensity profile (Right)

4.2.2 Camera function

As stated in (4-3), albedo retinal images can be restored from recorded retinal images when a good approximation of camera function $F(x, y, \lambda)$ is obtained. It is necessary to identify various features in retinal image and to distinguish between features attributable to the albedo image and those attributable to the camera function, as the camera function varies with eye position and illumination pattern. As can be seen from Figure 4.3 and Figure 4.4, images at the same wavelength ($\lambda=580$ nm) have different illumination patterns as the eye is in continuous motion.

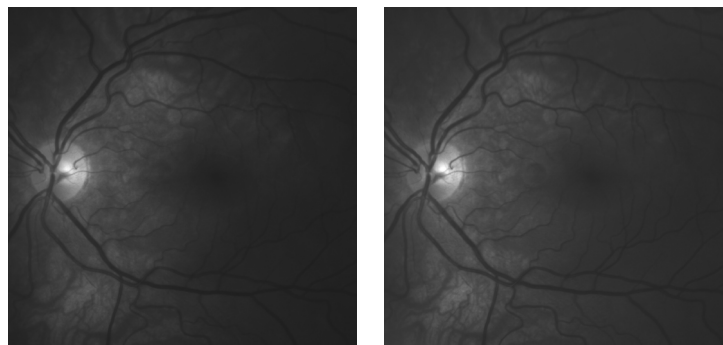


Figure 4.4: Retinal images at the same wavelength ($\lambda=580$ nm)

The retinal image consists of the vessel tree entering the image at the optic disk and spreading out around the macula. The capillary network extends throughout much of the retina and choroid and contributes to the image background. The consequence is that there are shading variations across retinal images which are inherent in the albedo image itself. These shading variations have to be discriminated from those due to imperfection in optical components and eye movement (Cree et al.1999). In Chapter 7, more details will be presented to separate and model illumination variation from retinal images, hence enabling quantitative analysis of spectral retinal images.

4.3 Image Registration

Image registration has been reported as a necessary post image processing technique in many practical fields, ranging through integrating information taken from different sensors, finding changes between images taken at different times and conditions, inferring three-dimensional information from images in which either the camera or the objects in the scene have moved to model-based object recognition (Goshtasby, 2005). Image registration is the process of finding the point- by- point correspondence between two images of a scene which involves calculating the transformation which matches the structures found in the images. Transformation type relies on the cause of the misalignments which might not be the only distortion between the sequential images. The main source of misregistration may be due to change in sensor and object geometry as a result of object movement. Other distortions due to imperfections in the optical system can be also present, which make it difficult to determine the source of misregistration and hence affect the selection of appropriate features necessary to perform registration (Brown, 1992). Distortions can be static or dynamic, internal or external, and geometric or photometric. Static distortions are the same in all images

and can be removed via calibration techniques. Internal errors are due to detector and imperfections in optical systems. External distortions, on the other hand, are due to the continuously changing alignment between the camera and the object in which there can be spatial and intensity errors. Internal distortions and many of the photometric ones can be considered as static errors and can be attenuated using calibration.

Several registration methods have been reported, and these methods can be classified based on the image data used, measure of similarity used, and the transformation applied (Brown 1992; Van den Elsen et al. 1993). There are local and global methods to register fundus images. Local methods perform registration only on distinctive features extracted from the retinal images. However, global methods use the whole image to calculate the best transformation function to get images into alignment.

One of the early attempts to register ocular images was performed by Algazi et al. (1985) to investigate and monitor changes in the optic disk of glaucoma patients, where misalignments are corrected manually. Drusen in age-related maculopathy was quantified by registering the red and green channels of a TV monitor to a reference frame (Peli et al, 1986). Early and late frames were registered depending on the gradient of fluorescence intensity (Phillips et al. 1991) to assess macular oedema. Extracting information such as the location of retinal blood vessels and their crossings has been implemented by enhancing the fluorescence angiograms and using cross-correlation in small windows around the features to find the correspondences (Nagin et al, 1985). Peli (Peli et al. 1987) has used an adaptive thresholding method to select blood vessels, and by using a similarity detection method, he found the correspondences between blood vessels. Vessels junction points have been used by Jagoe et al. (1993) to register fluorescence angiograms to investigate retinal vascular

occlusions during cardiopulmonary bypass surgery. Jasiobedzki et al. (1993) developed an algorithm to perform image registration by using the correspondence of curves approximating extracted blood vessel segments. Cideciyan (1995) has used the cross-correlation function in spatial frequency domain to account for translational, rotational, and scaling misalignments between ocular fundus images. Many global image registration methods have been implemented using all pixel values within images to determine the best transformation to register the images (Castro et al 1987; Lee 1988).

4.3.1 Retinal image registration method

The complexity of image registration depends on both the nature of misalignments encountered when images are recorded and the transformation required to bring images into registration. The type of spatial transformation needed to properly overlay images is the key in selecting an image registration technique. The chosen registration technique must remove the spatial distortion due to differences in acquisition and not that due to differences in scene properties which need to be detected. Due to the nature of the adopted time sequential technique, the main general transformations between recorded retinal images are expected to be affine which is composed of two translations (x , y), rotation, and scaling. Image distortion may occur due to varying imaging position within the pupil. The validity of this assumption will be discussed later in this chapter. Figure 4.5 presents the transformations encountered because the human eye is in continuous irregular involuntary movement. Eye movements consist of drifts with visual angles up to about 5 minutes of arc, microsaccades between 1 and 2 minutes of arc, and ocular tremors of about 30 seconds of arc.

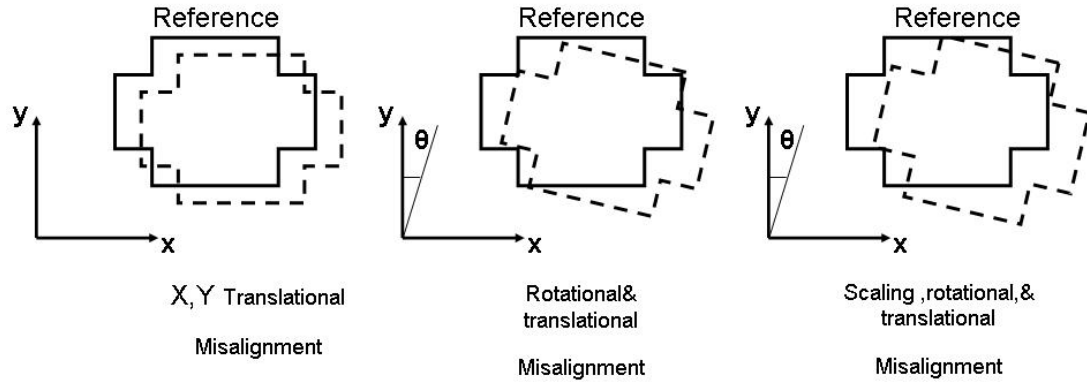


Figure 4.5: Transformations encountered when retinal images are recorded sequentially

A typical technique to register two images with affine misalignments entails calculating the two-dimensional cross-correlation function (Gonzalez, 1992). The offset at the maximum of the cross-correlation function represents the required translation and rotation to realign the images. Cross-correlation is a measure of the degree of similarity between an image f with dimensions $M \times N$ and template W of size $K \times L$, where $L \leq M$, $K \leq N$ and can be simply expressed mathematically:

$$C(i, j) = \sum_x \sum_y f(x, y)W(x - i, y - j) \quad (4-5)$$

where $i=0,1,2,\dots,M$, and $j=0,1,2,\dots,N$, and the summation is calculated over the image region where W and f overlap. According to (4-5) and as illustrated in Figure 4.6, the cross-correlation function, $C(i, j)$, will have values as (i, j) varies inside $f(x, y)$ where varying (i, j) is equivalent of moving $W(x, y)$ around the image area.

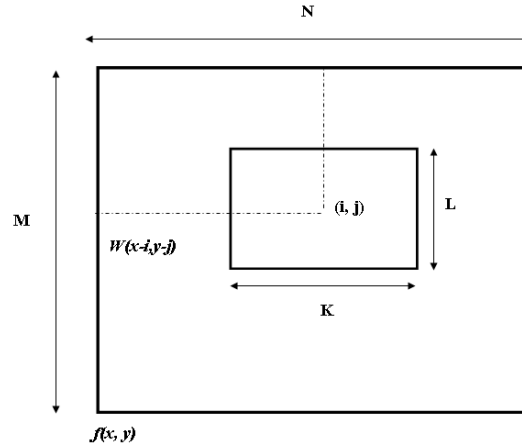


Figure 4.6: Illustration of cross-correlation function calculation

The maximum value of $C(i, j)$ indicates the position where $W(x, y)$ best matches $f(x, y)$. Using cross-correlation to correct for rotation and scaling can be achieved in the same way by searching for the maximum value of $C(x, y)$ as we rotate and rescale $W(x, y)$. To attenuate the effect of amplitude changes of both $W(x, y)$ and $f(x, y)$ a new version of (4-5) is used:

$$C(i, j) = \sum_x \sum_y (f(x, y) - \overline{f(x, y)})(W(x-i, y-j) - \overline{W}) \quad (4-6)$$

Amplitude variations might occur due to the changes in illumination pattern on the retina, spectral variation of retinal albedo, and the noise in the system.

Calculation of the cross-correlation can be implemented in the frequency domain using fast Fourier transform (FFT) when f and W have the same dimensions. As a result, large images of the same size can be registered with good efficiency. Cross-correlation using FFT can be given as

$$C(i, j) = F^{-1}[F[f(x, y)]F^*[W(x-i, y-j)]] \quad (4-7)$$

The terms F and F^{-1} account for Fourier and inverse Fourier transform respectively, and $*$ is the complex conjugate.

4.3.2 Steps in image registration

Recorded images, as depicted in Figure 4.3, are dissimilar as the wavelength changes, thus it is crucial to apply the registration algorithm only to those features that stay consistent in the images throughout the wavelength range. As a result, there are several steps that need to be considered when two images are registered:

4.3.2.1 Pre-processing

Distortion due to the imperfection in the optical components of the system (instrument and eye) is common in all images and affects the registration. Prior to feature selection and image registration, it is very important to reduce the influence of distortion. As illustrated previously, retinal images can be calibrated by reducing the effect of artefacts (reflections on the surfaces of the optical components and additive noise) encountered in the retinal images.

4.3.2.2 Feature selection

To register two images, a number of features are selected from images and correspondence is established between them. Spectral retinal images are dissimilar due to the spectral signatures of oxygenated and deoxygenated blood and the pigmentation in RPE, in addition to the irregular illumination variations between acquired images due to eye movements. Figure 4.7 illustrates the dissimilarity between retinal images as wavelength changes. This discrepancy between images necessitates one to searching for signatures that are invariant with wavelength. The optic disk and blood vessel tree in the retina, as seen in Figure 4.7, are distinctive characteristics that are approximately invariant throughout the wavelength range and can be used as landmarks to register the images. To facilitate extraction of these

spatial signatures (namely optic disk and vessels tree) from retinal images, recorded images are enhanced by passband and edge detection filters prior to image registration calculation.

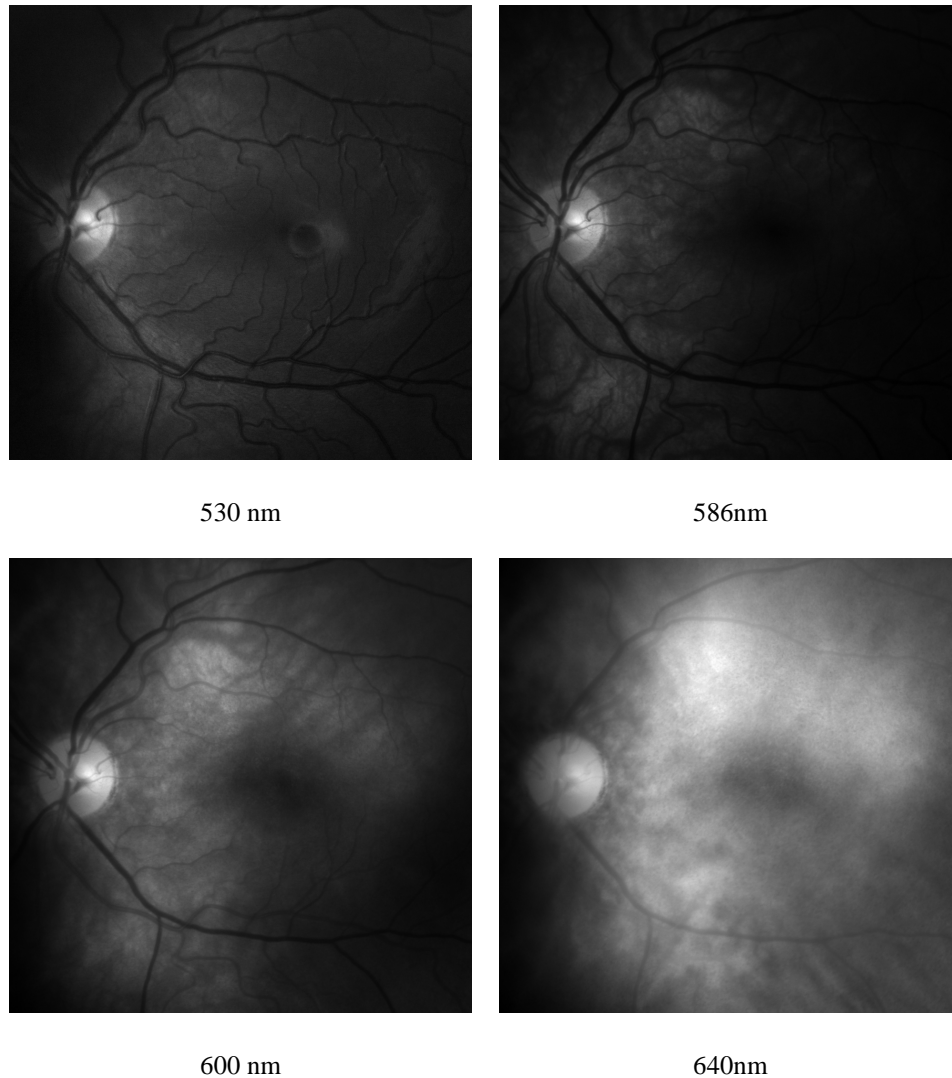


Figure 4.7: Retinal images at various wavelengths

4.3.2.3 Image Enhancement

Depending on the features to be selected, image enhancement techniques can be used to enhance certain features which are approximately invariant between spectral images and hence improve the reliability and accuracy of registration. Spatial enhancement techniques are applied to the pixels directly to enhance the retinal

vasculature using smoothing, deblurring or passband filtering operations (Gonzalez 1992).

Passband filtering offers an advantage over smoothing and deblurring filters by using their properties at the same time in which reducing the noise and sharpening the area of interest in the image. The size of the filter can be selected to provide a compromise between the noise attenuation and the amount of detail retained in the image. The kernel of the passband filter was designed to pass the retinal vessel tree in the image in which cut off frequencies of the passband filter were determined depending on vessels thickness and spatial frequency of occurrence. The dimensions and frequency of occurrence of the vasculature were measured directly from the recorded retinal images. Figure 4.8 shows the typical frequency response (or magnitude spectrum) of a passband filter designed to pass blood vessels of thickness ranging between 30 pixels and 8 pixels as measured in the recorded images.

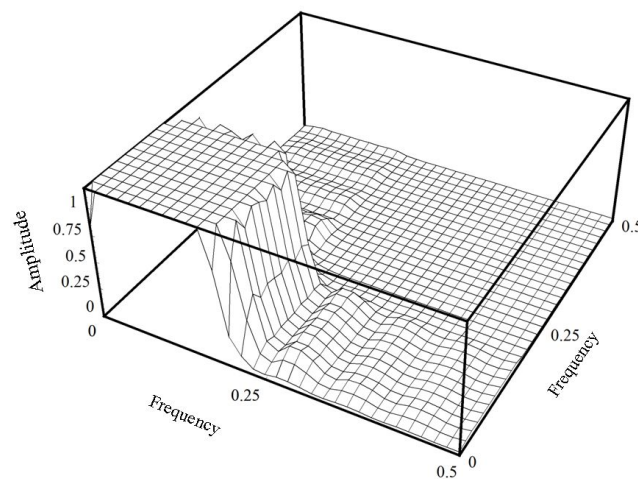


Figure 4.8: Passband filter frequency response

Figure 4.9 shows the effect of changing the cut-off frequencies on blood vessel tree enhancement. The cut-off frequencies were altered to control the pass and stop bands of the filter. In Figure 4.9 (a), the size (in pixels) of the passband was larger than the

stop band and enabled unwanted details to pass through. As the size of the passband reduced, more useful information (blood vessels) was obtained (Figure 4.9 (b) and (c)). In our algorithm, it was very crucial to select the passband filter parameters (cut-off frequencies, kernel size) to enable improved extraction of the retinal vasculature.

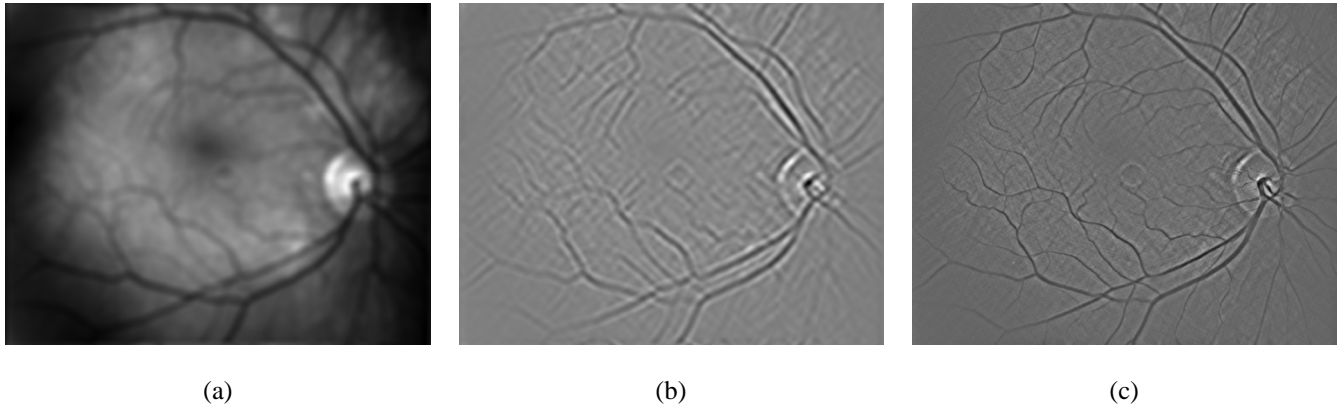


Figure 4.9: The influence of changing cut off frequencies on the enhancement achieved by passband filters

To improve image enhancement, the boundaries of the vessels can be identified by means of edge detection, which represents the discontinuities in scene reflectance into sharp changes in image intensity. There are two main approaches to perform edge detection: one approach determines the zero crossings of the second derivative of image intensities, while the second one finds the locally maximum gradient magnitudes of image intensities in the gradient direction. To enhance the boundaries of the vessel tree, the Laplacian of a Gaussian filter *LOG* is employed. Edge detection using *LOG* filter can be obtained by finding the Laplacian of the image and locating the pixels that separate positive and negative regions. The Laplacian operator can be used to compute the second derivative and is defined by

$$\frac{\partial^2}{\partial x^2} + \frac{\partial^2}{\partial y^2} \quad (4-8)$$

In the pixel domain, the kernel of Laplacian filter can be approximated by:

$$T = \begin{bmatrix} 0 & -1 & 0 \\ -1 & 4 & -1 \\ 0 & -1 & 0 \end{bmatrix}$$

Using the kernel T , The Laplacian of any image can be calculated using convolution.

To avoid detection of noisy edges, an image $f(x, y)$ is smoothed before its Laplacian is computed. Smoothing or convolving an image with Gaussian $G(x, y)$ and then determining its Laplacian is the same as convolving the image with Laplacian of Gaussian LOG . That is,

$$G(x, y) = e^{-\frac{x^2+y^2}{2\sigma^2}}$$

$$LOG[f(x, y)] = \frac{\partial^2 G(x, y)}{\partial x^2} + \frac{\partial^2 G(x, y)}{\partial y^2}$$

$$LOG(x, y) = \sigma^{-4} e^{-\frac{x^2+y^2}{2\sigma^2}} (x^2 + y^2 - 2\sigma^2)$$

where σ is the standard deviation of Gaussian filter.

As the standard deviation of the Gaussian smoother is increased, fewer edges are obtained, and the edge becomes smoother and displaced from its true position. Figure 4.10 shows a typical response of LOG .

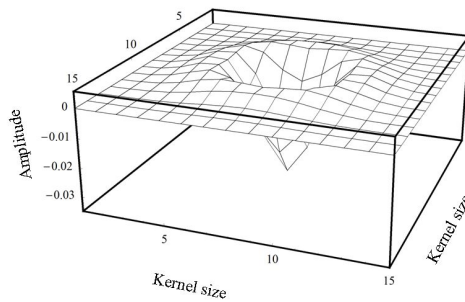


Figure 4.10: LOG response

The LOG filter has been applied to retinal images subsequent to vessel tree enhancement and prior to the cross-correlation function used to determine

translational and rotational misalignments. An example of edge detection by *LOG* filter in retinal images is shown in Figure 4.11 using two standard deviation values of Gaussian.

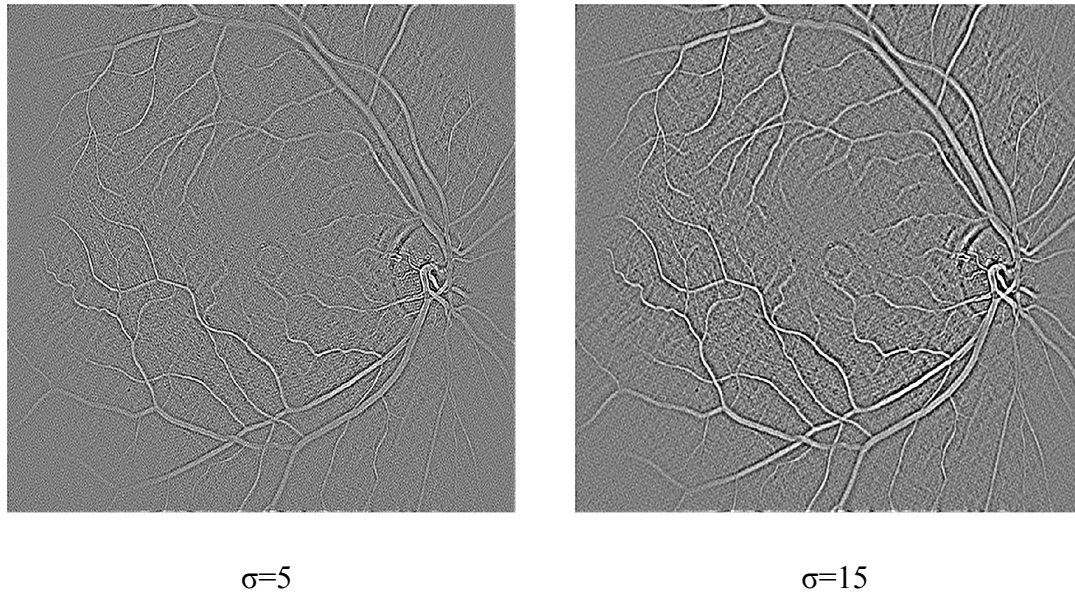


Figure 4.11: Edge detection using LOG filter

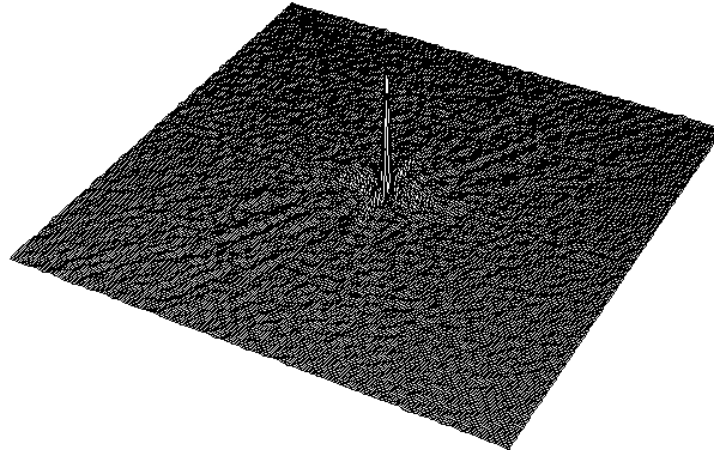
It has been shown that the retinal vessel tree can be extracted from the spectral retinal images as a distinctive feature common between the images across the wavelength range. Passband and LOG filter parameters were selected to suit the recorded retinal images within the field of view possible with our instrument.

4.3.2.4 Cross-correlation

After enhancing the retinal images, registration can be performed between each image and a reference image (a template) to determine the transformation required to correct for the misalignments. Retinal image at 580 nm was selected as a template in which blood vessels show higher contrast in comparison to the retinal background, due to the absorption properties of blood at this wavelength (see Figure 4.7). The cross-correlation function was employed to determine the translational, rotational, and scaling misalignments between the reference and the recorded images. Figure 4.12

shows a two-dimensional cross-correlation function between two images. The cross-correlation function shows a maximum peak when images are in alignment.

To calculate the required translations between two images shifted from each other by $(\Delta x, \Delta y)$, one can search for the position of the maximum of the cross-correlation function in two-dimensional space (X, Y) . Cross-correlation was calculated in the frequency domain, due to the shorter time required to perform the calculation.



3D cross-correlation function between two images

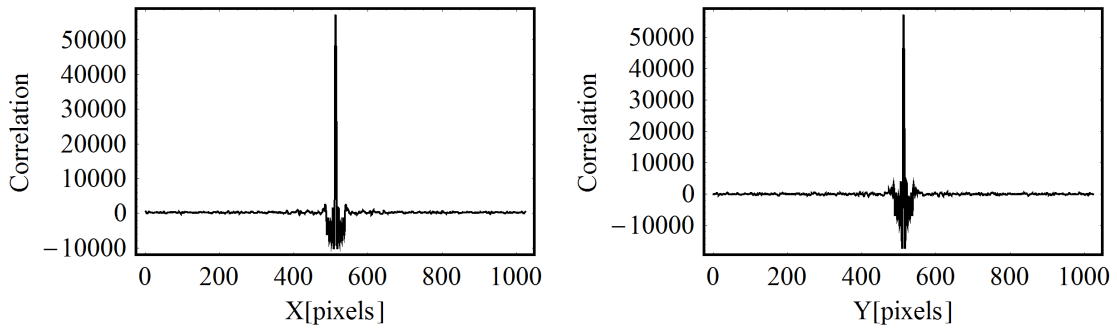


Figure 4.12: The maximum of the cross-correlation function between two retinal images

The rotational misalignment $\Delta\theta$ and scaling factor ζ can be deduced by employing a cross-correlation function, but in several steps, in contrast to the translational calculation, which was achieved in one step. During the calculation of rotational and scaling misalignments, recorded images needed to be rotated or rescaled with predefined steps in respect to the reference image and a cross-correlation function was

calculated at each step. Once the cross-correlation function was obtained for each step, an interpolation was used to extract the exact value of rotation and scaling which maximize the magnitude of the cross-correlation function (see Figure 4.13).

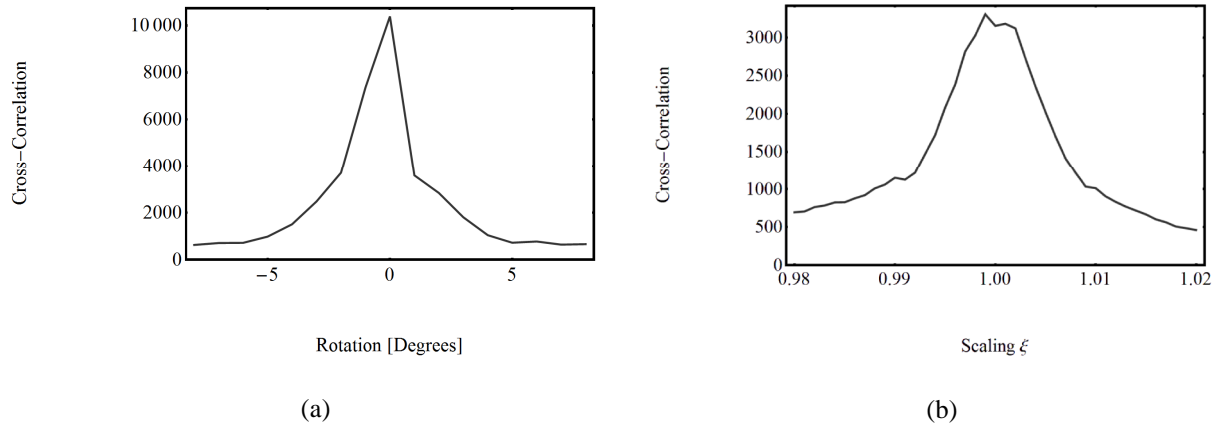


Figure 4.13: Cross-correlation as a function of rotation (a) and scaling (b)

After translational and rotational misalignments are calculated, transformation of the recorded image is implemented to shift, rotate, and rescale the recorded image by $(-\Delta x, -\Delta y)$, $(-\Delta\theta)$, and ζ to realign the images in respect to the reference template. Figure 4.14 presents a set of registered images at different wavelengths.

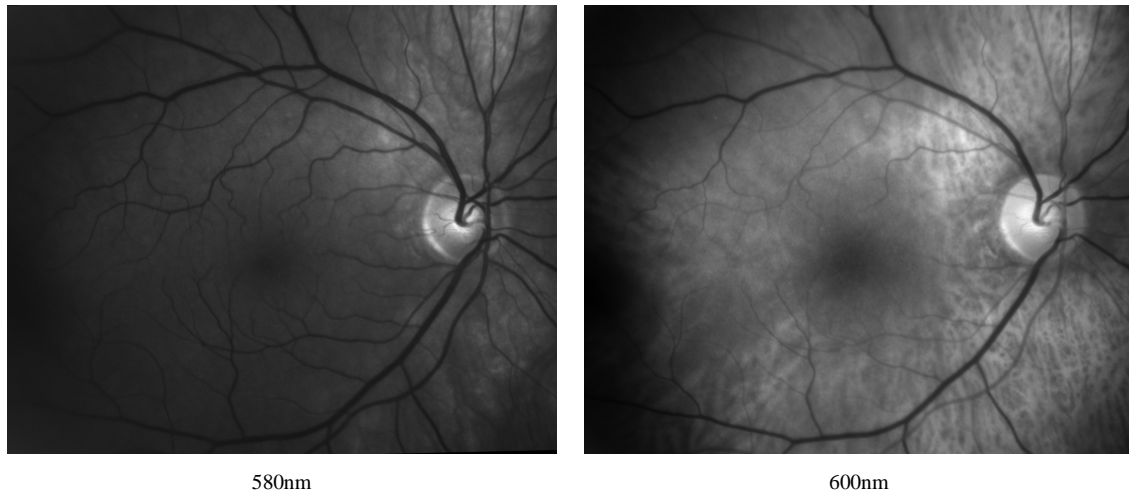


Figure 4.14: Registered retinal images taken from left eye of healthy subject in the wavelength range (580-600 nm)

The flow chart for implementing the registration algorithm is presented in Figure 4.15

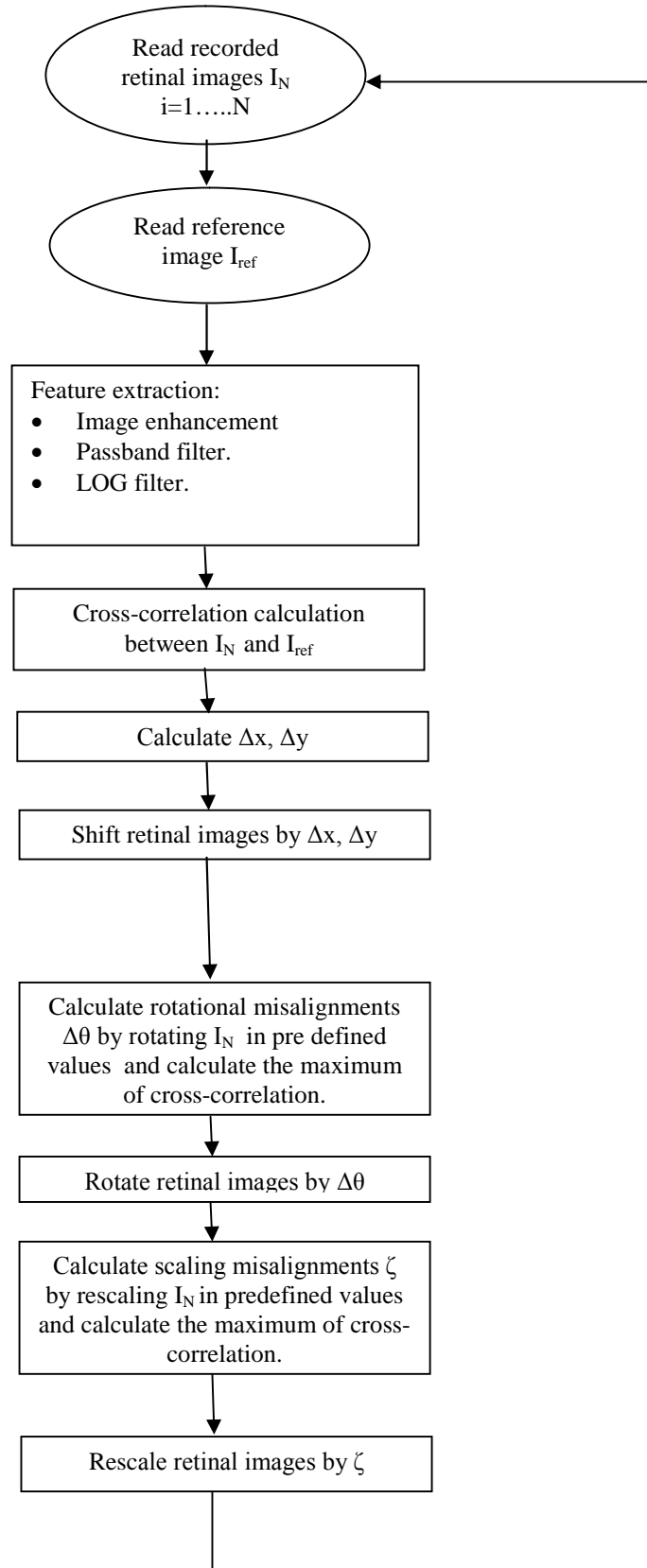


Figure 4.15: Flow chart of registration algorithm

4.3.3 Validation of co-registration algorithm

Recorded images suffer from deformations due to many reasons, such as imperfection in the optical system of the eye and the instrument, in addition to eye movement. Image deformation due to the non-uniform magnification across the whole field of view available by the fundus camera can be avoided by considering only the central area of interest to perform registration (Cideciyan 1992). Scaling changes as a result of recording images in time sequence and subject movement are restricted by asking the patient to keep his eye aligned with a fixating lamp. The accuracy of the registration algorithm is wavelength dependent, in which at long wavelengths the contrast of retinal vasculature will be reduced and that will affect the accuracy of registration compared with the green wavelength range, where contrast remains high, as depicted in Figure 4.7.

We have implemented a method to measure the accuracy of the registration algorithm based on fitting a centre line to the tracked vessel and looking at pixel to pixel registration of the cross-vessel profiles. This method enables us to study the spatial distortion between the central and the peripheral part of the retinal images, in addition to the distortion due to heart pulses.

4.3.3.1 Vessel tracking and fitting to a centre line

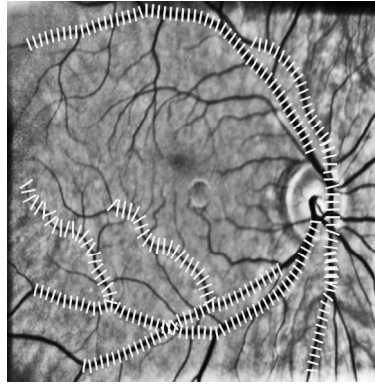
The skeleton of the blood irrigation network of the retina was extracted by employing basic image pre-processing, coupled to a fast marching based technique. The pre-processing step is required to overcome the artefacts associated with retinal images as a result of non-uniform illumination. *Prior* to tracking the vessels, an appropriate cost function is employed to highlight the blood vessel tree and minimize the noise, as it produces a map where lower values are assigned to inside the vessels than elsewhere

in the image. More details about the tracking algorithm are explained in Chapter 7. Vessel tracking determines the coordinates of the centre line for each tracked vessel, which enables the across-intensity profiles along each tracked vessel to be obtained as shown Figure 4.16 (a).

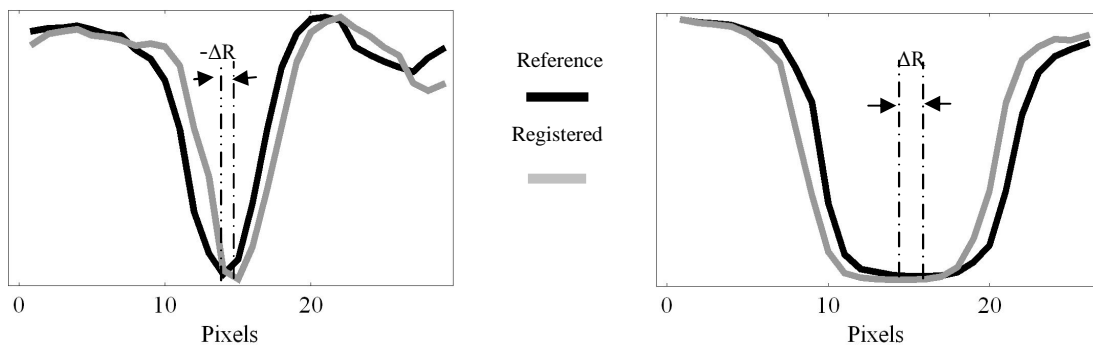
4.3.3.2 Registration accuracy evaluation

Registration error can be defined as the difference in geometry of a point in one image set taken as reference geometry compared to its geometry in the second registered set. To evaluate the accuracy of registration, a simple cross-correlation calculation is performed between two profiles obtained from two images after registration. The maximum of cross-correlation function determines the geometrical distortion due to optical deformation, de-synchronization between image recording and heart pulses, or misregistration error. A positive reference direction, corresponding to clockwise in respect to the reference profile, is assigned to explain a reference direction of the shift between the two profiles. The algorithm for calculating registration accuracy can be implemented through the following steps and as explained in Figure 4.16:

- Register retinal images as explained previously.
- Apply vessel tracking and profile extraction from registered images.
- Perform local cross-correlation calculation between extracted profiles.

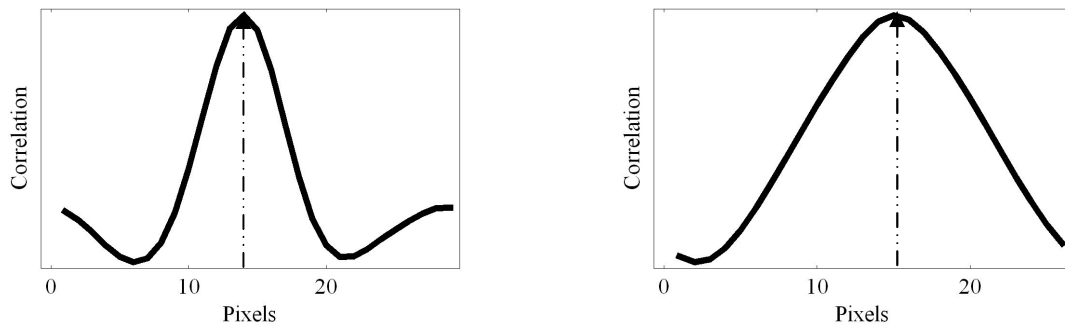


(a) Vessel tracking and cross profiles extraction along tracked vessels.



(b) Two profiles (left: from artery, right: from vein) obtained from the reference and registered images:

(Left) profile with negative shift. (Right) profile with positive shift with clock wise direction.



(c) Local correlation between two profiles, maximum value centred at the residual misregistration error.

Figure 4.16: (a) Vessel tracking and cross profiles extraction, (b) Vessel profiles, (c) Local cross-correlation function between two profiles

4.3.3.3 Results

The accuracy of the registration algorithm has been tested for two categories of images recorded from 10 subjects. In the first category, two identical images from each subject are recorded sequentially at the same wavelength (580 nm). In the second category, we considered the accuracy of registration throughout the wavelength range by investigating the registration error between two pairs (500, 580) nm and (580, 650) nm. The registration accuracy was expected to be the lowest for the images recorded at 650nm and 500 nm, due to low signal-to-noise ratio and poor image quality.

- **Two images at the same wavelength:**

Retinal images at 580 nm are chosen for the purpose of calculating registration accuracy, in which the blood vessel tree is well defined due to the spectral signatures of oxygenated and deoxygenated blood. As explained previously, residual registration errors are evaluated by looking at feature-to-feature registration. Our intention is to assess the accuracy and errors which are probably associated with changes in eye geometry and differential synchronization with heart pulses. The main arteries and veins near the optic disk and in the peripheral area far from the optic disk are tracked. Figure 4.17 shows a normalized histogram of misregistration errors obtained from a healthy subject. The histogram is approximately Gaussian with standard deviation less than one pixel (≈ 0.5 pixel).

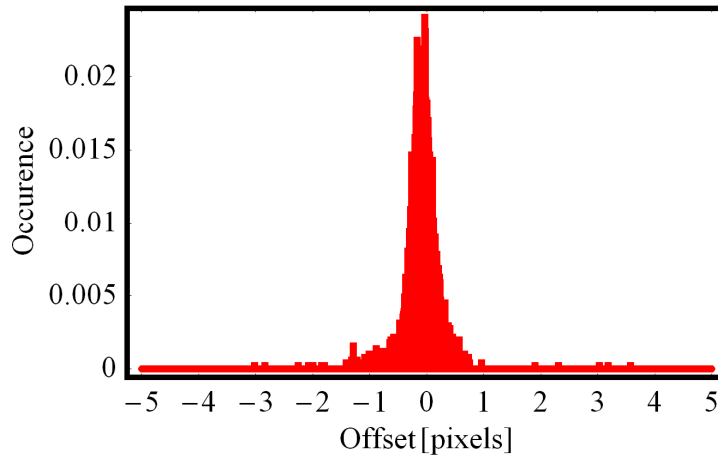
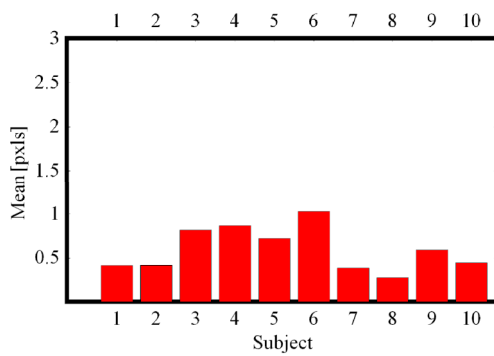
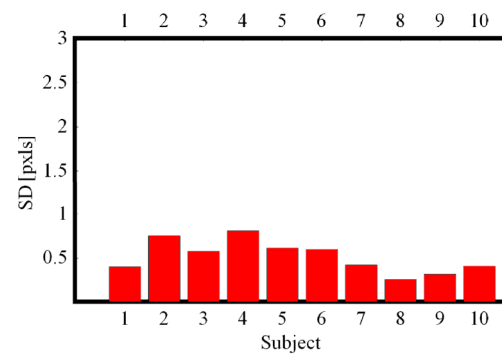


Figure 4.17: A sample histogram of geometrical errors obtained from healthy subject between two identical images at 580 nm

The accuracy of the registration algorithm has been investigated by applying the algorithm on registered images recorded from 10 subjects (5 healthy and 5 unhealthy patients). Retinal images recorded from patients were considered in this study to assess the registration accuracy in conditions encountering massive eye movements. The mean achievable accuracy was less than one pixel (0.6 ± 0.5 pixel), in the worst case as shown in Figure 4.18 which presents the mean and standard deviation of the errors for the 10 subjects.



(a) The mean value of 10 subjects at the same wavelength (580 nm)



(b) The standard deviation of 10 subjects at the same wavelength (580 nm)

Figure 4.18: The mean and standard deviation of the residual errors obtained from 10 subjects

The greatest deformations between registered images can be noticed in areas close to the optic disk, because of differential distortion of the retina for differential synchronizations of image recording times with heart pulses (more pronounced for arteries). Different types of distortion can be observed in the peripherals because of non uniform magnification across the available field of view. Misregistration errors are highlighted and coded in colour maps, as shown in Figure 4.19, where perfect registration is presented in blue, and residual registration errors are coded in different colours, as explained in colour code attached.

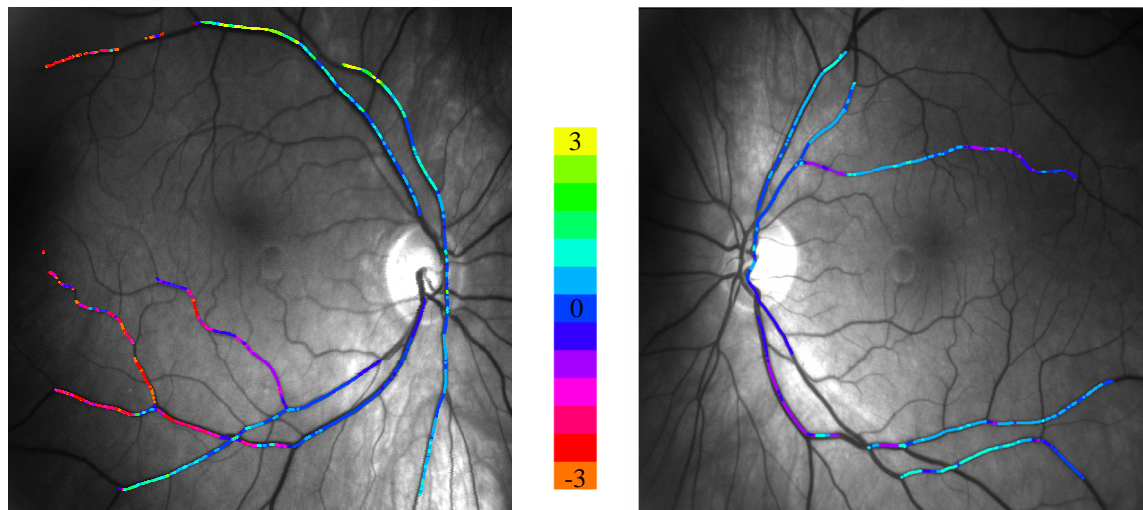


Figure 4.19: Colour coded maps of misregistration errors in pixels near the optic disk and in the periphery

- **Two images at different wavelengths:**

As wavelength varies, spectral retinal images show different appearance in which some important features vanish. To check how the registration accuracy is influenced by wavelength, two pairs of retinal images (500,580) nm and (580,650) nm are selected to represent the worst cases, where the signal-to-noise ratios are low in addition to the differences in image quality. Normalized histograms shown in Figure 4.20 were more expanded (standard deviation exceeded 1 pixel) than those calculated

when 580-580 nm was considered .The level of accuracy obtained from 10 subjects suggests that the accuracy will decrease as wavelength changes to exceed 1 pixel (0.96 ± 0.55 pixel) when wavelength at 500 nm was considered and less than two pixels for 650 nm (1.34 ± 0.5 pixel).

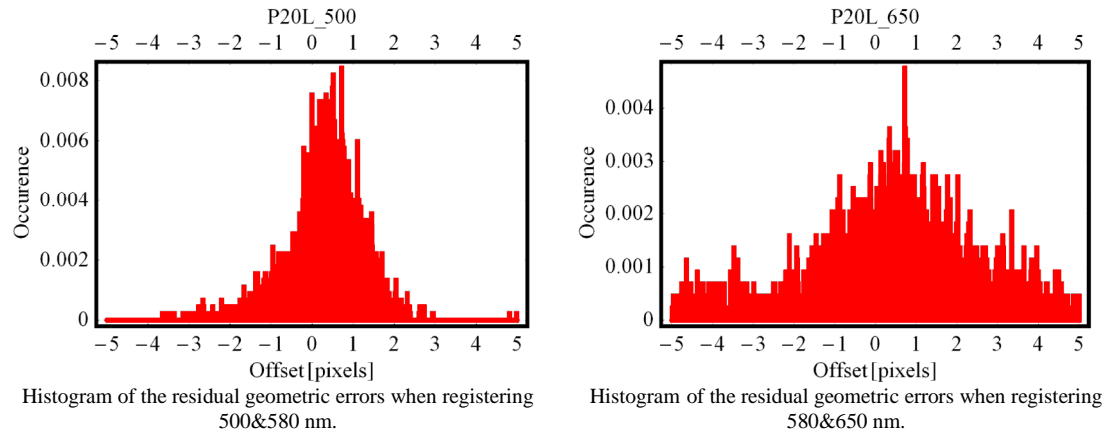


Figure 4.20: Normalized histograms of registration errors when two images at different wavelengths are considered: (500&580 nm) left and (580&650 nm) right

Figure 4.21 presents the standard deviation values for 10 subjects for the combination (500 &580) nm and (580&650) nm.

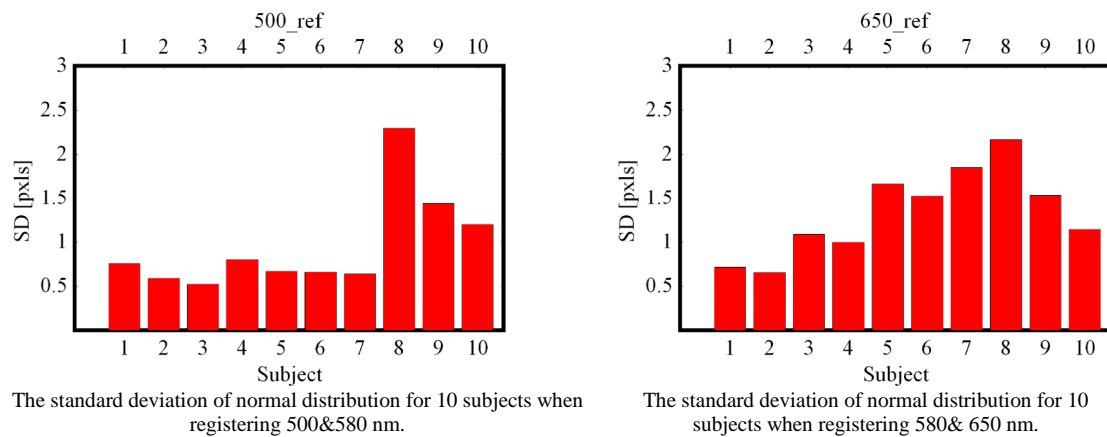


Figure 4.21: Normalized histograms registration errors when two images at different wavelengths are considered: (500&580 nm) left and (580&650 nm) right

Image registration accuracy refers to the mean, standard deviation of the distance between points in the reference image and corresponding points in the sensed image after they have been resampled to the space of the reference image. The smaller this

difference, the more accurate the estimate will be. The quality of the recorded images affected the accuracy causing it to vary between less than a pixel to almost 2 pixels. Heart pulses and optical system deformation are found to influence the performance of our registration algorithm. Their influences are significant when small features are of interest but for our purpose, measuring oxygen saturation in the blood vessels, the effect can be corrected as will be shown later in this thesis. The effect of wavelength was found to increase the errors in registration compared to those calculated when images at the same wavelength were registered. Spectral differences in appearance with wavelength are the main reason why the accuracy is reduced to almost 2 pixels. Patient comfort is an additional factor that might influence the accuracy of the registration. Images recorded from patients with poor vision encountered massive eye movements included large rotational and scaling misalignments which affected the calculation of the cross-correlation function and hence increased the error in estimating the real rotation angles.

4.4 Conclusion

We have shown in this chapter that time sequential retinal images suffer from artefacts inherited when the instrument was constructed or arising from human eye movements, such as specular reflection on the surfaces of the objective lens, imperfections in the optical components of the human eye and the fundus camera, illumination variation between recorded images, and detector chip noise. A calibration procedure was employed to correct for these artefacts by recording calibration images and applying an optimisation process to reduce the effect of artefacts. Affine misalignments between registered images were corrected by a registration algorithm. The retinal vasculature tree was enhanced by means of passband and edge detection

filters prior to registration. The maximum of cross-correlation function was used to calculate the translational, rotational, and scaling transformations required to perform registration. The accuracy of the registration algorithm was also measured at feature-to-feature level, in which a simple algorithm based on the cross-correlation function was developed to calculate the residual differences between profiles obtained from the images post to registration. The registration algorithm showed good accuracy (0.6 ± 0.5 pixel) when images at the same wavelength (580 nm) were considered. However, lower accuracy (0.96 ± 0.55 pixel and 1.34 ± 0.5 pixel) was reported when images at different wavelengths (500 and 650 nm) were registered.

Chapter 5

Light propagation and oximetric techniques

Accurate quantification of oxygen saturation in the retinal vessels necessitates better understanding of the primary events associated when light propagates toward the retina. These events are simply the scattering and absorption by different chromophores embedded in the retinal layers. In this chapter we explain the main principles of retinal oximetry and the existing oximetric techniques reported in literature and used in this project to assess oxygen saturation from the spectral retinal images. The main sources of scattering and absorption in the retina as light propagates are also described and optimum selection of wavelengths to minimize the saturation error is reported.

5.1 Light propagation in the eye

When light is incident upon the pupil, transmission and reflection by the eye media occur. Light passes through the cornea, aqueous humor, lens, and vitreous humor to the fundus. There, it is transmitted through the retinal layers towards the choroid and the sclera. As light passes down through the retina, a fraction of it is diffusely reflected back out, escaping the eye into the detector. Figure 5.1 shows a horizontal cross-section of a normal eye. The main components of the eye are shown with an incident beam of light which reflects from the fundus, the back of the eye, and emerges from the eye. As indicated in Figure 5.1(a) and in more detail in Figure

5.1(b), the fundus of the eye is a multilayered structure consisting mainly of the retina, retinal pigment epithelium (RPE), choroid, and sclera.

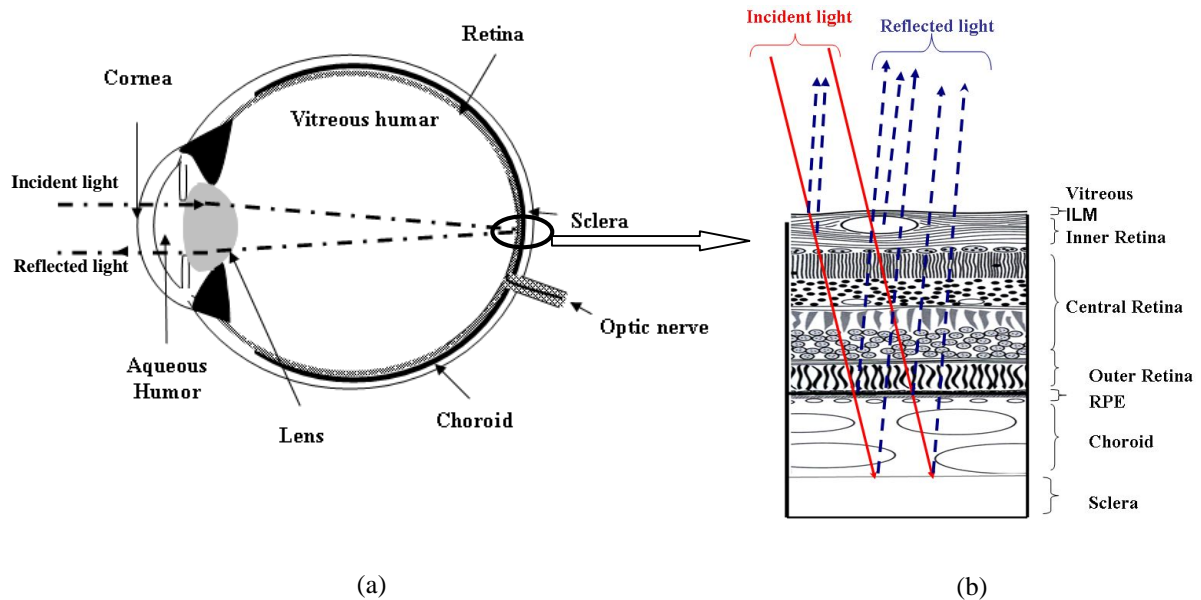


Figure 5.1: (a) Horizontal cross-section of eye; (b) Incident and reflected light through the multilayered structure of the retina.

The retina is composed mainly of neural tissues, visual receptors, retinal vessels, and supporting tissue. Except for the blood contained in the retinal vessels, all of the component parts of the retina can be considered to be transparent within the visible range. When light travels through the retina, reflection at the boundaries of *ILM* and *NFL* layers take place as was discussed previously in chapter 2. However, when light is incident upon an area occupied with retinal vessels, scattering and absorption by red blood cells occur, resulting in an enlarged and attenuated beam of light.

Escaping the top retinal layers, light reaches the retinal pigment epithelium (*RPE*), a thin layer of cells between the choroid and the retina, which contains a large concentration of melanin and absorbs and scatters light in an amount which is dependent on eye and subject. Leaving the *RPE*, light passes through the choroid,

which is a tissue layer having an extremely dense vasculature and containing melanin, which dominates the reflectance spectrum from the choroid, in addition to the spectral characteristics of haemoglobin. Finally, light is reflected at the sclera which is composed of randomly oriented collagen fibres and scatters the light strongly. Reflected light will be retransmitted back by the choroid, *RPE*, and the retina, emanating from the eye and resulting in double passage of light.

5.2 Absorption

Light is attenuated as it propagates through the ocular media towards the fundus. A transparent medium such as the cornea or lens permits the passage of the visible light with low absorption. In contrast, media such as blood vessels, the *RPE*, and choroid introduce significant attenuation. As a result, the spectral reflectance of the ocular fundus is strongly influenced by absorption by blood, melanin, and ocular media. The main absorption properties of each absorber will be discussed in the following section.

5.2.1 Ocular media

Absorption by the ocular media can be considered in two parts: the lens and the vitreous humor. Strong absorption by the human lens occurs for $\lambda < 430$ nm (Norren and Vos 1974; Stockman et al. 1993) and increases with age (Weale 1978; Sample et al. 1988). On the other hand, the transmission of the vitreous humor is very high in the visible spectrum, and can be considered equivalent to pure water. Light scattering in this medium is independent of wavelength and its effect can be added to the absorption term (Whittaker 1993).

5.2.2 Melanin

The reflectance spectra are affected by the degree of melanin pigmentation in the fundus. Melanin occurs in significant quantities in many sites in the ocular fundus such as the choroid, retinal pigment epithelium (*RPE*), and macular pigment in the fovea. The absorption spectrum of melanin is generally found to decrease monotonically with increasing wavelength throughout the visible range of light. Figure 5.2 shows the absorption spectra of melanin as reported in the literature (Jacques 1996).

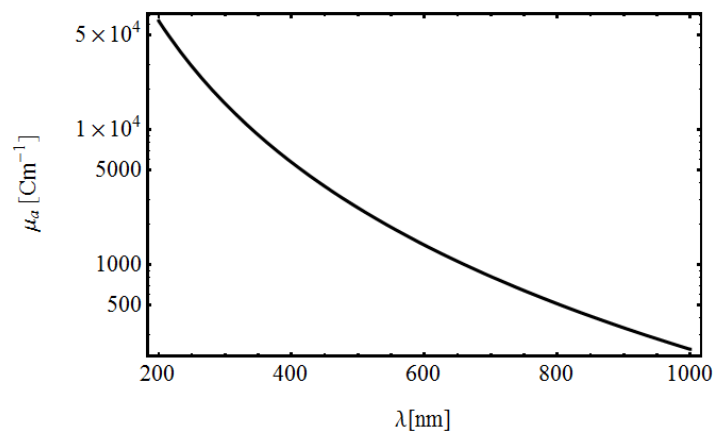


Figure 5.2: Melanin absorption spectra (μ_a)

Spectral dependence of the absorption coefficient on wavelength ($\lambda^{-4.6}$) has been reported in literature (Gabel 1978; Menon 1982). Other studies showed flatter response of the absorption spectra with weaker dependence on the wavelength ($\lambda^{-2.2}$) (Geeraets 1962).

5.2.3 Blood

Red blood cells contain haemoglobin which is one of the strongest absorbers of light in the human body. Haemoglobin molecules within the red blood cells (erythrocytes) carry 97% of the oxygen absorbed in the blood while the remaining 3% is dissolved in

the plasma. Haemoglobin occurs in two states: oxygenated (HbO_2) and deoxygenated (Hb) haemoglobin. The optical behaviour of blood is dependent on various physiological parameters such as oxygen saturation, osmolarity, flow condition, and aggregation (Meinke 2005; Lee 1991). The spectra of oxygenated and deoxyhaemoglobin are expressed in terms of the specific extinction coefficient as shown previously and depicted in Figure 5.3.

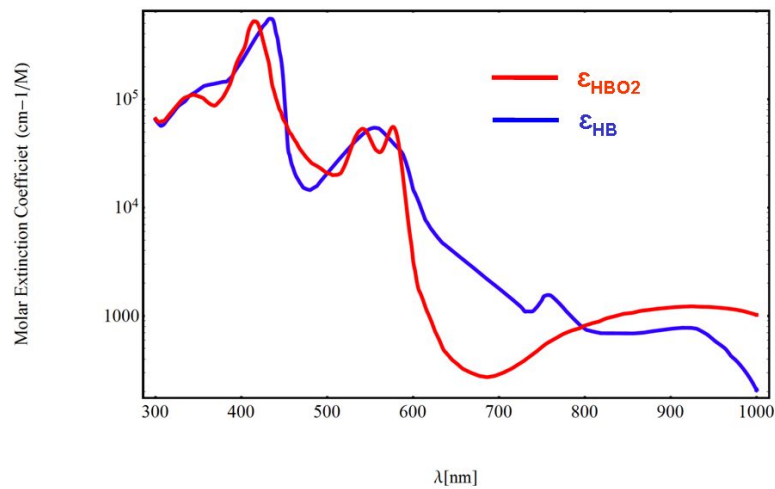


Figure 5.3: Molar Extinction of oxygenated and deoxygenated haemoglobin (ϵ_{HBO_2} , ϵ_{HB}) in the wavelength range (300-1000 nm)

Haemoglobin has low absorption for wavelengths longer than 600 nm and below that wavelength absorption increases sharply (Assendelft 1970). In the visible spectrum, oxygenated blood shows maxima at 416, 542, and 577 nm and minima at 510 and 560 nm. However, deoxygenated blood shows a minimum at 470 nm and maximum at 559 nm. The haemoglobin absorption spectrum can change massively as haemoglobin concentration and oxygen saturation vary, in addition to the hematocrit which considered one of the most important physiological parameters influencing blood absorption and scattering properties. Optical properties of blood in the wavelength range 400-2500 nm are discussed widely by many researchers (Roggan 1999; Meinke 2007; Lindberg 1993; Hammer 2001).

5.3 *Scattering*

Scattering of light in retinal tissue is one of the confounding aspects of whole-blood oximetry. The retina is considered to be an inhomogeneous and highly scattering medium and this can cause inaccuracies in spectroscopic measurement resulting from the nonlinear relationship between attenuation and absorption. Scattering of light by blood is due to the discontinuities in the refractive index between red blood cells and the plasma in which they are suspended (Macrae 1961; Borovoi 1998; Hammer 1998). The effect of scattering is to substantially increase the pathlength in which the photons travel within the tissue, and therefore increase the probability of absorption occurring. The reduction in intensity due to scattering is described in a similar way as that due to the absorption, in which a scattering coefficient by red blood cells can be used to account for these losses. This coefficient is influenced by various physiological parameters such as hematocrit concentration and oxygen saturation (Meinke 2007; 2009; Faber 2004).

5.4 *Lambert-Beer's Law*

The absorption of light in non-scattering media can be described by Lambert-Beer Law. Two Laws are frequently applied to express the effect on absorption of either the thickness or concentration respectively.

$$dI = -\mu_a I dz \quad (5-1)$$

where dI is the differential change of intensity of incident light traversing an infinitesimal path dz through a homogenous medium with absorption coefficient μ_a .

Integrating over a thickness z yields:

$$\begin{aligned}
I &= I_o \exp[-\mu_a z] \\
&= I_o \exp[-\varepsilon_\lambda c z]
\end{aligned}
\tag{5-2}$$

Where ε_λ is the molar extension coefficient [$cm^2.mol^{-1}$] at measured wavelength λ , C [$mol.cm^{-3}$] is the molar concentration of the absorption species, and z is the thickness [cm]. Transmission T is defined as the ratio of transmitted intensity I to incident intensity I_o :

$$T = \frac{I}{I_o} \tag{5-3}$$

The attenuation which is also referred as absorbance (A) or optical density OD of an attenuating medium is given as in:

$$A = OD = -\log_{10}(T) = \varepsilon_\lambda c z \tag{5-4}$$

Absorption by haemoglobin is given as a sum of two absorbing compounds (oxygenated and deoxygenated) as in:

$$OD = -\log_{10}(T) = [\varepsilon_{Hbo2} c_{Hbo2} + \varepsilon_{Hb} c_{Hb}] z \tag{5-5}$$

where $\varepsilon_{Hbo2}, \varepsilon_{Hb}$ are the molar extinction coefficients of oxygenated and deoxygenated haemoglobin respectively, S as presented previously in Figure 5.2.

5.5 Modified Lambert-Beer Law

Light transmitted through an absorptive and scattering medium is given as:

$$I(\lambda) = I_o(\lambda) \exp(-\mu_{ext}(\lambda).d) \tag{5-6}$$

The term μ_{ext} is the total extinction coefficient and can be given as a simple summation of the absorption $\mu_a(\lambda)$ and scattering $\mu_s(\lambda)$ coefficients and is represented by

$$\mu_{ext}(\lambda) = \mu_a(\lambda) + \mu_s(\lambda) . \tag{5-7}$$

The effects of light scattering and absorption on light transmittance can be evaluated separately (Naomi 1967). Combining (5-6) and (5-7) gives

$$I(\lambda) = I_o(\lambda) \exp(-[\mu_a(\lambda) + \mu_s(\lambda)].d). \quad (5-8)$$

The application of the previous equation is limited to media that do not experience significant multiple scattering. Multiple scattering occurs when the incident radiation has consecutive interactions with a number of particles prior to its ultimate exit from the medium. Whole blood shows multiple scattering due to the high concentration of *RBC*'s, so that (5-8) is not sufficiently precise to describe the propagation of light through blood. Transmission through whole blood sample is best presented in a more general form which accounts for absorption and scattering as:

$$T(\lambda) = \frac{I(\lambda)}{I_o(\lambda)} = T_s(\lambda, d) \exp(-\mu_a(\lambda).d), \quad (5-9)$$

where $T_s(\lambda, d)$ represents the scattering transmittance and is attributable to single or a multiple scattering. Twersky (1970) derived a theoretical expression for $T_s(\lambda, d)$ that may suit the whole blood. He considered transmission of light through media containing large tenuous scatters. Twersky's rule to account for scattering in the whole blood indicates that there is a significant relationship between the scattering transmittance and the physical parameters of blood. Scattering increases the optical pathlength to become greater than the geometrical (physical) distance and distorts the linear relationship between attenuation and absorption based on the Lambert-Beer Law. As a result, the dependence of attenuation A upon absorption coefficient μ_a , as depicted by (5-4), becomes non-linear. Modifications to Lambert Beer's Law (Delpy 1988) account for (i) an additive term $B(\lambda)$, due to scattering losses, and (ii) a multiplier, to account for the increased optical pathlength due to scattering; both of

these factors are wavelength dependent. As a result, attenuation due to the modified Lambert-Beer Law can be expressed as:

$$A = OD = -\log_{10}(T) = cd' \cdot \epsilon_{\lambda}(\lambda) + B(\lambda), \quad (5-10)$$

where d' is the increased optical path.

Figure 5.4 presents a graphical comparison between Lambert-Beer's Law, modified Lambert-Beer's Law, and the non linear relationship between A v. μ_a .

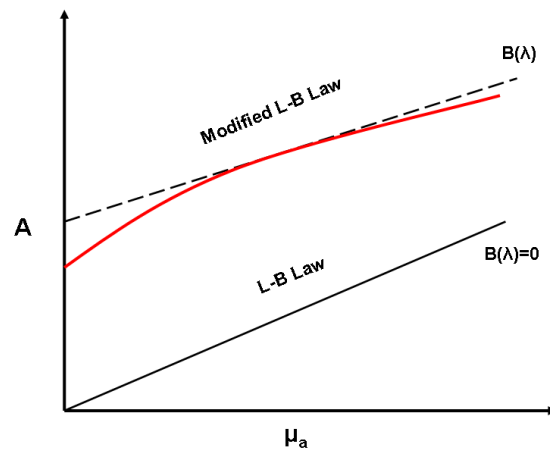


Figure 5.4: A comparison between L-B Law and Modified L-B Law

5.6 Principle of oximetric measurement

As has been shown previously, oxygen saturation can be expressed as:

$$OS\% = \frac{C_{HbO_2}}{C_{HbO_2} + C_{Hb}} \times 100\%, \quad (5-11)$$

where C_{HbO_2} and C_{Hb} are the concentrations of oxygenated and deoxygenated haemoglobin respectively. Many techniques have been developed to monitor and measure blood oxygen saturation by considering the difference in absorption spectra between Hb and HbO₂, such as pulse oximetry and near infrared spectroscopy. Generally, the two- and three-wavelength oxygen saturation systems have been the basis for oximetry calculation for four decades. Variations of these systems have been

proposed and applied by a number of researchers in attempts to both increase the accuracy of oxygen saturation measurements and simplify the description of the complex light-blood interaction. Most commonly, reasonable assumptions were included, especially in terms of simplifying or eliminating the scattered light component through modification of the sample, such as blood haemodialysis, or determining practically its contribution for each measurement device through instrument calibration. Employing many more wavelengths has received much attention to account for the complex scattering dependencies and the inhomogenous environment offered by whole blood. The common oximetry techniques will be briefly explained in the following sections.

5.6.1 Two wavelength oximetry

Two-wavelength oximetry is applicable to haemolysed blood, which maybe considered to be homogenous, non-scattering medium. According to Lambert-Beer Law the attenuation of light passing through a haemolysed blood sample is given by:

$$T(\lambda) = \frac{I(\lambda)}{I_o(\lambda)} = 10^{-[\varepsilon_{HbO_2}(\lambda) \cdot C_{HbO_2} + \varepsilon_{Hb}(\lambda) \cdot C_{Hb}] \cdot d}, \quad (5-12)$$

where ε_{HbO_2} and ε_{Hb} are the millimolar extinction coefficients of oxygenated and deoxygenated haemoglobin (Assenelt 1970), respectively, and C_{HbO_2} and C_{Hb} are millimolar concentrations of oxygenated and deoxygenated haemoglobin respectively. The symbol d is sample thickness and $T(\lambda)$ is the transmission through the sample. Other haemoglobin derivatives such as carboxyhemoglobin, methemoglobin, and sulphhemoglobin are also generally present in blood, but usually their contributions are assumed insignificant.

Two wavelengths (λ_1, λ_2) are sufficient to assess oxygen saturation of haemolysed blood as the concentrations of oxygenated and deoxygenated haemoglobin are the only unknown parameters. This technique is limited to a homogenous, non-scattering solution in which Lambert-Beer's Law is applicable. Generally, (5-12) can be expressed in optical densities (OD) as:

$$\begin{aligned} OD^{\lambda_1} &= [\varepsilon_{HbO_2}^{\lambda_1} C_{HbO_2} + \varepsilon_{Hb}^{\lambda_1} C_{Hb}] . d , \\ OD^{\lambda_2} &= [\varepsilon_{HbO_2}^{\lambda_2} C_{HbO_2} + \varepsilon_{Hb}^{\lambda_2} C_{Hb}] . d . \end{aligned} \quad (5-13)$$

Substituting (5-11) in (5-13) gives:

$$\begin{aligned} OD^{\lambda_1} &= [\varepsilon_{HbO_2}^{\lambda_1} OS + \varepsilon_{HB}^{\lambda_1} (1 - OS)] . d . C_{Hb_total} , \\ OD^{\lambda_2} &= [\varepsilon_{HbO_2}^{\lambda_2} OS + \varepsilon_{HB}^{\lambda_2} (1 - OS)] . d . C_{Hb_total} . \end{aligned} \quad (5-14)$$

where $C_{Hb_total} = C_{Hb} + C_{HbO_2}$ is the total haemoglobin concentration.

The ratio of the two equations results in an expression to calculate oxygen saturation depending on optical density measurements and independent from C_{Hb_total} and d :

$$OS = \frac{OD^{\lambda_2} \varepsilon_{Hb}^{\lambda_1} - OD^{\lambda_1} \varepsilon_{Hb}^{\lambda_2}}{OD^{\lambda_1} (\varepsilon_{HbO_2}^{\lambda_2} - \varepsilon_{Hb}^{\lambda_2}) - OD^{\lambda_2} (\varepsilon_{HbO_2}^{\lambda_1} - \varepsilon_{Hb}^{\lambda_1})} \quad (5-15)$$

Any combination of two wavelengths is sufficient, provided $\varepsilon_{HbO_2}^{\lambda} - \varepsilon_{Hb}^{\lambda} \neq 0$ for at least one wavelength. Oximetry using a two-wavelength technique can be implemented by choosing one of the wavelengths to be isobestic ($\varepsilon_{HbO_2}^{iso} - \varepsilon_{Hb}^{iso} \cong 0$).

The isobestic wavelength is chosen for ease of calibration and solution of (5-15) in which a linear relationship between oxygen saturation (OS) and optical density ratio (ODR) is assumed: when λ_2 is assumed to be isobestic, equation (5-15) becomes:

$$OS = \frac{OD^{\lambda_1}}{OD^{\lambda_2}} \frac{\varepsilon_{Hb}^{\lambda_2}}{\varepsilon_{HbO_2}^{\lambda_1} - \varepsilon_{Hb}^{\lambda_1}} - \frac{\varepsilon_{Hb}^{\lambda_1}}{\varepsilon_{HbO_2}^{\lambda_1} - \varepsilon_{Hb}^{\lambda_1}} = ODR \frac{\varepsilon_{Hb}^{\lambda_2}}{\Delta \varepsilon^{\lambda_1}} - \frac{\varepsilon_{Hb}^{\lambda_1}}{\Delta \varepsilon^{\lambda_1}}, \quad (5-16)$$

The parameter $\Delta \varepsilon^{\lambda_1}$ is given as $\Delta \varepsilon^{\lambda_1} = \varepsilon_{HbO_2}^{\lambda_1} - \varepsilon_{Hb}^{\lambda_1}$

The linear relationship between OS and ODR is expressed as

$$OS = a.ODR - b, \quad (5-17)$$

where a and b are $\frac{\varepsilon_{Hb}^{\lambda_2}}{\Delta\varepsilon^{\lambda_1}}, \frac{\varepsilon_{Hb}^{\lambda_1}}{\Delta\varepsilon^{\lambda_1}}$ respectively and can be calculated.

To consider the scattering effects in the whole blood, as a suspension of RBC 's in plasma, some investigators performed calibration under constant geometrical conditions of the blood layer, using blood with known oxygen saturation to obtain the constants a and b empirically (Schweitzer 1999; Tiedeman 1998; Cohen 1976; Hickam 1963; Beach 1999, 2006; Hammer 2008).

5.6.2 Three-wavelength oximetry

The two-wavelength oximetry technique can be applied to measure absolute oxygen saturation in a well-calibrated environment or to monitor changes of saturation in non-calibrated techniques. To compensate for multiple scattering by RBC 's, modified Lambert-Beer's Law is implemented as described in (5-10). The scattering term $B(\lambda)$ is a function of wavelength, RBC geometry, and the refractive indices of RBC s and blood plasma.

Scattering can be assumed constant for certain wavelength ranges which do not fall near a strong absorption by Hb derivatives, such as the blue range, as suggested by Pittman and Duling (1975). Across such a range, the refractive indices would remain approximately constant. The validity of this approximation is demonstrated experimentally for the green range (520, 546 and 555nm) (Pittman & Duling 1975). Scattering is hypothesized to be constant in the infrared range due to the lack of strong absorption by haemoglobin in this range.

A three-wavelength oximetry technique can be applied when scattering is assumed constant in (5-10); oxygen saturation can be estimated by solving the three equations:

$$\begin{aligned}
OD^{\lambda_1} &= [\varepsilon_{HbO_2}^{\lambda_1} OS + \varepsilon_{HB}^{\lambda_1} (1 - OS)] \cdot d \cdot C_{Hb_total} + B \\
OD^{\lambda_2} &= [\varepsilon_{HbO_2}^{\lambda_2} OS + \varepsilon_{HB}^{\lambda_2} (1 - OS)] \cdot d \cdot C_{Hb_total} + B \\
OD^{\lambda_3} &= [\varepsilon_{HbO_2}^{\lambda_3} OS + \varepsilon_{HB}^{\lambda_3} (1 - OS)] \cdot d \cdot C_{Hb_total} + B
\end{aligned} \tag{5-18}$$

$$OS = \frac{A}{B} \tag{5-19}$$

$$\begin{aligned}
A &= OD^{\lambda_1} (\varepsilon_{Hb}^{\lambda_3} - \varepsilon_{HB}^{\lambda_2}) + OD^{\lambda_2} (\varepsilon_{Hb}^{\lambda_1} - \varepsilon_{HB}^{\lambda_3}) + OD^{\lambda_3} (\varepsilon_{Hb}^{\lambda_2} - \varepsilon_{HB}^{\lambda_1}) \\
B &= OD^{\lambda_1} [(\varepsilon_{Hb}^{\lambda_3} - \varepsilon_{HbO_2}^{\lambda_3}) - (\varepsilon_{Hb}^{\lambda_2} - \varepsilon_{HbO_2}^{\lambda_2})] + \\
&OD^{\lambda_2} [(\varepsilon_{Hb}^{\lambda_1} - \varepsilon_{HbO_2}^{\lambda_1}) - (\varepsilon_{Hb}^{\lambda_3} - \varepsilon_{HbO_2}^{\lambda_3})] + OD^{\lambda_3} [(\varepsilon_{Hb}^{\lambda_2} - \varepsilon_{HbO_2}^{\lambda_2}) - (\varepsilon_{Hb}^{\lambda_1} - \varepsilon_{HbO_2}^{\lambda_1})]
\end{aligned}$$

The above equation gives the oxygen saturation value for a scattering solution such as whole blood. Using two isobestic wavelengths (λ_2, λ_3) (Pittman & Duling 1975; Delori 1988) simplifies the oxygen saturation calculation by transforming the relationship with OD^{λ_1} into a linear one, as both OD^{λ_2} and OD^{λ_3} are insensitive for oxygen saturation for the isobestic wavelengths.

$$OS = \frac{OD^{\lambda_1} (\varepsilon_{Hb}^{\lambda_3} - \varepsilon_{HB}^{\lambda_2}) + OD^{\lambda_2} (\varepsilon_{Hb}^{\lambda_1} - \varepsilon_{HB}^{\lambda_3}) + OD^{\lambda_3} (\varepsilon_{Hb}^{\lambda_2} - \varepsilon_{HB}^{\lambda_1})}{(OD^{\lambda_2} - OD^{\lambda_3}) (\varepsilon_{Hb}^{\lambda_1} - \varepsilon_{HbO_2}^{\lambda_1})} \tag{5-20}$$

The method necessitates employing three wavelengths that are closely placed across the measuring waveband, so that the scattering contribution is approximately independent of the wavelength. The apparent simplicity of the method for eliminating the complicated scattering contribution using the wavelength independence of scattering is an overestimation. Although this technique succeeds in theoretically eliminating the scattering dependence while maintaining the concentration and pathlength independence, the method is restricted to use over a limited range of wavelength bands which are less than optimal in terms of obtaining accurate oxygen saturation measurements.

5.6.3 Optical model of the fundus layers and the primary optical paths

The simplest reflectance model for the fundus layer is one in which the incident light is transmitted by the retinal and choroidal layers, reflected by the sclera and transmitted by the choroid and the retina again. However, reflections originating from retinal layers substantially contribute to the overall fundus reflectance, especially at short wavelengths and in a darkly pigmented fundus.

As has been shown previously, the retina is one of the main structures of the fundus which reflects light and is composed of a number of different layers with each possessing different reflectivity. The characteristics of the retinal layers have already been discussed in Chapter 2 and with that data it is possible to build a simple model of the fundus, consisting of the main reflectors ILM/NFL, RPE, and sclera, as already introduced by the Delori (1989) and Hammer (1995) models and shown in Figure 5.5.

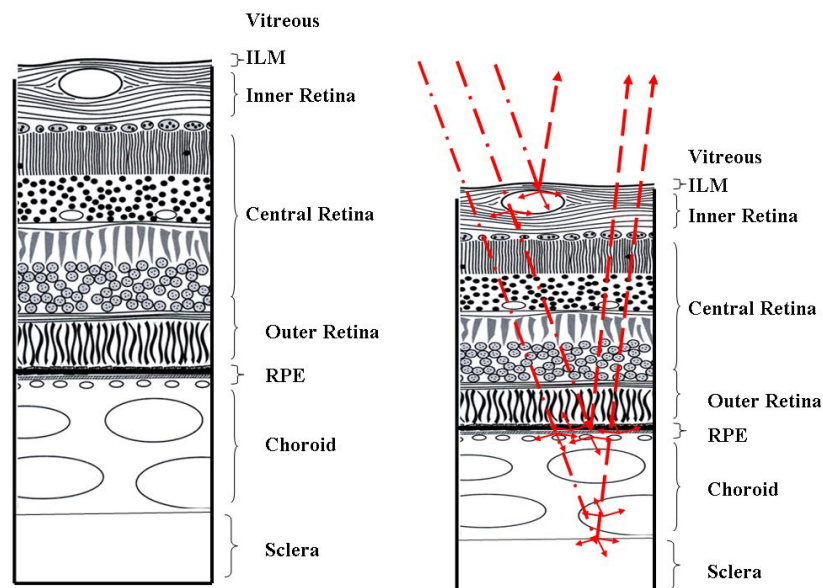


Figure 5.5: Multilayered structure of the retina

This simplified model of reflection and absorption in the human eye will be used in our measurements of retinal oximetry. Light is reflected and backscattered whenever a

significant change in reflective index occurs, i.e. the interference of ocular (vitreous humor) with ILM, retina with RPE, and choroid with sclera. Two types of reflection are expected as light travels towards the retina: a ray incident upon the inner limiting membrane is specularly reflected, whereas the other retinal structures reflect light diffusely into large solid angles. The reflectance of all reflectors is assumed to be independent of wavelength and validated experimentally by Norren et al. (1986). Light absorption first takes place in the ocular media and partially reflects from ILM. Then a part of the light is reflected beyond the absorbing layer of the retina, consisting of macular pigment or blood contained in blood vessels. This reflectance layer is identified by the *RPE*. The choroid is the next absorbing layer and consists of the melanin pigment and haemoglobin in which, as a homogenous scattering layer, blood and melanin are uniformly distributed. Finally, light transmitted through the choroid is reflected from the sclera. To quantify the effect of concentrations of chromophores, the transmission through the multilayered structure can be expressed as:

$$T(\lambda) = \frac{I(\lambda)}{I_o(\lambda)} = 10^{-OD} \quad , \quad (5-21)$$

$$OD = \sum_L OD_L$$

The term *OD* is assigned to the attenuation occurring at each layer (*L*), where *L* =1,2,....

Light transmitted through the retinal vessels as well as light reflected from the vessels contribute to the intensity measured at the centre of the retinal vessel. Due to light backscattering in the layers beneath the retinal vasculature, such as *RPE* and choroid, incident light transmits through the vessel in a single and double pass. However, light reflected from the vessel consists of: **(a)** specularly reflected light from the apex of the vessel which originates from the inner limiting membrane (ILM) (Delori 1977) or from the vessel wall; **(b)** back-scattered light from the blood within vessels as a

consequence of scattering by red blood cells (*RBC's*). In the same way, light transmitted by the retinal layers (on both sides of retinal vessels) will experience scattering and absorption by the existing chromophores. Diffusion of light by the *RPE* and choroidal layers is wavelength dependent, in that strong absorption of melanin and haemoglobin affects the size of the tissue point spread function (*PSF*) on the *RPE* (Smith 2000). The width of the *PSF* of returning light at the retina influences the primary optical paths through retinal vessels. The width of the *PSF* in the nasal fundus (near the optic nerve head) was measured by Hodgkinson (1994) to range between 60 μm for wavelength range (450-575 nm) and 150 μm for (600-750) nm. Figure 5.6 illustrates the effect of a diffusion-enlarged *PSF* on the optical paths through a retinal vessel. A capillary of typical diameter 100 μm positioned 240 μm from a reflecting layer, to resemble the ocular fundus layers, is considered. Two *PSF* sizes (60 μm , 150 μm) are considered for wavelength range corresponding to blue-green and red-infrared light.

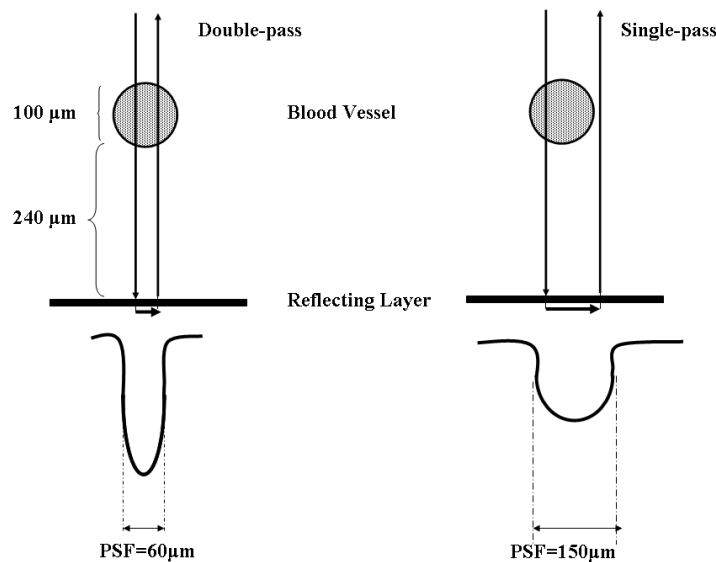


Figure 5: Enlarged PSF against reflecting layer for 100 μm , double pass (Left); single pass (Right)

For longer wavelengths, $\lambda > 600$ nm and $PSF \approx 150$ μm , lateral separating effects of light occur as light penetrates into deeper fundus layers (the choroid) before being reflected by the sclera. As a result, the beam of light is enlarged and reflected beyond the edge of the blood vessel, resulting in light being transmitted through the blood vessel in single pass. However, for shorter wavelengths, $\lambda < 575$ nm and $PSF \approx 60$ μm , light will be reflected back by *RPE* resulting in light transmitted through the blood vessel in a double pass. It is clear that knowledge of both single and double passes are required. Light reflected from the vessel centre (I_R) and detected by our instrument is a sum of light components: (a) light transmitted through the blood vessel once (single pass) I_{SP} , (b) light which has travelled through the blood vessel twice (double pass) I_{DP} , (c) back-scattered light by *RBCs* I_{BS} , and (d) specularly reflected light I_{glint} as:

$$I_R = I_{SP} + I_{DP} + I_{BS} + I_{glint} \quad (5-22)$$

The intensity of specularly reflected light I_{glint} is reduced by using a linear polarizer in front of the detector (see Chapter 3). Significant removal of glint is not possible by using only a linear polarizer; as a result, glint remaining can be reduced by applying a post-processing algorithm on transmission profiles to estimate the intensity in absence of glint. This will be discussed later, in Chapter 7. The intensity of reflected light becomes

$$I_R = I_{SP} + I_{DP} + I_{BS}$$

Monte-Carlo simulation results (Hammer 1997) predicted that single pass, double pass, and back-scattered light contribute equally in a 100 μm vessel. Moreover, single pass domination is reported for small vessels ($d \leq 25$ μm) and back scattered light domination for larger vessels ($d \geq 200$ μm). However, the contribution of both the single-pass and double-pass to the light reflected from blood vessels is affected by the

size of the *PSF*, the vessel diameter, specular and diffuse reflectance of the ocular fundus (Smith 2000).

To determine the transmittance at the centre of the blood vessel, incident light intensity has to be estimated. The intensity of incident light can be interpolated depending on the intensity at either sides of the blood vessel to estimate the intensity in absence of the vessel. The change in intensity at the centre of blood vessel is estimated by the ratio I/I_o . However, direct measurements of incident light can not be made and an intensity of $R_f I_o$ is measured instead, from the retinal background where R_f is the fundus reflectivity and I_o is the incident light.

The ratio $T = I/I_o$ becomes

$$T = \frac{I}{R_f I_o},$$

$$T = \alpha T_B + \beta T_B^2 + \gamma R_B, \quad (5-23)$$

where T_B is the transmission of blood according to Lambert-Beer's Law, R_B is the whole blood reflectance and α, β, γ are the fractions of light transmitted in single pass, transmitted in double pass and back scattered by red blood cells, respectively.

The reflectance of the whole blood sample R_B was found to be linearly related to the transmission in the range 600-630 nm (Anderson and Sekelj 1967)

$$R_B = a_1 + a_2 T_B. \quad (5-24)$$

The previous relationship (5-24) is predicted by Twersky (1970) and has been tested to be valid outside the range 600-630 nm (Anderson and Sekelj 1967). The parameters a_1, a_2 are dependent on blood sample properties such as hematocrit and the geometries of the source, detector, and sample.

By substituting (5-24) in (5-23) and by considering the transmission of blood to be

$$T_B = e^{-Cd(\epsilon_{HBo2}OS+(1-OS)\epsilon_{HB})}, \quad (5-25)$$

the ratio T can be expressed as

$$\begin{aligned} T &= \alpha T_B + \beta T_B^2 + \gamma(a_1 + a_2 T_B), \\ &= (\alpha + a_2 \gamma) T_B + \beta T_B^2 + \gamma a_1, \end{aligned} \quad (5-26)$$

$$T = (\alpha + a_2 \gamma) e^{-Cd(\epsilon_{HBo2}OS+(1-OS)\epsilon_{HB})} + \beta e^{-2Cd(\epsilon_{HBo2}OS+(1-OS)\epsilon_{HB})} + \gamma a_1. \quad (5-27)$$

The optical density is therefore

$$OD = -\text{Log}(T) = -\text{Log}((\alpha + a_2 \gamma) e^{-Cd(\epsilon_{HBo2}OS+(1-OS)\epsilon_{HB})} + \beta e^{-2Cd(\epsilon_{HBo2}OS+(1-OS)\epsilon_{HB})} + \gamma a_1). \quad (5-28)$$

When back-scattered light is neglected ($\gamma=0$), the optical density can be written as

$$OD = -\text{Log}(T) = -\text{Log}(\alpha e^{-Cd(\epsilon_{HBo2}OS+(1-OS)\epsilon_{HB})} + \beta e^{-2Cd(\epsilon_{HBo2}OS+(1-OS)\epsilon_{HB})}). \quad (5-29)$$

Back-scattered light can be neglected when $a_1 \ll 1$ and $a_2 \ll 1$. The back-scattered light is expected to be at the minimum due to the use of linear cross polarizer in front of the detector (see Chapter 3). On the other hand, measurements obtained by Smith (1999) on the optic disk where the fundus reflectivity is highest or measurement at the green range where the back-scattered light the lowest represented the situation in which $\gamma \rightarrow 0$.

To obtain a simplified version of (5-29), a series expansion around $Cd(\epsilon_{HBo2}OS + (1-OS)\epsilon_{HB})$ yields

$$\begin{aligned} OD &= -\text{Log}(\alpha + \beta) + \frac{\alpha + 2\beta}{\alpha + \beta} Cd(\epsilon_{HBo2}OS + (1-OS)\epsilon_{HB}) - \\ &\quad \frac{\alpha\beta}{2(\alpha + \beta)^2} (Cd(\epsilon_{HBo2}OS + (1-OS)\epsilon_{HB}))^2 + O[(Cd(\epsilon_{HBo2}OS + (1-OS)\epsilon_{HB}))^3]. \end{aligned} \quad (5-30)$$

(series expansion of $-\text{Log}[ae^{-x} + be^{-2x}]$ around x gives

$$- \text{Log}[ae^{-x} + be^{-2x}] = -\text{Log}[a + b] + \frac{a + 2b}{a + b}x - \frac{ab}{2(a + b)^2}x^2 + \frac{a(a - b)b}{6(a + b)^3}x^3 \dots + O[x^n]$$

The higher orders (second order and higher) of (5-30) can be ignored for small diameters ($<50 \mu\text{m}$) or longer wavelength ($\lambda > 620 \text{ nm}$) (Smith et al. 2000) and (5-30) becomes

$$OD = -\text{Log}(\alpha + \beta) + \frac{\alpha + 2\beta}{\alpha + \beta} Cd(\varepsilon_{HBo_2} OS + (1 - OS)\varepsilon_{HB}). \quad (5-31)$$

As wavelength varies, the contribution of single- and double-pass varies, i.e. for wavelength $\lambda < 575 \text{ nm}$ and $PSF \ll 150 \mu\text{m}$ double-pass is mainly dominant. However, for longer wavelengths $\lambda > 600 \text{ nm}$ and $PSF \approx 150 \mu\text{m}$, single-pass is dominant. The contribution of double-pass, β , was predicted by Hammer et al. (1997) and measured by Smith et al. (2000) to be smaller than single-pass, α , for all typical vessel diameters. As a result, it is possible that the double-pass component of the light collected at the centre of the blood vessel is negligible ($\beta \ll \alpha$).

When the double-pass is neglected ($\beta=0$), the optical density (OD) can be expressed as:

$$OD = -\text{Log}(T) = -\text{Log}((\alpha + a_2\gamma)e^{-Cd(\varepsilon_{HBo_2} OS + (1 - OS)\varepsilon_{HB})} + \gamma a_1) \quad (5-32)$$

The previous equation represents the attenuation of light by a blood thickness according to modified Lambert-Beer' Law with an additive term (γa_1). As was done before, the first-order expansion can be employed.

By neglecting either back-scattering light (when $\gamma=0$) or double-pass (when $\beta=0$), a simplified version of (5-28) can be expressed as

$$OD = S(\lambda) + \eta(\lambda) Cd(\varepsilon_{HBo_2} OS + (1 - OS)\varepsilon_{HB}), \quad (5-33)$$

where $S(\lambda)$ is the scattering function and $\eta(\lambda)$ is the optical path length coefficient with the limit $1 < \eta(\lambda) < 2$; when $\eta(\lambda)=1$ single-pass is dominant and $\eta(\lambda)=2$ when double-pass is dominant.

By employing a least-squares nonlinear regression of the model proposed in (5-33) to a multi-wavelength transmittance (or optical density) measurement, OS, $S(\lambda)$, and $\eta(\lambda)Cd$ can be determined. However, the scattering function $S(\lambda)$ and the optical-path length coefficient $\eta(\lambda)$ are both functions of optical path fractions (α , β , γ), the coefficients (a_1 , a_2), and fundus reflectivity (R_f), which, in turn, are dependent on the measured wavelength λ . As a result, better understanding of their dependency on wavelength is required. As stated previously, the scattering term $S(\lambda)$ is found to be a function of blood-oxygen saturation which complicates the proposed optical model and hence the accuracy of measurements. More simplified versions of the optical model (5-33) were used in the literature in which the scattering term is assumed constant (Delori 1988), a linear function (Drewes 1999), or an empirical function of wavelength (Schweitzer 1995).

5.7 Wavelength selection and error minimizing

Several techniques have been demonstrated to measure retinal oxygen saturation non-invasively by illuminating the retinal vessels with light having various combinations of wavelengths. Determining the saturation error necessitates establishing a relationship between an error in a blood oxygen saturation measurement and measurement errors in the respective transmittance (or optical density) of the blood vessel for light at various plurality of wavelengths and then selecting the combination with the lowest error. The optimum wavelength combination for retinal oximetry measurements varies as the number of wavelengths considered changes. Errors in retinal vessel oximetry have been reported in the literature for various vessel diameters and combinations of wavelengths. Table 5.1 shows the saturation error of a

range of vessel diameters at two and three wavelengths, reported by several investigators.

Investigator	Saturation error		Vessel diameter		Wavelength combination
	Vein	Artery	Vein	Artery	
	[%]	[%]	[μm]	[μm]	
Hickam,1963	6.4--18	3.3--7.5	50--160	50--120	640 and 800 nm
Tideman,1998	>100-4.8	17--2.9	50--160	50--120	569 and 600 nm
Delori,1988	90	100	standard	standard	558,569,586 nm
Smith,1998	17.5	3.4	50	120	670 and 803 nm

Table 5.1: Saturation error at various wavelength combinations

In spite of the fact that some wavelength combinations produce excellent sensitivity to oxygen saturation, this does not necessarily represent optimum combinations. There are several factors which influence the selection of the wavelength range, such as scattering by red blood cells, strong absorption by haemoglobin and ocular media, and the effect of deeper fundus layers. The selection of the wavelength range, based on Delori's work (Delori, 1989), depends on fundus reflectivity, which might vary significantly across the selected range and hence influences the calculation of retinal oxygen saturation. As a result, it would be desirable to choose wavelengths that are closer together, if sufficient sensitivity to oxygen saturation can be achieved. On the other hand, scattering was assumed to be constant over a narrow wavelength range that does not fall near a strong Hb absorption band as the refractive indices of the RBCs would remain approximately constant. Smith et al. (1999) and Hammer et al. (1995) suggested that any wavelength dependent scattering effects should at least behave monotonically.

Strong absorption by haemoglobin derivatives between 400 and 450 nm (see Figure 5.2) in addition to low haemoglobin absorption and deep tissue penetration for

wavelengths longer than 1000 nm restrict range of the wavelengths to perform retinal oximetry to $450 \leq \lambda \leq 1000$ nm.

5.7.1 Photometric error

An error in estimating optical density or transmission will influence oxygen saturation measurements. As the optical density, OD , is calculated from the measured transmittance, according to (5-4):

$$OD = -\text{Log}(T) ,$$

the absolute error in calculating OD is

$$\Delta OD = \left(\frac{dOD}{dT} \right) \Delta T . \quad (5-34)$$

To minimize the error in calculating oxygen saturation, the relative density error should be minimized (Assendelft 1970). The relative density-error can be expressed as

$$\begin{aligned} \frac{\Delta OD}{OD} &= \frac{\frac{dOD}{dT} \Delta T}{OD} , \\ \Delta OD &= \frac{dOD}{dT} \Delta T = -\frac{\Delta T}{\ln(10)} \frac{1}{T} \end{aligned} \quad (5-35)$$

$$\frac{\Delta OD}{OD} = \frac{\Delta T}{T \ln(T)} . \quad (5-36)$$

To minimize the relative error, the first derivative of (5-36) is set to zero as follows:

$$\frac{d\left(\frac{\Delta OD}{OD}\right)}{dT} = -\frac{\ln(T)+1}{[T \ln(T)]^2} \Delta T = 0 . \quad (5-37)$$

The realizable solution suggests that $\ln(T) + 1 = 0$ which yields

$$\begin{aligned} T &= \frac{1}{e} = 36.8\% \\ OD &= 0.434 . \end{aligned} \quad (5-38)$$

Therefore, the minimum sensitivity of error in absorption can be obtained when the transmittance measurement is 36.8% or optical density is 0.434. Assendelft (1970) considered the range (10% <T< 70%) or (1> OD> 0.15) of transmittance (T) or optical density (OD) to produce small errors. Figure 5.7 shows the relationship between relative density error and transmittance and the preferred range is highlighted.

To extend the previous technique to be applicable on more than one wavelength, we select the wavelengths which keep the transmittance measurements or optical densities in the preferred range with vessel thickness. Smith (1999) proposed a technique to find the optimum wavelength selection, based on Assendelft finding, to choose the best combination of wavelengths which minimizes the error in calculating oxygen saturation assuming the absolute transmittance error ΔT .

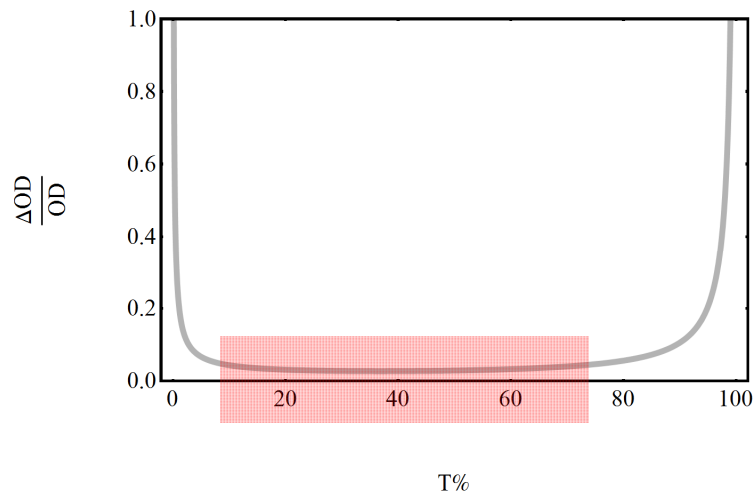


Figure 5.7: Relative density errors versus transmission

The criterion to select the optimum wavelength to achieve accurate retinal oximetry can be determined by minimizing the absolute error in saturation (ΔOS) due to an absolute error in transmittance (ΔT). The absolute saturation error for n wavelengths ($\lambda_1, \lambda_2, \dots, \lambda_n$) is expressed as follow:

$$\Delta OS = [(\frac{\partial OS}{\partial T^{\lambda_1}} \Delta T^{\lambda_1})^2 + (\frac{\partial OS}{\partial T^{\lambda_2}} \Delta T^{\lambda_2})^2 + + (\frac{\partial OS}{\partial T^{\lambda_n}} \Delta T^{\lambda_n})^2]^{\frac{1}{2}} , \quad (5-39)$$

where ΔT^{λ} is the measurement error in transmittance at a particular wavelength λ . To calculate the partial derivatives $\frac{\partial OS}{\partial T^{\lambda_n}}$, OS should be expressed as a function of transmission T instead of optical density OD . The saturation error ΔOS , as defined in (5-35), was employed to examine the optimum combination of wavelengths (in the case of two, three, and more than three wavelengths). To evaluate ΔOS the transmission was estimated according the Lambert-Beer Law for a typical range of vessel diameters (50 to 200 μm), typical haemoglobin concentration of 15 g/100 ml (8.9 m.mol/ml.cm²), and a range of oxygen saturations. Light is assumed to transmit a single path through the retinal vessels for the considered wavelength range, ignoring the effect of scattering by red blood cells and the extended light path. An absolute error in transmittance ($\Delta T=0.01$) is considered, to illustrate the uncertainty in the calculated T regardless of the experimental instrumentation. Transmission calculation at wavelengths longer than 600 nm might encounter larger error due to the increased variation in the fundus background, as light can penetrate towards deeper layers.

In this thesis, optimum selection of wavelengths is performed considering various combinations with different numbers of wavelengths across the useful wavelength range possible by our instrument. It is important to evaluate the impact of increasing the number of wavelengths on minimizing the saturation error. For this purpose, the saturation error at two and three wavelengths is also calculated.

5.7.2 Optimum selection for two-wavelength oximetry

The perfect combination of two wavelengths has been investigated by Smith (1999) for a wavelength range ($450 \leq \lambda \leq 950$ nm). To obtain oxygen saturation measurement

with minimum error, Smith found that at least one wavelength should fall within the range 600 to 700 nm and the range 800 to 1000nm (or 500 ± 20 nm) for the other one. The wavelengths 635 and 905 nm appeared the most favourable, based on Smith's criteria: commercial availability, high transmittance by ocular media and better sensitivity. However, transmission measurement errors at these wavelengths (635, 905) will increase, as the retinal vessels are highly transparent due to low absorption by haemoglobin, in addition to the effect of deeper fundus layers such as the choroid. All possible combinations of two wavelengths within the useful wavelength range of our instrument ($500 \leq \lambda \leq 650$ nm) were investigated. Wavelengths below 500 nm were eliminated as the SNR of our instrument is very low, due to the low transmission by the LCTF in the range ($400 < \lambda < 500$) in addition to the strong absorption by haemoglobin derivatives and eye media. On the other hand, retinal vessel and ocular media are highly transparent at wavelengths longer than 650 nm, and that will increase the transmittance error due to the spatial variations in the fundus background as light penetrates to the choroid. It is clear that the best sensitivity to oxygen saturation is suggested when the difference $|\varepsilon_{HbO_2} - \varepsilon_{Hb}|$ is large and, moreover, the sensitivity will increase when the difference $\varepsilon_{HbO_2} - \varepsilon_{Hb}$ is positive for one wavelength and negative for the other. Therefore, transmittance will increase at one wavelength and decrease for the other wavelength, as saturation changes. Our simulation results have shown that when an absolute error in transmission ($\Delta T = 1\%$) at each wavelength was assumed, the lowest saturation error ΔOS was observed for the wavelength pair 578 and 600 nm, as depicted in Figure 5.8, for venous and arterial blood respectively.

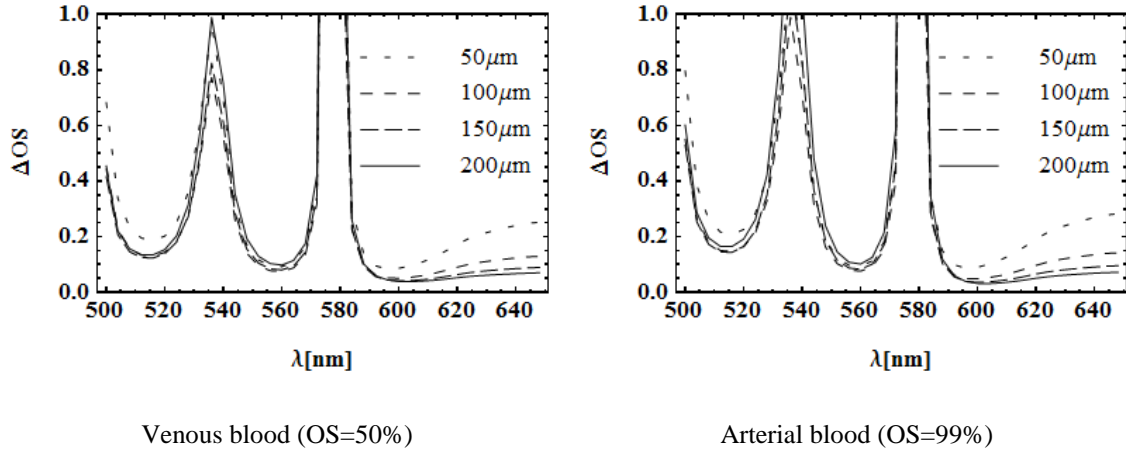
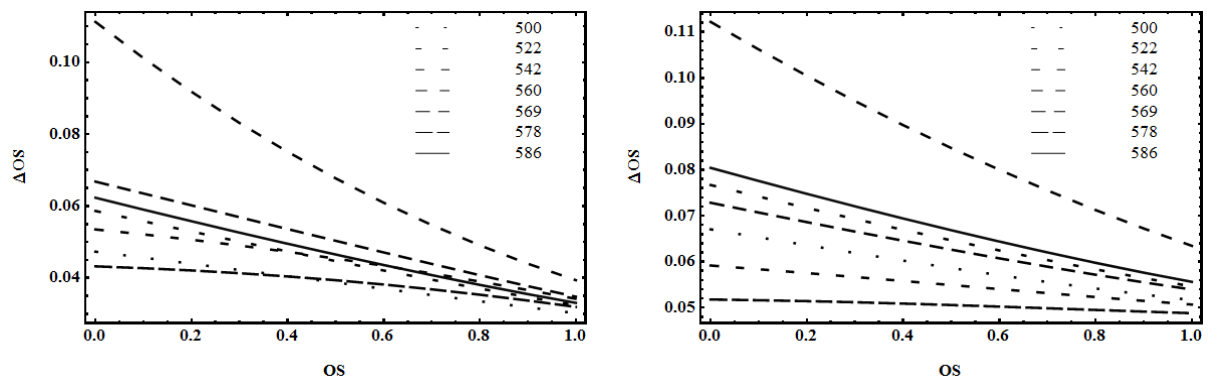


Figure 5.8: Absolute saturation error at four different vessel diameters for two wavelength combinations: 578 and 600 nm

The variations in the saturation error were investigated for six candidate combinations of wavelengths, such as 600 nm with isobestic wavelengths {522,600}, {569,600}, {586,600} in addition to {500,600}, {560,600}, and {578,600}. Figure 5.9 shows the variation of saturation errors ΔOS versus blood oxygen saturation OS for a range of vessel diameters from 50 to 200 μm . The calculation of ΔOS is performed based on (5-39) when the transmission is calculated according to the Lambert-Beer Law for typical haemoglobin concentration and single path transmission. As depicted in Figure 5.9 the saturation errors for smaller vessels ($\leq 50 \mu m$) are higher than those of other vessel diameters, for all combinations. An apparent increase in saturation errors is noticed at low oxygen saturations due to incomplete consideration of scattering as a function of oxygen saturation.



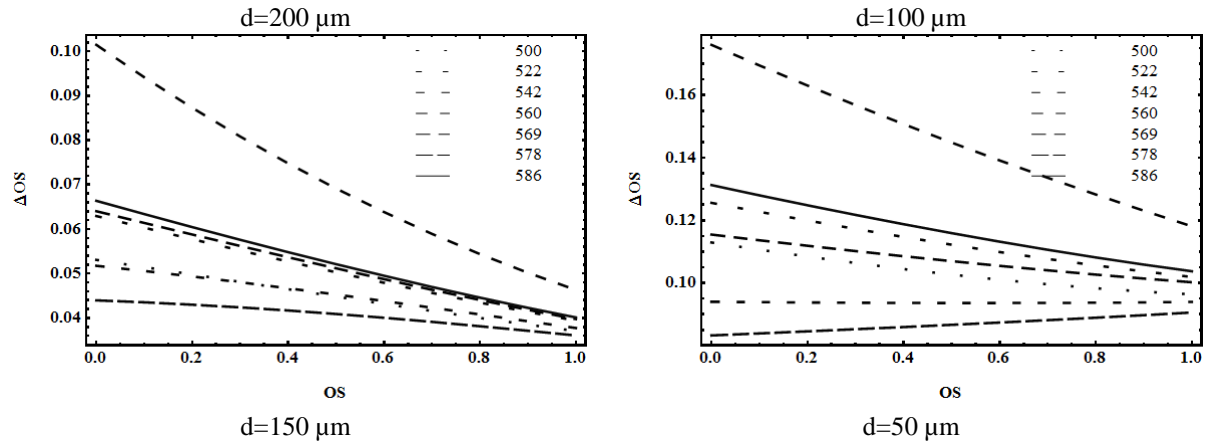


Figure 5.9: Variation in saturation error for different combinations of wavelengths with 600nm for different vessel diameters (d)

5.7.3 Optimum selection for three-wavelength oximetry

The constant scattering assumption in three-wavelength oximetry limits the range from which optimum wavelengths may be selected. Smith (1999) has found that expressing transmission according to modified Lambert-Beer's Law, with a constant scattering term across the 450-1000 nm wavelength range, will not affect the result of optimization significantly. To investigate the optimum combination which generates the lowest saturation error, we checked all the possible combination (76 triads) of three wavelengths in the range 500-650 nm, when absolute transmission error ($\Delta T=1\%$) is encountered for each particular wavelength. Two wavelengths, 596 and 646 nm, were found to be an excellent choice as they existed in most triads associated with lowest errors. Simulation performed by Smith (1999) based on (5-39) showed that the combination 488, 635 and 905nm allows for the most accurate oxygen

saturation measurements in retinal vessels. Smith found that the triad {488, 635, and 905 nm} was a remarkably stable combination, as it was associated with errors of less than 10 % across typical retinal vessel diameters and across all oxygen saturation values. Our simulation results showed that when the two wavelengths 596 and 646 nm are considered, there are a few wavelengths that appear to be a good third wavelength: Figure 5.10 shows the variation in saturation error as a function of the third wavelength.

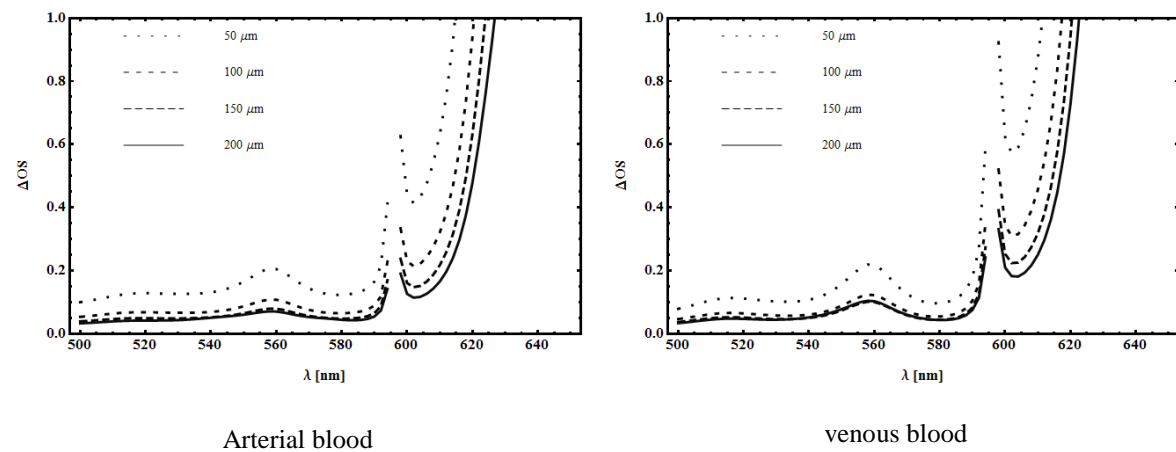


Figure 5.10: The variation of saturation error for arterial (left) and venous (right) blood, as the third wavelength varies with 596 and 646 nm

The smallest saturation errors occur at two combinations: {500,596, 646 nm} and {578, 596, 646 nm} for a wide range of vessel diameters and oxygen saturations. Figure 5.11 shows the variation in saturation errors as vessel diameters range between 50-200 μm and oxygen saturation varies between 0-100%. It is clear from the figure that the triad {500,596,646 nm} offers lower saturation errors especially for smaller vessels and higher oxygen saturation. Saturation errors for the other triad {578,596,646 nm} are increasing monotonically with oxygen saturation in comparison with {500,596,646 nm}.

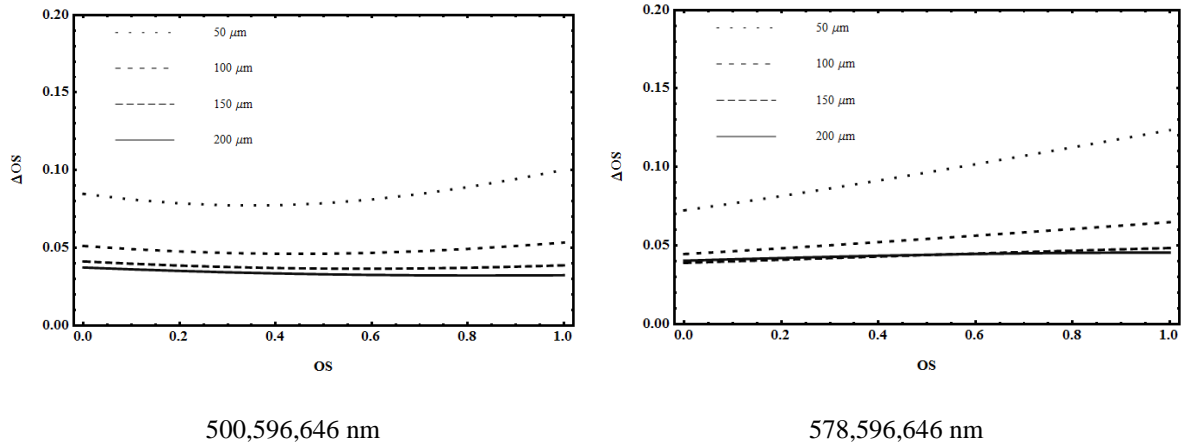


Figure 5.11: Variation in three-wavelength saturation error for two different wavelength triads

Transmittance measurement at 646 nm will suffer from higher transmission errors compared with 500 and 596 nm, due to scattering and spectral absorption properties of blood and ocular media, in which both blood and ocular media are highly transparent at wavelength ($\lambda=646$ nm), in addition to spatial variation effects from the underlying fundus layers, such as the choroid.

5.7.4 Optimum selection for multiple wavelength oximetry (76 & 16 bands)

Saturation error can be evaluated by using a number of wavelengths or a limited wavelength range, in order to minimize the variation in transmission due to wavelength dependency of scattering and the optical path. As discussed earlier, less information is available on the scattering by whole blood as a function of wavelength, in addition to the dependency on oxygen saturation and blood hematocrit concentration (Meinke 2007; Faber 2004). As a result, in this thesis, the scattering was assumed constant for the considered wavelength range. Saturation error was calculated according to (5-39) for a number of wavelengths in the range 500-650 nm in which a transmission error of ($\Delta T=1\%$) was assumed at each wavelength. Larger associated transmittance errors are expected at higher wavelength (>600 nm), due to spectral absorption and scattering properties of blood, in addition to the effect of

retinal background as light penetrates deeply. On the other hand, it seems unlikely that the scattering effects of whole blood will be sufficiently constant across the range 500-650 nm. The calculation of oxygen saturation was performed by means of least squares nonlinear regression to the optical model proposed in (5-33) when the scattering is negligible. Transmission at single path for a range of vessel diameters (50-200 μm) was estimated according to Lambert-Beer's Law, at different oxygen saturation levels. Figure 5.12 presents the variation of saturation error with different oxygen saturation levels at four different vessel diameters. Saturation error was investigated for various numbers of wavelengths: 500-650 nm sampled at 2nm and 500-650 nm sampled at 10 nm. Figure 5.13 and Figure 5.14, on the other hand, present the saturation error as a function of wavelength for arterial and venous blood. Saturation errors for small vessels ($\leq 50 \mu\text{m}$) are higher (see Figure 5.12, Figure 5.13, and Figure 5.14) as the transmission of such thickness will be much less than the optimal transmission (0.36) which offers the minimum error, as explained in (5-38), especially for longer wavelengths and higher oxygen saturation. However, as the number of wavelengths increases, the saturation error decreases.

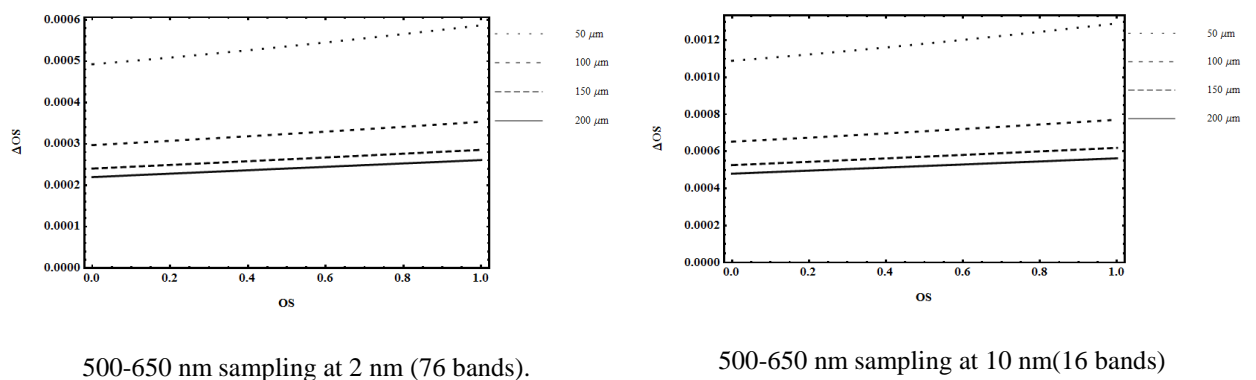
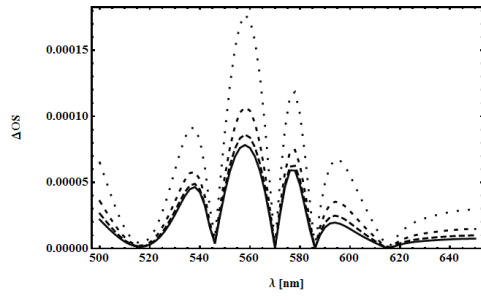
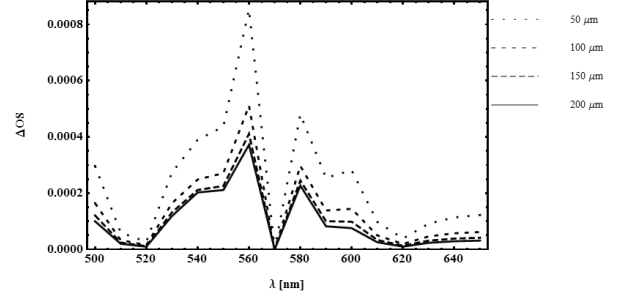


Figure 5.12: Saturation errors versus oxygen saturation at various vessel diameters

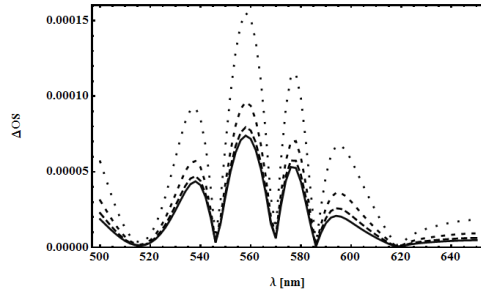


500-650 nm sampling at 2 nm (76 bands)

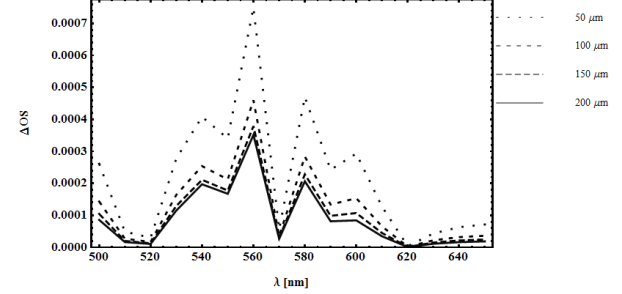


500-650 nm sampling at 10 nm (16 bands)

Figure 5.13: Saturation errors as a function of wavelength for arterial blood OS=0.99 at various vessel diameters



500-650 nm sampling at 2 nm (76 bands).



500-650 nm sampling at 10 nm (16 bands).

Figure 5.14: Saturation errors as a function of wavelength for venous blood OS=0.49 at various vessel diameters

It was clear that wavelengths (500, 542, 560, 580 nm) were associated with higher errors than other wavelengths. As a consequence, small errors in optical densities (or transmission) at those wavelengths can increase errors in calculation of saturation. Employing multi-wavelength oximetry has the advantage of reducing the effect of increased transmission errors at long wavelengths >600 nm due to the effect of varying structure and contribution of deeper layers such as the choroidal layer.

5.8 Conclusion

In this chapter, light propagation in retinal layers has been discussed. We have shown that light is absorbed by blood, melanin, and ocular media and scattered by red blood

cells due to discontinuity in refractive indices. We have explained the main principles of retinal oximetry, in which the modified Lambert-Beer Law was implemented to measure the oxygen saturation in the retinal vessels. Two techniques, two-and three-wavelength, used widely in the literature to measure retinal oxygen saturation, were reviewed. Scattering and multi-optical pass through the blood vessel were considered in the optical model to measure oxygen saturation. The optimum wavelength selection for the oximetry techniques was investigated. The results indicated that for only two-wavelength oximetry the best performance (the lowest saturation error) happens when the difference $|\epsilon_{HbO_2} - \epsilon_{Hb}|$ is large. The saturation error at various combinations of two wavelengths increased for small blood vessels and lower saturations. Saturation error at combinations of isobestic wavelength (522, 569 or 586 nm) and 600 nm had almost similar saturation error with the pair (569, 600 nm) having an advantage for smaller vessels ($\leq 50 \mu\text{m}$). In the three-wavelength combinations, the lowest error was found when the triads (500, 596 and 646 nm) and (578, 596 and 646) were used with the 500, 596, 646 nm triad having the advantage of producing less saturation error when oxygenated blood in small vessels ($\leq 50 \mu\text{m}$) was considered. However, transmission measurement at 646 nm was associated with higher errors, due to the effect of spatial variation in the retinal background as light penetrated deeply towards the choroid, in addition to the effect of spectral absorption and scattering properties of blood and other retinal chromophores. Oxygen saturation using multiple wavelengths (> 3 wavelengths) showed very low saturation errors when compared with that with two and three wavelengths. The increased number of wavelengths had the function of compensating the optical model to account for higher transmittance errors encountered at long wavelengths due to the influence of spatial variations of deeper. In Chapter 7, quantitative oxygen saturation measurements will be performed using

the range 500-650 nm. Optical densities will be measured along retinal vessel at each particular wavelength and a nonlinear fit algorithm will be utilized to obtain oxygen saturation measurements.

Chapter 6

Semi-quantitative oximetry

In this chapter we report how spectral data cubes were processed to generate semi-quantitative maps of blood oxygenation, based on spectral unmixing of the data into the spectra of oxygenated and deoxygenated haemoglobin. This involved preprocessing of the data to reduce sensitivity to illumination artefacts and supervised learning of *in-vivo* haemoglobin spectral signatures based on manual identification of arteries and veins. Oximetric maps were then produced for healthy and diseased retinas. These semi quantitative oximetric maps are clinically useful to monitor the improvement in the state of oxygenation levels in veins and arteries when treatment is applied.

6.1 Spectral processing techniques

A spectral data cube can most simply be considered as a stack of grayscale images. Each pixel in the data cube (voxel), as shown in Figure 6.1, is represented by a column vector in which each component represents the spectrum at a particular waveband.

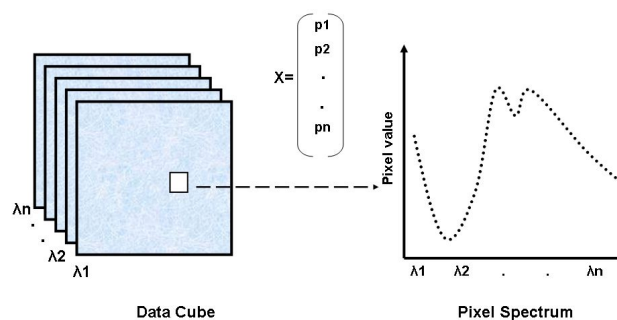


Figure 6.1: Spectral data cube

Spectral processing techniques can be divided into techniques that require *a priori* information about the object space and those for which no *a priori* information is necessary or available. Simple techniques such as the squared Euclidean distance $(x - y)^T (x - y)$ and the spectral angle mapper (SAM) $\cos^{-1}(\frac{x \cdot y}{\|x\| \|y\|})$ can be used to measure the similarity of a spectral measurement to reference spectra, which in turn can be selected from distinct structures in retinal images (such as retinal vessels), or from established spectral libraries. Figure 6.2 illustrates the application of the spectral angle mapper to a retinal data cube of a healthy subject in the wavelength range 500-620 nm, in which the spectrum of each pixel was compared with reference spectra obtained from retinal vessels. In the figure, Figure 6.2 (b), the intensities of the red, green, and blue channels are related to the spectral angles of each voxel, with manually selected spectra of arteries, veins, and background. There are many limitations that prevent accurate mapping between desired targets, such as when the pixel intensity of the retinal vessels differs from those of the retinal background by less than the level of noise due to artefacts such as reflections by system optical surfaces, in addition to illumination variation effects.

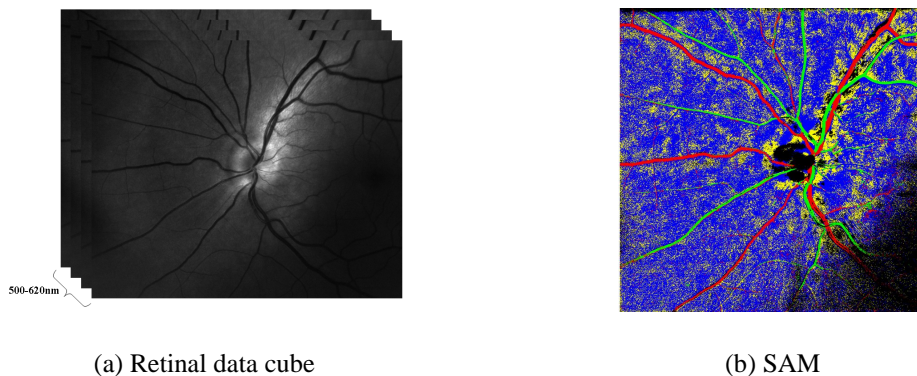


Figure 6.2: The application of SAM on retinal data cube

However, when multiple distinct spectral signatures are more likely to exist in a single pixel (voxel), as in the case of the spectrum of blood embedded in retinal vessels, a

more powerful technique such as spectral unmixing (Keshava 2002), can be employed. To perform that, informative spectra from the retinal data cube need to be defined by employing a statistical analysis method such as principle component analysis (PCA). This is discussed in the next sections.

6.1.1 Principle component analysis (PCA)

Multispectral images contain a large amount of data, although some bands have redundant information which impedes efficient spectral processing. One method of making the processing more efficient is to employ some sort of dimensional reduction by reducing the degree of redundancy through the statistics in the data. A technique is known as principle components analysis (*PCA*) (Tzeng et al. 2005) and has the benefit of being relatively powerful while being quite straightforward to calculate. *PCA* finds an alternative representation of the data which removes correlation between different bands in the data set. The procedure can often be used to find a reduced dimensionality set of orthonormal basis vectors that can be used to concentrate the variance of the data into a fewer dimensions. Figure 6.3 shows how data varies significantly along the direction \mathbf{v}_1 , where \mathbf{v}_2 accounts for less variation.

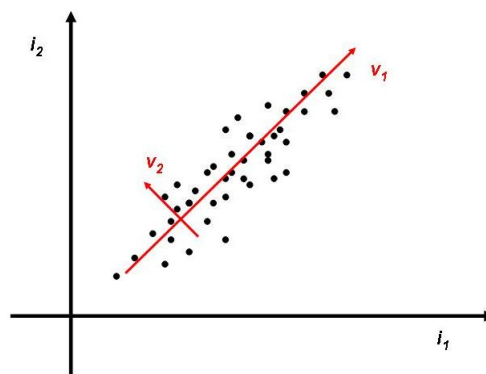


Figure 6.3: Example showing the direction of data variance.

The reduced dimensionality of the retained principle components will mean less computational power is needed for further processing. Also the approximate reconstruction of the data from the subset of principle components may have been stripped of some of the noise, meaning that some algorithms may work better after *PCA* has been carried out. The optimal answer depends on the application, the required accuracy, and how accuracy is quantified (Imai 2002).

6.1.2 Linear Spectral Unmixing

Linear spectral unmixing (Adams et al. 1985) is the simple form of spectral unmixing which expresses the spectral content of each pixel as a weighted summation of purest spectra (in the context, the pure spectra are usually referred as “*endmembers*”), each weight being equivalent to the abundance of that pure material. The number of endmembers chosen is typically far fewer than the dimensions of the data set. There are some assumptions that should be applied for the validity of the model (Settle and Drake 1993) such as:

- No significant amounts of multiple scattering exist between different materials in which each photon that reaches the sensor has interacted with only one material. This implies the spectrum of a pixel consisting of multiple components is a sum of the spectra of each individual component.
- Each endmember must be known, implying that for each pixel in the image, the sum of endmember fractions equals unity.

Figure 6.4 presents a mixed pixel which is a 1/3 linear mixture of classes 1 (C1) and 2 (C2). Mixed pixels are presented whenever two or more materials share a common boundary or whenever the material in question is, in actuality, an intrinsic mixture of two or more materials, such as blood which contains Hb and HbO₂.

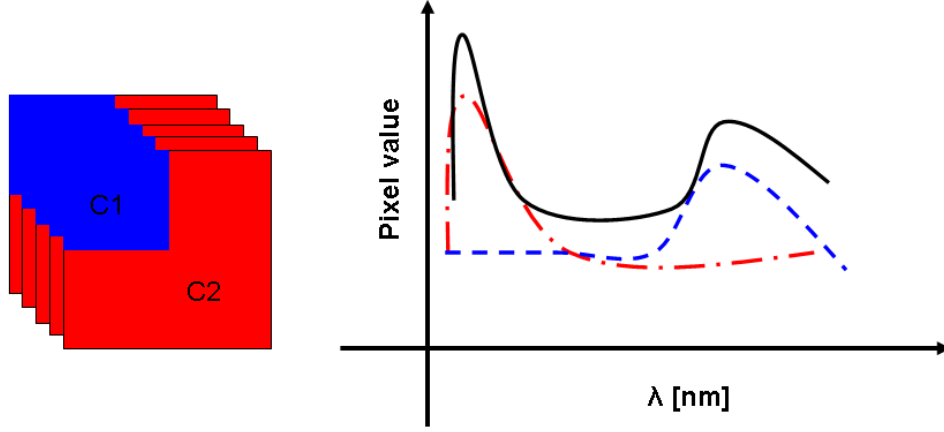


Figure 6.4: Mixed pixel spectrum

For a set of N pixels and M endmembers, the measured spectrum of the j^{th} pixel, x_j , can be expressed as a linear combination of the endmember spectra, S_j , as expressed mathematically

$$x_j = \sum_{i=1}^M a_{ij} S_j + \omega_j. \quad (6-1)$$

The proportion of the i^{th} endmember contributing to the j^{th} pixel is given by the coefficients of the abundance matrix, a_{ij} . The term ω_j is the residual error either due to noise or an inappropriate choice of endmembers. Each endmember can be represented as a vector whose length is the same as the number of bands. If the endmembers are known or can be determined by selecting relevant regions of interest as training data, then the unmixing problem can be solved through simple least squares inversion as

$$a = (S^T S)^{-1} S^T x. \quad (6-2)$$

These methods work well for linear mixing in the absence of noise, but when high levels of noise are added, the solutions can become unrealistic. One problem is that there exist physical constraints such as: mixing proportions should not be

positive ($a_{ij} \geq 0$), and the mixing proportions must sum to one ($\sum_{i=1}^M a_{ij} = 1$). To realize

the unity constraint a dark endmember is usually included to account for illumination effects. Due to these two constraints, the linear mixing model can be broken down into sub-models: unconstrained model, fully-constrained model, sum to one constrained model and non-negativity constrained model (Howes 2004).

6.1.2.1 Determination of endmembers

There are various methods used to define endmembers prior to unmixing and they can employ manual or automated endmember selection methods. The problem is to find pure pixels which represent the endmembers. Manual selection is potentially the most capable technique, particularly when undertaken by a knowledgeable and skilled interpreter. The most extreme data points (pixels) in the n-dimensional space are chosen by the operator as endmembers, often with reference to spectral libraries and their spatial context. On the other hand, automated selection depends on algorithms to select the purest pixels.

6.2 *Semi-quantitative oximetry*

One of main challenges of retinal vessel oximetry is the development of a robust and accurate method of calculating the oxygen saturation that accounts for the complex interaction of light in the ocular media, retinal vessels, and retinal tissues. Spectral processing techniques are capable of mapping spectral images according to the spectral signatures under investigation.

Prior to spectral processing, spectral retinal images were calibrated by subtracting the artefacts associated when images are recorded and registered by means of a

registration algorithm (see Chapter 4) and formed into a data cube in the wavelength range ($500 < \lambda < 620$) nm. Figure 6.5 shows a retinal data cube; the spectra of pixels corresponding to artery, vein, and background are also presented.

When light propagates through a multi-layered structure such as retinal layers, the spectrum of reflected light is a result of multiplying the spectrum of light transmitted by each chromophore embedded in each layer. For example, the spectrum of light reflected from a retinal vessel is a multiplication of the spectrum of light transmitted by blood in the retinal vessel and melanin in the retinal pigment epithelium. On the other hand, when light incident at a pixel contains a mixture of various chromophores, the spectrum of reflected light is an additive of the spectra of the chromophores. The spectrum of light reflected from the retina is dominated by the spectra of haemoglobin and melanin. However, the spectrum of blood in a retinal vessel comprises the spectra of oxygenated and deoxygenated haemoglobin.

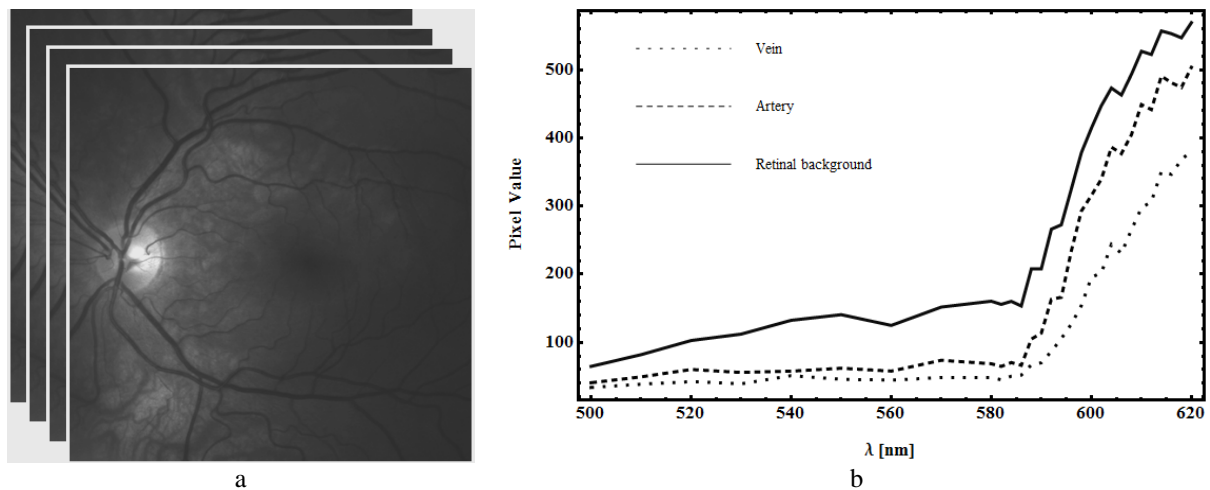


Figure 6.5: (a) Retinal data cube (Left); (b) Spectra of an artery, vein, and background (Right)

Lambert Beer's law was used to facilitate initial interpretation of the spectrum of transmitted light through retinal vessels by assuming that the main absorbers within the red blood cells (*RBC*'s) were the oxygenated and deoxygenated haemoglobin. The spectrum of reflected light from a retinal blood vessel, as given in (5-12), is

$$I(\lambda) = I_o(\lambda)10^{-(\epsilon_{Oxy}C_{Oxy} + \epsilon_{De-Oxy}C_{De-Oxy})d},$$

and the optical density (expressed previously in (5-13)) is

$$OD(\lambda) = (\epsilon_{Oxy}C_{Oxy} + \epsilon_{De-Oxy}C_{De-Oxy})d = a\epsilon_{Oxy} + b\epsilon_{De-Oxy}. \quad (6-3)$$

As can be seen, optical density is a linear combination of two endmembers: oxygenated and deoxygenated haemoglobin (Assendelft 1970). Thus, endmember fractions a and b can be determined and retinal images can be mapped semi-quantitatively, as Lambert-Beer's law is valid only for non-scattering, haemolysed blood. Scattering of light by red blood cells was neglected for the feasibility of applying linear spectral unmixing. As a result, optical density calculation and endmember derivation are two important preprocessing steps that should be accomplished prior to spectral unmixing.

6.2.1 Optical density map

To obtain a measure of the optical density of the whole retina for each wavelength, a definition of the albedo image that contains all illumination variations as an estimate of incident illumination is required.

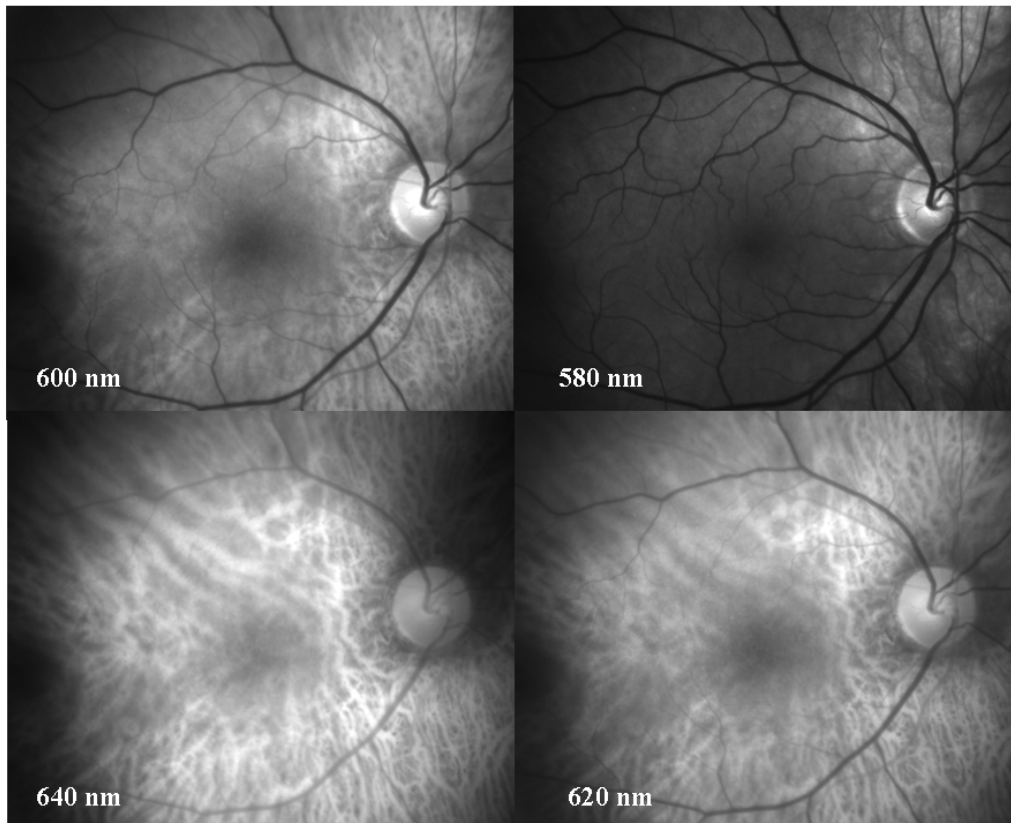
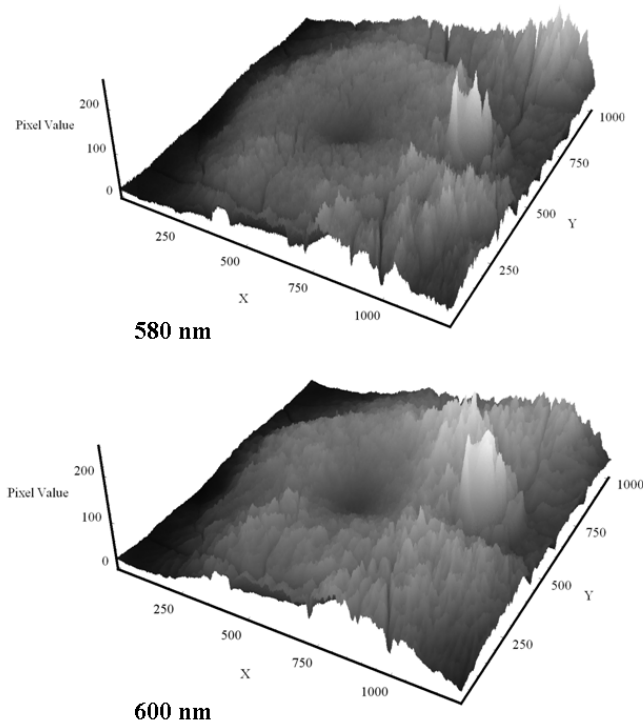


Figure 6.6: Retinal images at different wavelengths

Figure 6.6 shows a set of retinal images recorded at 580, 600, 620, and 640 nm. It is possible to see the capillary network but often the finest vessels are not visible (vessel diameter $\leq 10 \mu\text{m}$). This is due to the limited resolution of our system (1 pixel $\approx 10 \mu\text{m}$), in addition to the dependency of the retinal chromophore absorption properties on wavelength for example blood has high transmittance at $\lambda \geq 600 \text{ nm}$ when it is oxygenated. Therefore, retinal images can be thought of as having two main components: the vasculature retinal features, retinal vessel tree (microaneurysms and major vessels), and the background retina whose intensity varies gradually across the image and with wavelength.

The texture of the background of the retina is largely dictated by the distribution of both the capillary bed and the pigmentation of the retinal pigment epithelium. Figure 6.7 illustrates the variation of retinal background spatially across the captured image at different wavelengths (see Figure 6.6). As shown in Figure 6.6, the contrast of

retinal vessels varies with wavelength due to the absorption properties of blood. The choroidal structure is more apparent at 620 and 640 nm than at 600 and 580 nm, as light penetrates deeper and reaches the choroid at longer wavelengths. In addition to the spatial variations in the background, retinal images suffer from illumination variations due to the nature of the sequential technique and eye movement. Accurate separation of the retinal features (blood vessel-tree) from the background is the key step in obtaining accurate estimation of optical density.



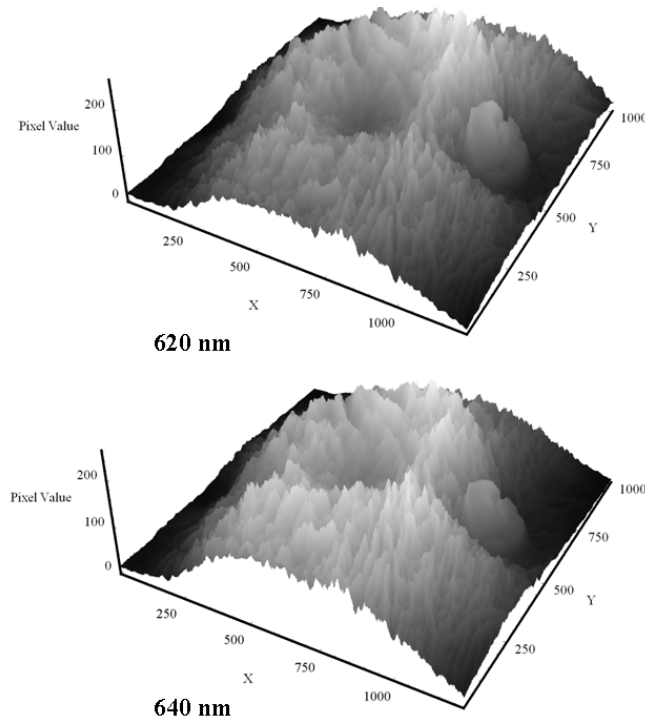


Figure 6.7: Spatial variation of retinal background

6.2.1.1 Illumination estimation

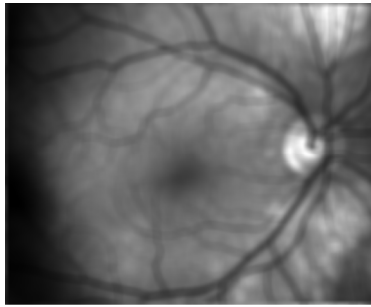
According to (5-13), the transmission, T , is obtained by dividing each retinal image at each particular wavelength by an approximation of incident illumination, I_o , which is estimated from the retinal image background in absence of the blood vessel tree.

$$T(\lambda) = \frac{I(\lambda)}{I_o(\lambda)}.$$

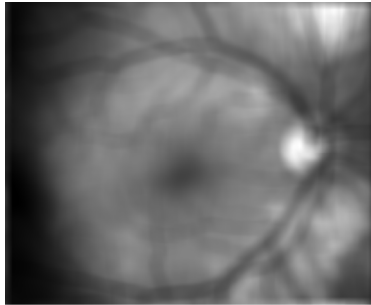
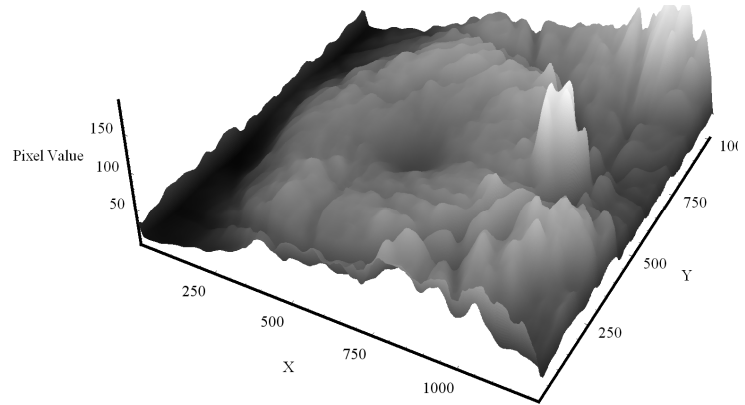
To facilitate extraction of retinal background, $I_o(x,y)$, and as explained in (6-4), each registered and calibrated retinal image, $I(x,y)$, is smoothed by a lowpass filter whose kernel size k is chosen to be significantly larger than the maximum size feature present in the image (Spencer 1996), but smaller than scale size for illumination variations.

$$I_o(x, y) = \sum_z \sum_z k(z, z) I(x - x_o, y - y_o) \quad (6-4)$$

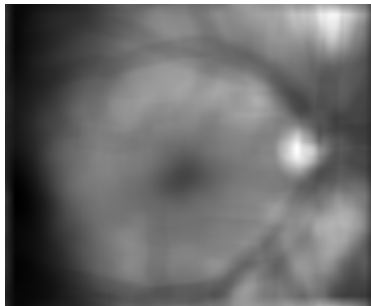
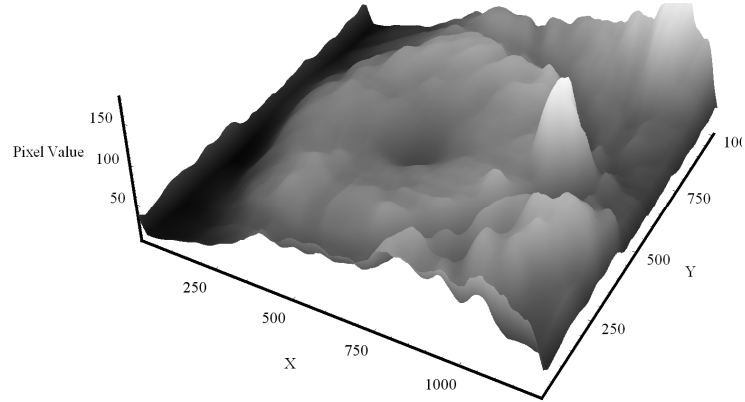
A kernel size of dimensions 91×91 pixels was found reasonable to maintain the background variations due to illumination variations and give an approximation of incident light in absence of the vessel tree at the same time. Figure 6.8 illustrates the effect of changing the kernel size on obtaining better approximation of image background.



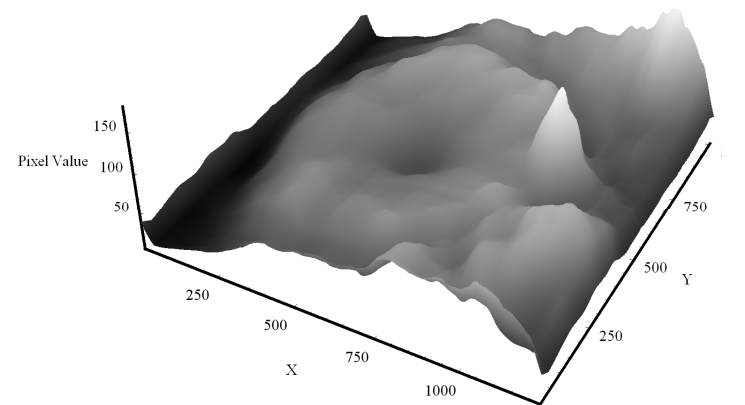
Kernel size 31×31



Kernel size 51×51



Kernel size 71×71



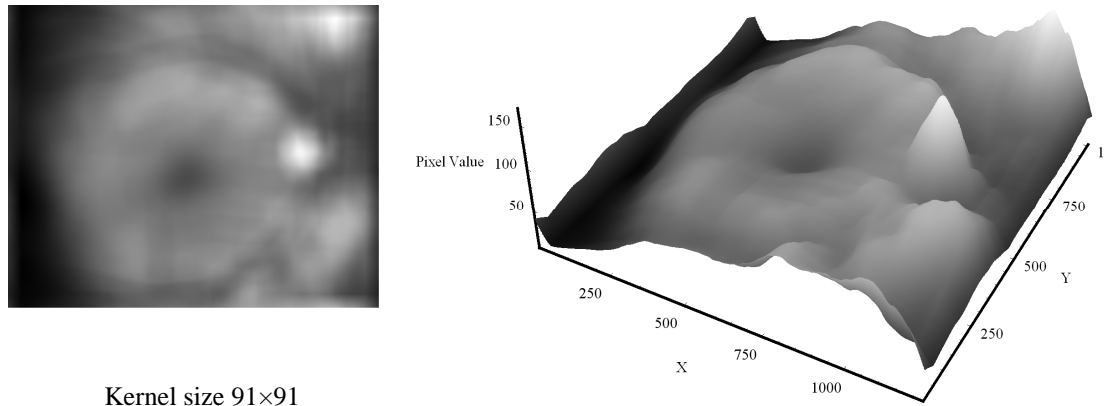


Figure 6.8: Smoothed retinal image by lowpass filter at different kernel sizes.

Each image was then divided by an estimated illumination to obtain transmission map, the optical density map was obtained by calculating the decimal logarithm of the transmission map. The transmission and optical density data cubes were then assembled prior to spectral processing; Figure 6.9 presents the optical density maps at various wavelengths: 580, 600, 620 and 640 nm.

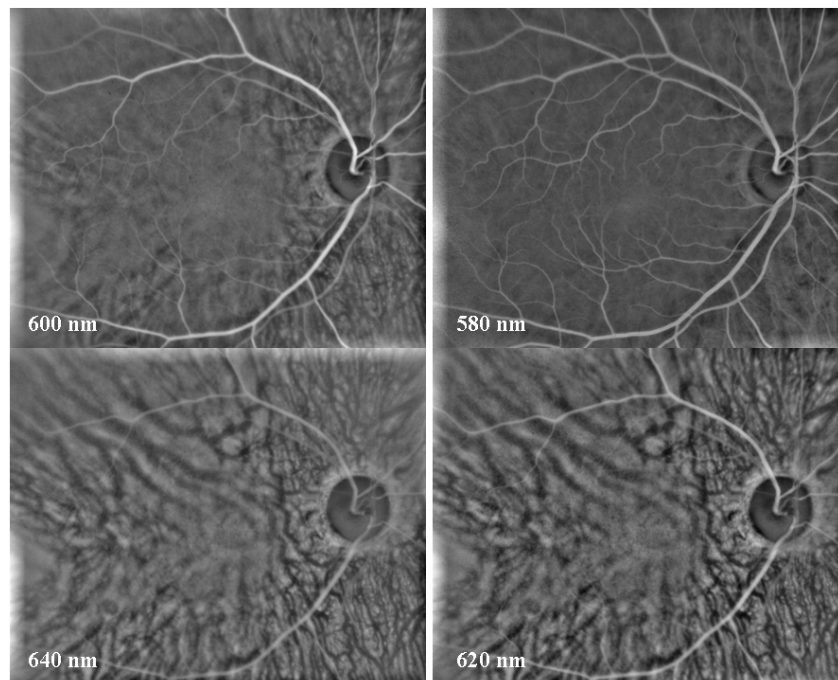


Figure 6.9: Optical density maps at different wavelengths

The optical density images then are used in a linear spectral unmixing algorithm to produce a relative oxygen saturation map of the retina.

6.2.2 Endmember selection

To identify the endmembers in the optical-density data cubes, principle component analysis, *PCA*, was employed. Optical density data cubes composed of 28 bands in the wavelength range $500 < \lambda < 620$ were used. *PCA* showed that two main components, oxygenated blood in arteries and deoxygenated blood in veins, were always dominant in the data cubes. Figure 6.10 presents the first five principle components (*PC's*); the first principle component (*PC1*) contained the most common features that have low variation with wavelength such as vascular tree and retinal background, the other principle components show the other signatures due to illumination variations and artefacts (*PC2* and *PC3*) in addition to the retinal arteries (*PC4*) and veins (*PC5*) where oxygenated and deoxygenated blood are present respectively.

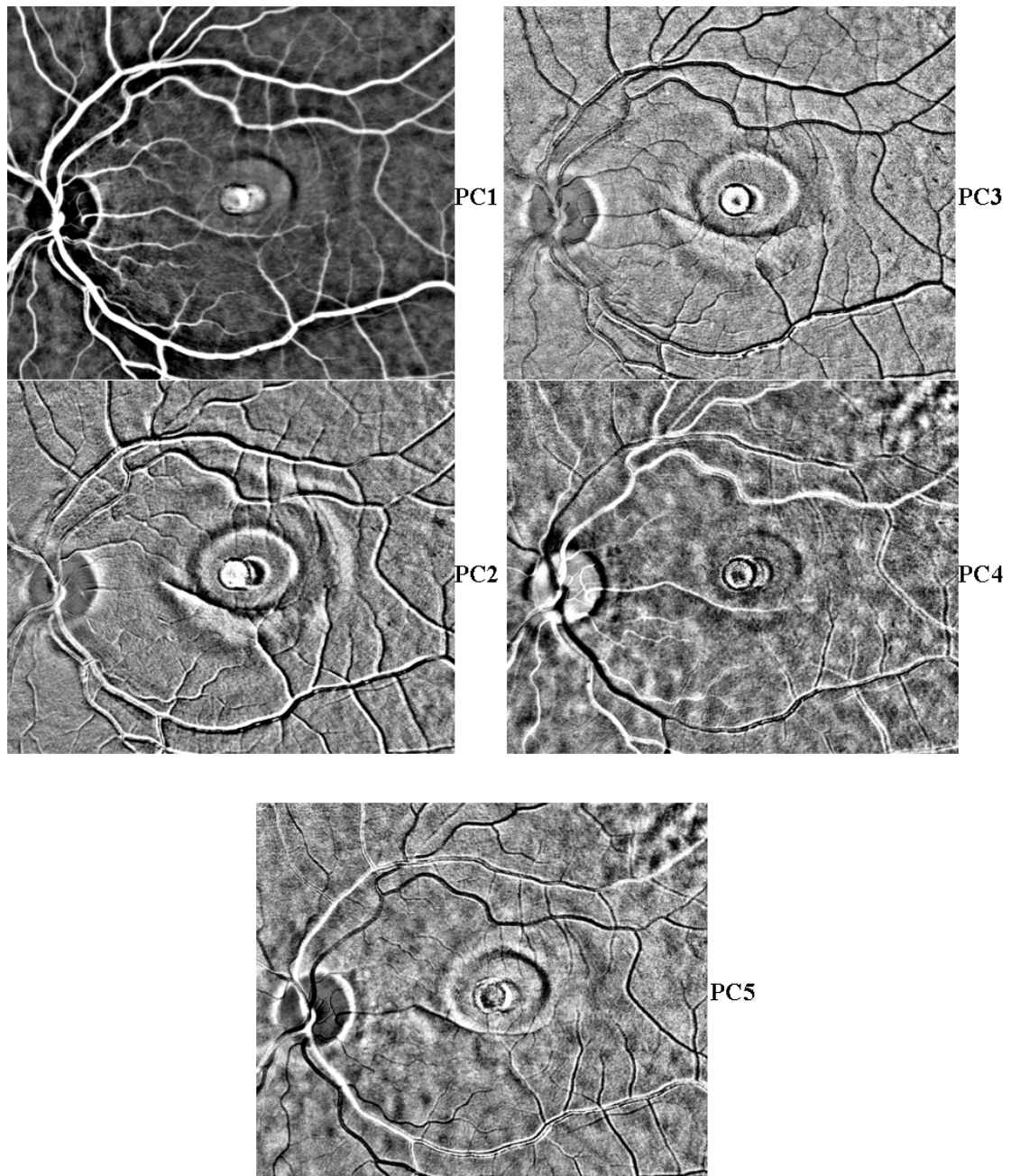


Figure 6.10: The first five principle components of the retinal data cube

Pixels overlying the retinal arteries and veins were assumed to be the closest representation of pure endmembers of oxygenated arterial blood and deoxygenated venous blood, as depicted in Figure 6.11.

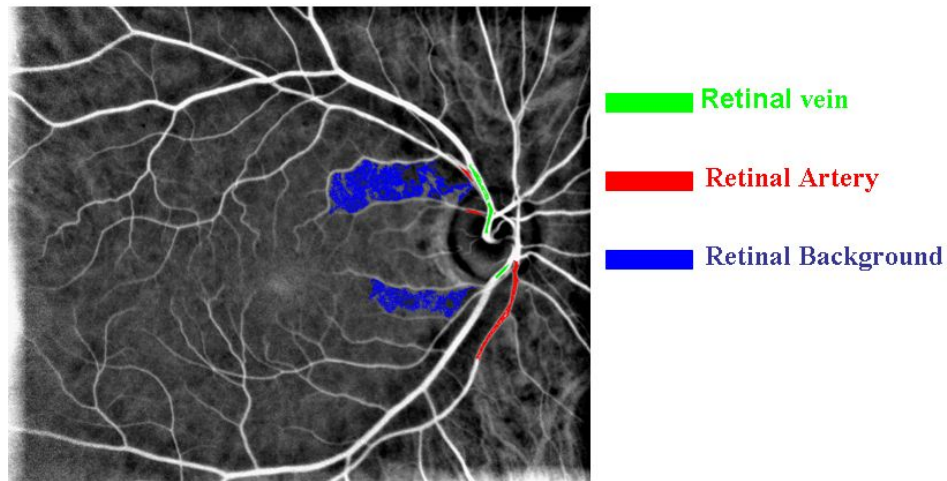


Figure 6.11: The selection of regions of interest

Twelve normal eyes were used to generate average spectral profiles of arteries and veins (see Figure 6.12). Regions of interest from the retinal background were selected to account for tissue components in the retina that do not contain signatures of oxygenated or deoxygenated haemoglobin. The spectrum of this endmember, as shown in Figure 6.12, was used to account for illumination variations and the legitimacy of sum to unity constraint ($\sum_{i=1}^M a_{ij} = 1$).

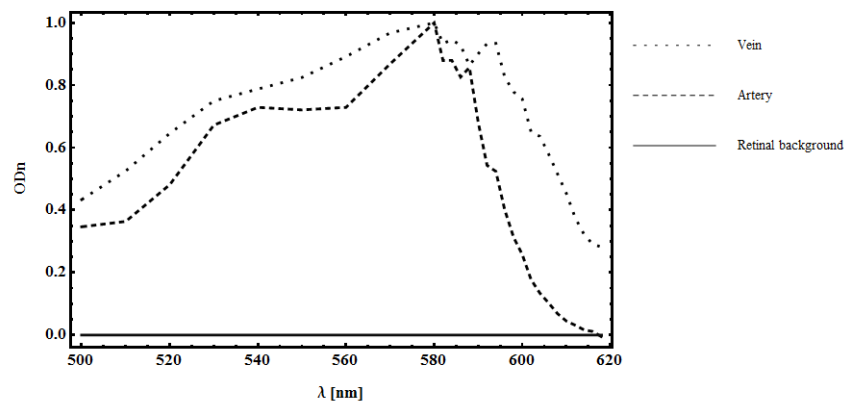
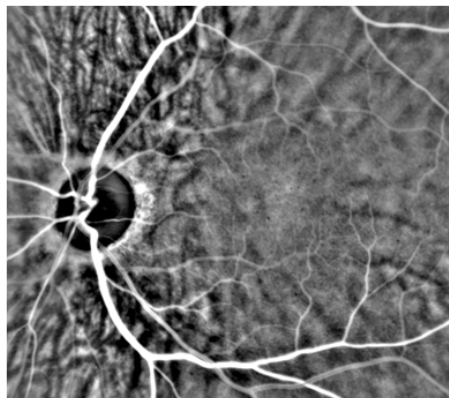


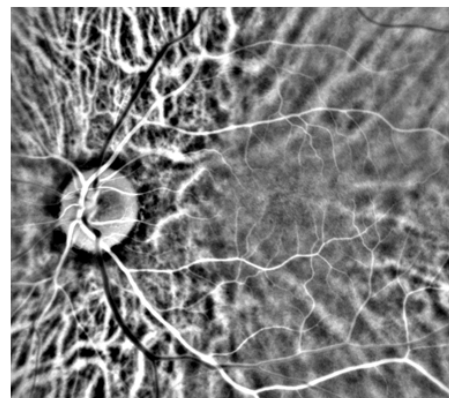
Figure 6.12: The averaged spectrum obtained from selected regions of interest

6.3 Results

Linear spectral unmixing was performed using these three endmembers to generate three abundance maps; each was associated with a particular endmember plus a root mean square (RMS) error image. Higher abundances (and higher RMS values for the RMS error image) were represented by brighter pixels. The unmixing results have a data range representing endmember abundance in the range (0-1). This analysis was performed using *ENVI 4.2* (ITT Visual Information Solutions, Boulder, CO, USA) which is a commercial software developed specifically for spectral image analysis. Figure 6.13 shows the abundance maps as a result of applying linear spectral unmixing on a healthy retina in addition to the RMS error map. The RMS error map helps in determining areas in the cube associated with inappropriate endmembers.



**Abundance map of
venous blood**



**Abundance map of
Arterial blood**

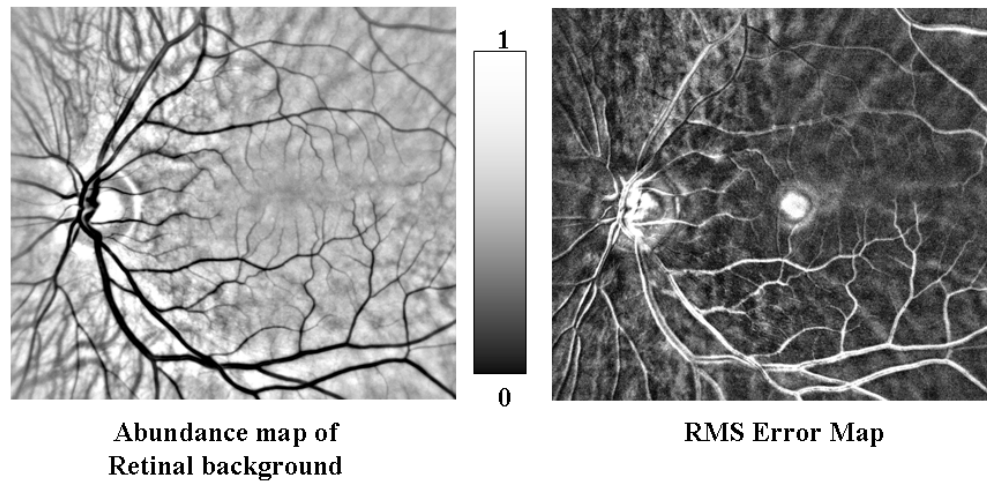


Figure 6.13: The abundance maps from a healthy subject and RMS error map

Negative values and values greater than one are possible in abundance maps. The results are dependent on the selected endmembers and will change if the endmembers are changed. Unfeasible abundances indicate erroneous endmembers. Residual errors in registration in addition to the artefacts associated with instrument calibration can produce greater RMS errors. The greatest RMS errors can be seen at the edge of vessels, in addition to the artefact in the central area of the RMS error map, as shown in Figure 6.13. A false colour map of the healthy retina, as presented in Figure 6.14, was generated, whereby colours were allocated to each pixel in the retinal image to represent the abundance of the purest endmembers.

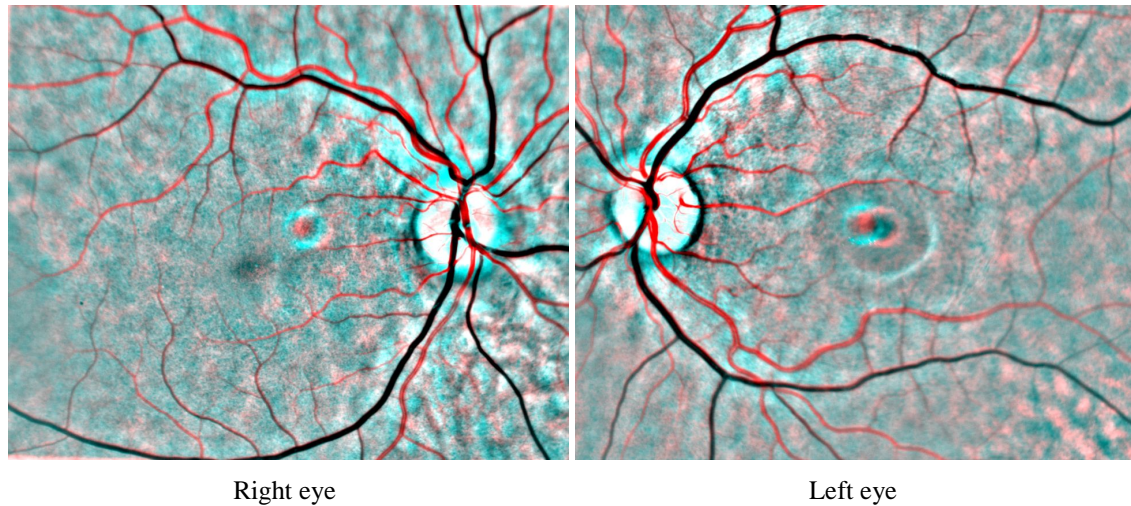


Figure 6.14: A false colour map of a healthy subject

To display a map of oxygenated blood (arterial blood) a red colour was used to represent pixels that contain a pure endmember of arterial blood; blue and green (cyan) colours were used to represent pixels that contain a pure endmember which represents the retinal background. The pure endmember of the retinal veins was not used in this colour allocation process. Therefore pixels that contain pure endmembers of retinal venous blood are shown in black. Pixels containing a mixture of the pure endmembers will contain a mixture of the red and cyan. The linear spectral unmixing technique when applied on four normal subjects, produced consistent retinal oximetry maps in which retinal arteries and veins were mapped in red (100% oxygenated blood) and black (50% oxygenated blood) respectively against the background, as illustrated in Figure 6.15. Due to the misregistration residuals, red lines at the edges of the retinal veins can be noticed.

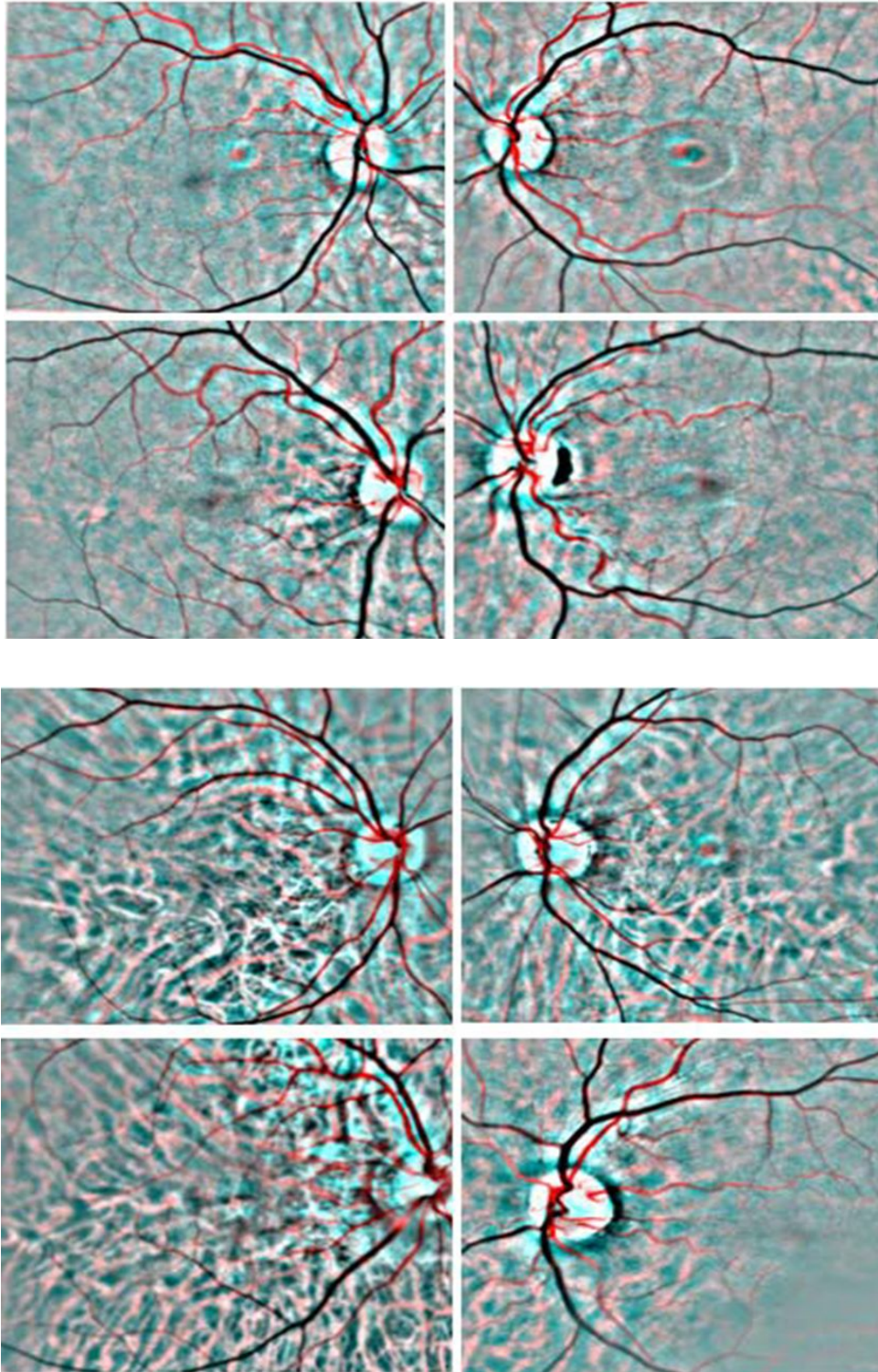


Figure 6.15: Eight retinal maps of oxygenated blood from 4 normal subjects

We note that the choroidal structure was clearly apparent in the maps. The application of linear spectral unmixing was investigated on retinal diseases such as retinal vein

occlusion, retinal artery occlusion, proliferative diabetic retinopathy, and asymmetrical primary open angle glaucoma.

6.3.1 Retinal Vein Occlusion

Figure 6.16 shows the retina of a 66-year-old female with a left supero-temporal branch retinal-vein occlusion. Snellen visual acuity was recorded at 6/12. The fluorescein angiogram shows an area of capillary non-perfusion in the supero-temporal retina (bottom left; yellow arrow). The oximetry maps of the two retinal areas (the ischaemic retina and the macula region) are shown (top right and bottom right). The oximetry maps show that the venous blood draining from the ischaemic supero-temporal retina has been mapped in red by the unmixing technique (top right; yellow arrow) which indicates that the spectra of the pixels overlying the segment of the retinal vein is similar to that of oxygenated arterial blood. This suggests abnormally high venous oxygenation in the respective segment of the retinal vein.

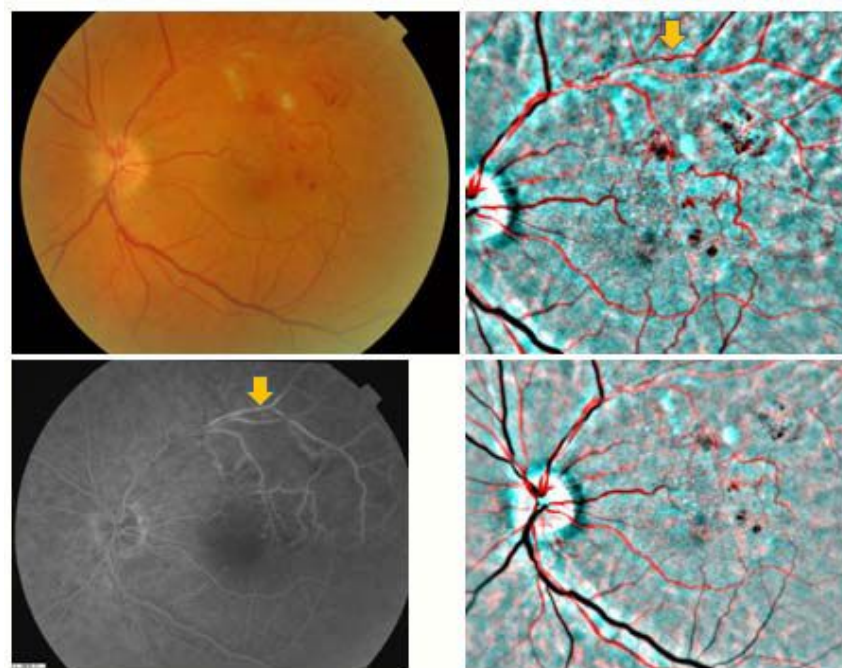
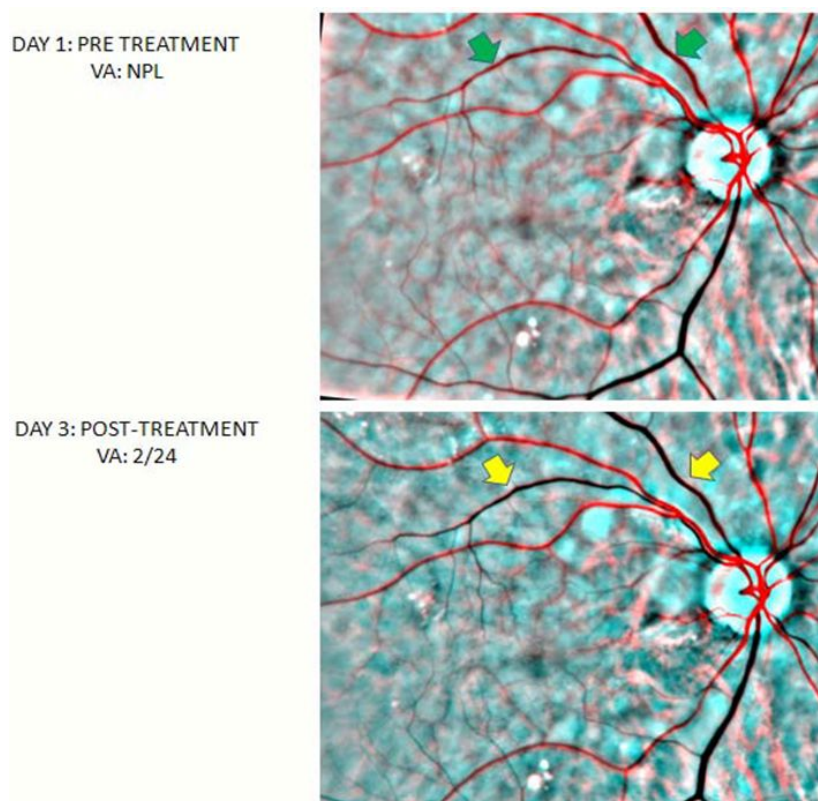


Figure 6.16: Oximetric map of retinal vein occlusion subject

6.3.2 Retinal Artery Occlusion

Figure 6.17 presents a retina of an 80-year-old female with a right retinal artery occlusion secondary to giant cell arteritis. Retinal oximetry maps are shown at presentation (visual acuity: no perception of light) and 3, 4 and 7 days following treatment with intravenous Methylprednisolone (visual acuities were 2/24, 2/18 and 2/24 respectively). The oximetry maps show that at presentation the venous blood draining from the ischaemic retina has been classified in red by the unmixing technique (green arrows), which changes to black (yellow arrows) following the treatment. This indicates that the spectra of the pixels overlying the affected retinal veins have changed, indicating a reduction of the increased venous oxygenation following treatment.



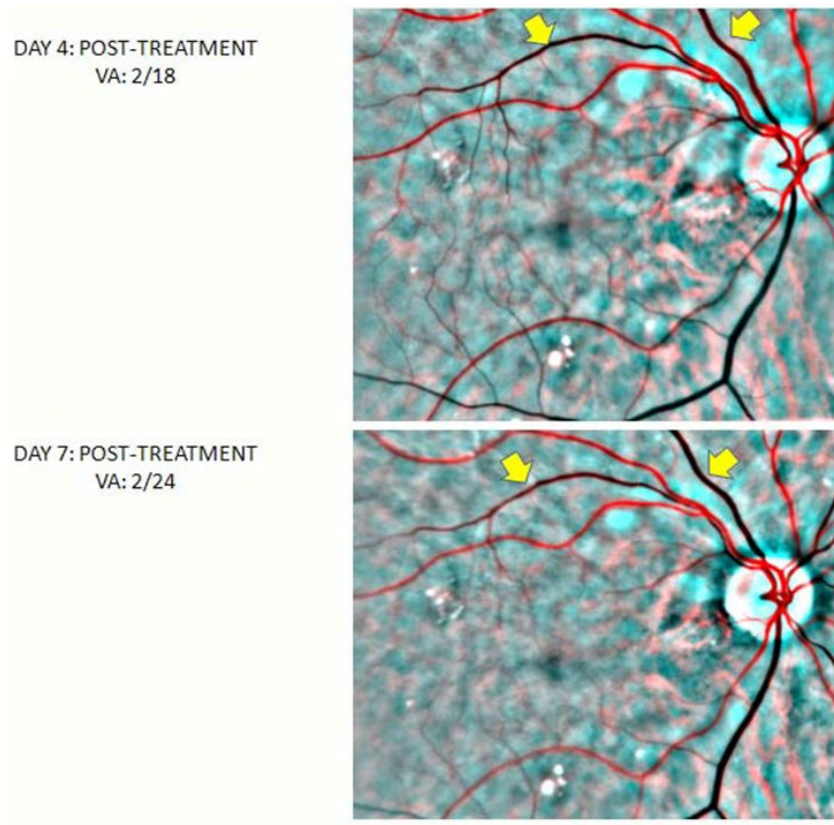


Figure 6.17: Oximetric map of retinal arterial occlusion subject

6.3.3 Asymmetrical Primary Open Angle Glaucoma

The oximetric map of retina of a 76-year-old with advanced asymmetrical primary open angle glaucoma (POAG) is shown in Figure 6.19. Oximetry maps of the retina (bottom left and right) suggest an increase in the oxygen saturation of the inferior retinal vein of the right eye (yellow arrow), which corresponds to the dense superior arcuate scotoma in the right visual field.

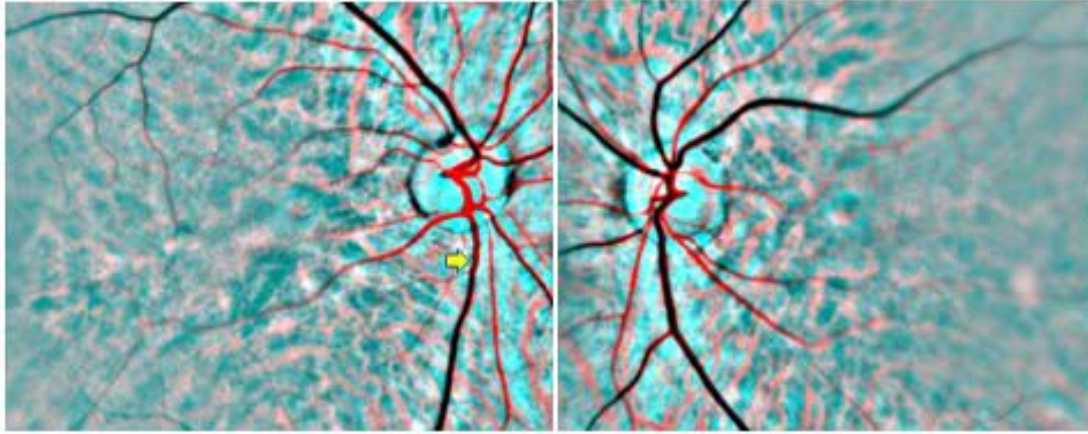


Figure 6.19: Oximetry maps of patient with asymmetrical primary open angle glaucoma.

6.4 Conclusion

In this chapter, we implemented linear spectral unmixing analysis on optical density data cubes of retinal images. Optical density data cubes were obtained by means of applying low passfilter with a kernel size appropriate to filter out variations due to the spatial signatures of the blood vessel tree and retain those due to illumination variations. Principle component analysis showed that two endmembers, the spectra of arteries and veins, were dominant in the data cube, in addition to the spectrum of retinal background. These endmembers were considered to map oxygen saturation in spectral retinal images. Semi-quantitative (qualitative) oximetric maps produced from healthy subjects indicated and confirmed that linear spectral unmixing can be used clinically to monitor the oxygenation status in retinal vessels. Linear spectral unmixing was then applied on subjects with retinal diseases such as artery and vein occlusion, and glaucoma. The analysis results indicated an increase in venous blood oxygen saturation associated with impaired function of the retina. Although these maps were useful to monitor the improvement in the oxygenation state post-treatment, incorporating a more elaborate technique, such as an optical model oximetry based

technique, is a requirement for clinicians to measure the oxygen saturation more accurately. In the following chapter, the analysis of spectral retinal images will take place, in order to define the sources of errors which might affect the oxygen saturation measurements.

Chapter 7

Image processing and data analysis towards quantitative oximetry

In this chapter, a method for local estimation of optical densities from retinal images at each wavelength and along the retinal vessel tree will be introduced. To obtain the optical density measurements along the vessels, a vessel tracking technique is implemented. The accuracy and reproducibility of optical densities are also assessed. The influence of retinal background irregularity on oxygen saturation measurements due to illumination variation between retinal images and local variation in retinal pigmentation is investigated. Oxygen saturation measurement from the optical density spectral profile is also explained.

Figure 7.1 presents the main steps in analysing retinal spectral images to extract oxygen saturation measurements.

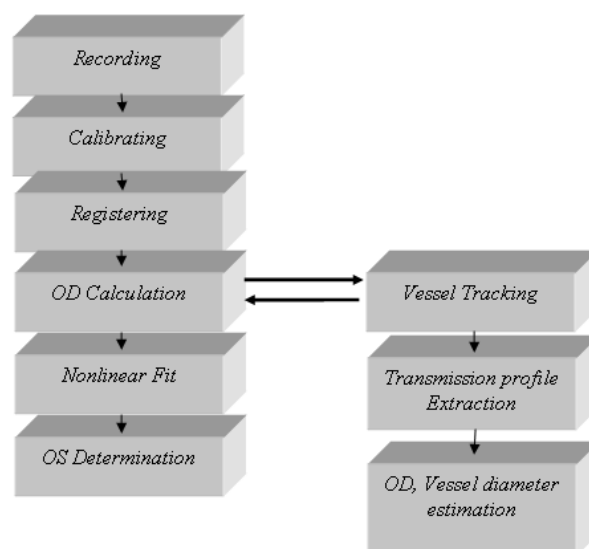


Figure 7.1: The main steps in analysing retinal images

7.1 Optical density measurement

To calculate the optical density at the centre of a blood vessel, the intensity profile across the retinal vessel is extracted from the retinal images. Figure 7.2 shows two intensity profiles across an artery (A) and vein (V) obtained from a retinal image recorded at 580 nm. It is clear from the figure that vein and artery profiles have different intensity due to the spectral properties of blood.

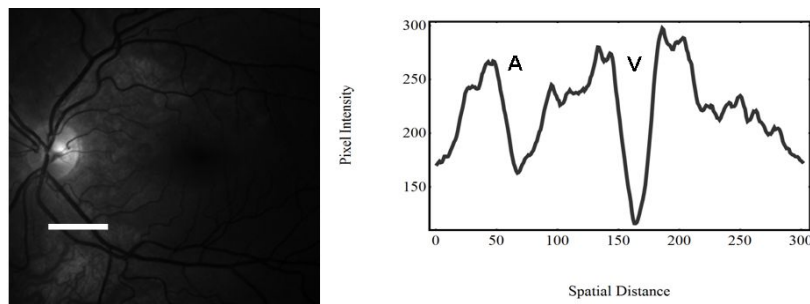


Figure 7.2: A retinal image at 580 nm (Left); Profile of Artery (A) and Vein (V) (Right)

The transmittance from the intensity profiles can be measured by dividing the intensity at the centre of blood vessel by the intensity estimated from the sides of the blood vessel. There are two practical methods to perform this measurement (Delori 1988; Beach 1999; Schweitzer, 1999; Smith 2000). (1) In the first technique, one-dimensional intensity profiles perpendicular to the retinal vessel are extracted, in which the transmission can be calculated by dividing the collected flux from the centre of the vessel by an estimate of the collected flux from the fundus background in absence of the vessel. A considerable number of profiles can be extracted along the vessel and averaged to minimize the irregularities in the fundus background. (2) The second technique involves measuring the transmittance in a similar way but is less affected by local variations of fundus pigmentation or glint from the apex of the vessel wall. In this technique, intensity profiles inside and outside the blood vessels at a fixed distance from the vessel wall are collected (see Figure 7.3). Averaging these

intensity profiles results in approximating the flux inside and outside the blood vessels and hence measuring the transmission.

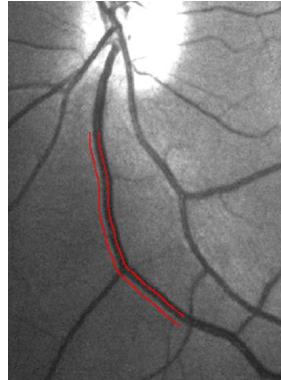


Figure 7.3: Intensity measurements inside and outside a blood vessel

Both methods have been used by researchers, depending on whether they have been looking for oxygen saturation in small segments of a vessel or along the vessel. To use the first technique, it is necessary to collect many intensity profiles across the vessel along the segment of interest (blood vessel tree). For example a segment length of N pixels along the blood vessel would involve N profiles being measured. This method enables the best curve fit to be used on the vessel profile to estimate the transmission in the centre of blood vessel and vessel diameter.

7.2 *Vessel tracking*

To automate optical density measurements, it was important to track the retinal vessel tree to enable extraction of transmission profiles. Tracking-based approaches apply local operators at points known to be on a vessel and track along the vessel. Tracking starts from an initial point and detects the vessel centre line or boundaries by analysing the pixels orthogonal to the tracking direction. Various methods are employed in determining vessel contours or centre lines. Edge detection followed by sequential tracing incorporating connectivity information is a straightforward

approach. However, one disadvantage of the vessel tracking approaches is that they are not fully automatic and require user intervention for selecting start and end points.

7.2.1 Fast marching algorithm

For segmenting blood vessels from retinal images, a vessel-tracking technique based on the fast marching algorithm (Sethian 1999) was utilized. This algorithm has been shown to be a useful technique to process many kinds of medical images (Cohen 1997; Malladi 1995; Hernandez 2003; Deschamps 2004). The retinal image is considered as a uniform Cartesian deterministic sampling scheme in which an efficient grid-search algorithm is used to find an optimal path, in the sense of a metric. The metric can be seen as the cost to go between two configurations (pixels in the images). At a configuration x , cost function $\tau(x)$ can be interpreted as the cost of one step from x to its neighbours; for obstacles, the cost function is infinite and at the starting configuration x , it is zero.

Two processes are implemented in fast marching technique: exploration and exploitation processes (Petres et al. 2007). The exploration process builds “a minimum cost to go” map, which is called the distance map, from the start to the goal configuration. The distance map is related to the value function in which the optimal path (the shortest path) between two points on the grid will follow pixels with lowest intensities. The exploitation process, on the other hand, is a backtracking conversely from the goal to the start configuration. See Sethian (1999) for more rigorous definition of a fast marching algorithm.

The main steps involved to track the retinal vessels are:

7.2.2 Nonlinear mapping

Prior to distance map calculation, it was important to highlight the retinal vessels, in which low values will be assigned to the pixels overlying the blood vessels compared with those overlying the retinal background. The nonlinear function is

$$\tau_{i,j} = \alpha \left(\frac{1}{\pi} (\arctan[\beta(I(i,j) - s)]) + \frac{1}{2} \right), \quad (7-1)$$

where $I(i, j)$ is the pre-processed retinal image, α is a gain and s is an offset. Figure 7.4 shows the nonlinear function for typical values of α , β and s .

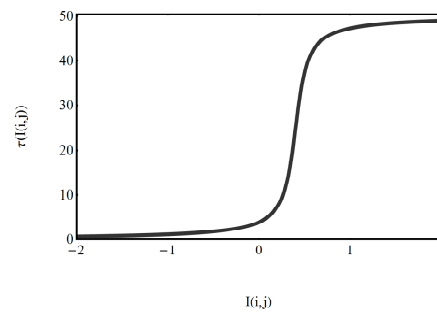


Figure 7.4: The nonlinear function for typical values of $\alpha=50$, $\beta=10$, and $s=0.4$

The pre-processed retinal image $I(i, j)$ is the optical density map, as defined previously in chapter 6. The result of applying the nonlinear function on the optical density map is shown in Figure 7.5 in addition to a cross-spatial profile along the x axis. It is clear from the figure that blood vessels are enhanced against the background.

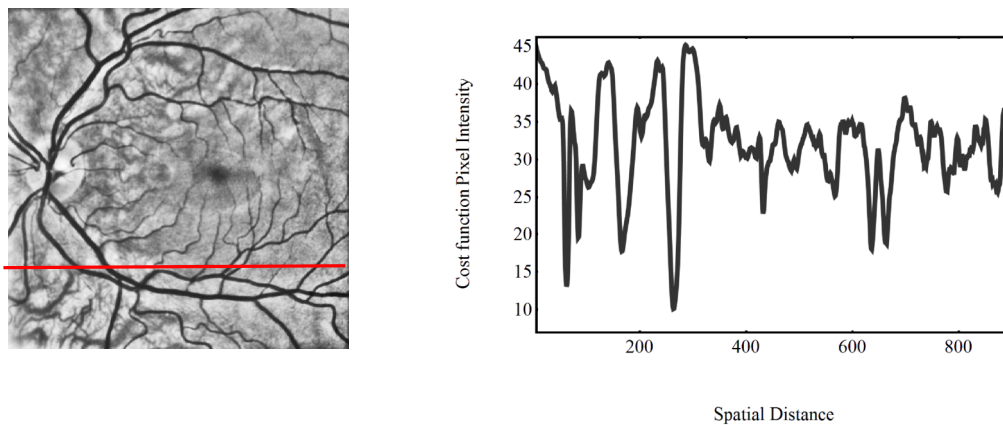


Figure 7.5: (Left) The application of nonlinear function, (Right) the cross profile along the red line

7.2.3 Fast marching algorithm

Once the cost function is implemented, we can perform the fast marching algorithm from the starting point (usually at the centre of the image) towards the target points (the tips of the selected retinal vessels). Single and multiple selections of blood vessels are possible, in which the fast marching algorithm incrementally builds a distance map outwards these points until all the considered vessels are reached. The last step is to backtrack the vessels from all the detected target points to the starting point. This process is achieved by performing a gradient descent over the distance map from each detected point. The fast marching code was developed in C at Heriot Watt University, Ocean Systems Laboratory (Petres 2007); a user interface was built in Mathematica around this code to employ it with retinal images. The fast marching process takes 70 seconds on a PC machine at 1.86 GHz with 1 GB memory.

The tracking was performed using retinal images at 586 nm, which is an isobestic wavelength, and where both veins and arteries have higher contrast in comparison with the background. By applying the tracking algorithm, the coordinates of the lowest intensities allocated inside the considered vessels are provided as shown in Figure 7.6. It can be noticed that sub-pixel accuracy is obtained due to the optimization process implemented when the vessels are backtracked.

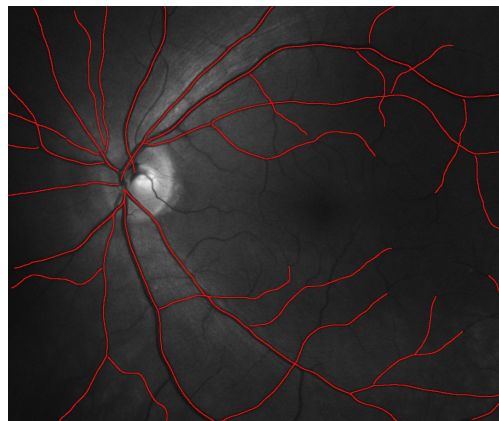


Figure 7.6: Vessel tracking

Mis-tracking is possible when veins and arteries are overlapped, in which the optimal path here is associated with lowest intensities. To overcome this problem, tracking can be performed on smaller sections along the retinal vessels.

7.3 Transmission profile extraction

On obtaining the coordinates of the centre line of the retinal vessels (x_i^n, y_i^n) , profiles perpendicular to the gradient between each two successive points, as depicted in Figure 7.7, can be extracted.

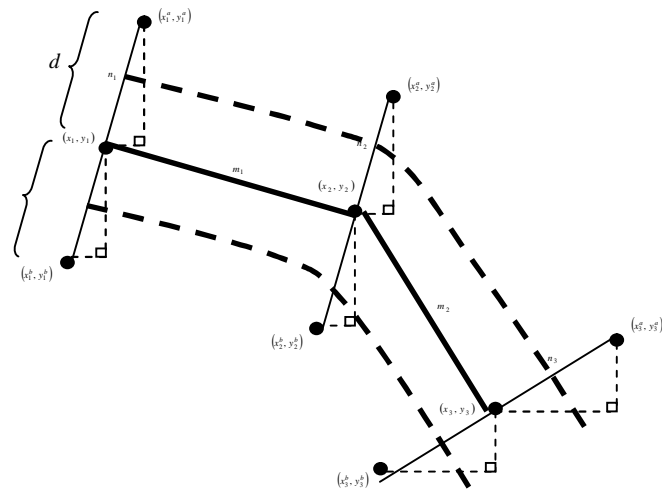


Figure 7.7: Vessel centre line coordinates and cross profiles

The gradient between two points $((x_i, y_i), (x_{i+1}, y_{i+1}))$ can be given as

$$m_i = \frac{y_{i+1} - y_i}{x_{i+1} - x_i}, \quad (7-2)$$

and the normal to the line joining points is

$$n_i = -\frac{1}{m_i}. \quad (7-3)$$

Each of these points, (x_i^n, y_i^n) , have adjacent points with coordinates (x_i^a, y_i^a) and (x_i^b, y_i^b) . The distance between points adjacent to positions along the vein/artery, d , is calculated such that

$$d = \sqrt{(y_1^a - y_1)^2 + (x_1^a - x_1)^2} . \quad (7-4)$$

Manipulation of the equations above leads us to expressions for the adjacent coordinates.

The length of the cross profile ($2d$) was chosen to be about three times an estimated average vessel width, as measured in the retinal images ($2d=30$ pixels). The intensity profiles can then be obtained as shown in Figure 7.8. and Figure 7.9.

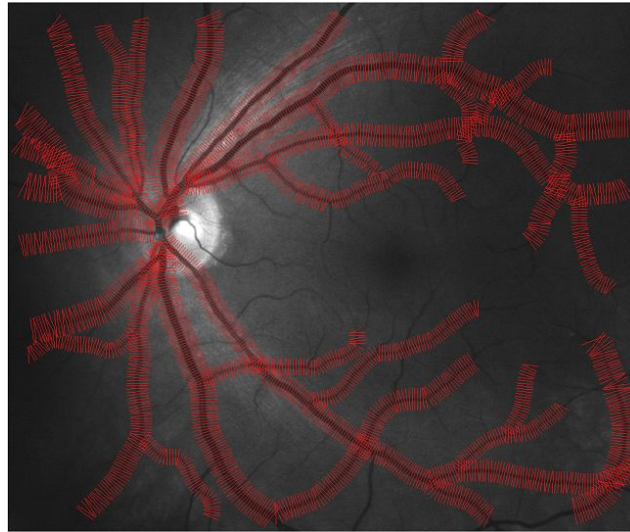


Figure 7.8 Cross-profile extraction.

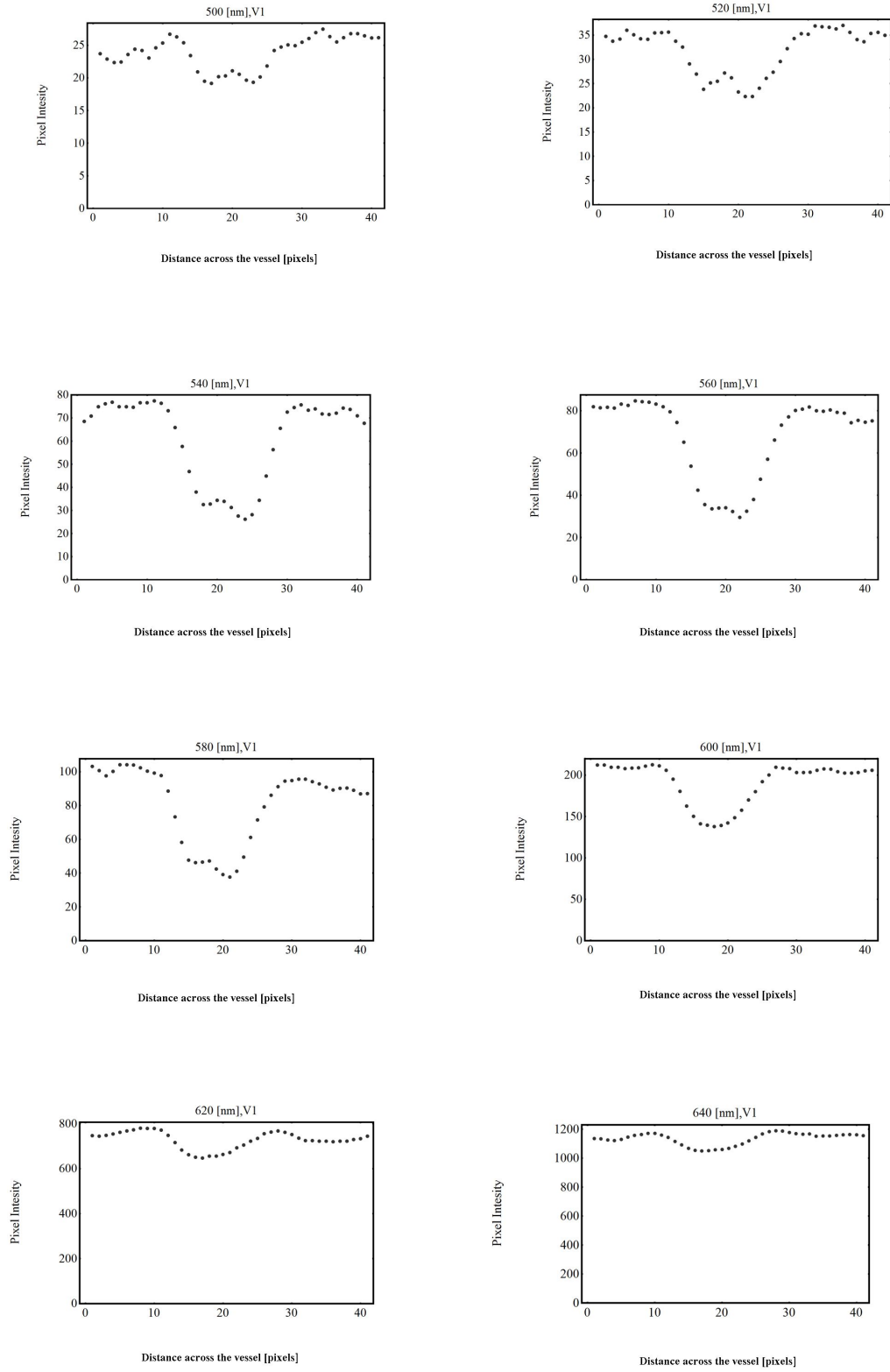


Figure 7.9: Intensity profiles obtained from retinal images at various wavelengths

7.4 Fitting transmission profiles to a model

The vessel transmittance was determined by the ratio of the intensity at the minimum of the fitted curve to the background intensity, determined from both sides of the vessel profile. For each intensity profile, linear interpolation using the intensity values on both sides of the vessel profile (see Figure 7.10) was utilized to calculate the reflected intensity in the absence of the blood vessel.

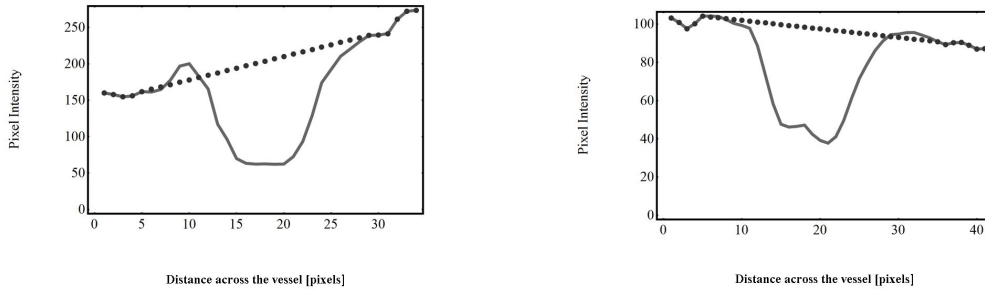


Figure 7.10: Linear interpolation from both sides of intensity profile

The transmission profile then can be obtained according to (5-1):

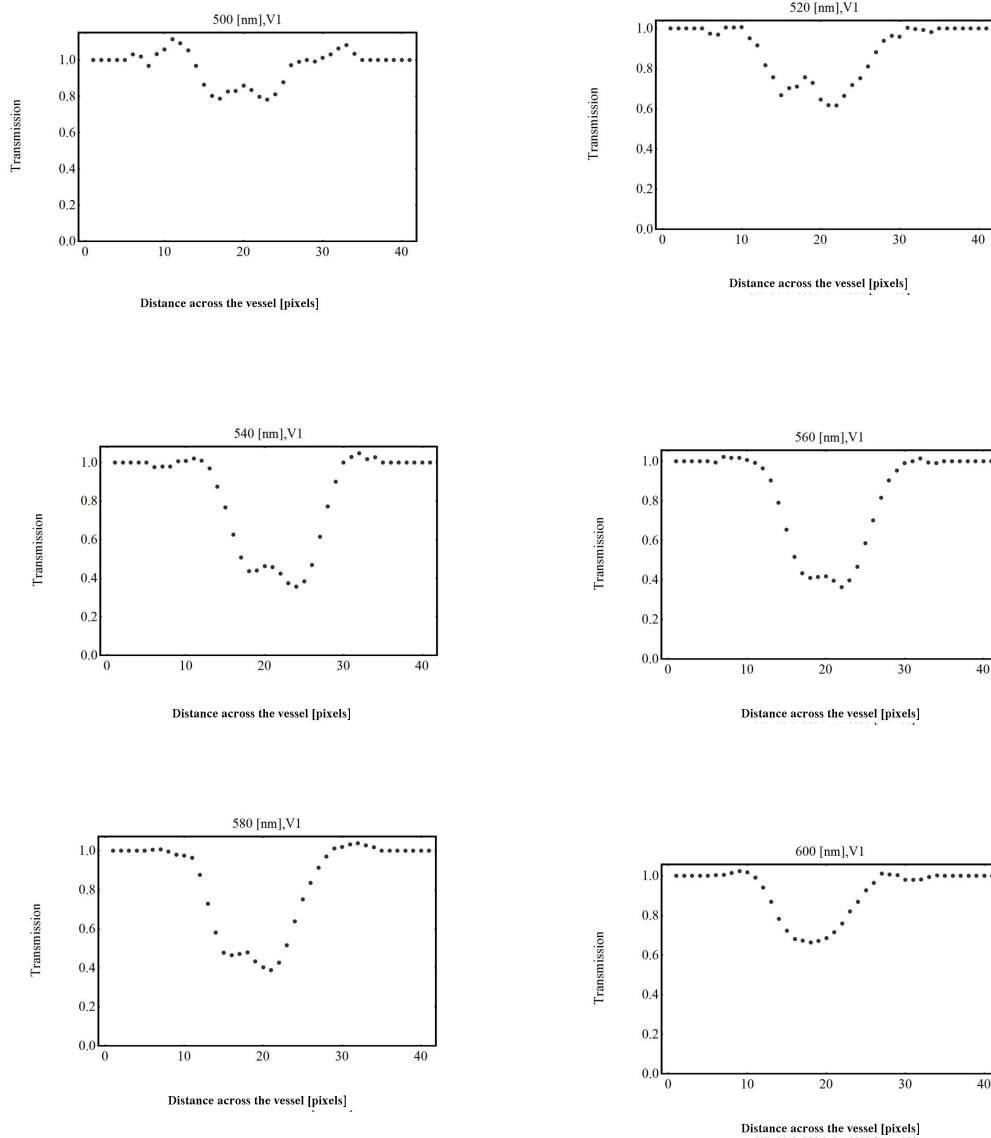
$$T = \frac{I}{I_o},$$

where I represents the intensity profile and I_o is the interpolated intensity in absence of blood vessel.

Using the intensity at both sides of the blood vessel to estimate the light that back illuminating the blood vessel depends on several factors such as tissue point spread function, vessel diameter, illumination wavelength, and fundus reflectivity. For example this is valid assumption for small vessels only and long wavelengths. However, for thick vessels and dark fundus (highly pigmented) the size of the shadow behind the vessel prevent from accurate quantification of back illuminating light. To

compensate for this effect and hence reduce the influence on oxygen saturation measurements, light transmitted through the blood vessel need to be measured independently at various vessel diameters and fundus reflectivities and compared with that estimated in reflection. A correction factor as a function of vessel diameter and fundus reflectivity can then be used.

Figure 7.11 shows various transmission profiles collected from veins and arteries and plotted as transmission against geometric distance across the vessel.



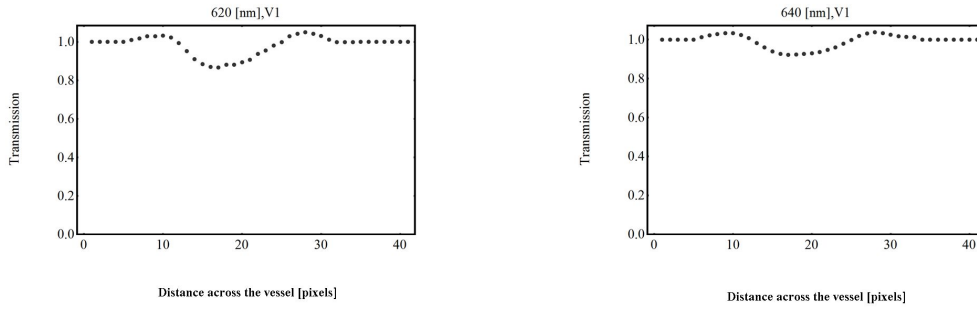


Figure 7.11: Transmission profiles

It is possible to fit a model of the transmission profile with an optimization procedure such as nonlinear least square fit, to obtain a measure of some parameters such as the transmission (or optical density) in the centre of the blood vessel and vessel diameter. A simple model for a transmission profile assumes that the change in transmission across the blood vessel is primarily due to the attenuation by haemoglobin in red blood cells. According to Lambert-Beer's law, the transmission is given as

$$I(x) = I_o \exp[-\mu_a dz] , \quad (7-5)$$

where μ_a is the attenuation coefficient of haemoglobin, x is the dimension in the plane of the retina across the vessel and z is the vessel depth. Considering μ_a as a constant throughout the vessel profile, and the blood vessel as symmetric and circular, as depicted in Figure 7.12:

$$dz = 2\sqrt{R^2 - (R-x)^2}$$

$$T = \frac{I(x)}{I_o(x)} = e^{-2\mu_a \sqrt{x(2R-x)}} , \quad (7-6)$$

where R is the radius of the blood vessel.

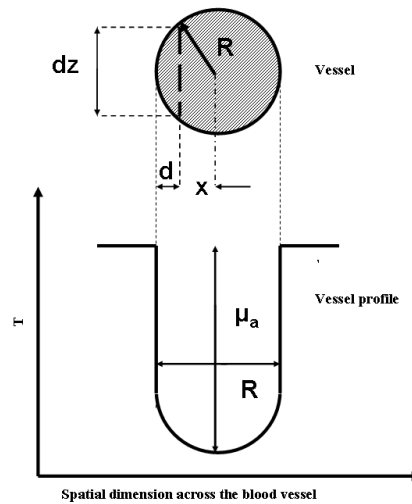


Figure 7.12: Mathematical model of a vessel

As shown previously (see Figure 7.11), some transmission profiles will exhibit a small increase in intensity in the centre of the vessel, which is believed to be due to specular reflection by the blood column. This small change in intensity appears as silver wire along the blood vessel and is more pronounced for arteries. A linear polarizer was employed in front of the detector, to attenuate the specular reflection effect (see section 3.4.2, Chapter 3). However, the remaining influence which might be due to the lens birefringence was compensated through the model profile fit (see Figure 7.13). Many models in the literature have been proposed to compensate the specular reflection by means of fitting a Gaussian function to the vessel profiles (Chaudhuri 1989). The vessel model was nonlinearly fitted to transmission profiles from both veins and arteries across the wavelength range. Figure 7.13 shows an example of fitting vein and artery profiles to the vessel model at 560 nm. Two important parameters can be estimated as an output of this fit: vessel diameter $2R$ and transmission (or optical density) at the centre of the blood vessel.

Vein profile

Artery profile

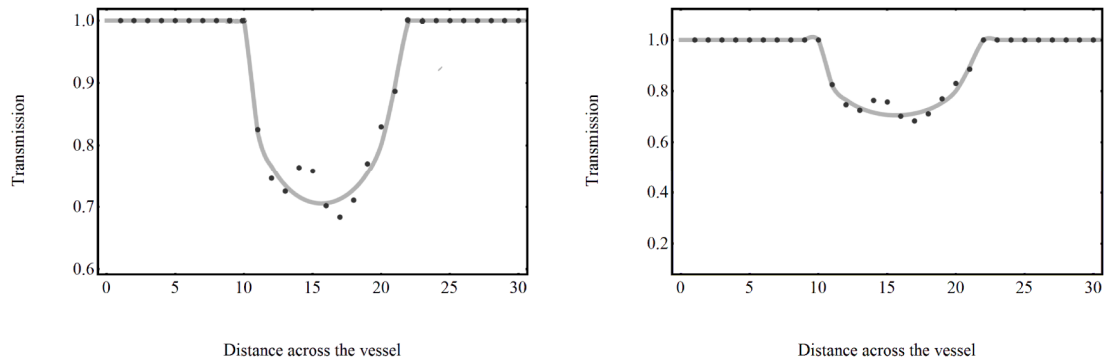


Figure 7.13: Fitting the vessel model (gray line) to the transmission profiles (black dots) of vein and artery at $\lambda=560$ nm

To assess the accuracy of the vessel model, measurements were performed by using a model eye (see Chapter 8 for more details on the model eye). The model eye provides an environment similar to the human eye in which parameters such as vessel diameter, blood concentration, and oxygen saturation can be controlled. Glass capillaries at inner diameters of 50, 100, and 150 μm were used. A pixel in the image was measured to be 10 μm (1pixel=10 μm) by introducing a calibration scale in the same plane as the glass capillaries. Figure 7.14 shows glass capillaries against a reflecting background consisting of three reflectivities (20%, 60%, and 99 %); profiles across the capillaries are also shown.

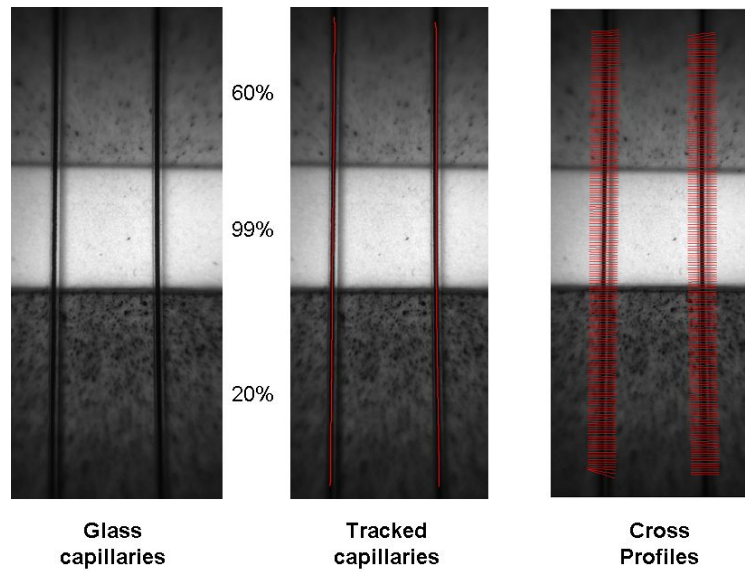
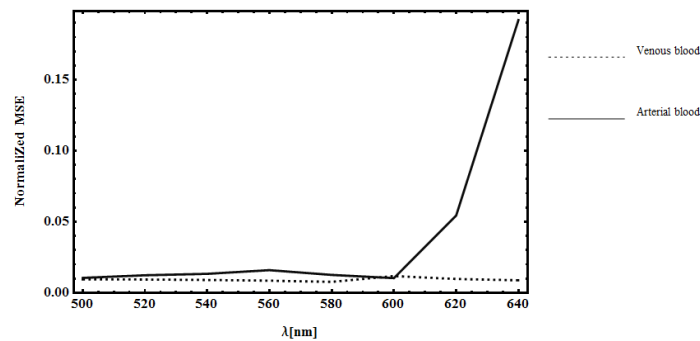


Figure 7.14: Glass capillaries tracked against a reflecting background

The accuracy of the vessel model was assessed by calculating the mean squared error (MSE) between the real profile and the fitted model (see Figure 7.13) across the wavelength range 500-650 nm. Vessels with arterial and venous blood were used. Figure 7.15(a) shows the difference between the real profile and the vessel model expressed as MSE values for arterial and venous blood. MSE values were normalized to the maximum optical density at each wavelength. Low MSE values (<0.01) were noticed, with an apparent increase at long wavelengths ($\lambda > 620$ nm) for arterial blood.



(a)

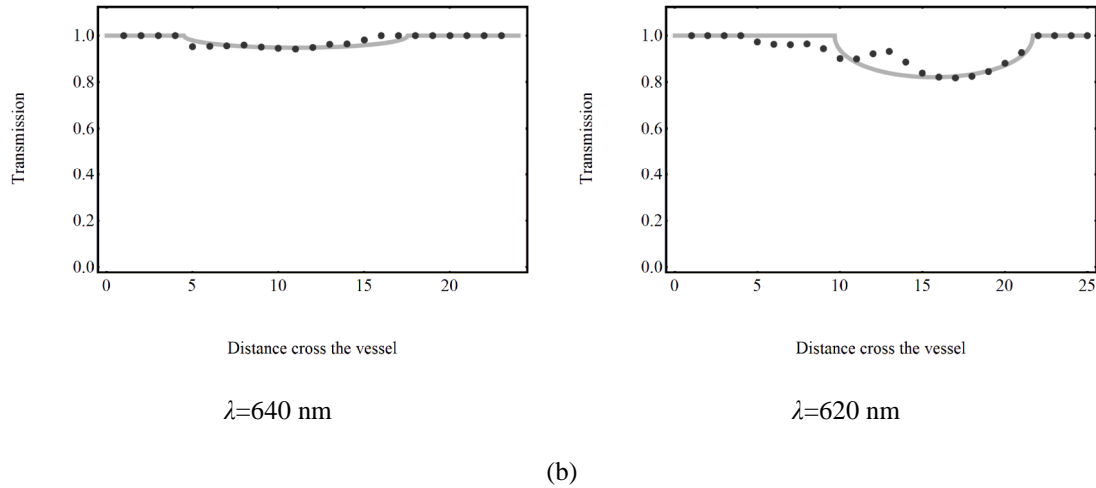


Figure 7.15: (a) MSE values between real and model profiles, (b) Fitting vessel model to vessel profiles at $\lambda=640$ nm (Left) and $\lambda=620$ nm (Right)

One explanation for the increased MSE values for arterial blood is due to the spectral properties of oxygenated haemoglobin, in which arterial blood at wavelengths $\lambda \geq 620$ nm looks translucent and permits high transmittance of light. Therefore, fitting the vessel model to such a transmission profile will encounter higher errors to converge the appropriate response (see Figure 7.15 (b)). However, the increased difference between the vessel model and the transmission profile obtained from the retinal artery is influenced by additional factors, such as the specular reflection by the blood column at the centre of the artery and the non-uniform background of the retina as light penetrates toward the choroidal layer.

The accuracy of measuring the vessel diameter was around 2 pixels or (20 μm) (vessel diameters ± 2 pixels). Figure 7.16 presents the results of calculating the diameters of three vessel thicknesses 50, 100, 150 μm . The measurements of the diameter were affected by Fresnel reflection due to refractive index mis-match as a result of using glass capillaries immersed in water. The variation in the distance between the glass capillaries and the reflective background in the model eye is an additional factor that

might increase the error in estimating the vessel diameter, in which a fixed distance ($\approx 250 \mu\text{m}$) along the glass capillary was intended (see Chapter 8).

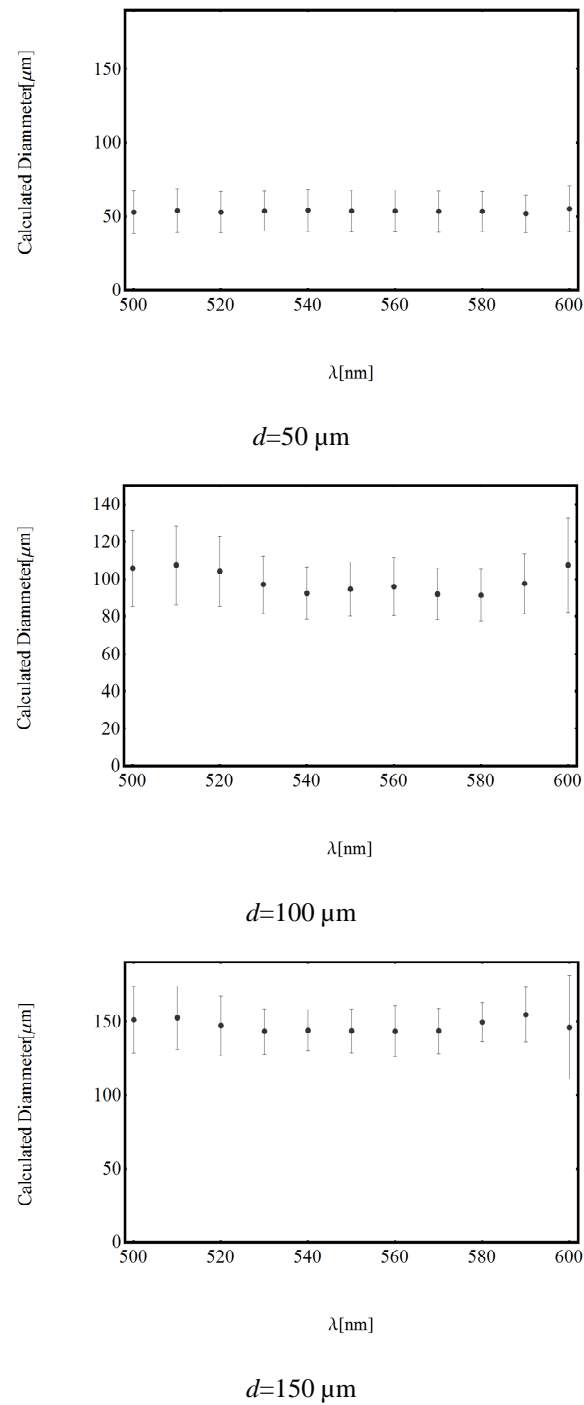


Figure 7.16: Diameter measurements obtained by applying vessel model on three glass capillaries (50, 100, 150 μm)

Hickam (1963), Delori (1988), and Beach (1999) found that their measurements of OS were dependent on vessel size. Smith and his colleagues (1998) claimed that using red

and infrared wavelength oximetry was restricted to use in retinal vessels larger than 50 μm in diameter. However, an absolute measure of vessel diameter is difficult to obtain, especially in the human eye where the variation in diameter measurements might occur throughout the cardiac cycle (Chen 1994), in addition to the difference between veins and artery, in which the internal diameter of a vein is wider than that for an artery with the same external diameter.

7.5 *Non-linear fit to a physical model*

After estimating the optical densities in the centre of the blood vessel at each particular wavelength, oxygen saturation measurement, OS , can be performed through a nonlinear fit of the physical model introduced in (5-29):

$$OD = S(\lambda) + \eta(\lambda)Cd(\varepsilon_{HBo_2}OS + (1 - OS)\varepsilon_{HB})$$

The parameters $S(\lambda), \eta(\lambda)Cd, OS$ can be estimated in the fitting process. The fitting is carried out by the application of nonlinear Levenberg-Marquardt method (Press 1990). From a given set of proper initial values for the unknown parameters, this method works iteratively to minimize a merit function, χ^2 , and to determine the best-fit parameters. Figure 7.17 gives an example showing the performance of the nonlinear fit for different spectral profiles at different oxygen saturation levels.

The extinction coefficients of oxygenated and deoxygenated haemoglobin ($\varepsilon_{HBo_2}, \varepsilon_{HB}$) were averaged over the width of the LCTF transmission bands (this will be discussed in more detail later in this chapter).

The term $S(\lambda)$ is assumed independent of wavelength and is regarded in the model to compensate for several factors which prevent giving a complete account by applying Lambert-Beer's Law, such as scattering by blood cells and the effect of the geometry of the eye. The validity of constant scattering was approved for the wavelengths that

do not experience high absorption by haemoglobin derivatives such as the green series wavelengths (520,546, and 555 nm) (Pittman and Duling 1975) range. However, further investigation of the scattering characteristics of the oxygenated blood will be introduced in Chapter 8. The multiplicative parameter $\eta(\lambda)Cd$ accounts for the effect of multi-optical paths $\eta(\lambda)$ in which single and double passages of light through the retinal vessel are possible, in addition to the light backscattered by red blood cells. The separation of $\eta(\lambda)Cd$ has proved difficult, as η is a wavelength dependent factor and haemoglobin concentration, C , varies between humans, depending on many physiological factors such as age, sex, and health. The value of η will depend on the pigment concentration within the retinal background, the vessel diameter, the cone of illuminating light. In Chapter 8 a detailed study of η behaviour will be reported.

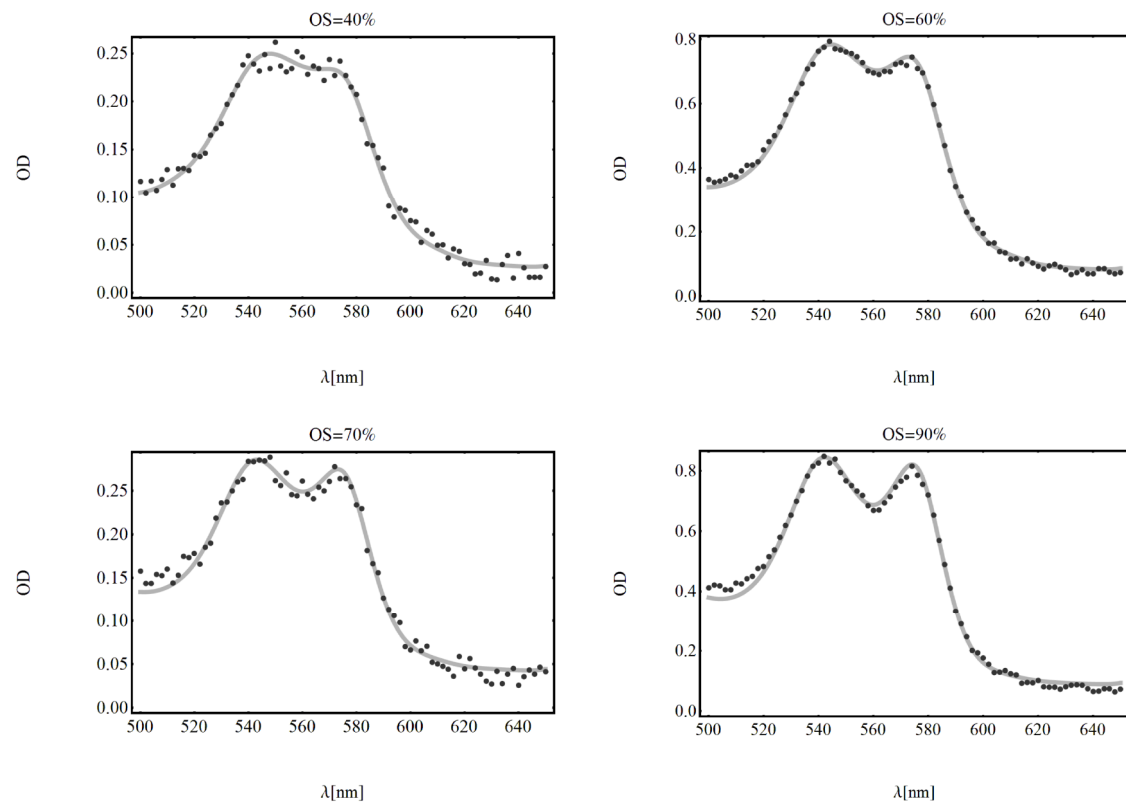


Figure 7.17: Nonlinear fit of physical model (gray line) to measured optical densities (Black dots)

7.6 Error sources and error quantification

Due to the nature of the adopted time-sequential technique, retinal spectral images suffer from illumination variation in addition to variation due to the movement of the eye. Calibration of retinal images was performed by reducing the artefact influence as explained in Chapter 3. Eye movement was corrected by applying co-registration algorithm (see Chapter 4). Extracting accurate oxygen saturation measurements from the data cube requires quantification of the possible errors that are encountered during the imaging procedure such as:

- Intensity variation between recorded retinal images and their effect on optical densities.
- The effect of background non-uniformity on optical density measurements.
- The effect of LCTF transmission band width on measured haemoglobin extinction coefficients.

The reproducibility of optical density measurements was measured to determine the sensitivity of oxygen saturation measurements to variations in illumination. Variations in illumination fall into two types: variation across the field of view of the instrument for each image, and variation through the sequence between images. These variations are due to a number of factors, including the optics of the eye, the instrument, and eye movements. The variations due to the change in light flash source were evaluated in Chapter 3 and their effect was found to be less than 2 % for all possible wavelengths (see Figure 3.11).

7.6.1 Reproducibility of optical density measurement

To assess the reproducibility of the optical densities, ten images at each wavelength were recorded in the range 500-650 nm. Registration and calibration were then

applied. Veins and arteries were tracked and the vessel model was applied on extracted transmission profiles to evaluate the optical densities in the centre of the retinal vessels, as described earlier in this chapter. Figure 7.18 presents a retinal image at 586nm, with one vessel tracked, in addition to the optical density measurements along the tracked vessel for ten repeated images.

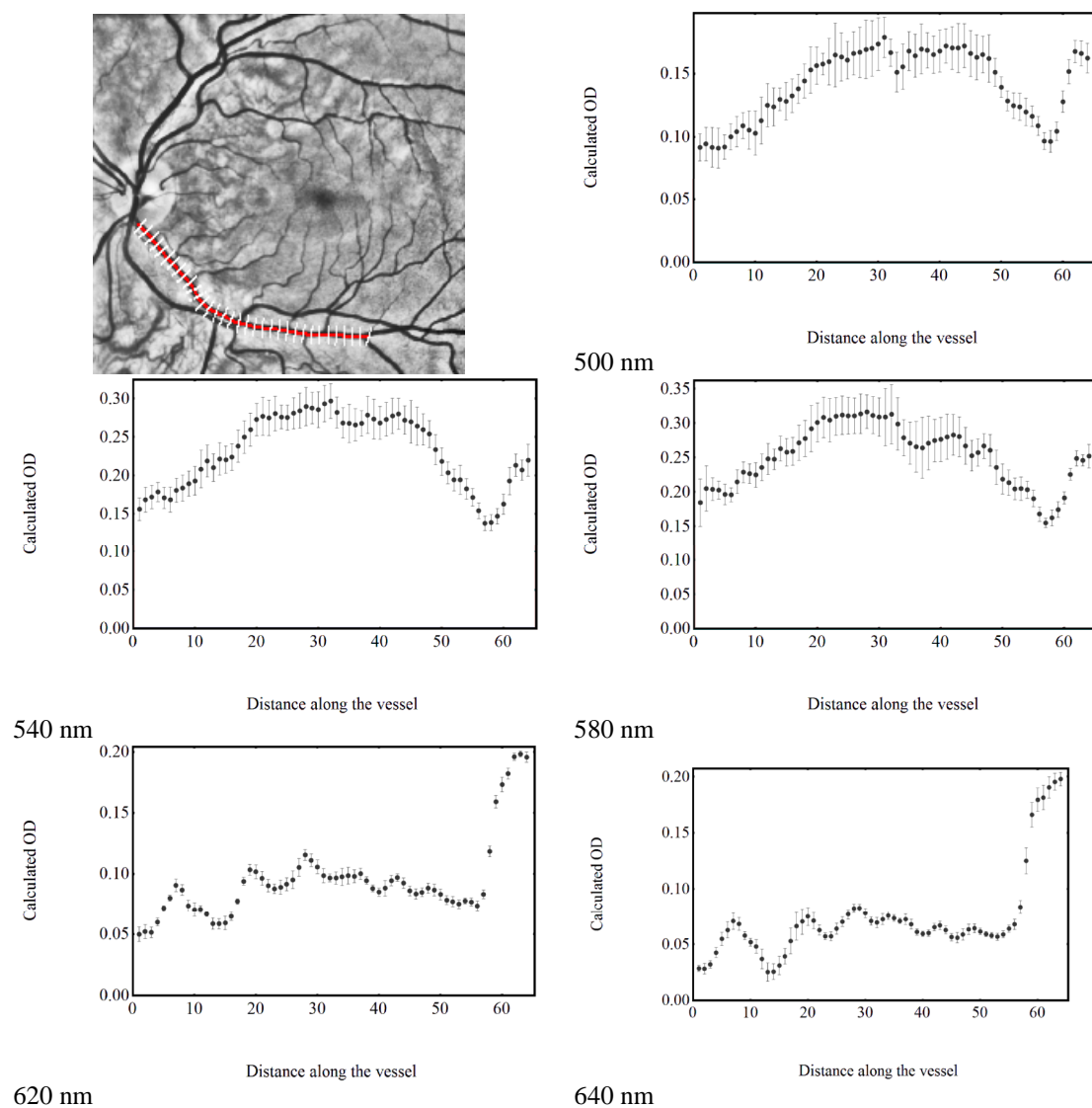
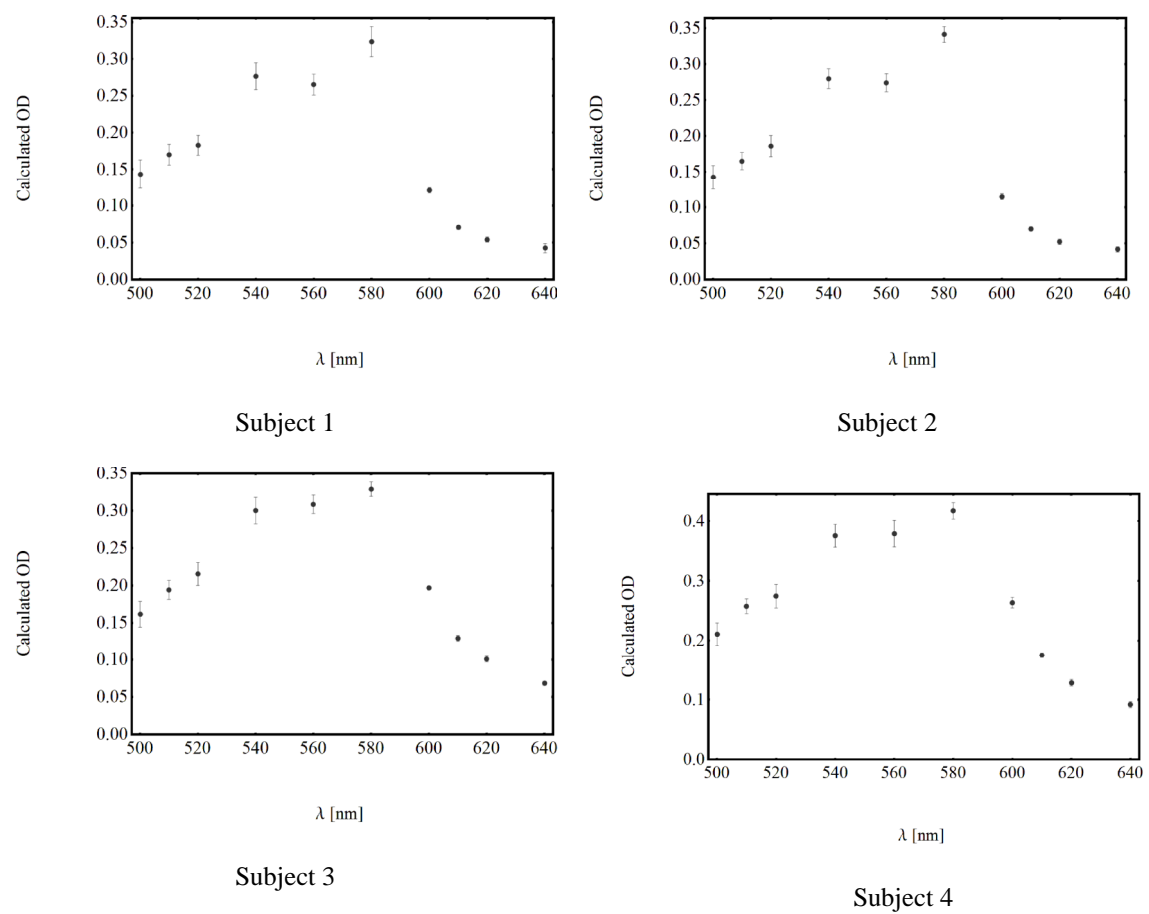
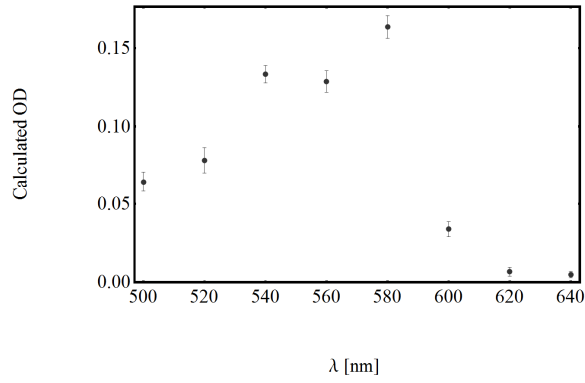


Figure 7.18: ODs along a retinal vessel for 10 repeated images

Figure 7.19 presents the repeated optical densities obtained from 5 healthy subjects through the wavelength range 500-650 nm. For each wavelength, the mean optical density of a 50 pixel section along the retinal vessel from ten repeated measurements was represented.





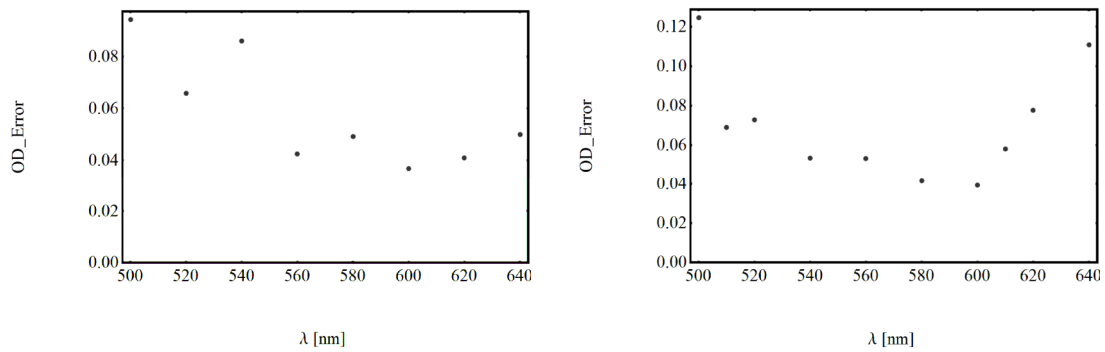
Subject 5

Figure 7.19: OD spectral profiles obtained from 5 healthy subjects.

The error in estimating the optical density along the retinal vessel is expressed as normalized standard deviation

$$OD_Error = \frac{SD[OD_n]}{Mean[OD_n]}; n=1, 2, \dots, 10. \quad (7-7)$$

The average normalized standard deviation OD_Error at each wavelength and along the retinal vessels is shown in Figure 7.20. Generally, OD_Error of about 8% was estimated for most wavelengths with an exception for optical densities at short and long wavelengths 500, 640 nm respectively, which encountered higher error up to 12% in the worst case. A value of 8% of the measured optical densities led to a maximum error in transmission of about ($\Delta T=0.026$) for a typical vessel diameter ($100\ \mu m$) filled with arterial blood ($OS=0.99$) when single pass was assumed.



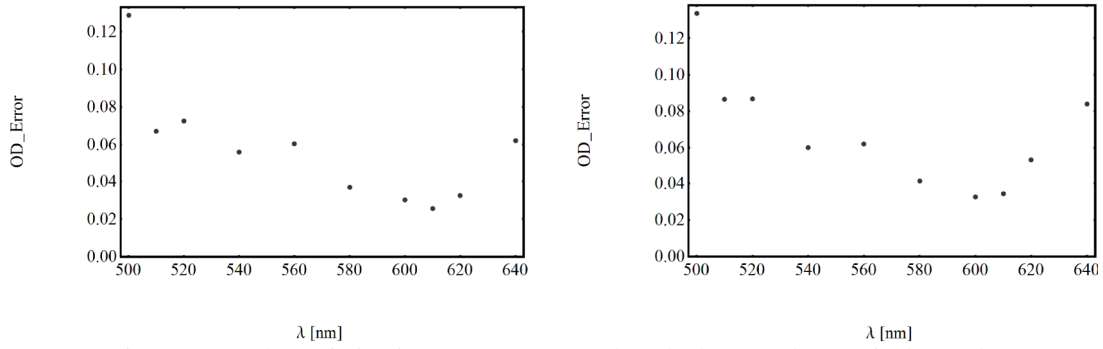


Figure 7.20: The variation in OD error as wavelength changes along retinal vessels

In the previous chapter, it was shown that an absolute transmission error ($\Delta T=0.01$) resulted in a small calculated saturation error $\Delta OS \ll 1\%$ for various combinations of vessel diameters and oxygen saturation levels. The saturation error due to $\Delta T=0.026$ is shown in Figure 7.21. As depicted in the figure, low saturation error ($<1\%$) is still possible when wavelengths are sampled at 2 nm. However, when wavelengths are sampled at 10 nm for 50 μm capillary size, a saturation error of value ($\Delta OS \approx 1\%$) is reported. Increased saturation errors of ($\Delta OS \approx 14\%$; $\Delta OS \approx 10\%$) were reported for two and three wavelengths combinations.

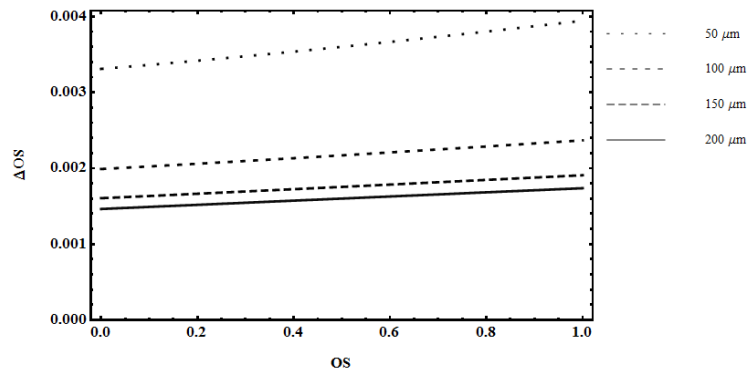


Figure 7.21: The saturation error for $\Delta T=0.026$

7.6.2 The effect of background non-uniformity on optical density measurements

Variation of optical density measurement along retinal vessels is due to:

- Spatial variation in illumination.

- Spatial variation due to the local distribution of the melanin pigment, in addition to other texture effects.

Figure 7.22 shows a representative retinal image recorded at 586 nm, profiles along one side of the blood vessel are also plotted.

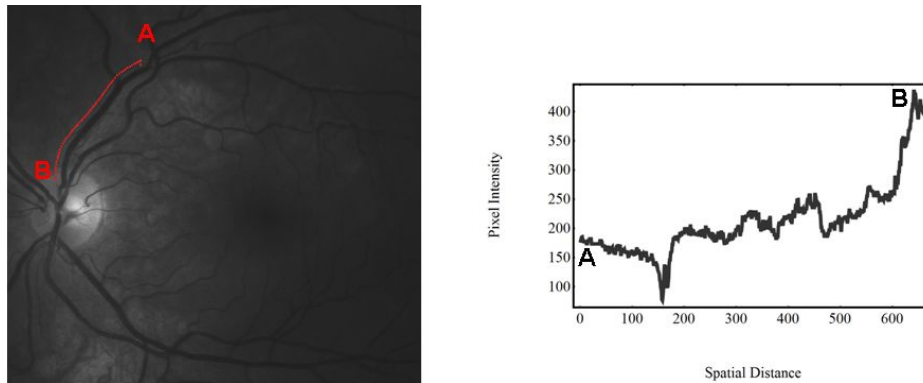


Figure 7.22: (Left) Retinal image at 586nm; (Right) A profile along one side of vessel

It is important to investigate the contribution of melanin on the spectral profiles obtained from the centre of retinal blood vessels and how the variation of melanin concentration along the vessel could affect the optical density measurements. The absorption spectrum of melanin decreases monotonically as wavelength increases (see Figure 5.3). This signature can affect the spectral profiles of the blood vessels as explained in Figure 7.23, which represents a spectral profile of oxygenated blood in the presence of melanin calculated according to Lambert-Beer's Law in a 100 μ m vessel.

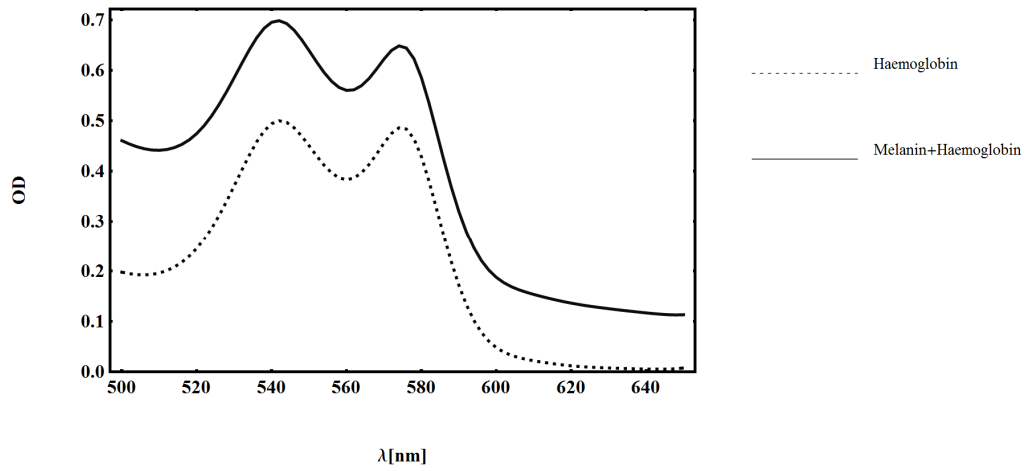


Figure 7.23: Spectral profiles in OD space with and without the presence of melanin

To understand the variation between optical density profiles due to the change in spectral response of each chromophore (oxygenated and deoxygenated haemoglobin and melanin) and the contribution of other factors, such as illumination variation, principle component analysis was applied on the spectral profiles along the blood vessel tree. The number of the largest Eigenvalue was used to define the dominant spectra contributing to the overall optical density profiles. Two data sets (spectral profiles) were calculated: the first set contained spectral profiles of various retinal vessel diameters (50, 100, and 150 μm) with various oxygen saturation levels, ranging between (0.5 -0.99 %). In the second set, the spectra of melanin (Jacques 1996) was added to the spectral profiles at various absorption coefficients ranging between ($9.7 \cdot 10^7$ - $9.7 \cdot 10^8 \text{ cm}^{-1}$). Optical densities for each wavelength in the range 500-650 nm were then calculated according to Lambert-Beer's Law, when the haemoglobin concentration was assumed 15 g/dl (for a normal subject). Figure 7.24 shows spectral profiles from both sets at different diameters and different oxygen saturation levels.

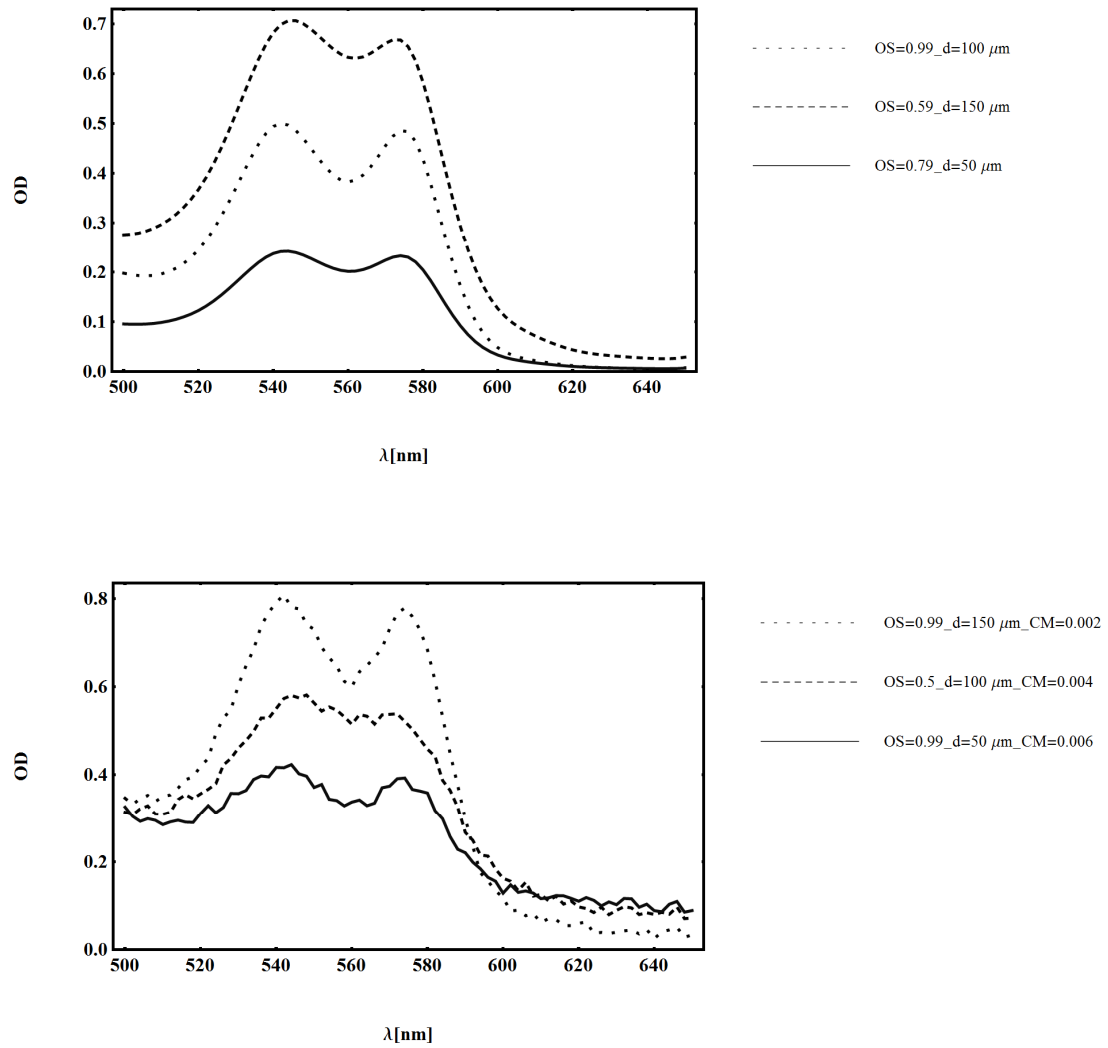


Figure 7.24: Spectral profiles from the first set (above) and the second set (below).

For the first set, two Eigenvectors were significant to represent data variation as shown in Figure 7.25, which accounts for the spectra of oxygenated and deoxygenated haemoglobin (note that the first principle component was not shown, as the graph was scaled to show the principle components which account for low variance in the data set). However, when melanin was present, three principle components have to be considered, in which two principle components were assigned to the spectra of oxygenated and deoxygenated blood and the third component accounts for the melanin spectrum.

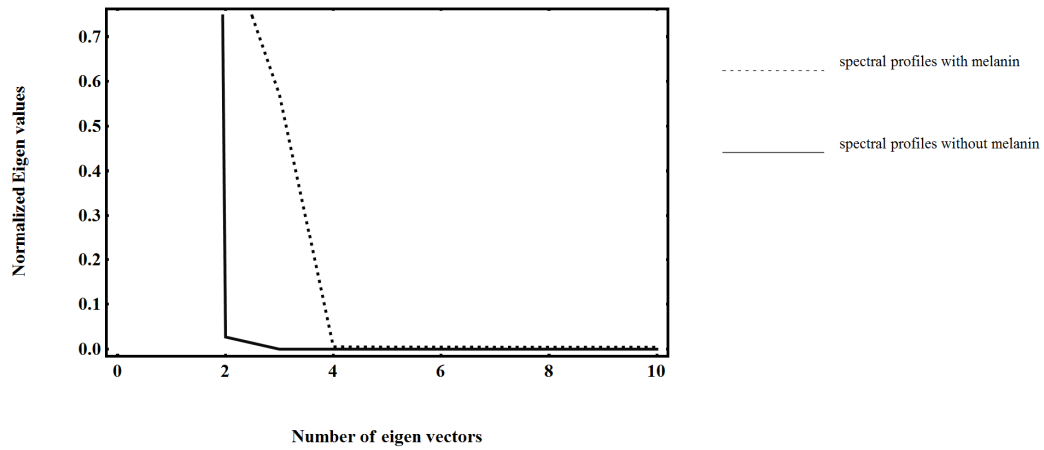


Figure 7.25: Eigen values from two sample sets with and without melanin effect

As explained in Figure 7.26, a significant error in reconstructing the optical density profiles from only two principle components was reported. Optical density profiles were retrieved more accurately when three principle components were used.

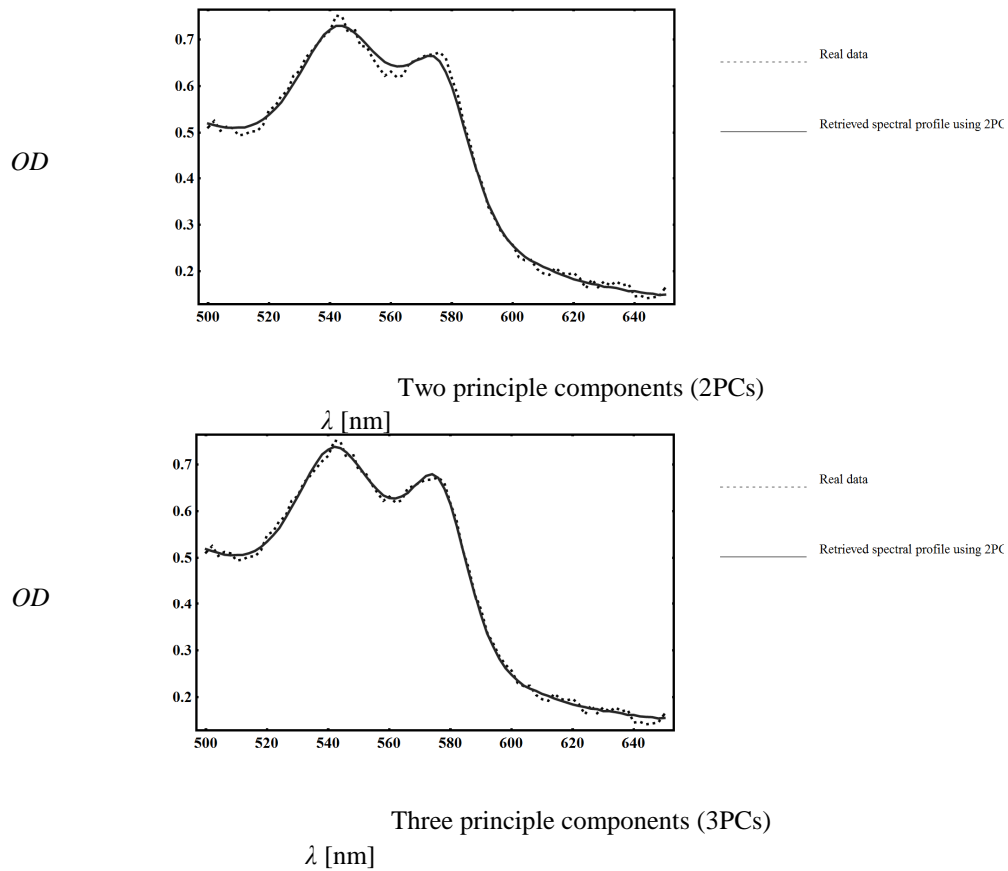


Figure 7.26: The original spectral profile and retrieved spectral profile when 2PCs (above) and 3PCs (below) were used

Principle component analysis was applied on spectral profiles measured from human retinas. Normalised Eigenvalues of these spectral profiles from two healthy subjects are presented in Figure 7.27 and Table 7.1. The analysis results showed that the spectral profiles were dominated by the absorption coefficient of oxygenated and deoxygenated haemoglobin in which the melanin effect can be ignored as long as the measurements were taken along the retinal vessels. However, the contribution of the third principle component is expected to be more significant for subjects with a high concentration of melanin.

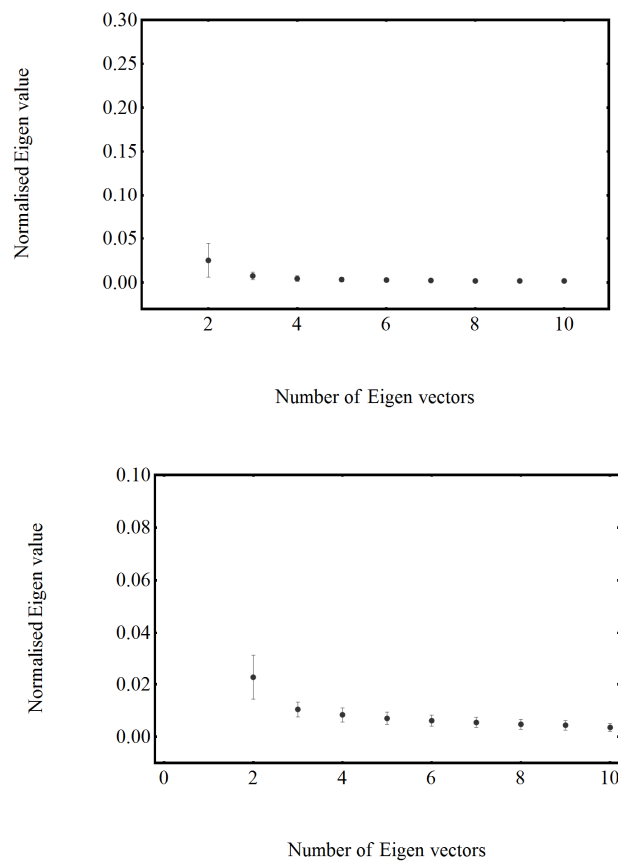
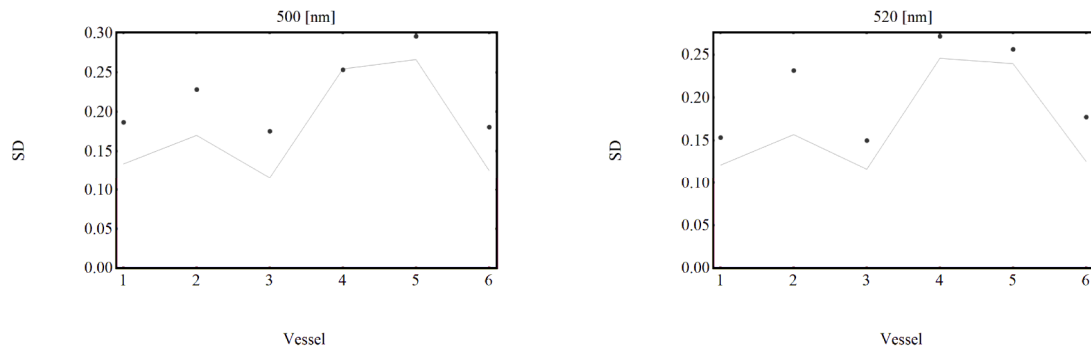


Figure 7.27: Normalised Eigenvalues obtained from applying PCA to spectral profiles of two healthy subjects

	PC1	PC2	PC3	PC4	PC5	PC6	PC7	PC8
N.Mean	0.927	0.025	0.007	0.004	0.003	0.002	0.002	0.002
N.SD	0.042	0.019	0.004	0.001	0.003	0.002	0.002	0.001

Table 7.1: The mean and standard deviation of normalized Eigenvalues of spectral profiles of healthy subjects

The principle component analysis was then used as a tool to minimize the effect of variation in measuring *ODs* along blood vessels. The first two principle components, *1PC* and *2PC*, were used to represent the most significant variation in the spectral profiles. To evaluate the influence of applying PCA on spectral profile, the standard deviations of the measured optical densities along each vessel were compared with those calculated by using only two PCs. Figure 7.28 shows the analysis results at various wavelengths across the vessel tree of healthy subject. As can be noticed from the figure, the variations in optical density measurements due to local variation in melanin concentration, retinal background, and illumination are minimized. It is also noted that the variations of *OD* measurements at short wavelength ≤ 540 nm and at long wavelength ≥ 590 nm are minimized significantly compared with those in the range 540-590 nm. These differences are due to the strong absorption by melanin at $\lambda \leq 540$ nm, in addition to the texture of the retinal background at $\lambda > 590$ nm as light penetrates towards deeper layers (the choroidal layer).



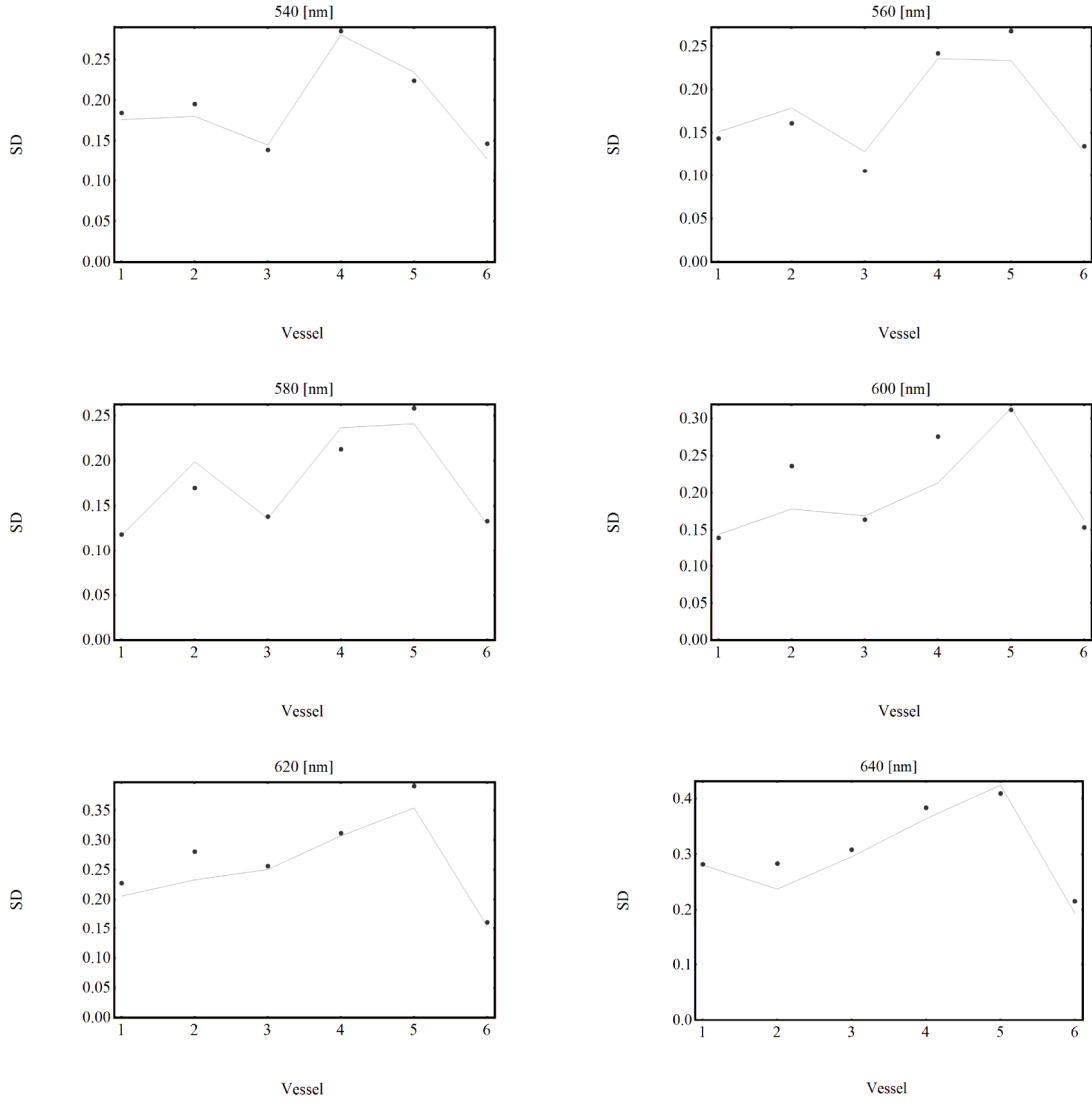


Figure 7.28: The standard deviation along retinal blood vessels before (black dots) and after (gray line) applying PCA

7.6.3 The effect of finite bandwidth of LCTF transmission bands

The calculation of OS using the optical model requires, in addition to optical density measurement, a knowledge of the specific extinction coefficients of oxygenated and deoxygenated haemoglobin $\epsilon_{HbO_2}, \epsilon_{Hb}$ respectively. The extinction coefficients are well known from the literature, with a spectral resolution 0.1 nm (Assendlft 1970). To apply the optical model based on the modified Lambert-Beer Law, the bandwidth of the LCTF transmission bands should be taken into account and hence, modifications

to the extinction coefficients are needed. Our instrument illuminates the retina with monochromatic light with finite bandwidth. As was discussed in Chapter 3, the FWHM bandwidth of LCTF spectral bands is about 10 nm but varies with the wavelength. The measured transmission of a column of blood, accordingly, for light in the range λ_1, λ_2 , is thus given by

$$T' = \frac{\int_{\lambda_1}^{\lambda_2} I_o(\lambda) F_\lambda e^{-cd\varepsilon(\lambda)} d\lambda}{\int_{\lambda_1}^{\lambda_2} I_o(\lambda) F_\lambda d\lambda}, \quad (7-8)$$

where $\varepsilon(\lambda)$ is the monochromatic extinction coefficient of oxygenated or deoxygenated haemoglobin (Assendlft 1970), F_λ is the spectral distribution corresponding to each wavelength λ , $I_o(\lambda)$ is the incident light. The above equation shows that for measurements in a waveband λ_1 to λ_2 , under conditions where $\varepsilon(\lambda)$ is not constant, the source wavelength dependency will also have an effect. Normally the most important effect is that $\varepsilon(\lambda)$ is varying over λ_1 to λ_2 .

Accordingly, The averaged extinction coefficient ε' is

$$\varepsilon' = \frac{1}{cd} \log \frac{\sum_{\lambda_1}^{\lambda_2} F_\lambda 10^{-cd\varepsilon} \Delta\lambda}{\sum_{\lambda_1}^{\lambda_2} F_\lambda \Delta\lambda}. \quad (7-9)$$

A maximum difference $\Delta\varepsilon = |\varepsilon - \varepsilon'|$ was measured at 577nm, in which the averaged extinction coefficient was 7% lower than the extinction coefficient measured by Assendlft (1970) at 0.1 resolution. This difference resulted in transmission error $\Delta T = 0.024$ for a typical vessel diameter (100 μm). The expected saturation error ΔOS was calculated and presented in Figure 7.21 for various vessel diameters and

saturation levels. The maximum saturation error was of value 0.004 for oxygenated blood and a 50 μm vessel.

7.7 Conclusion

It has been shown in this chapter that quantitative oxygen saturation measurements from retinal spectral images were obtained by calculating the optical densities locally. The calculation of the optical density along blood the vessel tree required employing a vessel tracking algorithm to extract the centre line of the retinal vessels. When the coordinates of the centre line were obtained, intensity profiles perpendicular to the retinal vessel were measured. Transmission at the centre of blood vessel was then calculated by applying a non-linear fitting to a model of geometric variation in transmission. Variations in optical density along the retinal vessel tree and between retinal images, due to illumination variation and melanin pigmentation, were investigated. The reproducibility of optical density showed an 8% error at each particular wavelength in the range 500-650 nm. The results of applying *PCA* on spectral profiles obtained from healthy subjects showed that the melanin contribution was small enough to be ignored. Two principle components were used to represent the most dominant spectra existing in the spectral profiles: the spectra of oxygenated and deoxygenated haemoglobin. The effect of the finite bandwidths of the LCTF filter was also considered, to study the influence on the averaged extinction coefficients. A maximum error of 0.024 in transmission was reported at 577 nm.

So far in this chapter, we have explained the main sources of error which influence accurate quantification of oxygen saturation measurements. In the following chapter validation results of applying the developed algorithm will be presented using a model eye. Oxygen saturation along glass capillaries will be calculated and compared with

gold-standard measurements performed by CO-Oximeter. The investigation of scattering and optical path factor will be presented.

Chapter 8

Model eye

In this chapter we describe the design, construction and use of an artificial eye to assess and validate our spectral imaging technique as a tool for blood oximetry of the retinal vessels. Arterial and venous blood from human subjects was analyzed using a CO-Oximeter to establish measured oxygen saturation, and then imaged in an artificial eye using our hyperspectral retinal camera. As the components forming the eye differ in refractive indices, ray retracing was used to aid in understanding of light propagation in the artificial eye. For comparison, a ray-tracing simulation for real blood vessels was also implemented. We show how the application of the physical model to the optical densities of the spectral images allows the calculation of the scattering and multiple optical path parameters, which are critical for accurate quantification of blood oxygenation. Finally, we report the results obtained for blood capillaries with a range of blood-oxygen saturations, haemoglobin concentrations and diameters, mounted in front of backgrounds of various diffuse reflectivities.

8.1 Background

The artificial eye offered a well controlled environment in which critical parameters such as vessel diameter, haemoglobin concentration, blood oxygenation and the degree of pigmentation can be varied to evaluate the accuracy of our blood oximetry technique.

Several attempts have been made by many researchers to build an environment similar to the human eye either by building an artificial eye or by utilizing the optics of animal eyes. For example, a model eye was built and used to measure the actual size of fundus features from images obtained by two fundus cameras (Rudnicka 1992). Rakebrandt (2003) built and evaluated an artificial eye for investigating laser tissue interaction in scanning laser ophthalmoscopy as well as for determining the accuracy of measuring retinal structure using optical coherence tomography. Norren et al, (1986) deduced the reflectance factor of the different parts of the retina by employing an artificial eye and a densitometer to calibrate the spectral output. Additionally, artificial eyes have also been produced as a means of validating and evaluating an optical model for blood oximetry. For example, Smith suggested a model eye in which human blood of known oxygen saturation was introduced into glass pipettes and a confocal scanning laser ophthalmoscope was used to measure the oxygen saturation (Smith et al. 2000; 2001, Denninghoff 2000). Other researchers (Khoobehi 2004) employed less controlled environments, such as eyes from animals, to assess their spectral processing algorithms for calculating oxygen saturation maps in the optic nerve head.

The main guideline driving the design of the artificial eye was to test the robustness of the optical model when variations in vessel diameter, blood oxygenation, and fundus reflectance occur by reproducing, as closely as possible, the conditions met in the real eye.

8.2 Construction of the artificial eye

The human eye is a complex structure composed of numerous parts (see chapter 2). A schematic cross section of the eye is shown in Figure 8.1.

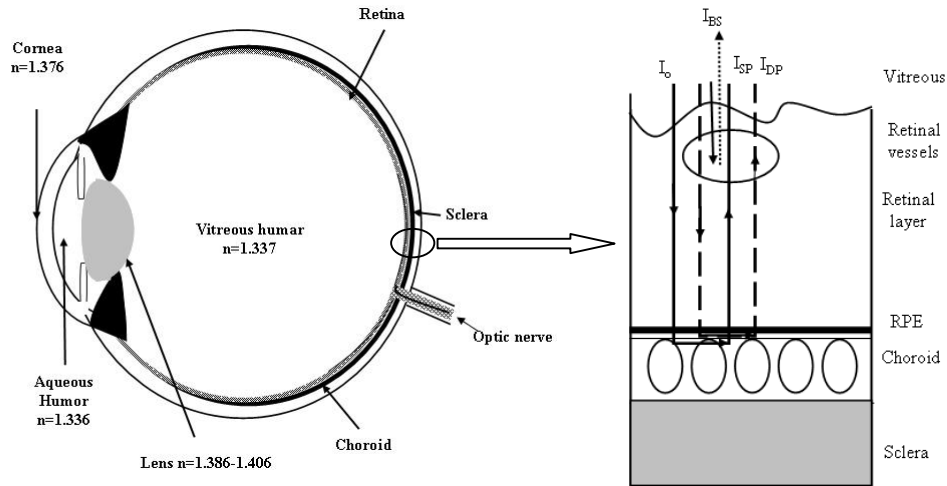


Figure 8.1: Left, diagram of human eye; Right, light paths through the fundus layers

We have explained previously that light incident on the eye passes through the cornea, the aqueous humour, the lens, the vitreous humour and onto the fundus, where only a fraction of it is diffusely reflected and exits the pupil. The amount of light exiting the eye is determined by the absorbing properties of the fundus since the refracting elements of the eye can be considered transparent in the visible and near infrared spectra. The ocular fundus consists of four main layers with distinctive optical characteristics: the retina, the pigment epithelium, the choroid and the sclera. The retinal layer, as has been explained previously, (see chapter 2) contains the visual receptors, several types of nerve cells, blood vessels and supporting tissue.

The artificial eye has been built with the intent of simulating the optical properties of the eye optics, the ocular fundus and the retinal vessels. A diagram of the manufactured model eye is shown in Figure 8.2.

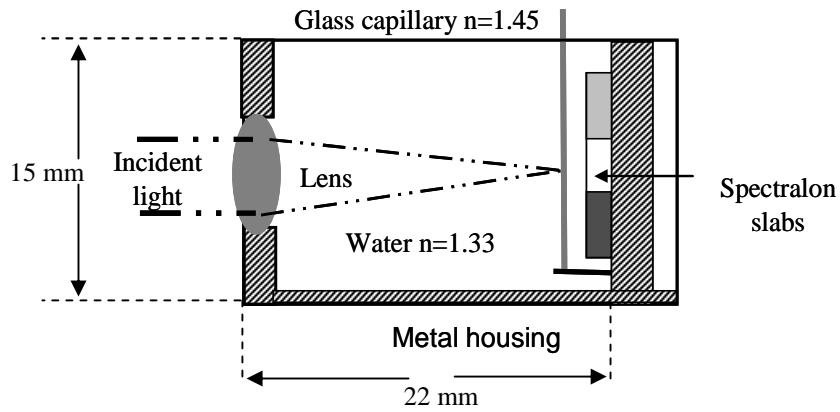


Figure 8.2: Diagram of the cross-section of the model eye.

The combined optical power of the cornea and crystalline lens is replicated by a doublet convex achromatic lens (Thorlabs AC080-016-A1) accommodated in the front surface of the metallic housing representing the eyeball. In air, the doublet lens has a focal length of 16mm, although when the artificial eyeball is filled with water so as to model the vitreous humour, the focal length becomes approximately equal to the typical image focal length of 22mm of the human eye.

The most common blood vessel diameters found in the human retina were simulated using micro-capillaries (VitroCom Inc.) with inner diameters of 50, 100 and 150 μm and outer diameters of 80, 170 and 250 μm , respectively. These micro-capillaries were made of fused silica with refractive index $n=1.4585$ at $\lambda=587.6\text{ nm}$. The wall of the micro-capillary operates as a cylindrical lens whose optical power needs to be attenuated in order to achieve a realistic eye model. Water ($n=1.33$) was used to fill the mechanical housing and provide a coupling medium to attenuate the effect of the refractive index mismatch of the silica capillaries and lens. There was still, however, a residual refractive index discontinuity in the capillary-water boundary which gave rise to a significant focusing effect. This residual optical power and its implications on the measurements obtained in the artificial eye are analysed in more detail below. The refractive index mismatch of glass capillaries can be minimized by using a material

which has a refractive index close to water and blood such as *FEP* (Fluoro Ethylene Propylene).

The layers and pigment concentrations of the fundus were simulated by a single artificial layer of Spectralon (Labsphere, Inc.). Spectralon is a spectrally neutral material available in a broad range of diffuse reflectances. Spectralon with 20%, 60% and 99% reflectances have been selected to simulate the effect of the different reflectivities across the eye fundus. A picture of the artificial fundus is displayed in Figure 8.3.

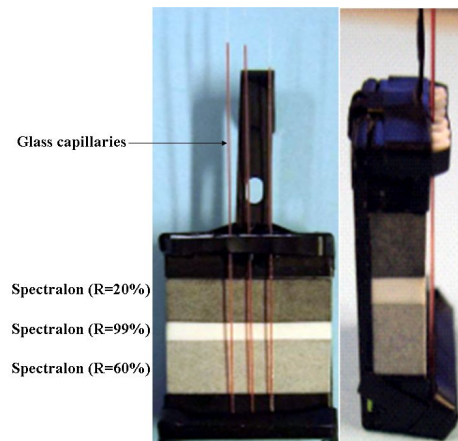


Figure 8.3: Holder of the artificial fundus, front view (left) and side view (right). It consists of three Spectralon slabs (20%, 60%, 99% reflectance) behind blood-filled fused-silica capillaries. The distance between the capillaries and the slabs is approximately 250 μm .

The Spectralon slabs were positioned at an adjustable distance of about 250 μm behind the capillaries in order to reproduce the typical distance between the retinal vessels and the retinal pigment epithelium. By mounting a rectangular slab of each type of Spectralon in the holder, we can study the influence of the variation of the fundus pigmentation along the blood capillary upon the accuracy of our oximetry algorithms, multiple light paths through blood capillary, and tissue point spread function. The

artificial fundus was positioned so the capillaries lie in the image focal plane of the lens. Figure 8.4 shows a photograph of the model eye construction.

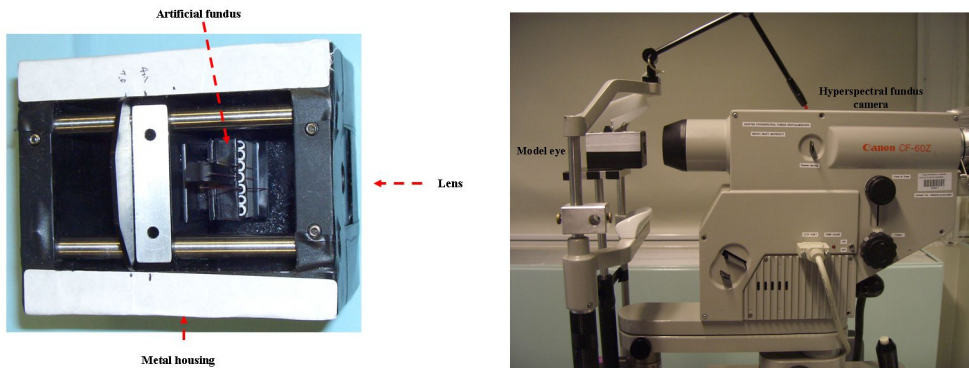


Figure 8.4: Model eye construction.

8.3 *Experimental set-up and acquisition of spectral images*

The capillaries were filled with human blood drawn from donors according to a protocol approved by an internal review board at Cheltenham Hospital NHS, (Cheltenham, UK). Blood was extracted using anti-coagulating syringes, to prevent blood-clotting during the measurements and each sample was analysed by an electrical CO-Oximeter (Gem Premier 4000) to measure the oxygen saturation and haemoglobin concentration. The readings from the CO-Oximeter are used as the gold standard for validating the oxygen saturation values obtained with our spectral imaging technique. The capillaries were filled with blood from the syringe, avoiding any contact with air, then sealed and re-positioned in the artificial fundus holder. Arterial and venous blood from ten subjects were analysed using the CO-Oximeter to enable oxygen saturation and haemoglobin concentration measurements. The range of CO-Oximeter readings for oxygen saturation and haemoglobin concentration across the blood samples are provided in Table 8.1.

Oxygen saturation (OS)	Haemoglobin concentration (C_{HBtotal})
$30\% \leq \text{OS} \leq 99.6\%$	$8.05 \text{ g/dl} \leq C_{\text{HBtotal}} \leq 18.5 \text{ g/dl}$

Table 8.1: The oxygen saturation and haemoglobin saturation obtained by the CO-Oximeter.

The acquisition of the spectral data was achieved by placing the model eye containing the blood capillaries in the object plane of our spectral retinal camera to record images from 500nm to 650nm in 2nm increment. Images were then calibrated to correct for the artefacts resulting from reflections on the surfaces of the optical components as well as electronic effects from the CCD (see section 4.2, chapter 4). From the calibrated spectral data cube, optical densities were calculated following the procedures explained in Chapter 7, which included capillary tracking and optical density calculation. Calibrated spectral images of the model eye at four wavelengths with arterial and venous blood in 150- μm capillaries are shown in Figure 8.5.

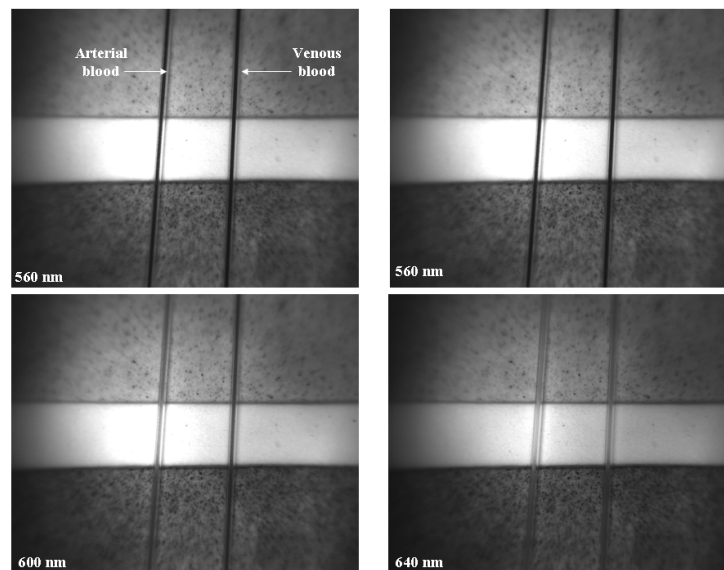


Figure 8.5: Calibrated spectral images at 580nm (left) and 620nm (right) of two 150- μm capillaries filled with arterial blood (left capillary) and venous blood (right capillary).

It can be observed how arterial blood becomes increasingly translucent at wavelengths longer than 600 nm.

Specular reflections due to the refractive index discontinuity between the inner capillary wall and blood and the outer capillary wall and water were attenuated by

illuminating the artificial retina with vertically polarized light and by recording the images through a horizontal analyser, as illustrated in chapter 3 (see section 3.4.2, chapter 3). The intensity profile of the capillary containing fully oxygenated blood imaged at $\lambda=580\text{nm}$ is displayed in Figure 8.6 (left).

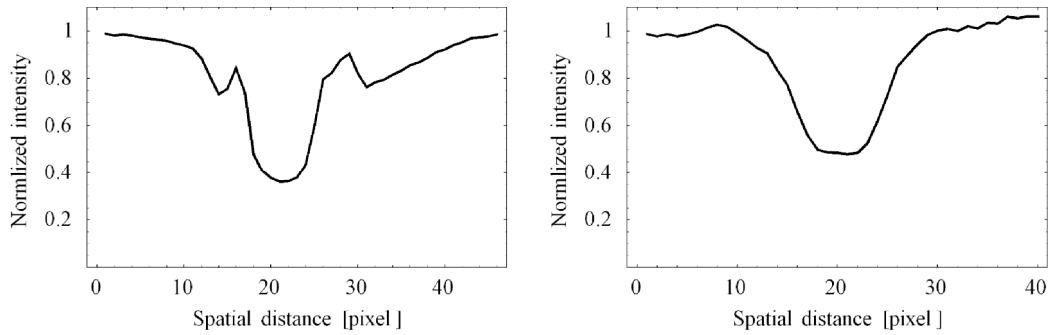


Figure 8.6: Measured profile (left) of 100 μm fused-silica capillary filled with 100% oxygenated blood in the model eye (right) of retinal artery imaged at 580 nm.

The reflectance of the Spectralon behind this capillary section was 99%. The background intensity was significantly more uniform than the actual intensity recorded from the fundus of the human eye. In the real eye, the fundus appeared highly irregular due to local variations in retinal pigmentation and the presence of structure in deeper layers (the choroidal layer) for wavelengths greater than 600nm. Note also in Figure 8.6 (left) that the profile includes two distinctive intensity peaks. These were caused by the residual lens effect produced by the slight refractive-index mismatch at both capillary-water and capillary-blood boundaries. This systematic shape occurred in all the capillary profiles acquired with the artificial eye as opposed to those from real blood vessels in the human retina (see Figure 8.6 (right)).

8.4 Ray-tracing simulation of the artificial eye

The optical software *ZEMAX* (*ZEMAX* Development Corporation, USA) has been used to validate the capillary profiles obtained in the experiments and simulate the light propagation in the artificial eye.

Non-sequential ray-tracing in *Zemax* allows visualisation and understanding of the light propagation in the artificial eye as well as a means to mimic the experimental data recorded with the spectral camera.

The implementation of the components of the artificial eye in *Zemax* was a straightforward procedure: the lens was available in the lens catalogue as well as the other optical surfaces (cylinder) and materials (water, blood and fused silica). Oxygenated blood was modelled using the *Zemax* model for water, with a modified absorption spectrum to match the spectrum of fully oxygenated haemoglobin as calculated by Assendelft (1970). No scattering was considered within the blood column. The Spectralon with 99% diffuse reflectance was simulated by employing the *Zemax* scattering model of a Lambertian surface. A layout of the *Zemax* model with annular illumination is shown in Figure 8.7 (top).

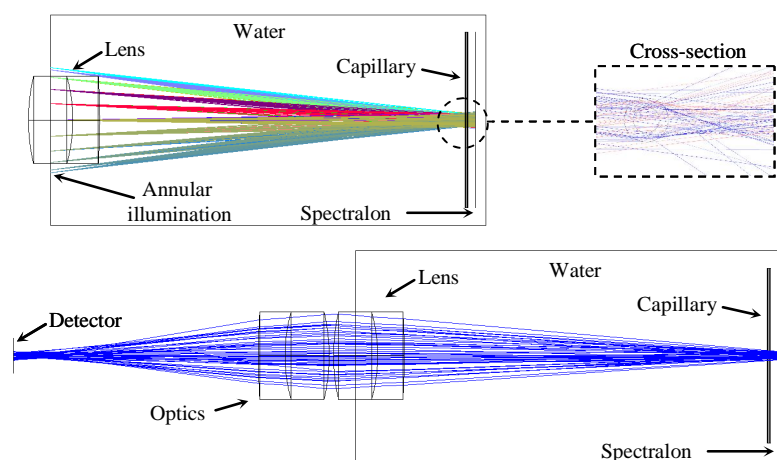


Figure 8.7 (Top) *Zemax* simulation of the artificial eye with annular illumination. Note the optical power of the capillary. Scattering from the Spectralon surface has been disabled for display purposes. (Bottom) Light exiting the artificial eye is collected by the optics of a retinal camera and focused onto a detector.

Light rays transmitted through the capillary were scattered by the Lambertian surface out of the eye, where the optics of a retinal camera focused it onto a detector, as shown in Figure 8.7 (bottom). The intensity profile of a 100 μ m blood-filled fused-silica capillary imaged at $\lambda=580$ nm is displayed in Figure 8.8 (left). Note the close resemblance between the simulated profile and the experimental results (Figure 8.6 (left)). It was also apparent in the model that the two distinctive peaks arise from the refractive power of the capillary. Let us observe that these peaks were not produced by real blood vessels in the retina, as shown in Figure 8.6 (right), where an imaged retinal vessel shows a continuous and regular intensity profile. In Figure 8.8(right), we present the result of a Zemax simulation of the artificial eye with a model for a real blood vessel. The effect of the vessel wall was neglected in the model and its effect is not significant on measured transmittance (see Figure 8.6 (right) and Figure 8.8 (right)). Note the good agreement between the experimental and simulated results.

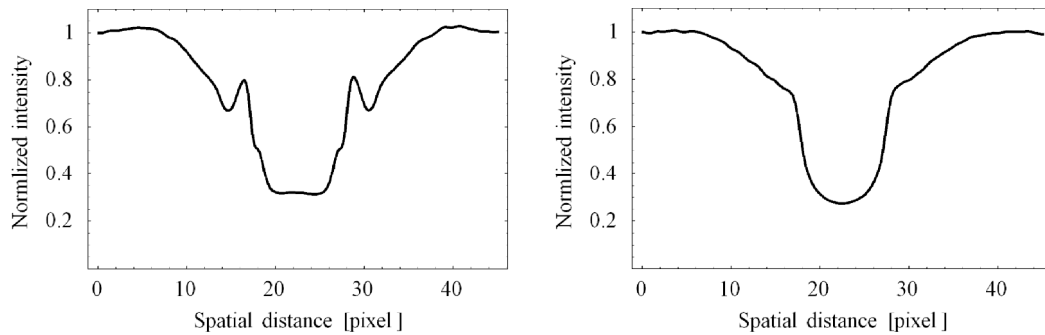


Figure 8.8: ZEMAX-simulated profile (left) of a fused-silica 100 μ m capillary filled with 100% oxygenated blood, (right) of a 100 μ m arteriole filled with 100% oxygenated blood imaged at 580nm.

8.5 Spectral analysis for blood oximetry: physical model of light propagation in the retina

We have shown previously that the spectral determination of oxygen saturation depends on the signatures of oxygenated and deoxygenated haemoglobin that dominate the spectrum of reflected light from the retina, in addition to the melanin

pigmentation which varies within the ethnicity (Delori, 1989). Optical densities at the centre of a blood capillary can be described, as proposed in (5-29), for a given illumination wavelength λ .

$$OD(\lambda) = a S(\lambda) + \eta(\lambda) C_{HBtotal} d[(\epsilon_{HBo_2}(\lambda) - \epsilon_{HB}(\lambda))OS + \epsilon_{HB}(\lambda)]$$

The new parameter a is introduced as scaling constant. The function S accounts for the backscattering effect of red blood cells and η describes the optical path length factor. The parameter a accounts for linear variations in S due to unknown physiological parameters such as hematocrit concentration, red-blood cell concentration, mean-corpuscular volume, mean corpuscular haemoglobin content, etc, between blood samples. It was illustrated previously that by employing a non-linear fit of this model to the optical density measurements, the oxygen saturation OS , together with other parameters such as S and an aggregate of $\eta(\lambda)$, $C_{HBtotal}$ and d , can be determined.

In a well-controlled environment such as the artificial eye, where most of the parameters of the model are known with reasonable accuracies, the optical path length $\eta(\lambda)$ can be easily extracted to provide valuable information about the typical photon paths. The parameter $\eta(\lambda)$ accounts for all possible single and double passes through the blood vessels. These light paths are depicted in Figure 8.1 (Right). It was explained earlier that three main components of light will contribute to the intensity measured by the detector: **(1)** A component I_{BS} backscattered by red blood cells within the vessel, **(2)** A component I_{SP} is transmitted through the blood vessel once and diffusely reflects off the fundus ($\eta=1$), and finally **(3)** A component I_{DP} that passes through the blood vessel, reflects off the fundus and again traverses the vessel before exiting the eye ($\eta=2$). When the ocular fundus is assumed to have highly diffuse reflectivity (i.e. white background) the measured intensity is a weighted sum of the

three components where η varies between $\eta=1$ for single pass and $\eta=2$ for double pass. On the other hand, when the background is assumed to have perfect absorption (black background) the only contribution to the measured intensity arises from the backscattered component I_{BS} , since the others are eventually absorbed and $\eta=0$. Hence, the parameter η is primarily predetermined by the optical properties of the fundus, in particular by the size of the intensity distribution created in the fundus when a point of light is projected on its surface. This is a type of “the tissue spatial point spread function” of the diffuse medium as discussed in the section 5.6.3 for the human retina. If the point spread function (*PSF*) of the fundus is relatively large with respect to the size of the vessel, the number of single paths of light will be dominant over that of double-pass and thus $\eta \rightarrow 1$. On the other hand, if the medium *PSF* is relatively small, double paths are dominant and therefore $\eta \rightarrow 2$.

Unlike to the human fundus and due to the spectrally neutral characteristics of Spectralon, the *PSF* of the artificial fundus can be assumed to be achromatic. As a result, the path length ηd is expected to be invariant across the wavelength range in which the spectral images were acquired. A simple experiment was carried out to test this supposition by measuring the edge-spread-function of Spectralon for a set of wavelengths (from 450nm to 680nm, in intervals of 20nm) and for the three reflectances (20%, 60%, and 99%). Using various reflectances is important as the degree of fundus pigmentation varies between subjects. After taking into account the effects of the optics *PSF* from the optical system employed to image the edge spread function, and considering Spectralon an isotropic material, it was found that the Spectralon *PSF* is invariant with wavelength. The *PSF* did, however, reduce in size with decreasing reflectance. For example, when a Gaussian function was fitted to the *PSF* we found that 95% of the energy was enclosed within 50 pixels, 32 pixels and 23

pixels for the 99%- 60%- and 20 %-reflectance Spectralon, respectively. The width of edge spread function reduces as the reflectivity of the spectralon decreases.

8.6 Results

Spectral images recorded by the model eye were used to assess the capability of our instrument to perform accurate oxygen saturation measurements. The accuracy of the measurements as well as the validity of our assumptions were investigated through implementing two main procedures:

- Experimental calculation of optical path length.
- Oxygen saturation calculation.

8.6.1 Experimental calculation of the optical path length η

From the optical model (5-29) and with *priori* knowledge of the capillary diameter d , oxygen saturation OS and haemoglobin concentration $C_{HBtotal}$ (from readings provided by the CO-Oximeter), the mean path length parameter η can be determined experimentally from the optical density of the spectral images by assuming that the scattering by the red blood cells $S(\lambda)$ follows the empirical model functions measured by Meinke at various hematocrit concentrations (Meinke et al, 2007) as depicted in Figure 8.9.

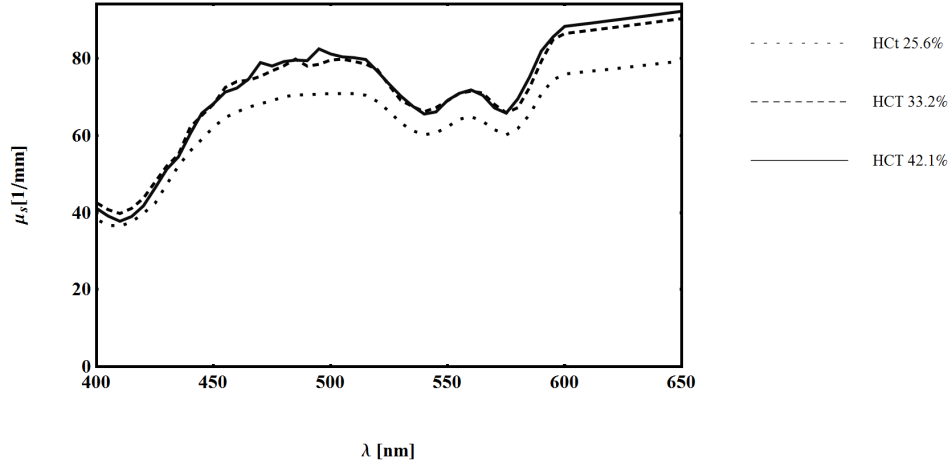


Figure 8.9: Empirical function of scattering of the blood cells for oxygenated blood at various hematocrit concentrations.

Since the values of $S(\lambda)$ are valid for fully oxygenated blood, η is deduced from only those capillaries that contain blood with high oxygen saturation (30 capillaries). The scattering as a function of OS is investigated recently by Friebe (2009) and found to vary by a value of less than 5% as the oxygen saturation changes from $OS=0\%$ to 100%. The extraction of η values was performed by using non-linear fit of the optical model introduced in (5-29) to the measured optical densities in the wavelength range 500-650 nm when $S(\lambda)$, d , and OS are known.

$$OD(\lambda) = a [S(\lambda) + \eta(\lambda)C_{HBtotal}d[(\epsilon_{HBo2}(\lambda) - \epsilon_{HB}(\lambda))OS + \epsilon_{HB}(\lambda)]] \quad (5-29)$$

This is a valid argument given that our model assumes that η is independent of blood oxygen saturation level. The values of η are shown in Figure 8.10 and Table 8.2 and clearly indicate that the number of single paths is dominant for Spectralon fundus with reflectances varying between 20% and 99%. The mean value of η for all background reflectances is 1.15 ± 0.08 .

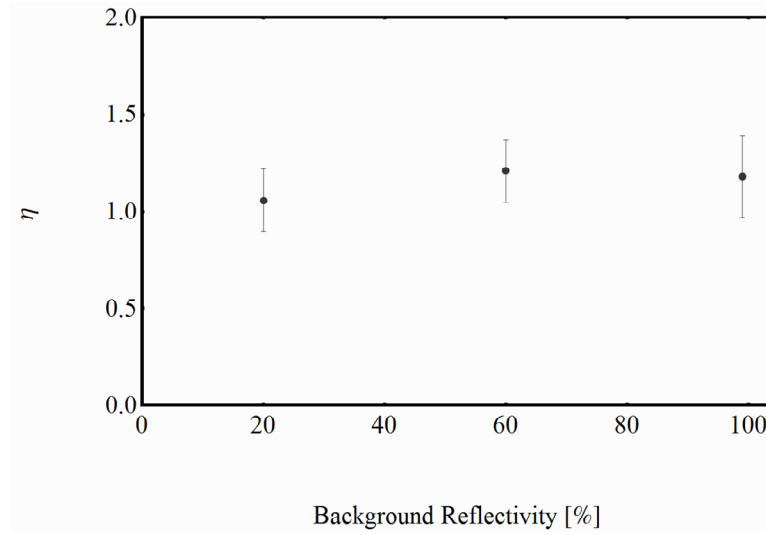


Figure 8.10: Empirical optical path length η as a function of fundus reflectivity.

$R=20\%$	$R=60\%$	$R=99\%$
$\eta = 1.06 \pm 0.16$	$\eta = 1.21 \pm 0.16$	$\eta = 1.18 \pm 0.21$

Table 8.2: Empirical optical path length η as a function of fundus reflectivity.

It is interesting to note a certain degree of similarity in the values of η for the artificial and human retinas. Hammer et al (1997) have shown, by means of Monte-Carlo simulations of light propagation in the human fundus, that the contribution of double pass is significantly smaller than the single pass ($\eta \rightarrow 1$).

8.6.2 Oxygen saturation measurements using empirical scattering function

As mentioned above, the oxygen saturation was calculated by fitting the physical model to the measured optical densities at the centre of the vessels from 500nm to 650nm, in intervals of 2nm. The nonlinear fit returns estimates for OS , a and the product of η , $C_{HBtotal}$ and d . All these parameters were wavelength-independent. For illustrative purposes the estimates of OS along two capillaries, one with arterial blood the other with venous blood, are displayed in Figure 8.11. The background behind the capillaries changes according to the three Spectralon reflectivities. The measured

oxygen saturation was independent of background reflectivity. There are sharp changes in measured oxygen saturation values at the boundaries between spectralon slabs as the vessel profiles obtained in these areas are notably irregular and distorted due to discontinuity in the background reflectivity at those boundaries.

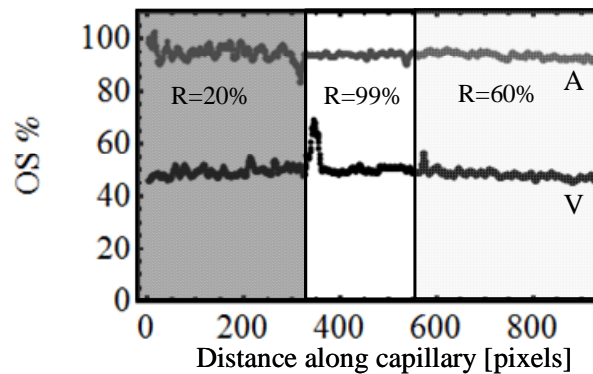


Figure 8.11: Calculated oxygen saturation (OS) of venous (V) and arterial (A) blood along two capillaries in front of three Spectralon slabs

It can be observed in Figure 8.11 that the standard deviation of oxygenation along the capillaries is 1% which is a factor of 5 lower than that we have measured in the human eye (Alabboud, 2007). This lower uncertainty of the inferred oxygenation in the model eye is due to the more uniform texture of the spectralon slabs compared to that of the retinal structure in addition to the intrinsic simplicity of the model eye setup.

The estimated *OS* for all capillaries, with several diameters, oxygen saturation levels and blood concentrations, is shown in Figure 8.12. A difference of ($\Delta OS = 3.31\% \pm 2.19$) was reported between the calculated and measured oxygen saturation by CO-Oximeter. The calculated *OS* (vertical axis) of each blood capillary is plotted versus the measured *OS* by means of the CO-Oximeter (horizontal axis). The accuracy of CO-Oximeter varies with oxygen saturation in which for high oxygen saturation values $>80\%$ the Co-Oximeter accuracy is of value $\pm 5\%$, however for lower oxygen saturation values $<80\%$ the accuracy is $>5\%$.

The degree of correlation obtained between the measured and calculated oxygen saturation is $\rho^2=0.975$ which is high and establishes the level of validity of our model to measure the oxygenation.

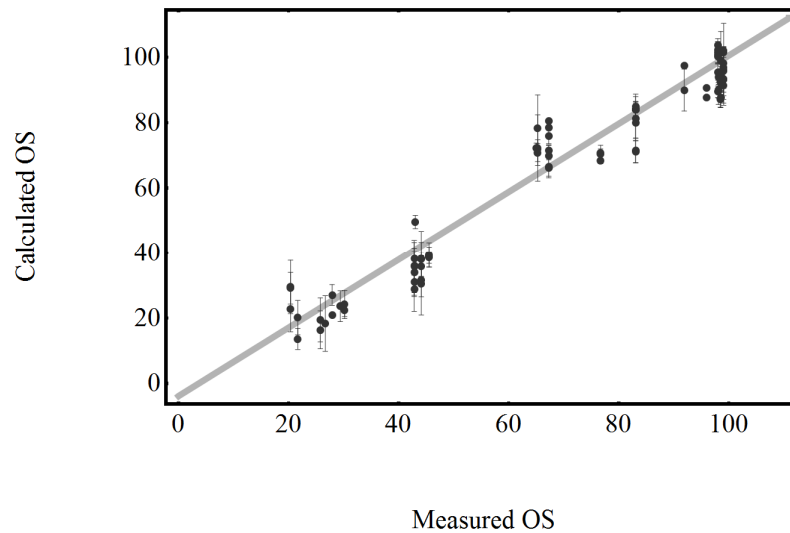


Figure 8.12: Calculated oxygen saturation versus measured oxygen saturation obtained from 130 capillaries with three different diameters and various degrees of oxygenation.

The error bars in Figure 8.12 which correspond to one standard deviation, account for the *OS* variability along the capillary and can arise from various factors. First, the distance from the capillary to the artificial fundus may change slightly from one end of the capillary to the other. This deviation, in conjunction with the refractive power of the capillary-water boundary, will produce variations in the value of the optical path length along the capillary and, as a result, in the estimate of *OS*. Second, lower Spectralon reflectances are achieved by introducing dark particles on a uniform gray background, as can be seen in Figure 8.5. The presence of non-uniformities in the artificial fundus introduces uncertainty in the calculated optical densities and hence in the *OS*. It can be observed in Figure 8.11 that for the white Spectralon, where there are no spatial non-uniformities, the variations in *OS* are negligible ($\leq 1\%$). Finally, the time of acquisition of the spectral data cube may give rise to alterations in the physiological properties of the blood sample and that can contribute to errors in *OS*, in

addition to the lack of scattering behaviour at different oxygenation levels especially for venous blood.

We were able to deduce the value of η from the product $\eta C_{HBtotal}d$ estimated by the nonlinear fit and compared it with that obtained with *prior* knowledge of *OS*. Because $C_{HBtotal}$ and d of each capillary are known, η is calculated,

$$\eta = \frac{\eta C_{HBtotal}d(\text{estimated from nonlinear fit})}{C_{HBtotal}d}.$$

The results of η for each background reflectance are displayed in Figure 8.13 and Table 8.3 and show that $\eta \rightarrow 1$, in good agreement with the values obtained in the previous section. This high correlation supports our belief that our spectral algorithms are robust and can estimates of oxygen saturation with an acceptable error. However, the separation of the product $\eta C_{HBtotal}d$ is proved difficult in the human retina especially the haemoglobin concentration which varies between humans depending on sex, age, and health.

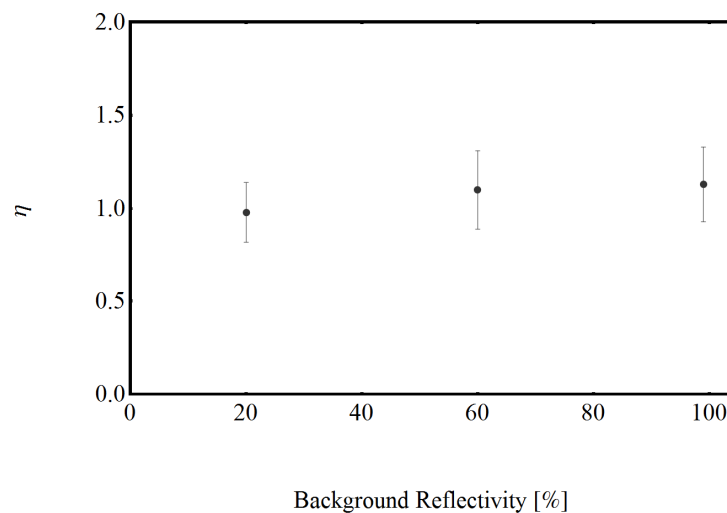


Figure 8.13: Optical path length η estimated by the nonlinear fit algorithm as a function of fundus reflectivity.

20% R	60% R	99% R
$\eta = 0.98 \pm 0.16$	$\eta = 1.10 \pm 0.21$	$\eta = 1.13 \pm 0.20$

Table 8.3: Optical path length η estimated by the nonlinear fit algorithm as a function of fundus reflectivity.

The scaling factor a for the scattering function $S(\lambda)$ increases for larger capillary diameters for the same oxygen content as depicted in Table 8.4.

100 μm	0.82 ± 0.25
150 μm	1.33 ± 0.39

Table 8.4: Mean scaling factor a of the scattering function S estimated by the nonlinear fit algorithm for two capillary thicknesses and three background reflectances.

This result is in agreement with the fact that a larger fraction of light is backscattered due to the presence of a larger number of scatterers. As the scattering function $S(\lambda)$ is dependant on many physiological factors such as hematocrit concentration and oxygen saturation, The notable standard deviation of a can be explained due to the use of one scattering function for all blood samples drawn from several subjects

8.6.3 Oxygen saturation measurements assuming constant scattering

The empirical scattering function $S(\lambda)$ by blood was utilized to calculate the oxygen saturation from the model eye experiments. As shown previously, this function is only valid for fully oxygenated blood and no detailed study was found in the literature describing the behaviour of scattering by whole blood at various levels of oxygen saturation. To obtain saturation measurements from the human retina, scattering was assumed constant for the wavelength range (500-650 nm). To evaluate the error from this supposition; oxygen saturation from fully oxygenated samples was measured in two cases: (1) when the empirical scattering function was considered and (2) when the scattering was assumed constant. The results acquired at diameters 100 and 150 μm showed that an average difference about (4.89%) was made due to the constant

scattering term. Using constant scattering assumption an increased saturation difference of 1.58% for oxygenated blood samples was yielded.

8.7 Conclusion

The validity of the spectral retinal imager is assessed for measurement of oxygen saturation of human blood by constructing a model eye to mimic the optical properties of human eye. Blood samples with known oxygenation have been used to deduce empirically the dependency of the optical path length ηd on background reflectivity. Arterial and venous blood samples from human subjects have been analyzed using a CO-Oximeter to establish its measured oxygen saturation and subsequently imaged in the model eye using the hyperspectral retinal camera. The oxygen saturation was calculated from a numerical fit to an analytical model of light propagation within the retina. The standard deviations of oxygenation along a capillary at ~1% were about a factor of 5 lower than those that we have measured in a human eye. The lower uncertainty in the inferred oxygenation in the artificial eye is probably due to the more uniform texture of the Spectralon compared to the retinal structure and emphasises that reducing this random uncertainty in human retinal oximetry requires a processing technique that incorporates and compensates for the retinal structure.

The results that demonstrate the validity of our spectral analysis algorithms for blood oximetry have been presented. We have shown significant agreement between the oxygenations inferred from the hyperspectral images and the measured oxygenations, with a correlation of 0.975. The maximum saturation difference of 3.31% for oxygenated blood was reported. The discrepancy was evaluated for the same capillaries when the scattering function was assumed to be independent of wavelength and was found to be 4.89 % for 100 and 150 μm capillaries. To gain more information

on the effect of the retinal structure on oxygen saturation measurements, a more sophisticated construction of the artificial eye is needed. Future plans will concentrate on simulating the fundus layers separately in the model eye setup.

Chapter 9

Quantitative retinal oximetry of healthy and diseased subjects

In this chapter, the analysis of oxygen saturation measurements in healthy and diseased retinas is described. Clinical trials are considered from patients with glaucoma and vein retinal occlusion which are both associated with irregularities in oxygen supply in the retina.

9.1 Retinal blood vessels

It was shown previously (chapter 2) that retina has a multilayered structure with a dual circulation system to provide it with oxygen and nutrients. Choroidal vasculature supplies the outer layers and the central retinal artery supplies the inner layers. The inner two thirds of the retina is nourished by some branches from the central retinal vessels while the outer one-third is nourished by the choroidal circulation (Forrester 2002). Any interruptions in this dual system supply causes lack of oxygen followed by damage to the normal function of the retina. There are four branches which supply the quadrants of the retina. These branches come from the central retinal artery which emerges on the nasal side of the optic disc (See Figure 9.1).

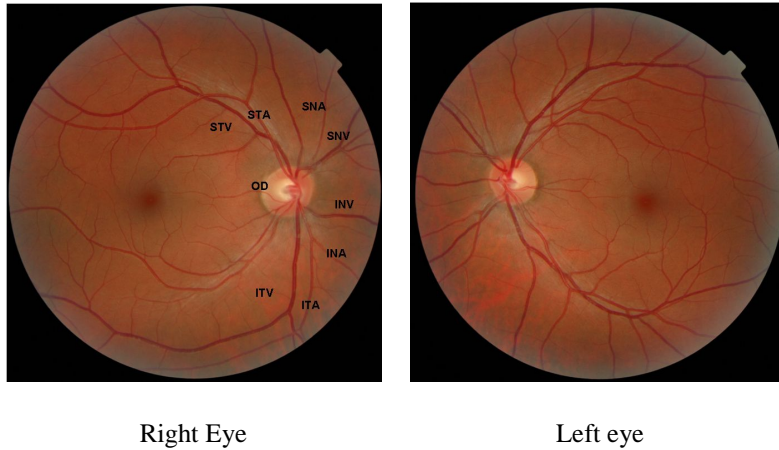


Figure 9.1: colour photograph of healthy retinas: OD, optic disc, STA and STV Superior temporal artery and vein; SNA and SNV Superior nasal artery and vein; ITA and ITV inferior temporal artery and vein; INA and INV, Inferior nasal artery and vein.

The temporal branches of the retinal artery extend in curves in the retinal segments from the optic disc towards the periphery. Nasal branches follow an almost direct path to the peripheral retina. Blood leaves the retinal artery and enters the retinal veins. There are also four quadrant veins converging onto the optic disc where they form the central retinal vein that leaves the eye along side the central artery. There is no anastomotic connection between retinal artery branches so that blood flow occlusion of one branch cannot be compensated by neighbouring branches and this can cause loss of oxygen supply to the corresponding region. Arteries commonly cross over the vein while veins less commonly cross over the arteries.

9.2 *Recording the spectral cube*

Sequential spectral retinal images were recorded in the wavelength range 500-650 nm in 2 nm increments. Eyes were dilated with 1% tropicamide and images were recorded using flash illumination. The optic disk was moved into the image area by instructing the subject to fixate on a movable LED light source provided with the fundus camera system while the image was observed under constant illumination.

Selecting the wavelength was performed by tuning the *LCTF* through software to synchronize acquisition of the image frame and triggering the flash gun. Flash intensity was varied to compensate for the variation in the spectral transmission caused by the eye, *LCTF*, detector sensitivity, and flash lamp. Due to the eye movement and the conditions of the patients, in some spectral cubes, images at short wavelengths (500-540 nm) were recorded with low *SNR*. As a result, those images were eliminated from the spectral cubes and the oximetric measurements were restricted in the range 560-650 nm.

9.3 Measurement of retinal vessel oxygen saturation

Oxygen saturation measurements were performed on spectral retinal images recorded from healthy and diseased retinas. The results are presented as false colour maps indicating the oxygen saturation along the retinal blood vessel tree.

9.3.1 Measuring oxygen saturation in normal (healthy) subjects

Normal subjects ($n=13$ retinas) were imaged and oxygen saturation measurements were obtained along the blood vessel tree. The arteriolar and venular oxygen saturation measurements and respective arterio-venular differences were calculated to establish a standard of oxygen saturation levels in healthy retinas. As explained previously (see section 7.5, chapter 7), the oxygen saturation measurements were performed through a nonlinear fit of an optical model to the optical density measurements at each particular wavelength. Two additional parameters: the scattering S and the product $\eta C d$ were calculated and the mean values of those two parameters were measured along the tracked vessels. Figure 9.2 shows the relationship between oxygen saturation OS and the parameter $\eta C d$ for arterial and venous blood ($n=146$ vessels).

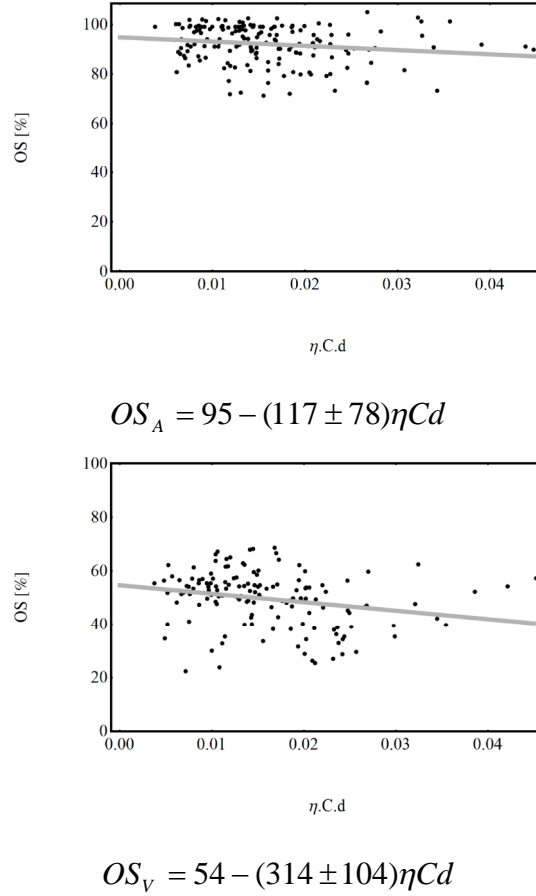


Figure 9.2: The relationship between OS and $\eta C d$ for arterial blood (Above) and venous (Bottom).

A linear regression was employed to predict the influence of $\eta C d$ variation on oxygen saturation measurements in both veins and arteries. The total variance of oxygen saturation measurements is represented by the value of the fraction R^2 . The deviation of the slope of the fitted line from zero is evaluated by calculating ρ (for $\rho < 0.05$ the slope is significantly non-zero). The linear fitting results in ($R^2=0.0235$, $\rho=0.046$) for arteries and ($R^2=0.0567$, $\rho=0.0034$) for veins. The low R^2 for oxygen saturation measurements in arteries suggests that only 2.3% of OS measurements depend on $\eta C d$ variation in comparison with OS measurements obtained from veins in which increased dependency (5.6%) is noticed. There is a significant slight decrease of OS ($\approx 4\%$) with $\eta C d$ and this is more pronounced for venous blood

($\approx 12\%$). This dependency is believed to be due to the simplicity of the optical model in which constant scattering was assumed. We have shown in the previous chapter (the model eye experiment) that the constant scattering term was responsible for an error ΔOS (4.89 ± 3.49) % in assessing oxygen saturation in fully oxygenated samples. However, using a scattering term that is function of oxygen saturation is necessary to perform more accurate oxygen saturation measurements.

Scattering S versus $\eta C d$ is shown in Figure 9.3 and linear relationship is predicted with $R^2=0.0702$, $\rho < 0.0001$. The value of R^2 suggests that only 7% of the scattering can be predicted by the value of $\eta C d$. However the remaining 93% is independent of variation of $\eta C d$. The dependency of scattering on the variation of $\eta C d$ was observed as an increase in the scattering as $\eta C d$ increased. This result is in agreement with the hypothesis that a larger number of photons are backscattered due to the presence of a larger number of scatterers (red blood cells).

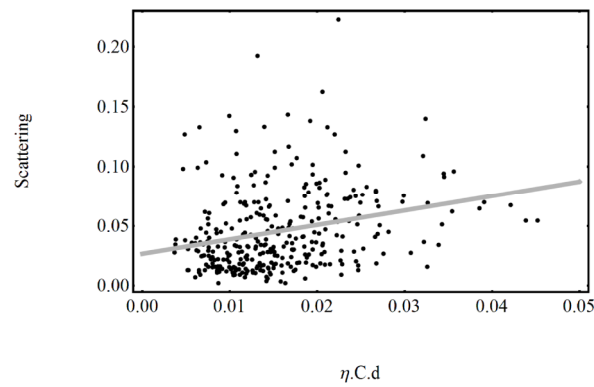


Figure 9.3: Scattering versus $\eta C d$.

Retinal vessel oxygen saturation was measured for all tracked vessels of 13 healthy retinas (150 arteries and 120 veins) and images of two subjects were recorded twice. Reliable oxygen saturation values which are comparable with literature (see chapter 1) were measured (see Table 9.1 and Figure 9.4)

	Artery OS	Venous OS	Arterio-venular difference
Mean	96 %	48 %	47 %
Standard Deviation	$\pm 5\%$	$\pm 9\%$	$\pm 7.28\%$

Table 9.1: Average saturation measurements in normals.

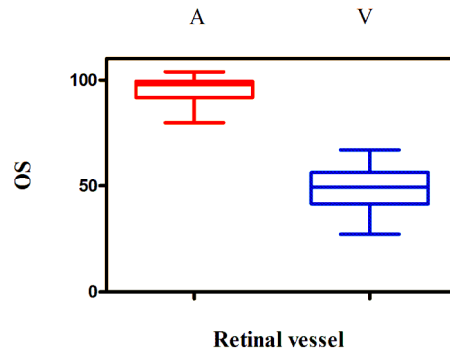


Figure 9.4: Arteries (A) and Veins (V) saturation measurements in normals.

The mean arterial oxygen saturation at 150 arteries from different locations of 13 retinas was $OS_A = (96 \pm 5)\%$, the mean of 120 veins at different positions in 13 retinas was $OS_V = (48 \pm 9)\%$ and the arterio-venular difference was $(47 \pm 7.28)\%$. However, the mean value and standard deviation of the oxygen saturation at each individual subject are depicted in Figure 9.5, Figure 9.6.

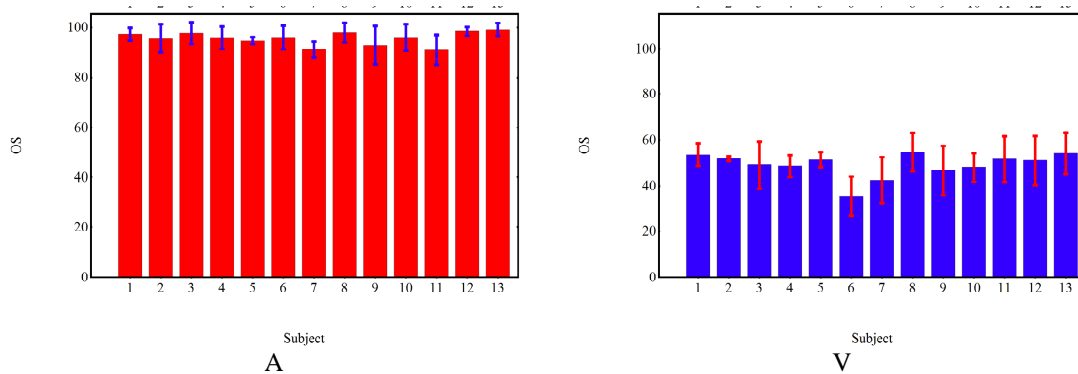


Figure 9.5: Average oxygen saturation measurements in arteries (A) and veins (V) of normals

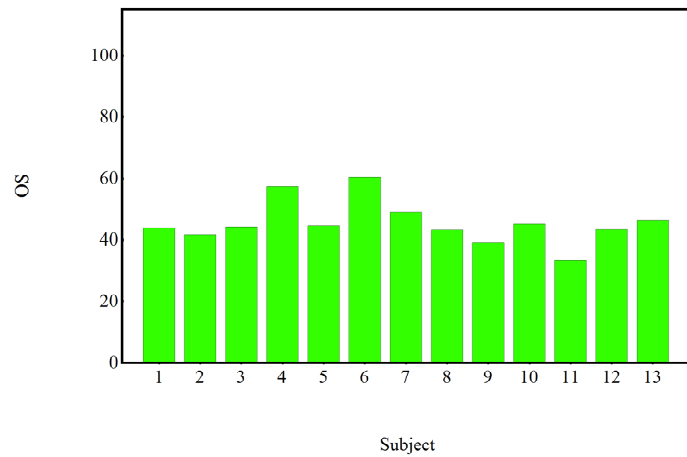
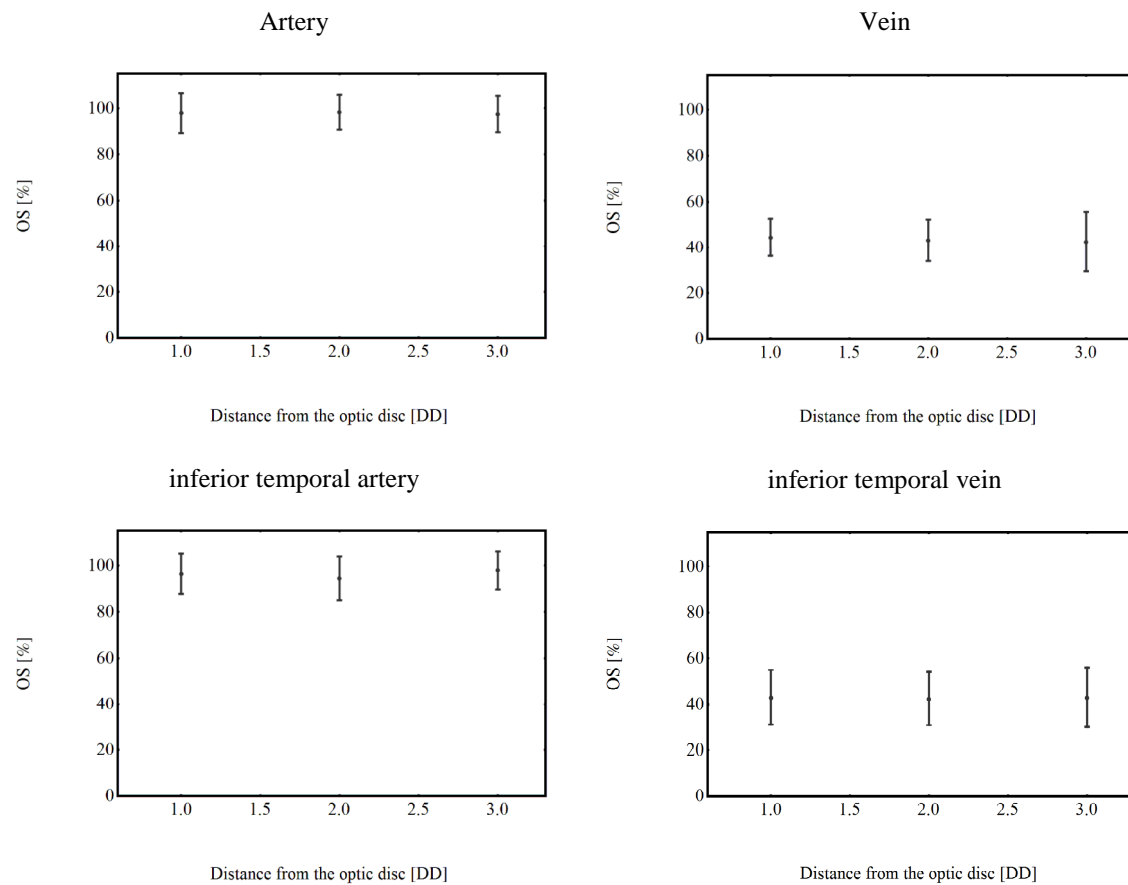


Figure 9.6: Arterio-venular oxygen saturation difference

The oxygen saturation was also calculated at three distances from the optic disc, determined in diameters of optic disc (DD), $1DD$, $2DD$, and $3DD$. The measurements were performed at different quadrants superior temporal and nasal, and inferior temporal and nasal veins and arteries. Constant oxygen saturation was found up to a 3 optical diameters from the optic disc (see Figure 9.7).



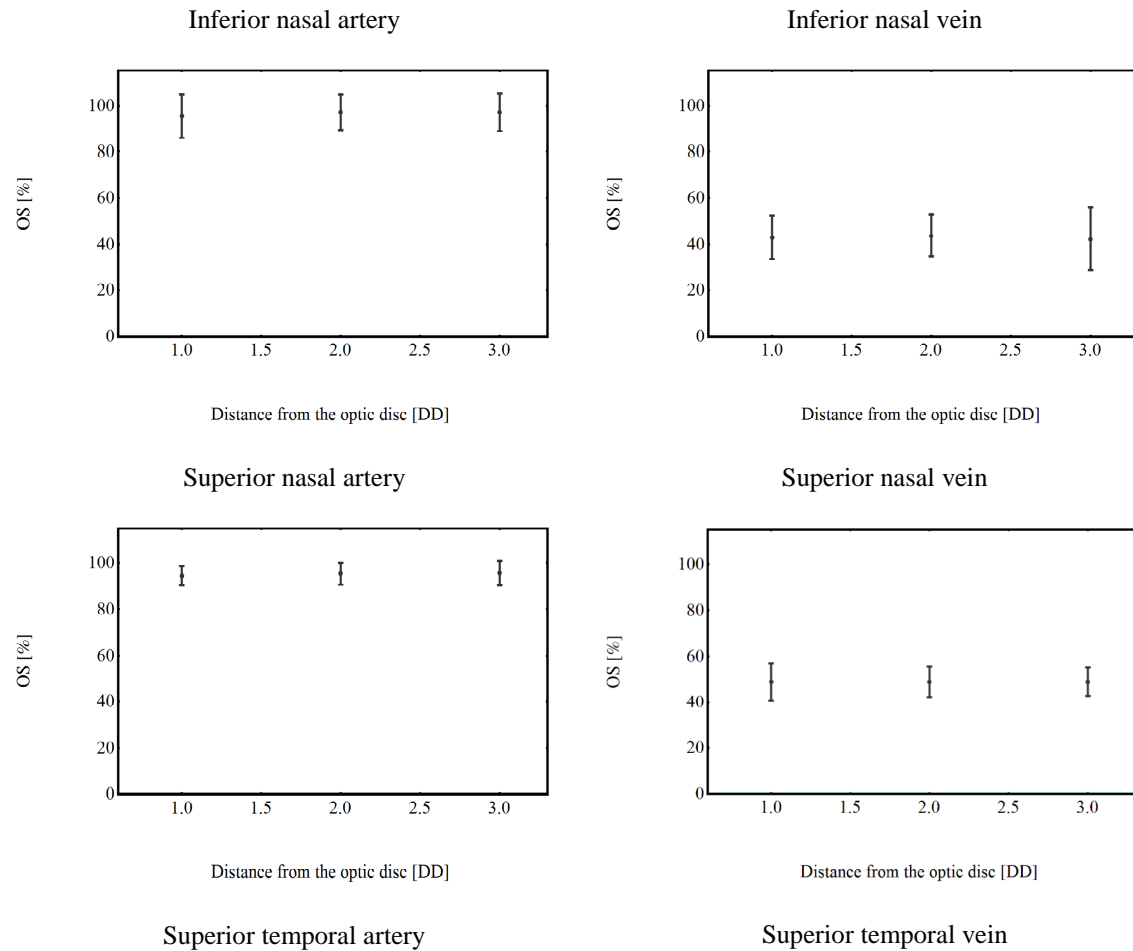


Figure 9.7: Oxygen saturation measurements obtained from Superior temporal artery and vein; Superior nasal artery and vein; inferior temporal artery and vein; Inferior nasal artery and vein.

The analysis results showed that the function of the retina is sustained through a regular supply of oxygen along the arteries. The absolute values of the arterial and venous oxygen saturation do not differ significantly between all quadrants and along the vessels up to three disk diameter distances from the optic disc. The mean oxygen saturation and mean standard deviation were measured at these four quadrants as ($OS_A = (96.51 \pm 7.31) \%$, $P > 0.05$, $R^2 = 0.014$) for arteries and ($OS_V = (44.43 \pm 9.55) \%$, $P > 0.05$, $R^2 = 0.057$) for veins. The statistical comparison between quadrants was performed by one-way ANOVA at a significant level of $P < 0.05$. Any variation in oxygen saturation status as long as the measurements are obtained along the retinal

vessels and at certain distances from the optic disk should be considered as an indication of damage to the function of the retina.

9.3.2 Reproducibility

The reproducibility of the *OS* measurement was assessed from repeated measurements of arteries and veins. Two normals were considered in this study and retinal images from each subject were recorded twice (set1, set2). The mean oxygen saturation values at each vessel selected from superior and inferior areas are presented in Figure 9.8.

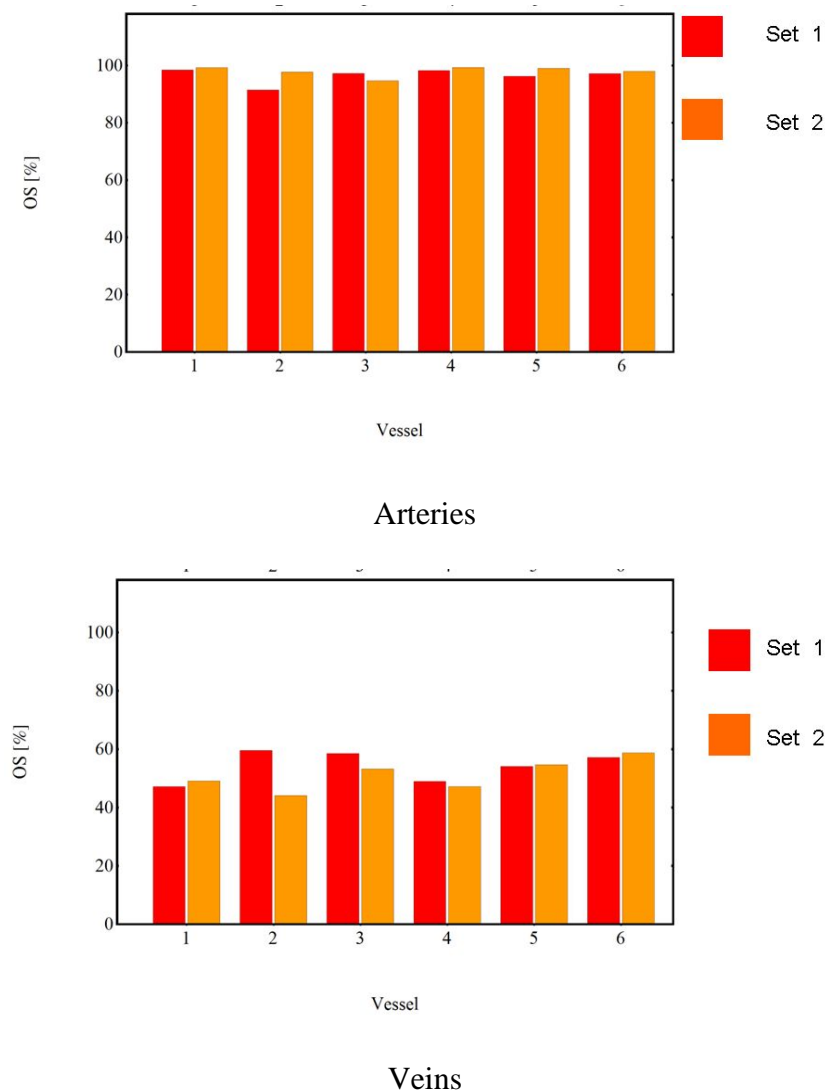


Figure 9.8:The reproducibility of *OS* measurements in veins and arteries obtained from healthy subject.

The standard deviations of OS measurements are presented in Table 9.2.

	OS_A	OS_V
Subject 1	96±5.5 %	52±1 %
	95±8.2 %	57±9 %
Subject 2	97±2.5 %	53±5 %
	96±5 %	51±5.4 %

Table 9.2: Reproducibility of OS measurements.

Repeated measurements in each subject were correlated and in good agreement in which the variations in the mean arterial oxygen saturation at 6 vessels were small ($\Delta OS_A \approx 1\%$). However, the mean venous oxygen saturation showed higher variance $2\% \leq \Delta OS_V < 5\%$. This increased variation is believed to be due to the variation in the metabolic activity of the retina as a result of exposure to many light flashes which increases the activity of the retina and hence the demand for oxygen.

Quantitative false colour maps of 6 healthy subjects are presented in Figure 9.9. These maps show the typical OS characteristics and variability of normal subjects. Consistent saturation measurements are obtained and can be compared with saturation maps of diseased retinas to establish a standard to help clinicians to assess the severity of the diseases as well as the effectiveness of the treatment.

In the following section, qualitative saturation maps from diseased retinas will be generated.

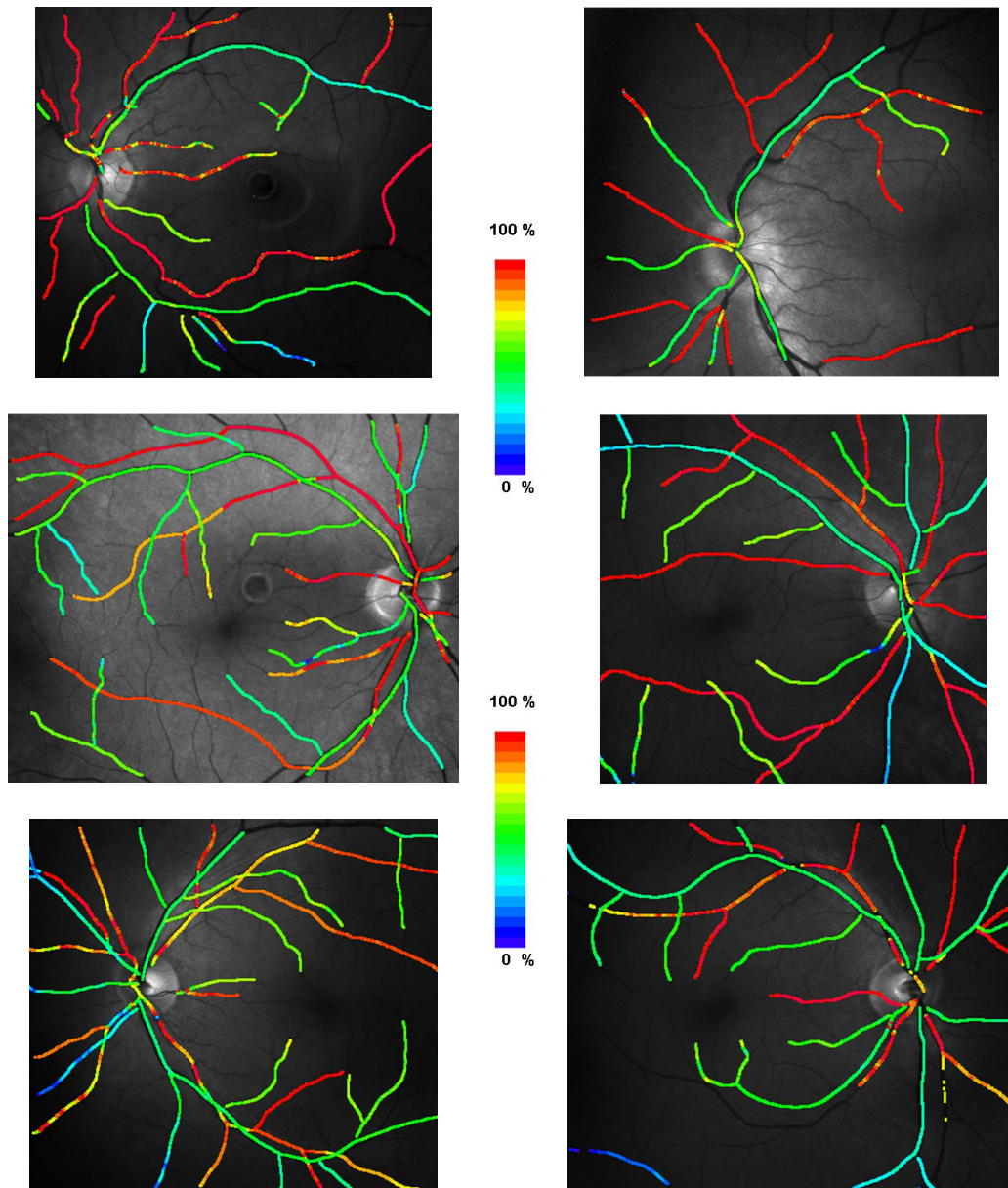


Figure 9.9: Quantitative retinal oximetric maps of 6 healthy subject.

9.3.3 Ischemia – related retinal diseases

As shown earlier, oxygen is delivered to the retinal layers (inner and outer) via a combination of retinal vasculature which lies within the inner retina and choroidal vascular bed. A large proportion of retinal blindness is associated with retinal vascular diseases which prevent sufficient oxygen supply to the retina. Hypoxia occurring in the retina is believed to be a major factor in the development of ocular vascular

disorders such as diabetic retinopathy (Denninghoff, 2000; Hardarson, 2008) and arterio-venous occlusion (Yoneya, 2002) and glaucoma (Stefansson,2005; Siesky,2008, Michelson, 2006; Khoobehi, 2004). The ability to assess the oxygen saturation in the human ocular fundus can aid diagnosis or monitor such disorders. For instance, measurement of changes in retinal oxygen saturation under controlled conditions can reveal the relationship between oxygen consumption, blood sugar levels, and vascular auto-regulatory function in diabetic retinopathy (Khoobehi, 2004). Retinal oxygen saturation estimation can aid early detection of glaucoma, a disease in which an early diagnosis is vital for effective treatment. The evaluation of oxygen saturation in this study involved patients with two disorders: glaucoma and retinal vein occlusion.

9.3.3.1 Measuring oxygen saturation in glaucoma

This section describes work aiming to detect oximetric changes in the retinal vasculature of patients with asymmetrical primary open angle glaucoma (POAG) using quantitative spectral analysis. Subjects with asymmetrical POAG ($n=9$) were imaged and oxygen saturation measurements were obtained along the superotemporal and inferotemporal arterioles and venules at approximately 3 optic disc diameters (DD) from the optic disc margin. The arteriolar and venular oxygen saturation measurements and respective arterio-venular differences were compared between normal eyes and glaucomatous eyes and between eyes with more severely affected visual field loss and less severely affected visual field loss.

The clinical data of the study population is shown in Table 9.3.

	Normal Subjects (n = 10) mean (\pm SD)	Glaucoma Subjects (n= 9) mean (\pm SD)	
		Eye with less visual field loss	Eye with more advanced visual field loss
Age (yrs)	34.1 (\pm 13.46)	62.6 (\pm 16.2)	
Male:Female Ratio	6:4	6:3	
Visual Acuity (LogMAR equivalent)	-0.08 (\pm 0.09)	0.15 (\pm 0.11)	0.19 (\pm 0.11)
Systolic BP (mmHg)	121.0 (\pm 8.1)	143.9 (\pm 14.5)	
Diastolic BP (mmHg)	76.0 (\pm 8.1)	72.8 (\pm 11.2)	
Pulse Oximetry (%)	97.0 (\pm 0.7)	96.1 (\pm 0.6)	
Intraocular Pressure (mmHg)	14.5 (\pm 1.5)	15.5 (\pm 4.7)	15.9 (\pm 4.6)
Vertical cup-to-disc ratio	0.28 (\pm 0.15)	0.72 (\pm 0.19)	0.81 (\pm 0.13)
Horizontal cup-to-disc ratio	0.29 (\pm 0.14)	0.68 (\pm 0.20)	0.77 (\pm 0.15)

Table 9.3: Clinical data of the subjects (Mordant et al, 2009).

The arterial and venous oxygen saturation were analysed in glaucomatous eyes and compared to normal eyes (Table 9.4). An unpaired non-parametric test (Mann-Whitney test) was performed at a significance level of $P < 0.05$. The analysis results showed significantly higher venular oxygen saturation ($P < 0.05$). The mean venous oxygen saturation in glaucomatous eye was ((68 \pm 18) %) in comparison with venous oxygen saturation of normals ((48 \pm 9)%). The variation in mean arterial oxygen saturation of glaucomatous ((95 \pm 7)%) and normal eye ((96 \pm 5)%) was significantly low ($P > 0.05$). As a result lower arterio-venular differences in glaucomatous eyes compared to normal eyes are reported. The comparison of arterial and venous saturation measurements between glaucoma and normal subjects is shown in Figure 9.10.

	Normal Subjects mean (\pm SD)		Glaucoma Subjects mean (\pm SD)		<i>p</i> value
Retinal Arteriolar Oxygen Saturation	96 \pm 5	%	95 \pm 7	%	0.45
Retinal Venular Oxygen Saturation	48 \pm 9	%	68 \pm 18	%	<0.05
Retinal Arterio-Venular Difference	46 \pm 7.28	%	27 \pm 13.65	%	

Table 9.4: Retinal blood oxygen saturation in normal and glaucoma subjects

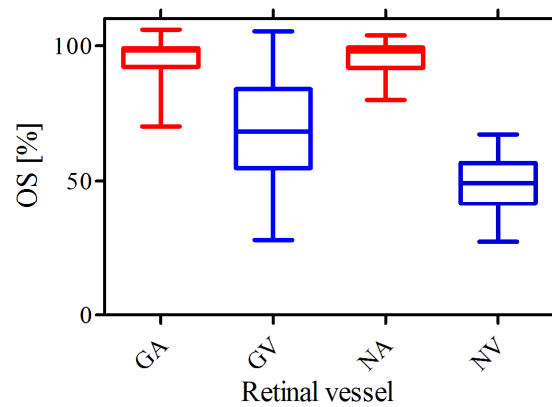
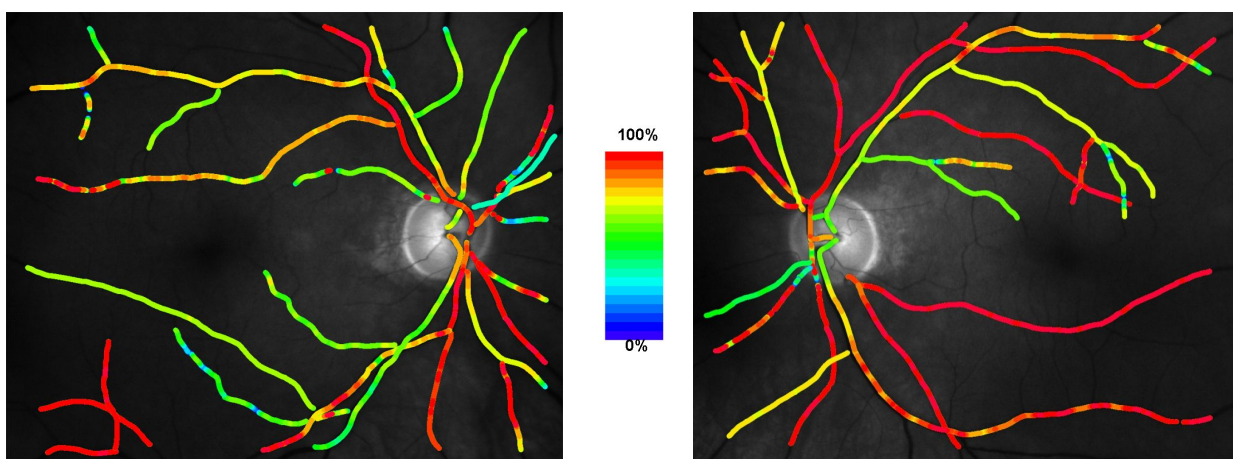
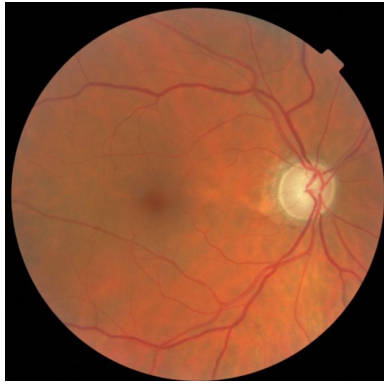


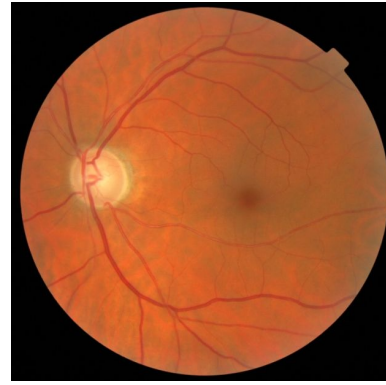
Figure 9.10: Comparison of retinal blood oxygen saturation between normal (NA,NV) and glaucoma subjects (GA, GV).

Quantitative oximetric maps (left and right eye) of a glaucoma subject with asymmetrical visual field loss prior to treatment with bilateral trabeculectomies are presented in Figure 9.11 (Trabeculectomy is a surgical procedure that removes part of the trabeculum in the eye to relieve pressure caused by glaucoma). As can be noticed from the oximetric map of the left eye, veins are mapped in yellow-orange colour indicating higher venous oxygen saturation comparing with venous oxygen saturation in normals (green colour in Figure 9.9).





Right eye



Left eye

Figure 9.11: Oximetric retinal maps of a glaucoma subject with asymmetrical visual field loss before bilateral trabeculectomies.

For eyes more severely affected by glaucomatous damage the venous oxygen saturation was significantly different ($P<0.05$) in contrast to the variation in arterial oxygen saturation which was significantly low ($P>0.05$). The arterio-venular difference for more affected eyes was $22\pm 13\%$ in comparison to the less affected eye which was $28\pm 13.41\%$. Table 9.5 and Figure 9.12 present the analysis results.

	Eye with less visual field loss mean (\pm SD)		Eye with more advanced glaucomatous visual field loss mean (\pm SD)		p value
Retinal Arteriolar Oxygen Saturation	94 \pm 7	%	95 \pm 6	%	0.11
Retinal Venular Oxygen Saturation	66 \pm 17	%	73 \pm 18	%	0.02
Retinal Arterio-Venular Difference	28 \pm 13	%	22 \pm 13.41	%	-

Table 9.5: Retinal blood oxygen saturation in asymmetrical glaucoma.

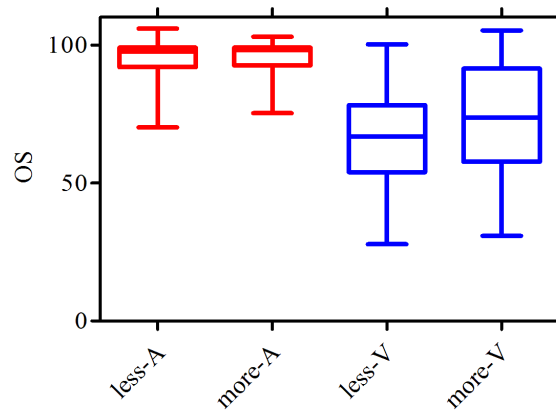


Figure 9.12: Glaucoma sub-group analysis: comparison of retinal blood oxygen saturation in asymmetrical glaucoma subjects less affected (less-A, less-V) or more affected (more-A, more -V).

Oxygen saturation measurements from a patient suffering from POAG were obtained before and after bilateral trabeculectomies as a treatment. Table 9.6 presents the *OS* measurements, intraocular pressure, and visual acuity pre- and post-treatment. The arterio-venular differences were increased from 20 ± 11.51 % to 29 ± 12.36 % and 26 ± 14.71 % to 38 ± 16.44 % as the treatment applied on both right and left eyes respectively. The increased arterio-venular was associated with decreased intraocular pressure and improved visual acuity.

	Visual Acuity (LogMAR equivalent)	Intraocular pressure(mmHg)	Arteriolar OS (Mean \pm SD)	Venular OS (Mean \pm SD)	Arterio- venular difference
Pre-treatment	0.22	20	91 \pm 11 %	71 \pm 12 %	20 \pm 11.51 %
Post-treatment	0.12	12	93 \pm 9 %	64 \pm 15 %	29 \pm 12.36 %
Right eye					
Pre-treatment	0.04	19	94 \pm 12 %	68 \pm 17 %	26 \pm 14.71 %
Post-treatment	-0.04	12	92 \pm 10 %	54 \pm 21 %	38 \pm 16.44 %
Left eye					

Table 9.6: Retinal blood oxygen saturation pre- and post-treatment.

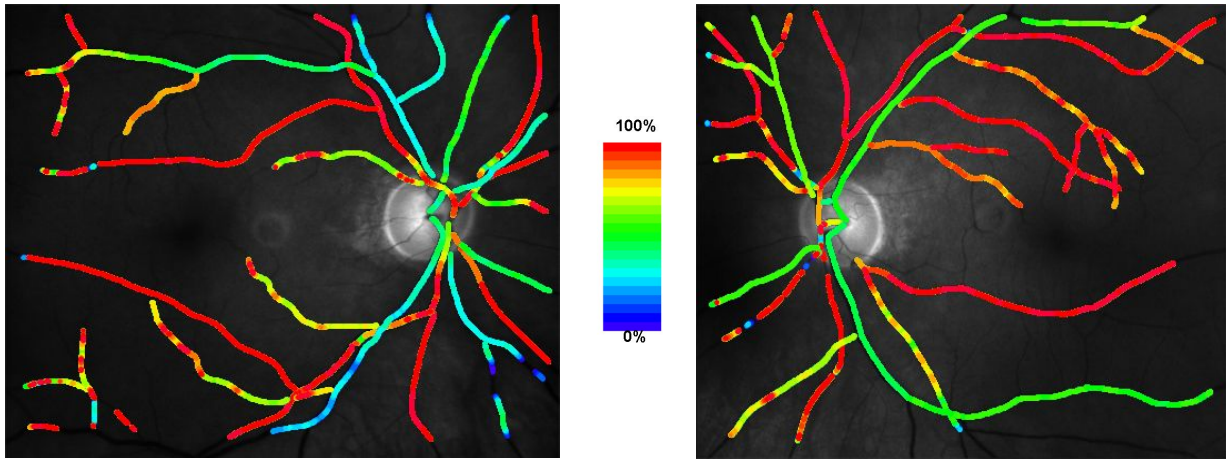


Figure 9.13: Oximetric retinal maps of a glaucoma subject with asymmetrical visual field loss after bilateral trabeculectomies.

Quantitative oximetric maps post to bilateral trabeculectomies treatment are shown in Figure 9.13 and decreased venous oxygen saturation along the veins can be noticed.

Spectral imaging in subjects with asymmetrical POAG is able to detect oxygen saturation variations within the venular retinal circulation. The increased venular oxygen saturation in the more severely affected glaucomatous eye may indicate reduced inner retinal oxygen consumption as a result of reduced functional ganglion cell mass (Mordant et al. 2009). Further improvements in the imaging techniques using a snapshot spectral camera (See chapter 10) and analysis algorithms could enable the measurement of oxygen saturation in the retinal capillaries and other retinal chromophores (e.g neuroglobin) relevant to assessing the functional health of the retina in glaucoma. Snapshot technique could be used to screen for glaucoma and monitor the effects of medical and surgical treatment.

9.3.3.2 Measuring oxygen saturation in vein occlusion

Central retinal vein occlusion is one of the most common eye diseases and is classified as a vision-threatening disease. It occurs when a blood clot forms in a retinal vein. Blockage of one of the veins draining blood from the eye causes blood and other fluids to leak into the retina causing bruising and swelling as well as a change in oxygen saturation levels. This interferes with light receptor cells and reduces vision. Vision occlusion can be categorized into ischemic and non-ischemic types based on fluorescein angiographic finding.

To demonstrate the detection of oxygen saturation changes in the retinal vasculature of subjects with ischaemic and non-ischaemic retinal vein occlusion, retinal images were obtained from subjects with angiographically confirmed ischaemic ($n=3$) and non-ischaemic retinal vein occlusions ($n=2$).

In subjects with ischaemic retinal vein occlusion the quantitative retinal oximetry maps showed increased retinal venular oxygen saturation associated with areas of capillary non-perfusion. The areas of capillary non-perfusion are surrounded with white rectangles in the qualitative oximetric maps presented in Figure 9.14. The increased venous oxygen saturation is noticed along the veins.

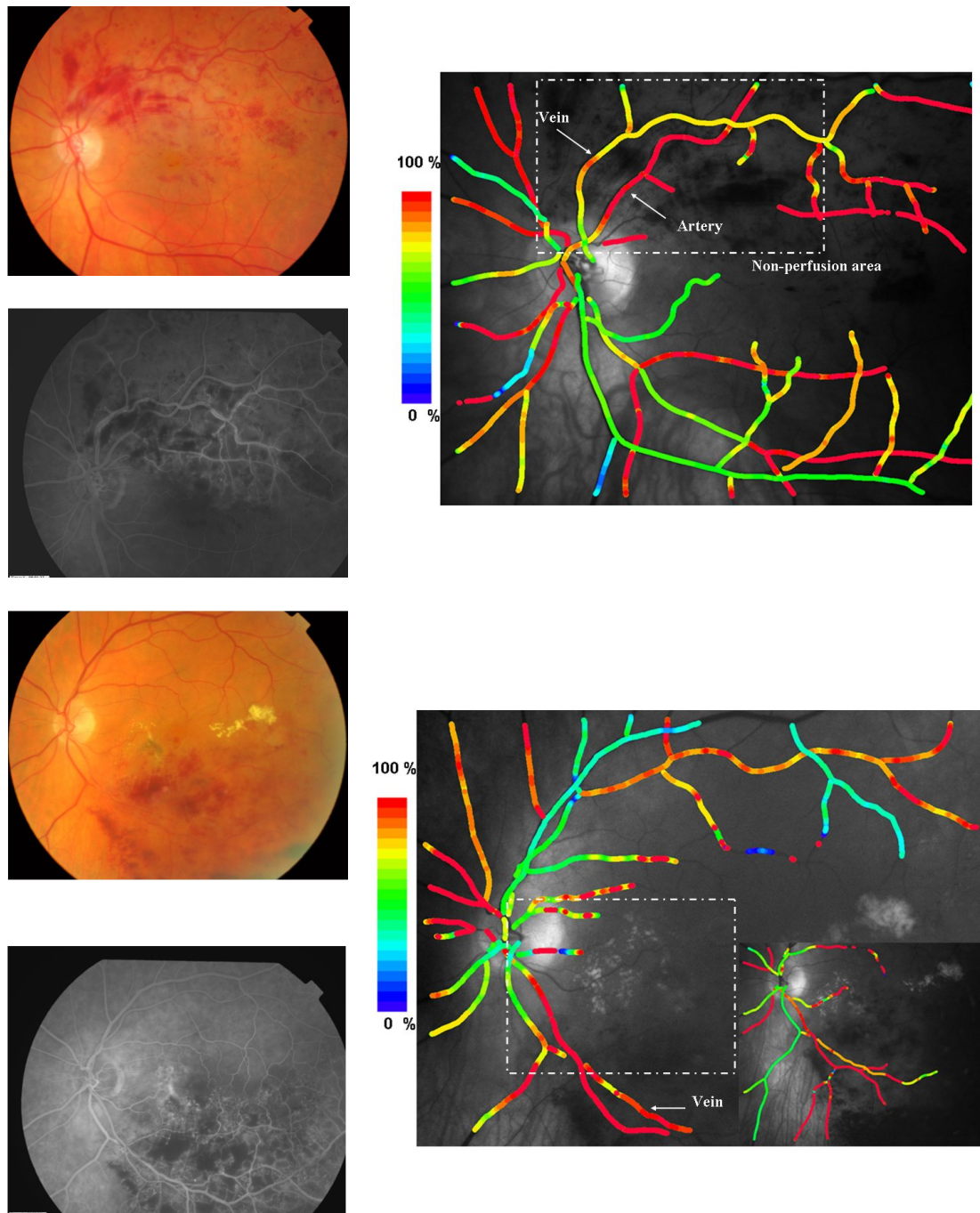


Figure 9.14: colour fundus images, Fluorescein Angiogram, and quantitative oximetric maps of Ischaemic RVO subjects (continues next page).

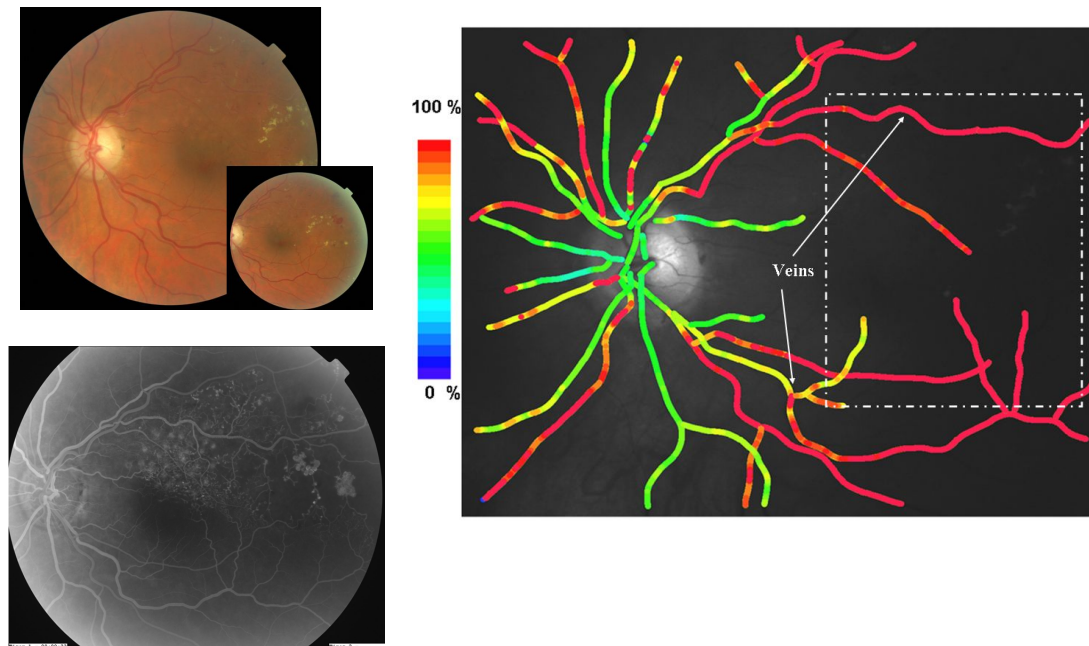


Figure 9.14 (from previous page): colour fundus images, Fluroescein Angiogram, and quantitative oximetric maps of Ischaemic RVO subjects.

The average oxygen saturation measurements obtained from Ischaemic RVO subjects were compared with those measured from normal subject. The difference in arterial oxygen saturation was significantly low ($\approx 1\%$). However, venous oxygen saturation measurements between normals and Ischaemic RVO subjects reported high difference ($\approx 25\%$) and this caused the arterio-venular difference to be higher in Ischaemic RVO subjects ($22 \pm 13.41\%$). The average saturation measurements are displayed in Table 9.7 and Figure 9.15.

	Normal Subjects mean (\pm SD)		Ischemic RVO Subjects mean (\pm SD)	
Retinal Arteriolar Oxygen Saturation	96 \pm 5	%	95 \pm 6	%
Retinal Venular Oxygen Saturation	48 \pm 9	%	73 \pm 18	%
Retinal Arterio-Venular Difference	46 \pm 7.28	%	22 \pm 13.41	%

Table 9.7: Average saturation measurements in Normal and Ischaemic RVO subjects.

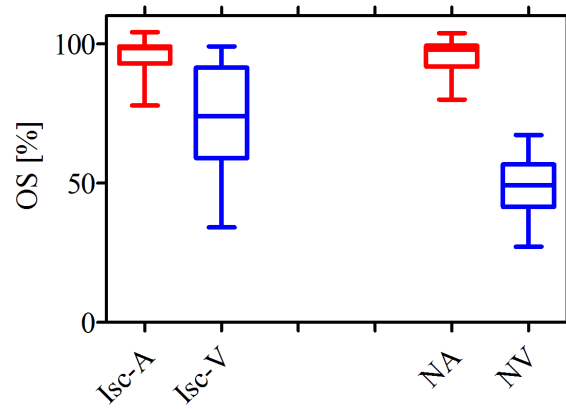


Figure 9.15: Oxygen saturation measurements in Normal subjects (NA,NV) and Ischaemic RVO subjects (Isc-A, Isc-V).

In subjects with non-ischaemic retinal vein occlusion, the retinal venular oxygen saturation appears to be lower than normal. Figure 9.16 shows quantitative oximetric maps of two subjects. Low venous oxygen saturation values were indicated and represented in blue colour.

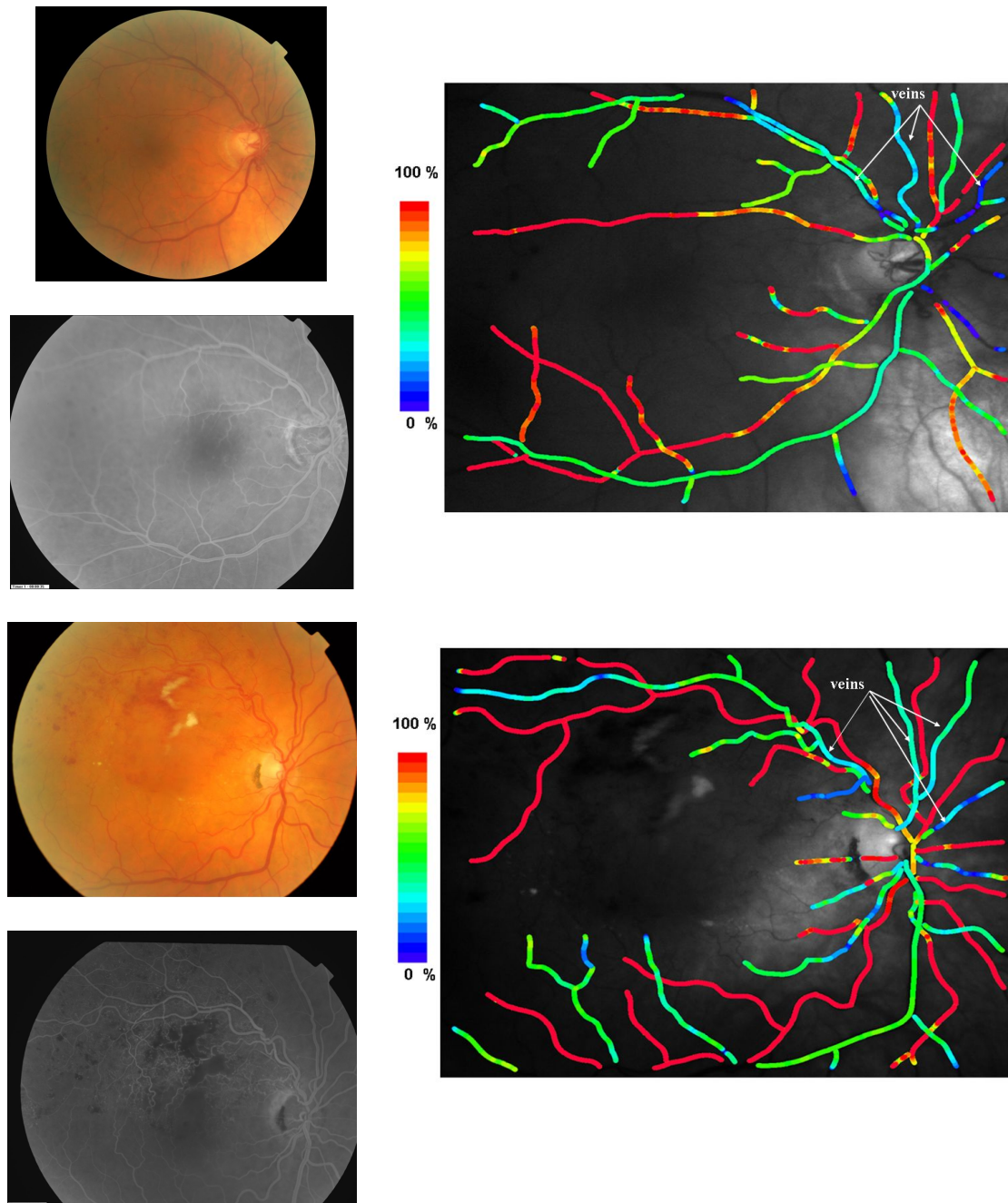


Figure 9.16 Colour fundus images, Fluroescien Angiogram, and quantitative oximetric maps of 2 Non-Ischaemic RVO subjects.

The analysis results of comparing the oxygen saturation measurements between normal and non-Ischaemic RVO subjects are presented in Table 9.8 and Figure 9.17. The mean arterial oxygen saturation was almost similar in healthy and RVO subjects in which small difference ($\approx 2\%$) was reported. The mean venous oxygen saturation

was of value $(40 \pm 11)\%$ which is 8% lower than those obtained from normals. The arterio-venular difference in non-Ischaemic subjects showed 8 % increase.

	Normal Subjects mean (\pm SD)		N Subjects mean (\pm SD)	
Retinal Arteriolar Oxygen Saturation	96 \pm 5	%	94 \pm 6	%
Retinal Venular Oxygen Saturation	48 \pm 9	%	40 \pm 11	%
Retinal Arterio-Venular Difference	46 \pm 7.28	%	54 \pm 8.86	%

Table 9.8 Saturation measurements in Normal subjects & Non-Ischaemic RVO subjects.

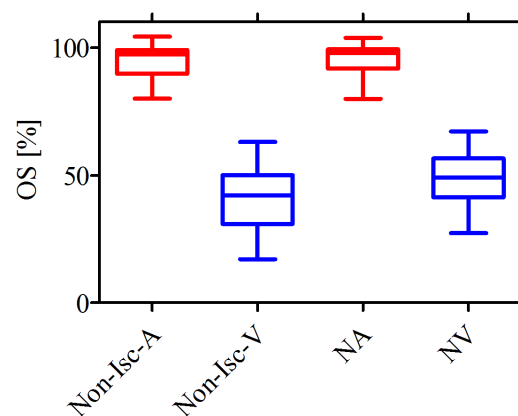


Figure 9.17 Oxygen saturation measurements in Normal subjects (NA,NV) and Non-Ischaemic RVO subjects (Non-Isch-A, Non-Isch-V).

Quantitative analyses of hyperspectral retinal images have the potential to detect oximetric changes in the retinal vasculature in ischaemic and non-ischaemic retinal vein occlusions. Increased venular oxygen saturation in ischaemic retinal vein occlusion may indicate either reduced metabolic consumption of oxygen in the inner retina or an arterio-venous shunting phenomenon within the retinal circulation. On the other hand, reduced venular oxygen saturation in non-ischaemic retinal vein occlusion may indicate the consumption of residual venular oxygen diffusing out of stagnant

retinal venules by functioning retinal tissues. Further analysis of a larger population of subjects with retinal vein occlusion is required to confirm this finding.

9.4 Conclusion

Quantitative oxygen saturation measurements were analysed for normal and diseased retinas. Oxygen saturation measurements performed on healthy subjects were in good agreement with those found in the literature. However, saturation errors are introduced due to simplicity of the adopted optical model. The dependency of OS on η , C , d generated 4% and 12 % saturation variation for arterial and venous blood respectively. To overcome this dependency, an appropriate scattering function is needed. Oxygen saturation measurements were reproducible with a notable variance in venous blood saturation due to metabolic activity of the retina. The ability of the technique to detect oxygen saturation changes was also evaluated by considering two common diseases Glaucoma and central vein occlusion. Analysis results showed significant changes in venous oxygen saturation in subjects suffering from these conditions. On the other hand, arterial blood showed no significant variation. Future directions will consider looking at subjects with different conditions such as diabetic retinopathy and age related macular degeneration in addition to increasing the number of cases to enable to define a merit of the studied diseases. Recording spectral images using a snapshot camera, more suitable for clinical application and patient comfort, will be discussed in the following chapter.

Chapter 10

IRIS:Image Replicating Imaging Spectrometer

In this chapter, a unique snapshot spectral imaging technique dubbed IRIS will be presented. A construction of retinal imager based on IRIS will be described. Results of early clinical trials acquired with this technique will be shown using semi-quantitative and quantitative retinal oximetries.

10.1.Introduction

In this thesis we have described how one solution to recording the required three-dimensional data cube using a two-dimensional detector array is to record images in time sequence in a way that scans one of the cube dimensions (particularly the wavelength λ). In this technique, a sequence of narrow-band images are recorded and subsequently calibrated and co-registered. This time-sequential nature is undesirable as the time required to record the data cube may prevent capture of time varying scenes. Combined with the infirmity that is common in patients with eye diseases, the increased time can be problematic for both patient comfort and on the impact of image quality. We have shown earlier (section 4.3.3 ,chapter 4) that in spite of the implementation of spectral calibration and image co-registration algorithms, some sort of residual errors remain and hence influence accurate quantification of retinal chromophores. Calibration and registration can be highly problematic and it is not possible to record *en face* time-resolved spectral images. Unfortunately, a putative snapshot spectral camera; the spectral imaging equivalent of the conventional RGB colour camera has been notable by its absence. In this chapter, we report the

development of a novel two-dimensional snapshot retinal camera that records a spectral data cube directly onto a conventional detector array and requires no complicated inversion algorithm to retrieve the spectral information. The snapshot capability removes some fundamental problems associated with time-sequential techniques which affect accurate blood oximetry.

10.2. Instrumentation: Retinal oximeter

The retinal oximeter consists of an image replicating imaging spectrometer (*IRIS*) together with a digital camera (Monochrome Cooled Retiga-4000R by Qimaging, Canada) at the output port of a conventional retinal camera (Discam by Marcher Enterprises Ltd. UK). The experimental setup is shown in Figure 10.1.

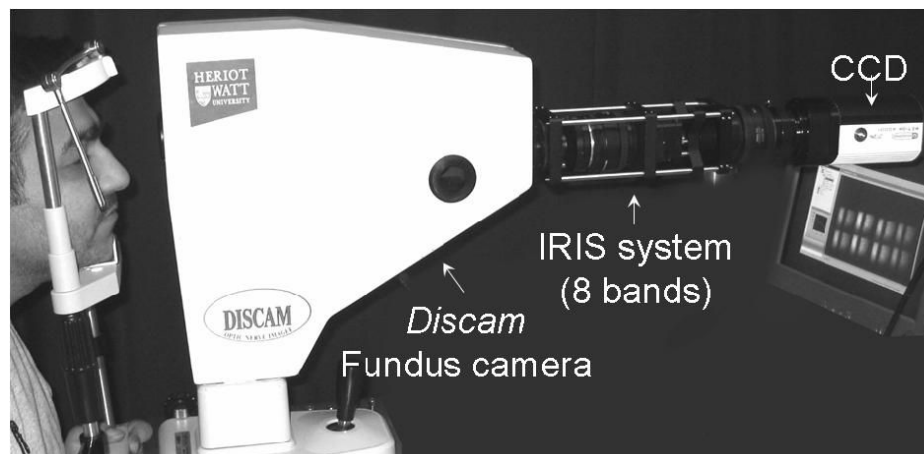


Figure 10.1: Experimental setup of IRIS retinal oximeter.

IRIS is a spectral demultiplexer that employs polarising interferometry and Wollaston prism polarising beam splitters to simultaneously replicate images of the retina in multiple spectral bands onto a single detector array. IRIS is an innovative and patented technique developed at Heriot-Watt University and offers significant potential for a snapshot HSI sensor, to enable benefits for the wider public beyond aerospace imaging (Harvey and Holmes 2004).

The principle of operation of an 8-channel IRIS ($N=3$) is depicted in Figure 10.2. Essentially, IRIS combines N retarders and N Wollaston prisms to generate 2^N replicated quasi-monochromatic images. The thicknesses of the N retarders determine the spectral transmission for each of the 2^N channels. Since no rejection of light occurs through either spectral or spatial multiplexing, this technique is in principle 100% optically efficient enabling the intensity of light at the retina to be minimised. A complete description of the functioning principles of *IRIS* can be found in Harvey et al. (2005).

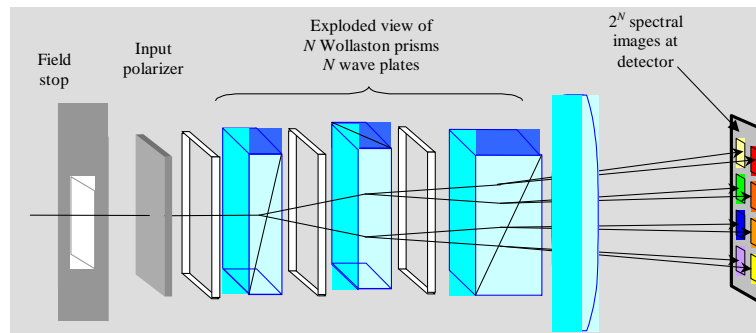


Figure 10.2: Principle of operation of IRIS

IRIS can be considered as a generalisation of a Lyot filter, which enables high efficiency spectral demultiplexing of broadband light. To describe the principle of operation of IRIS, the principle of a conventional Lyot filter should be considered (see Chapter 3).

A generalisation of this technique is employed with the IRIS concept described here whereby the film polarisers are replaced with Wollaston prism polarising beam splitters as shown in Figure 10.2. The use of a polarising beam splitter means that after transmission through each waveplate the light is resolved into polarisations both, aligned with, and orthogonal to, the input polarisation state. As with the Lyot filter, for the co-polarised component the transmission function is given by $\cos^2(\pi v(n_o - n_e)t)$;

for the cross-polarised component the transmission function is $\sin^2(\pi v(n_o - n_e)t)$. Furthermore, these two orthogonally polarised components are displaced in angle by the beam-splitting action of the Wollaston prism and this enables two spatially separated and spectrally filtered replica images to be formed. Subsequent Wollaston prism polariser pairs further spectrally filter and replicate the images. After transmission through n Wollaston prism polariser pairs, 2^n replicated images are formed, each with a unique product of \sin^2 and \cos^2 transmission functions. It can be seen then that the IRIS technique simultaneously replicates the image formed at the field stop whilst applying a unique spectral filtering function to each image; this filtering function is determined by how light arriving at each image was steered and spectrally modulated. The images at the detector array are prevented from overlapping by the field stop. The orientation and magnitude of the splitting angles of the splitting angles of the Wollaston prisms determine the locations of the replicated images at the detector;

The spectral transmissions for the IRIS channels have been selected to allow oximetry. The dominant factor determining the reflectivity of the retina is the absorption spectrum of haemoglobin (oxygenated and deoxygenated), which was shown previously. (See Figure 5.3). We have discussed earlier (see section 5.7, Chapter 5) the best wavelength combinations to perform accurate retinal oximetry for two, three and multiple wavelength combinations. When two-wavelength oximetry was considered, the combination of 578 and 600 nm generated the lowest saturation error. On the other hand, for three wavelength oximetry the triad 578, 596 and 646 nm produced low saturation error. We have also shown that as the number of wavelengths increases, the accuracy of the oximetry increases. The integration of these findings

with the capability of *IRIS* to create 8 spectral bands with a reasonable field of view suggests that the suitable spectral region for retinal blood oximetry using *IRIS* occurs from 560nm to 600nm. Within this interval (see Figure 10.3), the haemoglobin absorption coefficient experiences rapid variations with oxygen saturation and there are two isobestic points (i.e. where the absorption coefficient is independent of the oxygenation state of blood).

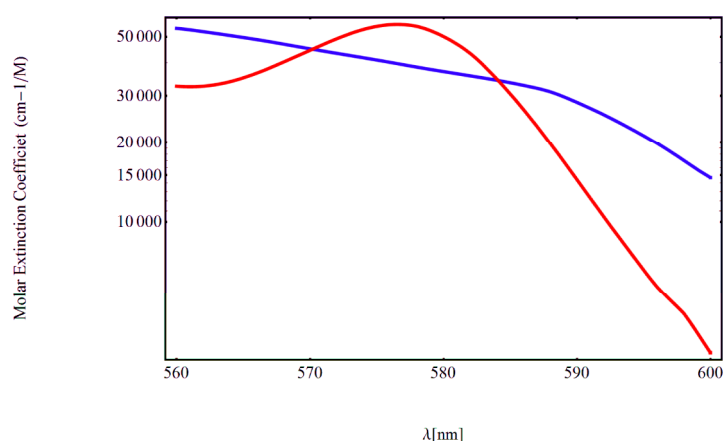
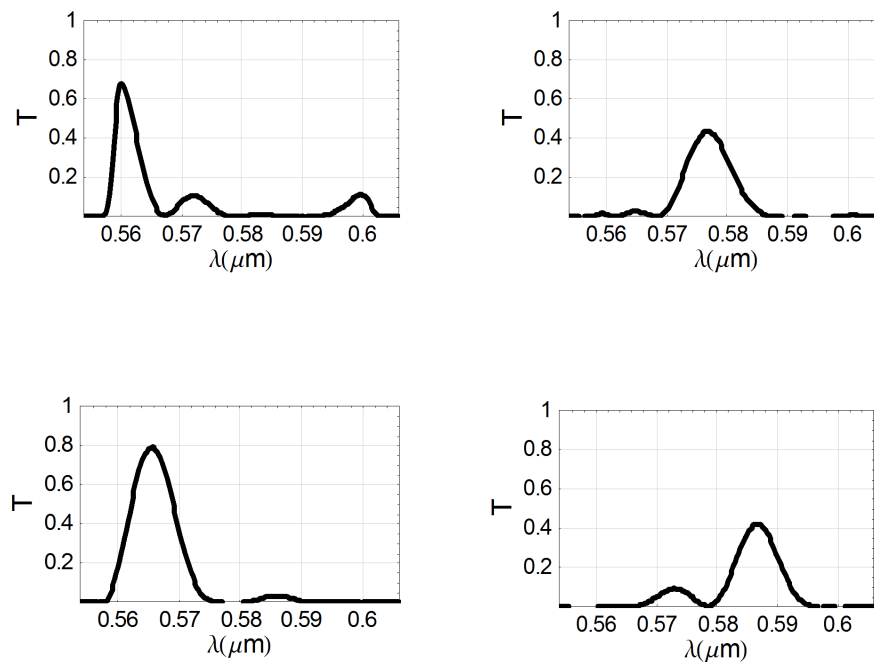


Figure 10.3: The extinction coefficients of both oxygenated (red) and deoxygenated (blue) haemoglobin in the range 560-600 nm.

Recording retinal images at isobestic points enables simple calculation of retinal oximetry depending on two or three wavelengths (Delori 1988; Beach, 1999; Handarson, 2006; Hammer 2008). The selection of the 560-600nm interval is also motivated by the fact that for wavelengths greater than 600nm, light starts to penetrate the choroid and therefore the retinal background becomes highly spatially variable, possibly introducing significant errors in the apparent vessel transmission recorded by the detector. At these longer wavelengths, the optical depth has considerably exceeded the thickness of all blood vessels and hence arteries and veins become effectively translucent. In contrast, for wavelengths shorter than 560 nm the optical depth for both oxygenated and deoxygenated blood is significantly less than the diameter of all

but the smallest blood vessels and so both oxygenated and deoxygenated blood within the vessels are effectively opaque.

The thicknesses of the three retarders have been appropriately optimized to provide eight spectral bands from 560nm to 600nm. The optimization of the thickness values has been performed against a cost function that maximizes the optical power of the main peaks of each transmission function (hence, reducing the sidelobe power). Additionally, some transmission bands were modulated by spectral blood transmission according to Lambert-Beer's law to maximize the spectral separation between oxygenated and deoxygenated blood, while others were modulated to produce retinal images practically insensitive to oxygen saturation (isobestic bands). An unusual aspect of *IRIS* is that the spectral transmission bands are not quite orthogonal in spectral space, but this issue is not significant relative to the high signal-to-noise ratio and snapshot characteristic. The measured spectral passbands are shown in Figure 10.4.



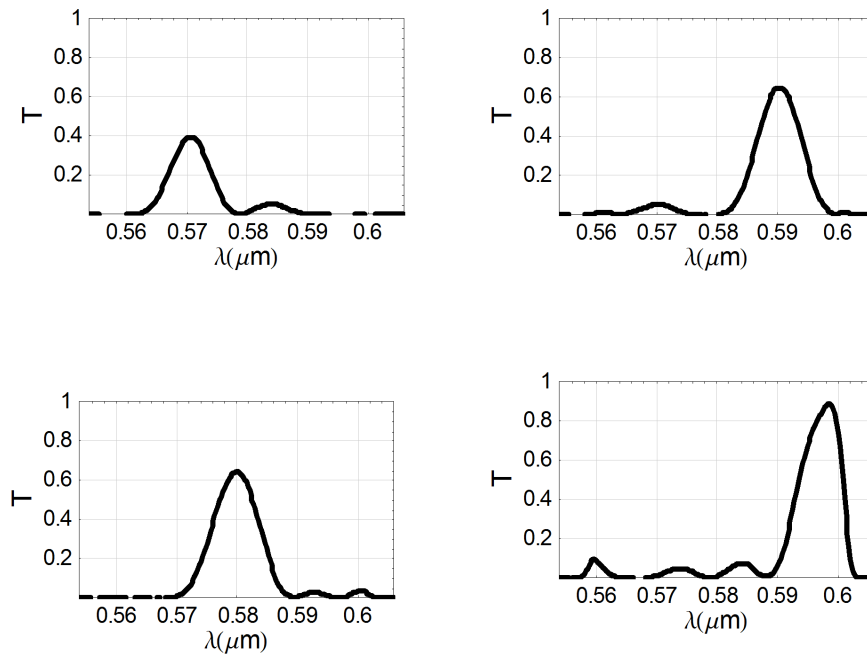


Figure 10.4: IRIS transmission bands.

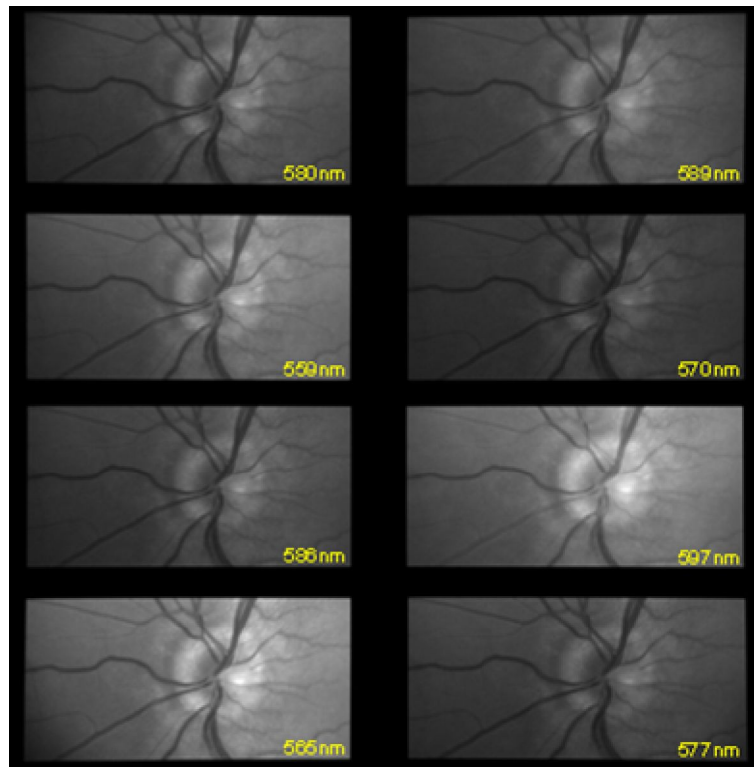


Figure 10.5: Eight narrow-band images of an optic disc recorded at the detector. The wavelength associated with each sub-image corresponds to the maximum peak transmission of the spectral band..

On integrating *IRIS* into the optical path of the Discam camera, eight replicated narrow-band images can be recorded in a single snapshot. Each single snapshot was recorded in synchronization with triggering a custom-made flash lamp. Figure 10.5 shows 8 *IRIS* retinal images taken at single snapshot. The variations of the gray levels between images are due to the spectral filtering functions of the *IRIS* system. There was a clear discrimination between veins and arteries due to the systematic variation of optical density as a function of wavelength. Clearly, the snapshot spectral capability enables improved oxygen measurements in the retina by eradicating illumination variations and misregistration problems associated with the time-sequential technique. Real time spectral retinal imaging was also possible, albeit of lower quality, using only low power continuous tungsten inspection lamp.

10.3. Post-processing and data analysis

Prior to retinal oximetry, each snapshot was decomposed into its constituent eight images. Then the spectral image cube was constructed by co-registration of these eight sub-images. The registration process is a calibration step which corrects for geometric distortions introduced by the imaging lens. After performing this calibration step, subsequent sets of sub-images can be registered, using a simple two-dimensional polynomial transformation.

After constructing the data cube, spectral processing and oximetry calculation can take place by applying the same procedures applied to the sequential images (see chapter 6 and 7) to calculate optical densities along the blood vessels.

10.4. Retinal oximetry

Preliminary oxygen saturation measurements from *IRIS* images were performed using two techniques: semi-quantitative, based on spectral linear unmixing and two-wavelength oximetry. A third technique, currently under development, performs more accurate oximetry by numerically fitting experimental measurements from all eight *IRIS* images into a physical model of light propagation in retinal vessel. *Prior* to oxygen saturation calculation, the effect of *IRIS* transmission bands on the extinction coefficients of oxygenated and deoxygenated haemoglobin has to be taken into account. This involved an extraction of the new extinction coefficient as discussed earlier for the LCTF (see section 7.6.5). Due to the effect of the side bands, as depicted in Figure 10.4, the wavelength space is replaced by *IRIS* band space. The new extinction coefficients in *IRIS* space are given in Figure 10.6. As shown in the figure, band 3 shows the same properties as an isobestic band. However, bands 1, 4, and 8 exhibit the maximum difference.

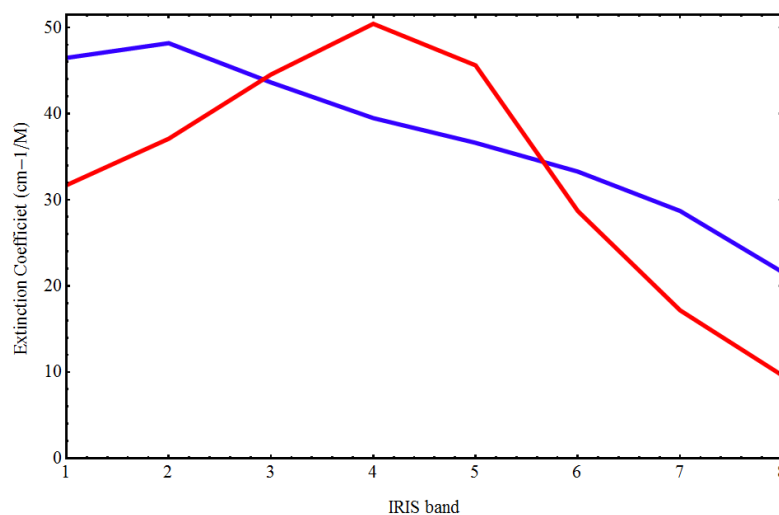


Figure 10.6: Extinction coefficients of oxygenated and deoxygenated haemoglobin in *IRIS* space.

10.4.1 Semi-quantitative retinal oximetry

It was reported previously, in chapter 6, that oxygen saturation can be mapped by means of linear spectral unmixing, depending on the spectra of oxygenated and de-oxygenated blood in the retinal vessels.

This processing method employs the spectra of oxygenated and de-oxygenated blood to produce a semi-quantitative oximetry map. The model assumes that the spectrum of each pixel in the data cube can be decomposed into a linear combination of the endmembers. PCA was employed *prior* to unmixing to determine the main components contributing to the blood spectra. Three endmembers were considered: the oxygenated blood, the deoxygenated blood and retinal background. As a result, regions of interest were selected from arteries, veins, and retinal background. Linear unmixing then was applied to the 8 sub-image data cube. The final mapped images for a healthy subject are shown in Figure 10.7 (images are displayed in colour). It can be observed that the retinal vasculature can be mapped as a function of the oxygenation levels. Oxygenated (99% oxygen saturation) and deoxygenated blood (50% saturation) are represented by red and black respectively. The intermediate oxygen levels in retinal vessels are given by a linear combination of these two colours.

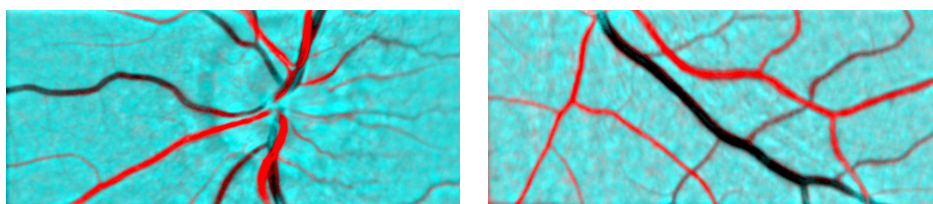


Figure 10.7: Semi quantitative oximetry maps using linear spectral unmixing.

10.4.2 Quantitative oximetry using two-wavelength

As was shown in chapter 5, two-wavelength oximetry requires calibration. This is due to the fact that spectrum of the light reflected from the blood sample depends not only on the oxygen saturation but also on the blood concentration, blood sample thickness and light scattering. Simple calibration was found by considering one of the wavelengths to be isobestic. Considering *IRIS* space, oxygen saturation for two wavelengths can be given as:

$$OS = \frac{OD^{i2} \varepsilon_{Hb}^{i1} - OD^{i1} \varepsilon_{Hb}^{i2}}{OD^{i1} (\varepsilon_{HbO2}^{i2} - \varepsilon_{Hb}^{i2}) - OD^{i2} (\varepsilon_{HbO2}^{i1} - \varepsilon_{Hb}^{i1})}, \quad (10-1)$$

where OD^i denotes the optical density at i *IRIS* band, $\varepsilon_{HbO2}, \varepsilon_{Hb}$ are the extinction coefficients of oxygenated and deoxygenated haemoglobin respectively, after taking into account the effect of *IRIS* transmission bands. A linear relationship between oxygen saturation (OS) and optical density ratio (ODR) was anticipated: when isobestic band ($i2$) is assumed:

$$OS = a.ODR - b \quad (10-2)$$

$$ODR = \frac{OD^{i1}}{OD^{i2}}, \Delta\varepsilon^{i1} = \varepsilon_{HbO2}^{i1} - \varepsilon_{Hb}^{i1}, a = \frac{\varepsilon_{Hb}^{i2}}{\Delta\varepsilon^{i1}}, b = \frac{\varepsilon_{Hb}^{i1}}{\Delta\varepsilon^{i1}}$$

The parameters a and b can be extracted from the extinction coefficients of oxygenated and deoxygenated haemoglobin directly. Due to the scattering by red blood cells, the parameters a and b have to be determined from *IRIS* sub-images (Hardarson, 2006). Average values for saturation, 96% and 54% were assumed for arterial and venous blood (Harris et al, 2003). By considering the following *IRIS* bands ($i_1=1, i_2=3$), we calculated the average ODR of 0.73 for arterioles and 0.89 for veins (optical densities were measured from 5 healthy subjects). Assuming the linear relationship as in (10-2), we can write:

$$\begin{aligned} 0.96 &= 0.73a + b \\ 0.54 &= 0.89a + b \end{aligned} \tag{10-3}$$

Solving the two equations resulted in $a = -2.625$ and $b=2.88$. As a result the equation to calculate the oxygen saturation is given in

$$OS = -2.625ODR + 2.88 \tag{10-4}$$

The application of (10-4) on 4 healthy subjects was in agreement with the literature. The mean arterial and venous oxygen saturations (98 ± 11 % and 52 ± 11 %) at different locations were in good agreement with oxygen saturation measurements obtained by time-sequential technique. The variation in oxygen saturation measurements along veins and arteries is shown in Figure 10.8 and Table 10.1.

	Artery OS	Venous OS	Arterio-venular difference
Mean±SD %	98±11 %	52±11 %	46±3 %

Table 10.1: Oxygen saturation along veins and arteries.

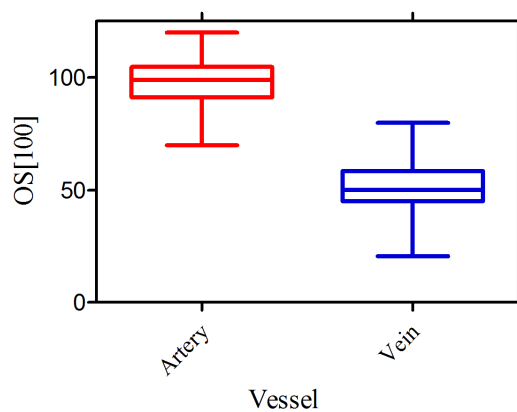


Figure 10.8: Oxygen saturation measurements from 4 healthy subjects.

The colour coded oximetric maps are presented in Figure 10.9, and consistent oxygen saturation can be noticed along the considered vessels.

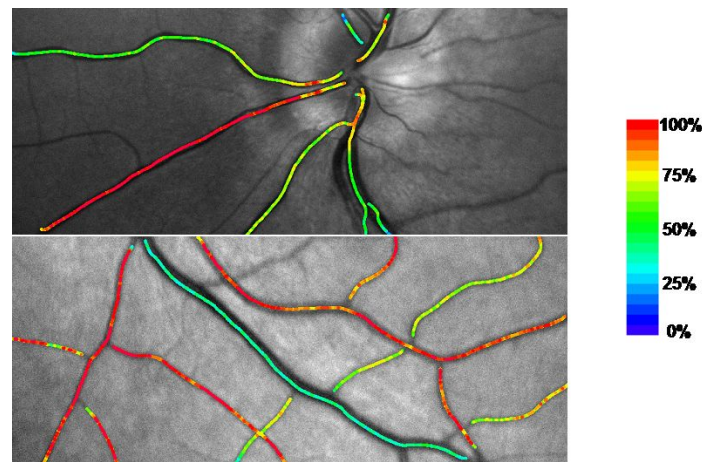


Figure 10.9: Colour coded map of oxygen saturation in retinal vessels.

The level of simplification employed in this study by using only 2 bands explains the increased standard deviation especially for arterial blood. To obtain more accurate quantitative measurements, further processing is necessary, including incorporating all *IRIS* bands into a physical model of light propagation as discussed earlier in this thesis. Additionally, a validation of the technique using a model eye setup is under development at the time of writing this thesis.

10.5. Conclusion

This chapter has introduced a novel spectral imaging technique that offers real-time and snapshot capability which is highly desirable for oximetry and for usability in a clinical instrument. Multiple acquisitions of spectral images in a single frame have been reported using the *IRIS* snapshot technique. The shape and number of *IRIS* spectral bands were optimised to perform snapshot oximetry. The resulting optimised snapshot spectral retinal imager will enable enhanced biochemical measurements in the retina by eradicating calibration and misregistration problems associated with

time-sequential techniques. Oximetric saturation maps from healthy patients were generated using two quantitative and semi-quantitative techniques. Preliminary results showed the capability of *IRIS* to perform retinal oximetry. Future work using all spectral images from this snapshot technique will include the development and refinement of the physical model for light propagation, to accurately measure oxygen saturation in the retinal circulation, as well as validation with artificial eye measurements.

Conclusion and future work

The work in this thesis has shown that it is possible to extract an absolute measure of percentage oxygen saturation in retinal blood vessels, using spectral imaging. The application of oximetric techniques to study the functional health of the retina has the potential to enhance the understanding of the pathophysiology of certain retinal diseases and may also in the future influence the management of the patient. The transparent media of the eye allow the possibility of a non-invasive study of the ocular fundus by analysing the reflected light at multiple wavelengths. The characteristics of the reflected light are dependent on the response of the tissue of the retinal layers, which in turn depends on wavelength, the subject, and the fundus area under investigation.

The selection of a time sequential technique to record spectral retinal images was motivated by many factors, such as the need to obtain an extended two-dimensional field of view suitable for retinal disease screening programs, and the ability to record a selective number of narrow spectral bands. The possibility of reducing the number of wavelengths to those that contain the variation necessary for accurate quantification of oxygen saturation can improve the signal-to-noise ratio and patient comfort and reduce the time necessary to construct an informative data cube. Therefore, this technique serves as a non-invasive research tool to detect functional

changes in the retina and retinal vessels to provide the possibility of investigating many wavelength combinations to detect the presence of various chromophores associated with certain diseases in the retina.

As retinal images were recorded in a time sequence, there were additional associated problems such as the need to register the retinal images and to calibrate the effects of varying retinal illumination between images. The variation in illumination was due to the varying amount of light entering the pupil due to the eye movement and the variation of flash light intensity between two consecutive images. Calibration of retinal images was applied to reduce the effect of the artefacts and reflections from the surfaces of the optical components (fundus camera) in addition to detector noise (fixed pattern noise). The calibration, shown in chapter 4, was performed throughout an optimization process employing a subtraction of the artefact effect from the retinal images. Images at shorter wavelengths (<500 nm) showed low signal to noise ratio ($<<10$ dB) when compared with those recorded at longer wavelengths. Retinal images were recorded in the useful wavelength range 500-700 nm.

A two dimensional cross-correlation function was employed to correct for the translational and rotational misalignments. Registration was applied on pre-processed images to extract distinctive features (such as the retinal blood vessel tree) shared between retinal images. The accuracy of the registration algorithm (chapter 4) was quantified to be less than 1 pixel when images at the same wavelength (580 nm) were registered and less than 2 pixels when dissimilar wavelengths such as 500 and 650 nm were registered. Several factors influenced the registration accuracy, such as patient comfort, heart pulses, and off-axis optical aberrations. For our purpose the registration

accuracy obtained (1 pixel) was sufficient to measure the oxygen saturation along the blood vessel tree but for smaller features sub-pixel accuracy is needed, this can be achieved by employing local registration on small areas (areas of interest) selected from the retinal images.

To perform oxygen saturation measurements, optical densities along blood vessels were measured. Optical density maps and, shown in chapter 6, were generated globally by means of estimating the intensity in the absence of blood vessels. This was done by employing a lowpass filter whose kernel size was adjusted to separate the changes in illumination from those due to retinal background. Once the optical density maps were calculated, linear spectral unmixing was applied to map oxygen saturation semi-quantitatively. The level of uncertainty in this method was quite high, due to the errors in estimating the optical densities and the simplified linear model in which scattering was neglected. Semi-quantitative maps are valuable tool to monitor the oxygen saturation status in the retina by minimally processing the data cube, which according to clinical trials we carried out, show changes in venous oxygen saturation associated with certain diseases.

Local calculation of optical densities along the blood vessel tree suppressed the saturation error due to residual errors in registration. Local calculation of *ODs* was performed by implementing a vessel tracking algorithm to extract the transmission profiles and calculate the optical density in the centre of the blood vessel. This thesis proposed an analytical model based on blood vessel geometry and Lambert-Beer's law to calculate the optical density and vessel diameter in the presence of specular reflection. An optical model of light propagation through blood vessels was then employed to calculate oxygen saturation. An ideal optical model should take into account the effect of scattering as a function of both wavelength and oxygen

saturation in addition to the multi-optical path factor which is a result of single and double passage of light within the blood vessel. Single and double pass proportions were found to be a function of vessel diameter, tissue PSF width, wavelength, and fundus reflectivity. However, it was difficult to assess the contribution of these parameters within the retina.

The effect of illumination variation was studied and its effect on the saturation measurements was quantified. Two types of variations were introduced between retinal images: variation due to the sequential nature between images and spatial variation within the field of view of the image and along the blood vessels. Variations between the images in the sequence were evaluated by calculating the reproducibility of the optical density measurements. We have found that acquiring images in sequence resulted in a calculated transmission error around ($\Delta T=2.6\%$) which in turn can produce a maximum saturation variation of ($\Delta OS=0.4\%$) for a wavelength range 500-650 nm measured at 2 nm intervals. It was shown in chapter 5 that as the number of wavelengths to measure oxygen saturation decreased, the saturation error increased. The increased number of wavelengths has the effect of reducing the contribution of higher transmission errors encountered at longer wavelengths >600 on *OS* measurements.

The effect of spatial illumination variation along the blood vessels was also investigated in chapter 7 and reduced by employing principle component analysis. PCA suggested that only two main absorbers, the oxygenated and deoxygenated haemoglobin, contribute to the overall spectrum of the blood. This implies that the effect of melanin absorption spectra or other chromophores can be ignored. In this project, therefore, PCA was used as a tool to minimize the variation along retinal vessels due to spatial illumination variation and the effect of retinal background.

A model eye in chapter 8 was designed and constructed for the purpose of investigating the ability of our instrument to carry out retinal oximetry. The model eye was used as a tool to study the validity of the optical model as well as the developed algorithms. It offered an environment similar to the human eye, in which some parameters, such as vessel diameter, blood oxygen saturation, and fundus reflectivity, could be controlled and varied. Oxygen saturation calculations were compared with gold- standard OS measurements obtained by the Co-Oximeter.

It was clear from the model eye experiments that a scattering term that varies as a function of oxygen saturation is required to obtain accurate results. An assumption of constant scattering was responsible for a saturation error of $\Delta OS=4.89\%$. On the other hand, when an empirical scattering function was considered, analysis results showed that single pass is dominant and independent of fundus reflectivity.

For measurements on human subjects, scattering was considered as wavelength independent. The application of the optical model has shown differences in oxygen saturation levels between veins (less than 60%) and arteries (more than 90%) along the blood vessel tree. The saturation measurements (as shown in Table 11.1) were in good agreement with ophthalmologist expectations, in which a clear discrimination between veins and arteries was achieved on various areas along the blood vessels. Measurements performed on healthy subjects showed some degree of dependency of OS on $\eta C d$ and was more pronounced for venous blood. This dependency increased the uncertainty in estimating blood vessel saturation ($\Delta OS_A=4\%$ for arterial blood and $\Delta OS_V=12\%$ for venous blood) and was believed to be due to the relative simplicity of our model, which does not completely take into account scattering that depends on various factors such as blood hematocrit concentration and oxygen saturation. The

dependency of scattering on $\eta C d$ was modelled linearly with $R^2=0.0702$, $\rho<0.0001$ and was found to increase slightly as the value of $\eta C d$ increased.

The mean value of arterial and venous blood oxygen saturation were $OS_A=96\%$ and $OS_V=48\%$ respectively. Arterial blood oxygen saturation measurements reported fairly constant saturation with 5% error, in contrast to venous blood saturation which showed significant variation of 9%. The artery-vein saturation difference (47%) was higher than that those reported in the literature (35%) (Drewes et al., 1999; Smith et al., 2000; Haris,2003; Michelson et al 2006; Hardarson et al.,2006) as shown in Table 11.1.

Authors	Technique	Wavelength	In Vitro	Oxygen saturation[%]	
		[nm]	measurements	Artery	Vein
Hickam et al.	Beam splitter +filters	640,800	6% and 9%	-	58%±10%
Beach et al.	Beam splitter +filters	600,569	-	-	55%±3.39%
Delori et al.	Filter wheel incorporating to fundus camera	586,569,558	3.5%-5.9%	98±8%	45%±7%
Schweitzer et al.	Line scan(spectrograph)	510 to 586	—	92%±4.1%	57.9%±9.9%
Hardarson et al.	Beam splitter+ filter	586,605	—	96% ± 9%	55% ±14%
Hammer et al.	Pass band filters	548,610	—	98%±10.1%	65%±11.7%
AlAbboud et al	LCTF based technique	500-700 nm	3.3%-4.89%	96%±5%	48%±9%

Table 11.1: Oxygen saturations veins and arteries of normal subjects

The saturation measurements of arteries and veins repeated on two subjects were correlated with a higher variance for venous saturation which might be due to the metabolic activity of the retina. The results were presented as colour-coded maps which reflected the oxygen saturation status into the major blood vessels of the retinal vasculature. For clinical applications, absolute accuracy of OS measurements is

important in that any alteration in the difference of oxygen saturation between veins and arteries in response to the retinal disease is vital.

To assess the clinical potential of our technique, two common retinal disorders were considered: glaucoma and retinal vein occlusion. Venous oxygen saturation was noticed to increase in retinas associated with these diseases. A comparative study between healthy and diseased subjects was carried out to establish a merit for each disease. Decreased oxygen saturation was noticed for one patient after treatment, which supported our interpretation that increased venous saturation is related to the function of the retinal tissue. Measuring retinal oxygen saturation was important because it was possible to: indicate the onset of the retinal disease, the severity of the condition and monitor the progression of the disease and the effect of the treatment.

Thus far in this thesis, we have introduced the time-sequential technique as a highly flexible approach to acquiring a wide-field spectral data cube for research and clinical exploration. However, in terms of clinical applications, a wide-field snapshot technique is desirable. We have proposed in chapter 10 a novel snapshot system spectral retinal imager in which acquisitions of multiple spectral images in a single frame have been performed using the *IRIS* snapshot technique. *IRIS* bands were optimized to enable retinal oximetry in the wavelength range 560-600 nm. Within this range, the haemoglobin absorption coefficients varied rapidly as a function of oxygen saturation and two isobestic wavelengths were found to exist. This technique holds the promise of enabling improved retinal oximetry by eradicating calibration and misregistration problems associated with a time sequential technique. Semi-quantitative and quantitative (two-wavelength oximetry) oximetric maps were generated to demonstrate *IRIS* capability. Results were in agreement with measurements obtained using the time-sequential technique.

Future work

To this point, we have verified that accurate quantification of oxygen saturation of the retina necessitates an imaging system with high performance, in addition to a unique optical model. Several issues related to the imaging system and developed algorithms still need to be addressed and resolved in the future work.

Accurate oxygen saturation measurements require a precise optical model which completely accounts for scattering by red blood cells, the contribution of melanin and other haemoglobin derivatives, and the effect of multi-optical paths as light propagates toward the retinal vessels. To perform that, a modified version of the model eye (model eye-2) is being constructed to enable measurement of backscattered light from the blood column in addition to the other light components. In the new setup, it is important to incorporate several layers to enable variable texturing of the albedo to assess blood oximetry within an environment as similar as possible to the human retina. In this way, the contributions of the multiple light paths can be varied in a controlled manner. Additionally, the new model eye should enable easy removal of the layers, to allow the measurement of individual components of multiple scattered light. This involves measurement of forward scattered light and the image of blood vessels and other clinically important structures in reflection and transmission. Furthermore, a Monte-Carlo simulation can be employed to simulate backscattered and transmitted response from a blood vessel inside a bulk (clear or light scattering) layer which can be investigated in front of various layers simulating the retinal layers. Once complete understanding of scattering, the effect of optical paths and the contribution of different chromophores is obtained, a physical model can be built and employed to perform retinal oximetry.

We have shown previously that retinal images acquired at shorter wavelengths (<500 nm) encountered low SNR. One practical option to improve the SNR is replacing the detector chip with one that has higher quantum efficiency at blue wavelength range, as neither the illumination intensity nor the LCTF response can be changed at this range. Measuring the spectrum of reflected light at wavelengths shorter than 500 nm is important to quantify the chromophores present in the retina and dominant at this range such as macular pigment, lipofuscin, and melanin.

For clinical application, future work will concentrate on developing a wide-field snapshot technique based on *IRIS*. To obtain oxygen saturation measurements, a physical model should take into account the spectral transmission of *IRIS* bands, with side lobes, and their effect on the measured blood absorption and scattering coefficients. The developments will consider also inversion techniques to apply on experimental *IRIS* data based on Backus-Gilbert algorithms.

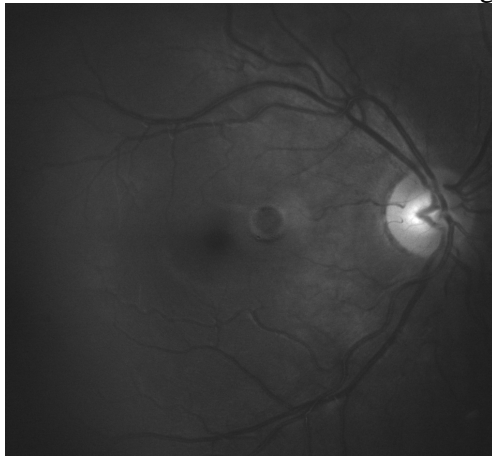
The clinical validity of hyperspectral imaging is still to be demonstrated by means of recruiting a sufficient number of patients. This will help to establish a well defined merit of certain retinal disease associated with alteration in blood oxygen saturation, such as glaucoma, age related macular degeneration, diabetic retinopathy, vein and artery occlusions. As the work in this thesis has enhanced the understanding of spectral signatures of haemoglobin to enable development and design of spectral fundus camera for retinal oximetry, there is a potential to investigate the spectra of other chromophores associated with the pathogenesis of retinal diseases such as cytochrome oxidase and neuroglobin, .

Appendix A

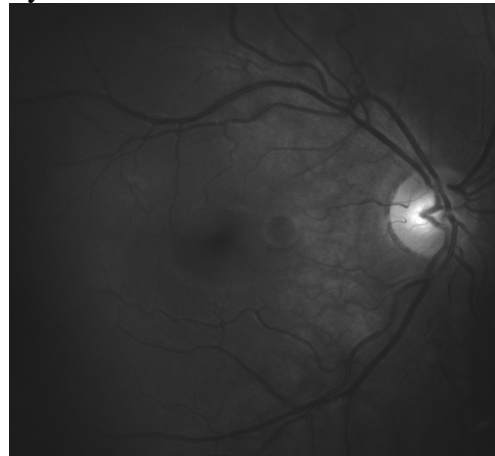
Healthy subject

This appendix includes retinal images of the left and the right eye of healthy subject:

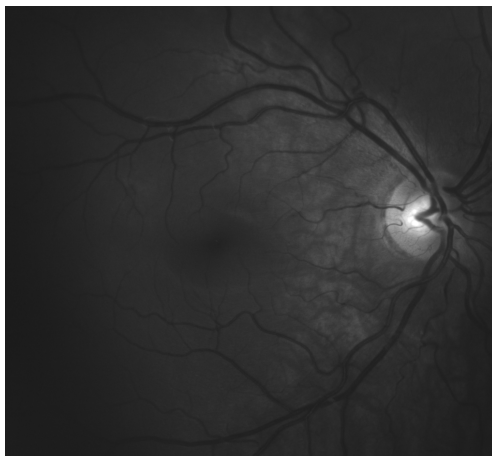
Right eye



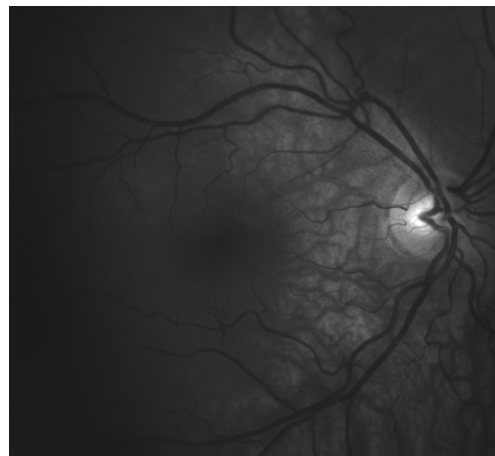
500 nm



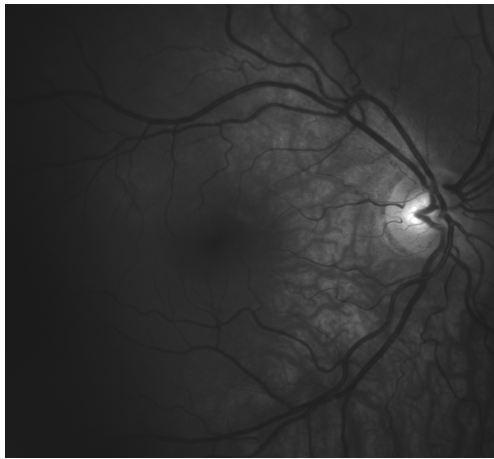
520 nm



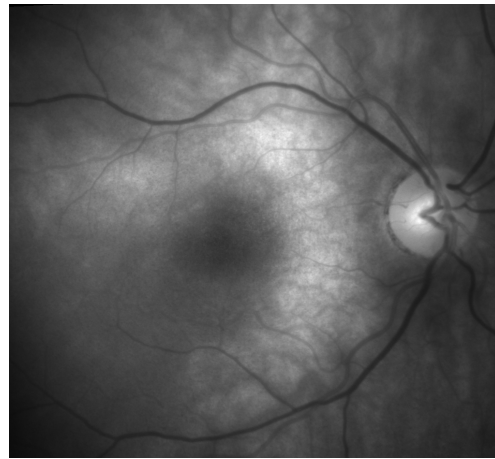
540 nm



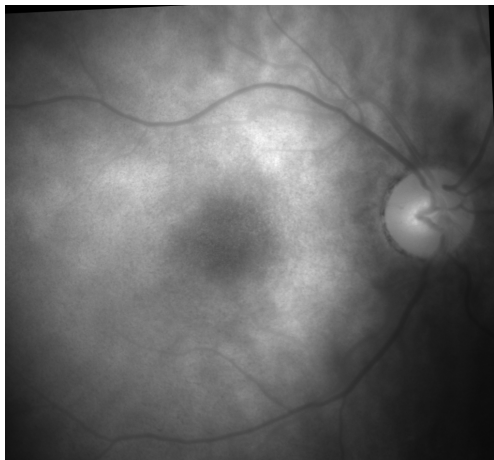
560 nm



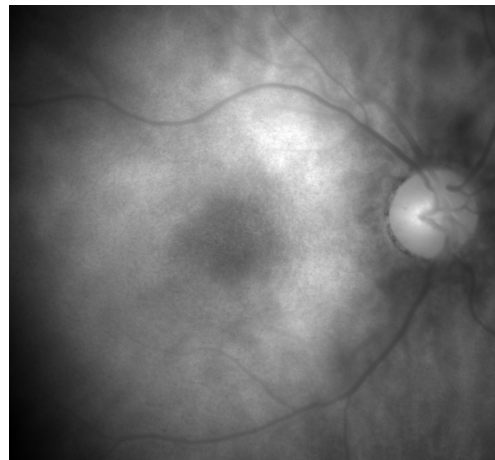
580 nm



600 nm

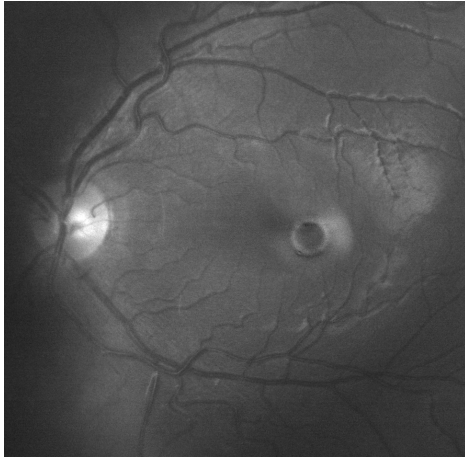


620 nm

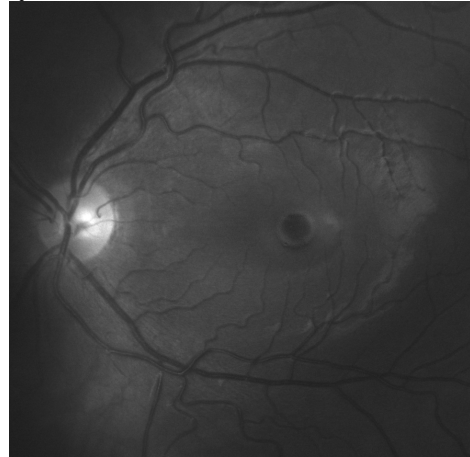


640 nm

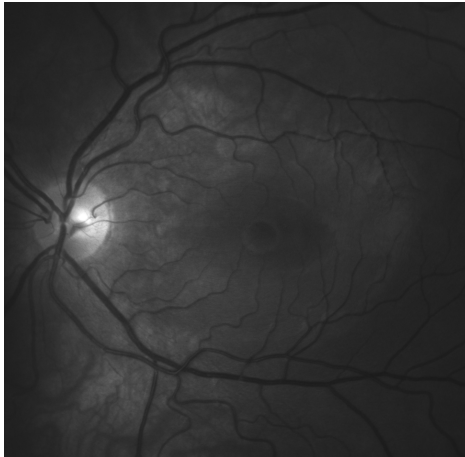
Left eye



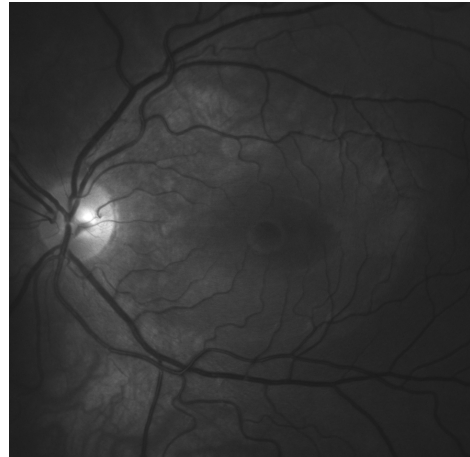
500 nm



520 nm



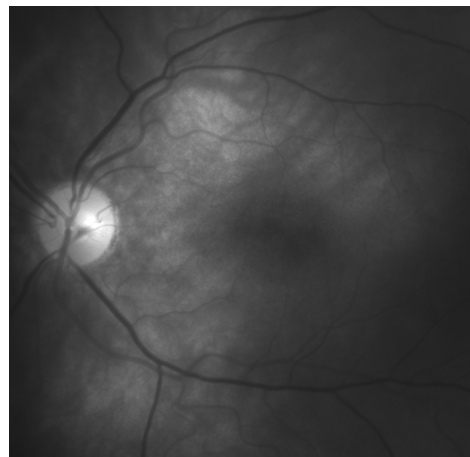
540 nm



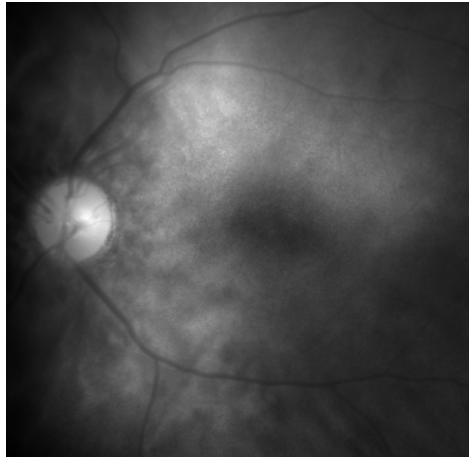
560 nm



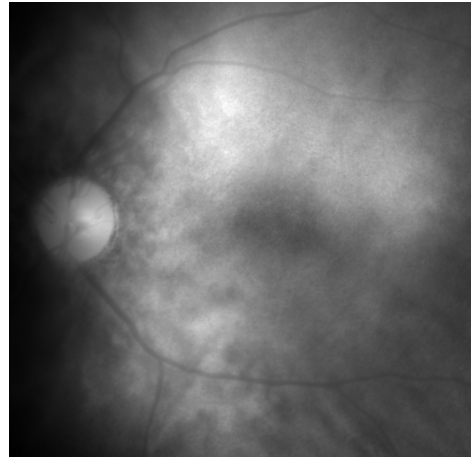
580 nm



600 nm



620 nm



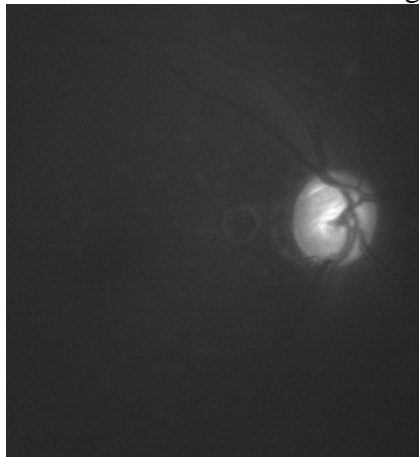
640 nm

Appendix B

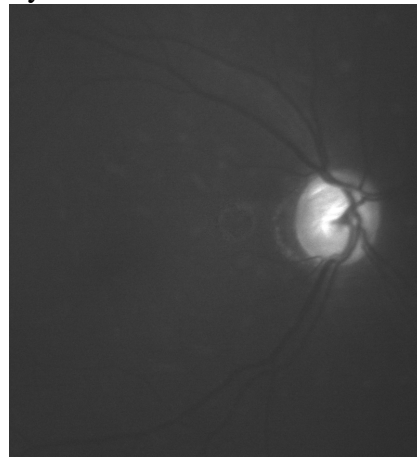
Glaucoma

This appendix includes retinal images of the left and the right eye of Glaucoma subject:

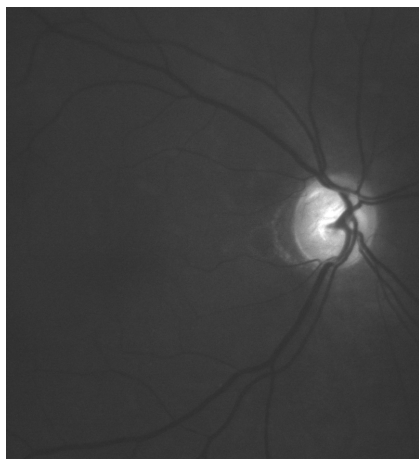
Right eye



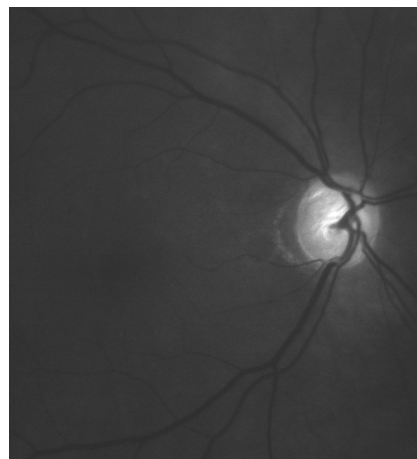
500 nm



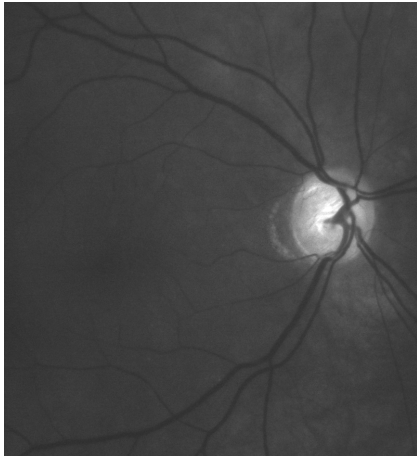
520 nm



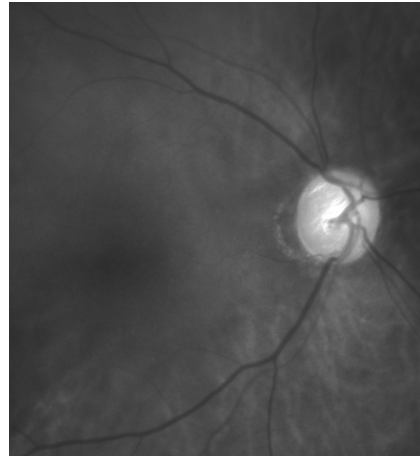
540 nm



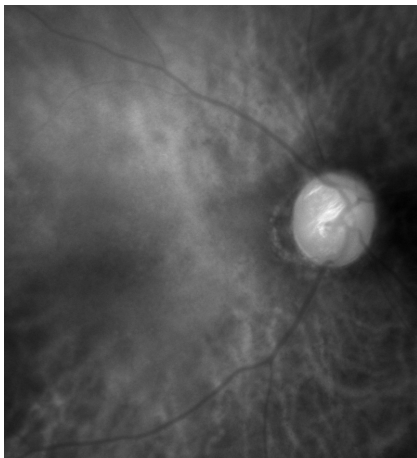
560 nm



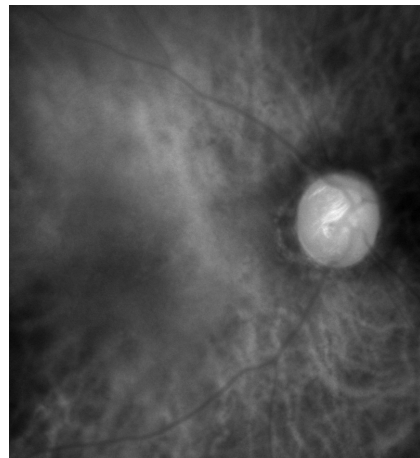
580 nm



600 nm



620 nm



640 nm

Appendix C

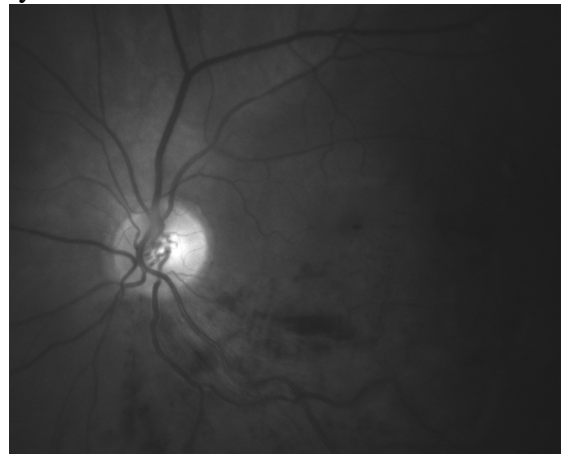
Retinal vein occlusion

This appendix includes retinal images of the left and the right eye of retinal vein occlusion subject:

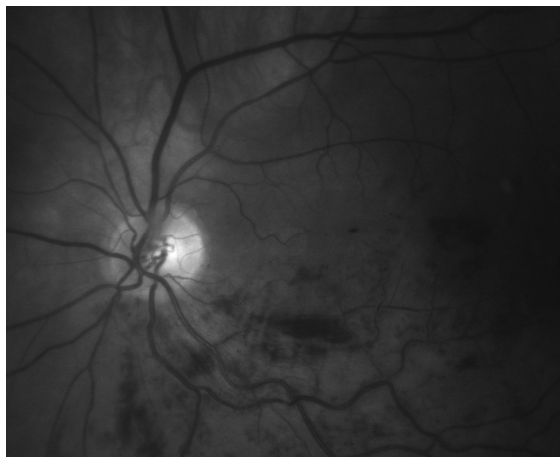
Left eye



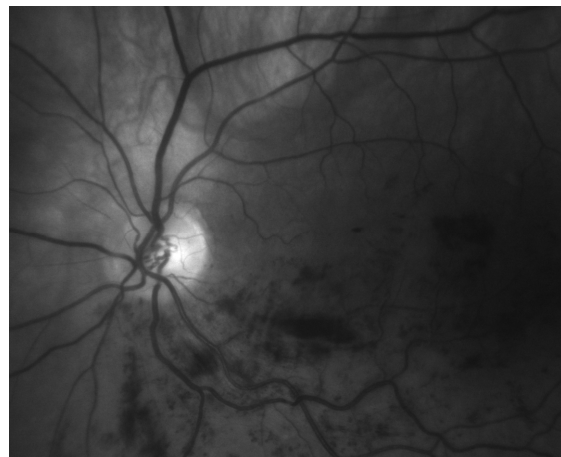
500 nm



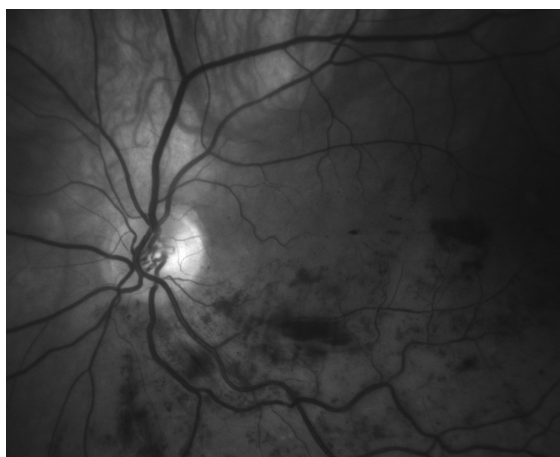
520 nm



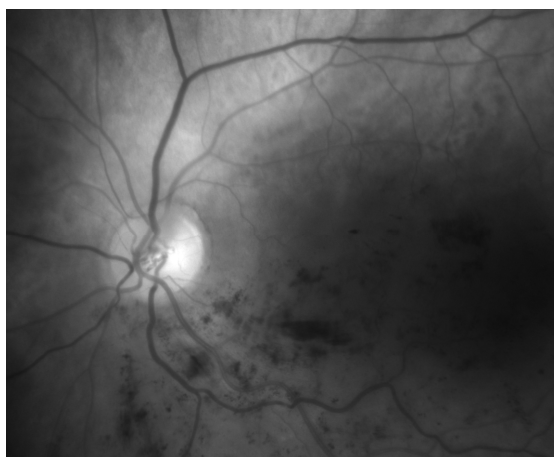
540 nm



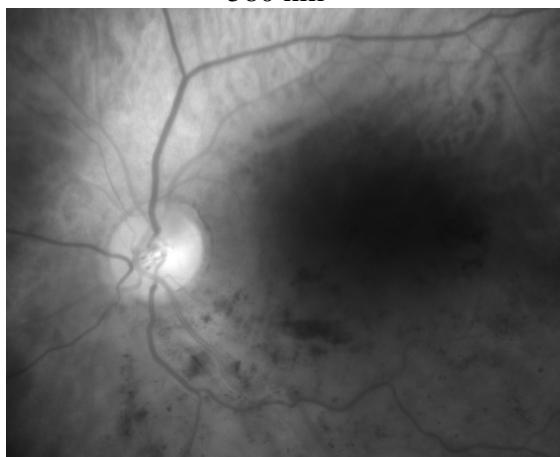
560 nm



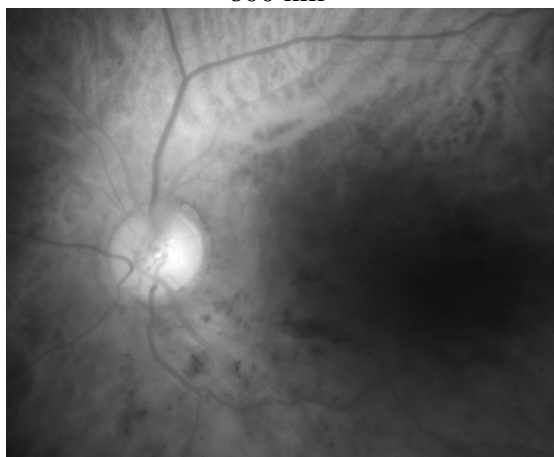
580 nm



600 nm



610 nm



620 nm

References

Aloni.E.H, Pollack.A, Grinvald.A, Vanzetta.I,Nelson.D.A, Non-invasive imaging of retinal flow and oximetry by a new Retinal Function Imager. *Invest Ophthalmol Vis Sci.* 43: E-Abstract 2552, 2002.

Arimoto.A, Furukawa.H, Retinal blood oxygen saturation mapping by multispectral imaging and morphological angiography. *IEEE Eng Med Biol Soc*,1627-30,2007.

Alabboud.I, McNaught.A, Mordant,D, and Harvey.A.R, Quantitative Spectral Imaging of the Retina. *Invest. Ophthalmol. Vis. Sci*,48: E-Abstract 2581, 2007.

Adams.J.B, Smith.M.O, Johnson.P.E, Spectral mixture modeling: A new analysis of rock and soil types at the Viking Lander 1 site, *Journal of Geophysical Research*,91:8090-8112, 1985.

Alpern.M, Thomsen.S, Lee.M.S, Spectral transmission of visible light by the living human eye.*J.Opt.Soc.Am*,55: 723,1965.

Anderson.N.M and Sekelj.P, Light-absorbing and scattering properties of nonhemolysed blood, *Phys. Med. Biol.* 12, 173–184 ,1967.

Anderson.N.M and Sekelj.P, Reflection and transmission of light by thin films of nonhaemolysed blood, *Phys. Med. Biol.*12, 185–192 ~1967.

Algazi.V.R, Keltner.J.L, Johnson.C.A, Computer analysis of the optic cup in glaucoma. *Invest Ophthalmol Vis Sci.* 26(12):1759-70,1985.

Alabboud.I, Muyo.G, Gorman.A, Mordant.D, McNaught.A, Petres.C, Petillot.Y.R, Harvey.A.R, New spectral imaging techniques for blood oximetry in the retina. *Proc. SPIE*, 6631: 66310L, 2007.

Assendelft.V O.W. Spectrophotometry of Hemoglobin Derivatives,C.C. Thomas, Springfield, IL, 1970.

Borovoi.A.G, Naats.I.E, Oppel.U.G, Scattering of light by a red blood cell, *J. Biomedical Optics*, 3(03): 364-372, 1998.

Beach.J.M, Schwenzer. K.J, Srinivas.S, Kim.D, Tiedeman.J.S, Oximetry of retinal vessels by dual-wavelength imaging: calibration and influence of pigmentation. *J Appl Physiol*,86(2):748-58,1999.

Beach.J.M, Ning.J, Khoobei.B, Hyperspectral Algorithm for Mapping Tissue Oxygen Saturation. Signal Processing Symposium, *Proceedings of the 7th Nordic*, 142-145,2006.

Broadfoot.K.D, Gloster.J, Greaves.D.P, Photoelectric method of investigating the amount and oxygenation of blood in the fundus oculi. *Br J Ophthalmol*, 45(3):161-82, 1961.

Brown.L, A survey of images registration techniques. *ACM Comput. Surv*,24(4), 1992.

Cohen. A.J, Laing.R.A, Multiple scattering analysis of retinal blood oximetry. *IEEE Trans Biomed Eng*,23(5):391-400, 1976.

Cideciyan.A.V, Registration of ocular fundus images. *IEEE Eng Med. Biol.* 14:52–58, 1995.

Chen.H.C, Pael.V, Wiek.J, Vessel diameter changes during the cardiac cycle. *Eye*,8:97-103,1994.

Cohen.L & Kimmel.R, Global minimum for active contour models: A minimal path approach. *International Journal of Computer Vision* 24(1), pp. 57–78, 1997.

Cree.M.J, Olson.J.A, McHardy.K.C, The preprocessing of retinal images for the detection of fluorescein leakage. *Physics in Medicine and Biology* 44(1): 293–308, 1999.

Chaudhuri.S, Chatterjee.S, Katz.N, Nelson.M, Goldbaum.M, Detection of Blood Vessels in Retinal Images Using Two-Dimensional Matched Filters, *IEEE transactions on medical imaging*.8(3),1989.

Charman.W.N, Jennings.J.A, 1976. Objective measurement of the longitudinal chromatic aberration of the human eye. *Vision Research*, 16:999–1005, 1976.

Cideciyan.V, Jacobson.S.G, Kemp.C.M, Knightton.R.W, and Magel.J.H, Registration of high resolution images of the retina. *Proc SPIE*, 1652: 310-322, 1992.

Delpy.D.T, Cope.M, Van der Zee.P, Arridge.S, Wray.S and Wyatt.J, Estimation of optical pathlength through tissue from direct time of flight measurement. *Phys. Med. Biol.* 33:1433-1442, 1988.

De Castro.E, Cristini.G, Martelli.A, Morandi.C, and Vascotto.M, Compensation of random eye motion in television ophthalmoscopy: preliminary results. *IEEE Trans Med Imag*, 6:74-81, 1987.

Delori.F.C. Noninvasive technique for oximetry of blood in retinal vessels. *Appl Opt*, 27(6):1113-1125,1988.

Delori.F.C, Gragoudas.E.S, Francisco.R, Pruett.R.C, Monochromatic ophthalmoscopy and fundus photography,The normal fundus. *Arch of Ophthalmol*,95:861–868,1977.

Delori.F.C, Pflibsen.K, Spectral reflectance of the human ocular fundus. *Appl Opt*, 28:1061-1077, 1989.

Drewes.J, Smith.M.H, Denninghoff. K.R, and Hillman.L.W, An instrument for the measurement of retinal vessel oxygen saturation. *Proc SPIE* 3591: 114-120, 1999.

Denninghoff.K.R, Smith.M.H, Optical model of the blood in large retinal vessels. *J Biomed Opt*, 5(4):371-4,2000.

Denninghoff.K.R, Smith.M.H, Chipman.R.A, Hillman.L.W, Jester.P.M, Hughes.C.E, Kuhn.F ,Rue.L.W, Retinal Large Vessel Oxygen Saturations Correlate with Early Blood Loss and Hypoxia in Anesthetized Swine. *The Journal of Trauma: Injury, Infection, and Critical Care*, 43: 29-34, 1997.

Denninghoff.K.R, Smith.M.H, Hillman.L, Retinal Imaging Techniques in Diabetes.Diabetes Technology & Therapeutics, 2000.

Descour.M.R, Volin.C.E, Dereniak.E.L, Thome.K.J, Schumaker.A.B, Wilson.D.W, P. D. Maker, Demonstration of a high speed non-scanning imaging spectrometer. *Opt. Letters*, 22 (16):1271-1273, 1997.

Deschamps.T, Schwartz.P, Trebotich.D et al, Vessel segmentation and blood flow simulation using level-sets and embedded boundary methods. *In CARS 2004 Computer Assisted Radiology and Surgery*. Chicago, USA, June 2004.

Ege.B.M, Hejlesen.O, V.Larsen.O, Moller.K, B.Jennings, D.Kerr, and D.A.Cavan, Screening for diabetic retinopathy using computer based image analysis and statistical classification, *Computer Methods and Programs in Biomedicine*, 62:165-175, 2000.

Fercher.A.F, Optical coherence tomography. *J. Biomed. Opt*, 1:157–173,1996.

Faber.D, Aalders.M, Mik.E, Hooper.B, Gemert.M, and Van Leeuwen.T, Oxygen saturation-dependent absorption and scattering of blood. *Physical Review Letters*, 93, 2004.

Forrester.J.V, Dick.A.D, McMenamin.P.G, and Lee.W.R, The eye: Basic sciences In Practice, second edition edn,W.B.Saunders,London,2002.

Friebel.M, Helfmann.J, Netz.U, Meinke.M, Influence of oxygen saturation on the optical scattering properties of human red blood cells in the spectral range 250 to 2000 nm. *J.Biomed.Opt*, 14(3)034001.2009.

Goshtasby.A, 2-D and 3-D Image Registration: for Medical, Remote Sensing, and Industrial Applications. Wiley-Interscience, 1 ed ,2005.

Gloster.J, Fundus oximetry. *Exp Eye Res*, 6(3):187-212, 1967.

Gorrand.J.M , Alfieri.R , and Boire.J.Y, Diffusion of the retinal layers of the living human eye.*Vision research* ,24(9):1097-106, 1984.

Gorrand.J.M, Delori.F.C, Reflectance and curvature of the inner limiting membrane at the foveola. *J opt soc of Amer*,16(6): 1229-1237,1999.

Gloster.J, 1983. Fundus reflectometry in the study of the choroidal circulation. *Int. Ophthalmol*,6:109–118,1983.

Gottfredsdottir.M, Hardarson.S.H, and Stefansson.E, The Effect of Glaucoma Surgery on Retinal Oxygen Saturation. *Invest. Ophthalmol. Vis. Sci*,49: E-Abstract 4614,2008.

Gat.N, Imaging spectroscopy using tunable filters; a review. *Proc SPIE*, 4056: 50-64, 2000.

Gonzalez.R, Woods.R, Digital image processing, Addison-Wesley Pub (Sd), 3rd edition (1992).

Gabel.V.P, Birngruber.R, Hillenkamp.F, Visible and near infrared light absorption in pigment epithelium and choroid. *Excerpta Medica, International Congress Series*, 658–662, 1978.

Geeraets.W.J, Williams.R.C, Chan.G, Ham.W.T , Guerry.D, and Schmidt.F.H, The Relative Absorption of Thermal Energy in Retina and Choroid. *Invest. Ophthalmol.* 1:340,1962.

Harvey.A.R, Fletcher-Holmes.D.W, Birefringent Fourier-transform imaging spectrometer. *Optics Express*, 12(22):5368-5374, 2004.

Harvey.A.R and Fletcher-Holmes.D.W, Imaging Apparatus International Patent WO2004-005870-A1 (2004)

Harvey. A.R, Lawlor. J, McNaught. A.I, Williams. J.W and Fletcher-Holmes. D.W, Hyperspectral imaging for the detection of retinal diseases. *Pro.SPIE*, 4816:325-335, 2002.

Harvey. A.R, Fletcher-Holmes. D. W, Gorman.A, Altenbach.K, Arlt.J and Read. N. D, Spectral imaging in a snapshot. *Proc. SPIE*, 5694: 110-119,2005.

Harvey.A.R, AlAbboud.I, Goreman.A, McNaught.A, Ramachandran.S, Theofanidou.E, Spectral imaging of the retina. *Proc.SPIE*, 6047:604713/1-604713/9, 2005.

Harvey.A.R, Lawlor.J, McNaught.A.I, Williams. J.W and Fletcher-Holmes. D.W, Hyperspectral imaging for the detection of retinal diseases. *Pro.SPIE*, 4816:325-335, 2002.

Harris.A, Dinn.R.B, LKagemann.L, Rechtman.E, A review of methods for human retinal oximetry. *Ophthalmic Surg Lasers Imaging*, 34:152–16, 2003.

Howes.D, Clare.P, Oxford.W, Murphy.S, Endmember selection techniques for improved spectral unmixing. *Proc SPIE*,5425, 2004.

Heachts.E,Optics. Fourth Edition, Addison Wesley Longman, 2002.

Hodgkinson.I, Greer.P.B, and Molteno.A.C.B, Pointspread function for light scattered in the human ocular fundus. *J Opt Soc Am*,11:479–486,1994.

Hickam.J.B, Frayser.R, Ross.J.C, A study of retinal venous blood oxygen saturation in human subjects by photographic means. *Circulation*, 27:375-385, 1963.

Hickam.J.B, Frayser.R, Spectrophotometric determination of blood oxygen. *J Biol Chem*, 180(1):457-465, 1949.

Hammer.M, Schweitzer.D, Leistritz.L, Scibor.M, Donnerhacke.K, and Strobel.J, Imaging spectroscopy of the human ocular fundus in vivo, *J.biomed optics* 2(4): 418–425, 1997.

Hammer.M, Leistritz.S, Leistritz.L, Schweitzer.D, Light paths in retinal vessel oximetry. *IEEE Trans Biomed Eng*, 48(5):592-8,2001.

Hee.M.R, Izatt.J.A, Swanson.E.A, Huang.D, Schuman.J.S, Lin.C.P, Puliafito.C.A, Fujimoto.J.G, Optical coherence tomography of the human retina, *Arch of Ophthalmol*, 113:325–332,1995.

Hernandez.M, Barrenab.R, Hernandezb.G et al. Pre-clinical evaluation of implicit deformable models for three-dimensional segmentation of brain aneurysms in cta. *SPIE Medical Imaging*, volume 5032, pp. 1264–1274. 2003.

Hammer M, .ARoggan, Schweitzer.D, Müller.G, Optical properties of ocular fundus tissues : an in vitro study using the double-integrating-sphere technique and inverse Monte Carlo simulation, *Phys. Med. Biol*,40: 963-978,1995.

Hammer.M,Yaroslavsky.A.N, Goldbach.T, and Schweitzer.D, A scattering phase function approximation for blood with physiological haematocrit. *Phys.Med.Biol*.46:65-69,2001.

Hammer.M, Schweitzer.D, Michel.B, Thamm.E, and Kolb.A, Single Scattering by Red Blood Cells. *Appl Opt*,37:7410-7418,1998.

Smith.M.H, Denninghoff.K.R, Lompad.A and Hillman.L.W, Effect of multiple light paths on retinal vessel oximetry. *Appl. Opt*, 39:1183-1193,2000.

Hammer.M, Leistritz.S, Leistritz.L, Schweitzer.D, Thamm.E, Donnerhacke.K, Monte-Carlo simulation of retinal vessel profiles for the interpretation of in-vivo oxymetric measurements by imaging fundus reflectometry. *Proc SPIE*,3192:211-218,1997.

Hammer.M, Vilser.W, Riemer.T, and Schweitzer.D, Retinal vessel oximetry-calibration, compensation for vessel diameter and fundus pigmentation, and reproducibility. *J.Biomed Opt*, 13, 2008.

Hardarson.S.H, Harris.A, Karlsson.R.A, Halldorsson.G.H, Kagemann.L, Rechtman.E, Zoega.G.M, Eysteinnsson.T, Benediktsson.J.A, Thorsteinsson.A, Jensen.P.K, Beach.J and Stefánsson.E, Automatic Retinal Oximetry. *Investigative Ophthalmology and Visual Science*, 47: 5011-5016,2006.

Hardarson.S.H, Karlsson.R.A, Eysteinnsson.T, Beach.J.M, Benediktsson.J.A, Stefansson.E, Retinal Oxygenation After Laser Photocoagulation in Patients With Proliferative Diabetic Retinopathy. *Invest. Ophthalmol. Vis. Sci*,49: E-Abstract 5366,2008.

Holst.G.C, CCD Arrays cameras and displays. JCD publishing, *SPIE PRESS*, 2ed, 1998

Imai.F.H, Rosen.M.R, Berns.R.S, Comparative study of metrics for spectral match quality. *Proceeding of CGIV*, 492-496, 2002.

Ito.M, Murayama.K, Deguchi.T, Takasu.M, Gil.T, Araie.m, Peyman.G, Yoneya.S, Oxygen saturation levels in the juxta-papillary retina in eyes with glaucoma. *Exp Eye Res*, 86(3):512-8,2008.

Jasiobedzki.P, Registration of retinal images using adaptive adjacency graphs. *Proc. Sixth Annual IEEE Symposium Computer-Based Medical Systems*, 40-45, 1993.

Jacques.S.L, Glickman.R.D, Schwartz.J.A, Internal absorption coefficient and threshold for pulsed laser disruption of melanosomes isolated from retinal pigment epithelium. *Proc SPIE*, 2681:468-477, 1996.

Johnson.W.R, Wilson.D.W, Fink.W, Humayun.M, Bearman.G, Snapshot hyperspectral imaging in ophthalmology. *J Biomed Opt*, 12(1):014036, 2007.

Jagoe.R, Arnold.J, Blauth.C, Smith.P, Taylor.K.M, and Wootton.R, Retinal vessel circulation patterns visualized from a sequence of computer-aligned angiograms. *Invest Ophthalmol Vis Sci*, 34: 2881-2887, 1993.

Khoobehi.B, Beach.J.M,H. Kawano.H, Hyperspectral imaging for measurement of oxygen saturation in the optic nerve head. *Invest Ophthalmol Vis Sci*, 45(5):1464-72,2004.

Keshava.N and Mustard.J.F, spectral unmixing. *IEEE signal processing Magazine*,44-57, 2002.

Knighton.R.W, Jacobson.S.G, Kemp.C.M, The spectral reflectance of the nerve fiber layer of the macaque retina.*Invest.Ophthalmol.Vis.Sci*,30: 2392–2402, 1989.

Knighton.R.W, Baverez.C, Bhattacharya.A, The directional reflectance of the retinal nerve fiber layer of the toad.*Invest.Ophthalmol.Vis.Sci*.33: 2603–2611, 1992.

Knighton.R.W, Huang.X.R, Directional and spectral reflectance of the rat retinal nerve fiber layer.*Invest.Ophthalmol, Vis.Sci*,40:639–647,1999.

Knighton.R.W, Qian.C, 2000. An optical model of the human retinal nerve fiber layer: implications of directional reflectance for variability of clinical measurements. *J.Glaucoma*, 9:56–62,2000.

Lompado.A, Smith.M.H, and Hillman.L.W, Multispectral confocal scanning laser ophthalmoscope for retinal vessel oximetry. *Proc. SPIE*, 3920: 67 ,2000.

Lyot.B, Filter monochromatique polarisant et ses application en physique solaire. *Ann. Astrophys*,7:32,1944.

Lee.D, Krile.T, and Mitra.S, Power cepstrum and spectrum techniques applied to image registration. *Appl Opt*, 27:1099-1106, 1988.

Liou.H.L & Brennan.N.A, Anatomically accurate finite model eye for optical modelling, *J opt soc of Amer* ,14: 1684-1695,1997.

Lindberg.L.G and Oberg.P.A, Optical properties of blood in motion. *Opt.Eng*,32:253-257,1993.

Laing.R.A, Danisch.L.A, Young.L.R, The choroidal eye oximeter: an instrument for measuring oxygen saturation of choroidal blood in vivo. *IEEE Trans Biomed Eng*, 22(3):183-95,1975.

Laing.R.A, Cohen.A.J, Friedman.E, Photographic measurements of retinal blood oxygen saturation: falling saturation rabbit experiments. *Invest Ophthalmol*,14(8):606–610, 1975.

Lee.V.S, Tarassenko.L, Absorption and multiple scattering by suspensions of aligned red blood cells. *J.Opt.Soc.Am*.8:1135-1141,1991.

Mordant.D, AlAbboud.I, Muyo.G, Harvey.A.R, and McNaught.A, Retinal Vessel Oxygen Saturation Measurements in Asymmetrical Primary Open Angle Glaucoma Using Hyperspectral Imaging. *Invest. Ophthalmol. Vis. Sci*,50: E-Abstract 5803, 2009.

.Menon.I.A , Persad.S , Haberman.H.F , Kurian.C.j, Basu.P.K, A qualitative study of the melanins from blue and brown human eyes. *Exp Eye Res*,34(4):531-7,1982.

Meinke.M, Gersonde.I, FriebeI.M, Helfmann.J, and Muller.G, Chemometric determination of blood parameters using visible-near infrared spectra. *Appl Spectroscopy*,59:826-835,2005.

Meinke.M, Muller.G, Helfmann.J, and FriebeI.M, Empirical model functions to calculate hematocrit-dependant optical properties of human blood. *App Opt*, 46(10): 1742-1753, 2007.

Magotra.N, Wu.E, Soliz.P, Truitt.P, Gelabert.P, Stetzler.T, Hyperspectral biomedical image formation, *IEEE LEOS annual meetings conference proceedings*, 1:462-465,1999.

Macrae.R.A, McClure.J.A, and Latimer.P, Spectral transmission and scattering properties of red blood cells. *J Opt Soc Am*, 51: 1366-1372, 1961.

Malladi.R, Sethian.J & Vemuri.B, Shape modelling with front propagation: A level set approach. In *IEEE Transaction on Pattern Analysis and Machine Intelligence*, 17:158–175. 1995.

Michelson.G, Scibor.M, Intravascular oxygen saturation in retinal vessels in normal subjects and open-angle glaucoma subjects. *Acta Ophthalmologica Scandinavica*, 84(3):289-295, 2006.

Naomi.A.M and Sekelj.P, Light-absorbing and Scattering Properties of Nonhaemolysed Blood. *Phys. Med. Biol.* 12:173-184, 1967.

Norren.D.V, Vos.J.J, Spectral transmission of the human ocular media. *Vision Research*, 14:1237–1244, 1974.

Norren.V.D, Tiemeijer.L.F, Spectral reflectance of the human eye. *Vision Research*. 26:313–320, 1986.

Nagin.P, Schwartz.B , Reynolds.G, Measurement of fluorescein angiograms of the optic disc and retina using computerized image analysis. *Ophthalmology*,92(4):547-52,1985.

Ohman.Y, On some new birefringent filter for solar research. *Ark.Aston*,2:165,1958.

Pittman.R.N, Duling.B.R, A new method for the measurement of percent oxyhemoglobin. *J Appl Physiol*,38(2):315-320, 1975.

Pittman.R.N, Duling.B.R, Measurement of percent oxyhemoglobin in the microvasculature. *J Appl Phys*, 38(2): 321-327, 1975.

Phillips.R.P, Spencer.T, Ross.P.G, Sharp.P.F, Forrester.J.V, Quantification of diabetic maculopathy by digital imaging of the fundus. *Eye*,5(1):130-7,1991.

Polyak.S.L,The Retina. University of Chicago Press, Chicago,1941.

Preece.S.J, Claridge.E, Monte Carlo modelling of the spectral reflectance of the human eye, *Phys. Med. Biol*, 47:2863–2877, 2002.

Poger.S, Angelopoulou.E, Multispectral sensors in computer vision. Stevens Institute of Technology, Department of Computer Science, Technical Report, CS-2001-3. August 2001.

Poger.S, Angelopoulou.E, Selecting Components for building multispectral sensors. IEEE CVPR Technical Sketches (CVPR Tech Sketches) 2001. *IEEE Computer Society Press*, 2001.

Press.W.H, Flanney.B.P, Tenkolsky.S.A, Vetterling.W.T, Numerical Recipes in C --- The art of Scientific Computing, Cambridge University press, Cambridge, England,1990.

Puliafito.C.A, Hee. M.R, Lin. C.P, Reichel. E, Schuman. J.S, Duker. J.S,Izatt. J.A, Swanson. E.A, Fujimoto. J.G, Imaging of macular diseases with optical coherence tomography. *Ophthalmology*, 102:217–229,1995.

Petres.C, Pailhas.Y, Patron.P, Petillot.Y, Evans.J and Lane.D, Path Planning for Autonomous Underwater Vehicles, *IEEE transactions on Robotics*,32(2),331-341,2007.

Petres.C,Trajectory planning for Autonomous Underwater Vehicles,PhD thesis, Heriot-Watt University,2007.

Peli.E, Lahav.M, Drusen measurement from fundus photographs using computer image analysis. *Ophthalmology*,93:1575-1580,1986.

Peli.E, Augliere.R.A, and Timberlake.G.T, Feature-based registration of retinal images. *IEEE Trans. Med. Imag* 6:272-278,1987.

Roggan.A, Friebel.M, Dorschel.K, Hahn.A, and Muller.G, Optical properties of circulating human blood in the wavelength range 400-2500 nm. *J.Biomed.Opt*, 4:36-46, 1999.

Rakebrandt.F, North.R.V, Erichsen.J.T, Drasdo.N, Fowler.C, Cowey.A, and Morgan.J.E, The Construction of a Model Eye for Investigation of Laser-Tissue Interactions in Scanning Laser Ophthalmoscopy. *Optometry and Vision Science*, 80(3):252–258, 2003.

Ramella-Roman.J, Mathews.S.A, Spectroscopic Measurements of Oxygen Saturation in the Retina. *IEEE Journal of Selected Topics in Quantum Electronics*,13(6):1697-1703,2007.

Rudnicka.R, Edgar.D.F, Bennett.A.G, Construction of a model eye and its applications. *Ophthalmic Physiol Opt*, 12:485–90,1992.

Stockman.A, MacLeod.D.I, Johnson.N.E, Spectral sensitivities of the human cones. *J.Opt. Soc.Am.* 10:2491–2521,1993.

Siesky.B, Harris , Cantor.L, Kagemann.L, Weitzman.Y, McCranor.L, Marques.C, Werne.A, E.Stefansson. A comparative study of the effects of brinzolamide and dorzolamide on retinal oxygen saturation and ocular microcirculation in patients with primary open-angle glaucoma. *Br J Ophthalmol*, 92(4):500-4,2008.

Schweitzer.D, Guenther.S, Scibor.M, Hammer.M, Spectrometric investigations in ocular hypertension and early stages of primary open angle glaucoma and of low tension glaucoma-multisubstance analysis. *Int Ophthalmol*,16(4-5):251-257, 1992.

Schweitzer.D, Hammer.M, Kraft.J, Thamm.E, Königsdörffer.E, Strobel.J, In vivo measurement of the oxygen saturation of retinal vessels in healthy volunteers. *IEEE Trans Biomed Eng*,46(12):1454-1465,1999.

Schweitzer.D ,Thamm.E, Hammer.M, Kraft.J, A new method for the measurement of oxygen saturation at the human ocular fundus. *Int Ophthalmol*, 23(4-6):347-353, 2001.

Schweitzer.D, Lang.G.E, Remsch.H, Beuermann.B, Hammer.M, Thamm.E, Spraul.C.W, Lang. G.K, Age-related maculopathy: comparative studies of patients, their children and healthy controls. *Ophthalmologe*,97:84–90, 2000.

Stratis.D.N, Eland.K.L, Carter.J.C, Tomlinson.S.J, and Angel.S.M, Comparison of Acousto-optic and liquid crystal tunable filters for Laser-induced breakdown spectroscopy. *Appl spectroscopy*, 55:999-1004,2001.

Stefánsson.E, Pedersen.D.B, Jensen.P.K, Cour.M, Kiilgaard.J.F, Bang.K and Eysteinnsson.T, Optic nerve oxygenation. *Progress in retinal and eye research*, 24(3):307-332, 2005.

Sethian. J.A, Level Set Methods and Fast Marching Methods. Cambridge University Press, Cambridge, Massachusetts, 1999.

Settle.J.J, Drake.N.A, linear mixing and the estimation of ground cover proportions. *International journal of remote sensing*,14:1159-1177,1993.

Smith.M.H, Optimum wavelength combinations for retinal vessel oximetry. *Appl Opt*, 38(1):258-267,1999.

Smith.M.H, Denninghoff.K.R, Hillman.L.W, and R.AChipman. Oxygen saturation measurements of blood in retinal vessels during blood loss. *J Biomed Opt* 3: 296-303, 1998.

Smith.M.H,Denninghoff.K.R, Lompado.A, Hillman.L.W, Effect of multiple light paths on retinal vessel oximetry. *Appl Opt*,39(7):1183-93,2000.

Smith.M.H, Denninghoff.K.R, Lompado.A, Woodruff.J.B and Hillman.L.W, Minimizing the influence of fundus pigmentation on retinal vessel oximetry measurements. *Proc SPIE*, 4245,2001.

Sample.P.A, Esterson.F.D, Weinreb.R.N, Boynton.R.M, The aging lens: in vivo assessment of light absorption in 84 human eyes. *Invest Ophthalmol Vis Sci*, 29: 1306–1311,1988.

Smith.R.S, Stein.M.N, Ocular hazards of transscleral laser radiation. *Am. J. Ophthalmol*,66: 21,1968.

Standring.S, Gray's Anatomy: The Anatomical Basis of Clinical Practice, Churchill Livingstone, 39th Edition,2008.

Spencer.T, Olson.J.A, Mchardy.K.C, Sharp.P.F, and Forrester.J.V, An Image-Processing Strategy for the Segmentation and Quantification of Microaneurysms in Fluorescein Angiograms of the Ocular Fundus. *Computers and biomedical research*, 29:284–302,1996.

Schweitzer.D, Leistritz.L, Hammer.M, Scibor.M, Bartsch.U, and Strobel.J, Calibration-free measurement of oxygen saturation in retinal vessels of men. *Proc SPIE*,2393:210-218,1995.

Tzeng.D, Berns.R, A review of principle component analysis and its applications to color technology. *Color research and application*,30,2005.

Thamm.E , Schweitzer.D, Hammer.M, A data reduction scheme for improving the accuracy of oxygen saturation calculations from spectrometric *in vivo* measurements. *Phys. Med. Biol*,43: 1401-1411, 1998.

Tiedeman.J.S, Kirk.S.E, Srinivas.S, Beach.J.M, Retinal oxygen consumption during hyperglycemia in patients with diabetes without retinopathy. *Ophthalmology*.105(1):31-6,1998.

Truitt.P.W, Soliz.P, Meigs.A.D, Otten.L.J, Hyperspectral fundus imager. *Proc.SPIE*, 4132:356-364, 2000.

Twersky.V, Interface effects in multiple scattering by large, lowrefracting absorbing particles. *J Opt Soc Amer*, 60:908-914, 1970.

Twersky.V, Absorption and multiple scattering by biological suspensions. *J Opt Soc Amer*, 60:1084-1093, 1970.

Vanderkooi.J.M, Erecińska.M, Silver.I.A, Oxygen in mammalian tissue: methods of measurement and affinities of various reactions. *Am J Physiol*,260(6 Pt 1):C1131-50, 1991.

Van de Kraats.J, Berendschot.T.T, Van. Norren.D , The pathways of light measured in fundus reflectometry. *Vision research*, 36(15):2229-47, 1996.

Van.den.Elsen.P, Pol.E.D, and Viergever.M, Medical image matching - A review with classification. *IEEE Eng Med Bio*, 12: 26-39, 1993.

Van Buren.J.M, The retinal ganglion cell layer. Charles C. Thomas, Springfield, Illinois, 1963.

Weale.R.A, Polarized light and the human fundus oculi, *J.Physiol*,186:175–186,1966.

Weale.R.A, 1978. The eye and aging. *Interdiscipl Top Gerontol*, 13:1–13,1978.

Whittaker.D, Steen.R, Elliot.D.B, Light scatter in the normal young, elderly, and cataractous eye demonstrate little wavelength dependency. *Ophthalmol Vis Sci*,70: 963–968,1993.

Yoneya.S, Saito.T, Nishiyama.Y, Deguchi.T, Takasu.M, Gil.T, Horn.E, Retinal oxygen saturation levels in patients with central retinal vein occlusion. *Ophthalmology*, 109(8):1521-6, 2002.

Zeimer.R.C, Mori.M.T, Khoobehi.B, Feasibility test of a new method to measure retinal thickness noninvasively. *Invest. Ophthalmol. Vis. Sci*, 30:2099–2105, 1989.

Zeimer.R.C, Shahidi.M, Mori.M.T, Benhamou.E, In vivo evaluation of a noninvasive method to measure the retinal thickness in primates. *Arch of Ophthalmol*, 107:1006–1009, 1989.